Hydro-chemo-mechanical characterisation of sand/bentonite mixtures, with a focus on the water and gas transport properties

THÈSE N° 6790 (2015)

PAR

Donatella MANCA

EPFL

ÉCOLE POLYTECHNIQUE
FÉDÉRALE DE LAUSANNE

Suisse
2015

Alla mia famiglia

Table of contents

Acknowledgments

This thesis is the result of about four years of work that would have not been possible without the support of many people.

First of all I would like to thank my supervisor Prof. Lyesse Laloui for his mentorship and support during all these years. Thank you for giving me this incredible opportunity to work in such active and multicultural environment. I am deeply thankful to my co-supervisor Prof. Alessio Ferrari for being the first one who believed I could do a PhD, and for the long scientific discussions that gave a fundamental contribution to this work.

I am deeply thankful to Prof. Christoph Ancey, Prof. Mario Manassero, Dr. Paul Marschall and Prof. Marie Violay for their effort on revising my thesis work and help on improving the quality of the whole document.

For the all technical support in the laboratory I would like to thank Gilbert Gruaz, Laurent Morier, Laurent Gastaldo and Patrick Dubey. Many thanks also to Rosa Ana, Barbara, Jessica and Michela for the help with all the administrative issues

I would like to thank all my friends at LMS and LEMR who supported me during the good and the bad moments of the PhD life and always made me feel like a queen: Felipe, Francesco, Alessandro, Dimitrios, Etienne and Eleonora. Many thanks also to all the past and present LMS and LMR people: Erika, Andrea, Abdu, Roman, Victor, Quazim, Chao, Yafei, Valentina, Azad, Samila, Fabrice, John, Thomas, Suzanne, Albin, Sergio, Julien, Samuel, Bastian, Swann.

A great thank, as well as some apologies, to Paul, Ali, Timur and Giovanni, the lucky people that had the chance to share the office with me. In particular I thank Ali for the infinite moral support and the endless discussions about work and life and I apologise to Giovanni who was the victim of my end-of-the-thesis madness.

Tante grazie alla mia amica e collega Alice per avermi "convinto" a iniziare un dottorato qui, per le numerose birre al SAT, e per avermi aiutata in mille occasioni diverse. Grazie mille ai miei due life style supervisors Losannesi, Federica e Pierino, per il sostegno e per avermi mostrato tutto quello che questa città e la Svizzera hanno da offrire. Merci beaucoup à tous les amis lausannois pour le temps passe ensemble à parler et à boire des bonnes bières: Mozzi et Elisa S., Louise, Stefania, Aurora et Cristina. Ringrazio anche il gruppo di sardi a Torino, Grazia, Laura, piccolo Mocci, Tobia e Latticino, sempre pronti ad riaccogliermi per dei bellissimi weekend fuori dalla mia bolla svizzera. Grazie mille a tutti gli amici e amiche di più vecchia data che pur essendo lontani centinaia (o migliaia) di kilometri da me continuano ad essere una parte importanete della mia vita: Irene (a.k.a. "il capo"), Pablo, Giovanna e Marco, Elisa B., Ivan, Andrea (Sannino), Susanna, Andrea P., Alina.

Infine il grazie più grande va a tutta la mia famiglia (fortunatamente troppi per essere nominati tutti), per avermi sempre sostenuto e supportato durante tutti questi anni studio. Prometto che questo è l'ultimo titolo che prenderò.

Abstract

According to Swiss regulations, low and intermediate level wastes (L/ILW) should be disposed in deep geological repositories excavated about 300 to 700 meters below the ground surface, in suitable rock formations. The materials used for the construction of these repositories must guarantee a perfect isolation of the wastes from the surrounding geological formations under strong variations of environmental conditions.

Sand Bentonite (S/B) mixtures, at low bentonite content (i.e. 20 to 30 % of bentonite), are considered as appropriate sealing and backfilling material for these underground structures.

In this framework, understanding and quantifying the hydro-chemo-mechanical (HCM) phenomena governing the water and gas transport through an 80/20 sand/bentonite mixture is crucial for ensuring the safety of L/ILW repositories at both short and long terms. To this purpose, following a systematic approach, this research conducts an experimental characterisation of the mixture at macroscopic and microscopic level.

At macroscopic level, free and confined swelling tests are performed on specimens compacted to different dry densities and wetted with different pore fluids. Controlled suction confined swelling tests are carried out for determining the water retention curve, as well as the suction-swelling pressure relationship for two different densities. The water retention capacity is determined for a wide suction range. The water permeability of the mixture is measured under full saturation conditions, for a wide range of densities and using different pore fluids. The relationship between the unsaturated water permeability and the degree of saturation is determined for two target dry densities.

Gas injection tests on the mixture are performed in both saturated and unsaturated conditions. Two different experimental setups are adopted to investigate the influence of the method used for preparing the specimens, as well as how the boundary conditions affect the gas permeability and the breakthrough pressure. A highly advanced triaxial cell, equipped with a laser scanning system for measuring the radial deformations, allows analysing the volumetric response of the mixture during the gas injection.

The results reveal that the swelling pressure and the saturated hydraulic conductivity depend on the applied matric suction and on the pore water chemistry. In particular, at a low dry density, the mixture in contact with aqueous solutions loses most of its swelling capacity which causes strong increases of the saturated hydraulic conductivity. For a higher dry density, the swelling capacity of the mixture is better preserved and thus its hydraulic conductivity remains relatively low. Two distinct regions are identified in the water retention curve of the mixture: the first at a high suction, where the curve does not

depend on the void ratio, and the second at a low suction, where the curve is significantly affected by it.

Finally, an extensive microstructural characterisation is performed using the mercury intrusion porosimetry and a high-resolution scanning electron microscope. This allows relating the observed HCM behaviour at the laboratory scale to the evolution of the different pore networks during a wetting-drying cycle. The transition from double to single structure is clearly detected upon wetting. This transition justifies the generation of the swelling pressure, as well as the significant reduction of the gas permeability upon wetting. A specific relation is proposed for determining at any HCM state the relative dry density of the bentonite as a function of bentonite content in the mixture. This enables the comparison of swelling data for others bentonite-based materials prepared at different mixing ratios. The microstructural analyses, allows also the derivation of an expression for describing the geometrical permeability of the mixture upon different HCM loadings. Thanks to the proposed relation, it is possible to identify the contribution of the different pore families to water and gas transport through the active porous media.

Keywords: *Sand/bentonite mixture; MX-80 bentonite; partially saturated soils; hydro-chemo-mechanical loadings; gas injection test; swelling; water retention; two phase flow; water and gas permeability; breakthrough pressure; microstructure*

Riassunto

Secondo le normative svizzere, i rifiuti nucleari, a bassa e media intensità, devono essere stoccati in depositi geologici profondi, scavati in formazioni rocciose a bassissima permeabilità. Al fine di garantire la sicurezza di tali siti di stoccaggio, i materiali coinvolti nella costruzione del deposito dovranno garantire l'isolamento dei rifiuti sotto una grande varieta di condizioni ambientali.

Le miscele di sabbia e bentonite (S/B), contententi tra il 20 ed il 30% di bentonite, sono state selezionate come materiale di riempimento delle strutture di stoccaggio.

Al fine di garantire la sicurezza dei siti di stoccaggio nel breve e lungo periodo si richiede la profonda comprensione e la quantificazione dei fenomeni idro-chemo-meccanici (HCM) accoppiati che governano il trasporto di acqua e gas attraverso i mezzi porosi rigonfianti. Nel presente lavoro di tesi si vuole quindi caratterizzare sperimentalmente, sia a livello macroscopico che microscopico, una miscela di sabbia e bentonite di tipo 80/20 al fine di determinare i parametri che governano il flusso bifase al suo interno.

Prove di rigonfiamento libero e confinato sono state eseguite su campioni compattati a diverse densità ed utilizzando diversi fluidi permeanti. Le relazioni tra pressione di rigonfiamento e suzione, e quella tra conducibilità idraulica e suzione, sono state determinate per due densità di riferimento. Inoltre, è stata analizzata l'influenza della densità di compattazione, del tipo di fluido interstiziale e del grado di saturazione sulla conducibilità idraulica della miscela.

Le prove di iniezione al gas sulla miscela sono state eseguite sia in condizioni di completa saturazione, sia in condizione di parziale saturazione. L'influenza del metodo di imbibizione dei campioni e delle condizioni al contorno sulla permeabilità al gas, e sulla pressione di breakthrough, è stata studiata attraverso due differenti configurazioni sperimentali: in condizioni di confinamento isotropo ed a volume costante. I campioni sottoposti a confinamento isotropo sono stati testati all'interno di una cella triassiale dotata di un sistema laser per la misura del raggio del campione.

I risultati sperimentali hanno dimostrato che la pressione di rigonfiamento e la conducibilità idraulica di una miscela completamente satura dipendono fortemente dalla suzione applicata e dalla composizione chimica del fluido interstiziale. Nel caso di miscele compattate a basse densità, il contatto con soluzioni acquose provoca una notevole riduzione della capacità di rigonfiamento, con il conseguente aumento della conducibilità idraulica. Ad alte densità, la capacità di rigonfiamento della miscela e la conducibilità idraulica risultano meno alterate dalla composizione del fluido interstiziale. La curva di ritenzione della miscela è caratterizzata da due regioni distinte; ad alti valori

di suzione, essa risulta indipendente dall'indice di porosità, a bassi valori di suzione, essa è significativamente influenzata dalla variazione, seppure minima, dell'indice di porosità.

Al fine di correlare il comportamento HCM, osservato alla scala macroscopica (scala di laboratorio), all'evoluzione delle diverse famiglie di pori durante un ciclo di imbibizione ed essiccamento, si è eseguita un'approfondita caratterizzazione del materiale a livello microscopico. L'imbibizione del materiale confinato causa il passaggio, da doppia a singola struttura, dei pori. Tale analisi ha permesso l'individuazione del parametro di "densità secca relativa" della bentonite; parametro chiave per l'analisi dei dati di rigonfiamento di miscele preparate a diversi contenuti di bentonite. Si è inoltre potuto deteminare un equazione generale capace di esprimere la variazione della permeabilità geometrica della miscela sotto qualsiasi carico idro-chemo-meccanico.

__Parole chiave:__ Miscele di sabbia e bentonite; bentonite MX-80; suoli parzialmente saturi; sollecitazioni di tipo idro-chemo-meccanico; test di ignezione al gas; rigonfiamento; curve di ritenzione; flusso bifase; permeabilità ad acqua e gas;pressione di breakthrough; microstruttura

Résumé

Selon les règlementations suisses, les déchets à faible et moyenne activité (L/ILW) doivent être stockés dans des dépôts géologiques profonds, creusés entre 300 et 700 mètres sous la surface du sol, dans des formations rocheuses appropriées. Les matériaux utilisés pour la construction de ces dépôts doivent garantir une parfaite isolation entre les déchets et la milieu géologique alentour, même en cas de grandes variations des conditions environnementales.

Les mélanges Sable Bentonite, avec un faible contenu bentonitique (i.e. 20% to 30% de bentonite), sont considérés comme un matériau de remblayage adapté pour ces structures.

Dans ce contexte, la compréhension et la quantification des phénomènes hydro-mécano-chimiques (HCM) qui gouvernent le transport de l'eau et du gaz dans le mélange sable/bentonite 80/20 est cruciale pour assurer la sécurité des dépôts L/ILW, à court et à long termes. Dans ce but, une caractérisation expérimentale du mélange aux niveaux microscopique et macroscopique est menée dans ce travail de recherche en suivant une approche systématique.

Au niveau macroscopique, des tests de gonflement libre et confiné sont réalisés avec des éprouvettes de différentes densités sèches et imbibées avec différentes solutions porales. Des tests de gonflement confiné avec contrôle de la succion sont effectués pour déterminer la courbe de rétention d'eau, ainsi que la relation succion-pression de gonflement, pour deux densités différentes. La capacité de rétention d'eau est déterminée pour une large plage de variation de la succion au moyen de la méthode du papier filtre et des technique de translation d'axe et de microcellule. La perméabilité à l'eau du mélange est mesurée en conditions saturées, pour une large gamme de densités de compaction et en utilisant différents fluides poraux. La relation entre la perméabilité non-saturée à l'eau et le degré de saturation est déterminée pour deux densités sèches ciblées.

Des tests d'injection de gaz dans le mélange sont réalisés en conditions saturées et non-saturées. Deux configurations expérimentales différentes sont choisies pour étudier l'influence de la méthode utilisée pour la préparation des éprouvettes, ainsi que la manière dont les conditions de bord affectent la perméabilité au gaz et la pression critique d'ouverture. Une cellule triaxiale très avancée, équipée d'un système de balayage laser pour la mesure des déformations radiales, permet d'analyser la variation de volume du mélange pendant l'injection de gaz.

Les résultats montrent que la pression de gonflement et la conductivité hydraulique saturée dépendent de la succion matricielle appliquée et de la composition chimique de l'eau contenue dans les pores. En particulier, pour une faible densité sèche, le mélange en contact avec une solution aqueuse perd la plus grande part de sa capacité de gonflement,

ce qui cause une forte augmentation de la conductivité hydraulique saturée. Pour une densité sèche plus élevée, la capacité de gonflement du mélange est mieux préservée et sa conductivité hydraulique reste ainsi relativement basse. Deux régions distinctes peuvent être identifiées dans les courbes de rétention d'eau du mélange : la première lorsque la succion est forte, où la courbe ne dépend pas de l'indice des vides, et la seconde lorsque la succion est faible, où la courbe est cette fois affectée de façon significative par l'indice des vides.

Finalement, une description approfondie de la microstructure est réalisée au moyen de la porosimétrie à intrusion de mercure et d'un microscope à balayage électronique haute résolution. Cela permet de relier le comportement HCM observé à l'échelle du laboratoire à l'évolution des différents réseaux de pores au cours d'un cycle de mouillage-séchage. La transition d'une structure double à une structure simple est clairement mise en évidence lors du mouillage. Elle justifie la génération de la pression de gonflement, ainsi que la réduction significative de la perméabilité au gaz lors du mouillage. De plus, cette transition d'une structure double à une structure simple est partiellement réversible pour les plus petites densités sèches testées, tandis qu'elle est complètement irréversible pour les densités sèches les plus élevées. Une relation spécifique est proposée pour la détermination à n'importe quel état hydro-mécano-chimique de la densité sèche relative de la bentonite en fonction du contenu en bentonite du mélange. Cela permet de comparer les données sur le gonflement de différents matériaux basés sur la bentonite et mélangés dans différentes proportions. Les analyses microstructurelles permettent aussi de déterminer une expression décrivant la perméabilité géométrique du mélange sous différents chargements HCM. Grâce à la relation proposée, il est possible d'identifier la contribution des différentes familles de pore dans le transport de l'eau et du gaz à-travers le milieu poreux actif.

Keywords: Mélange sable/bentonite; MX-80 bentonite; sols partiellement saturés; chargements hydro-mécano-chimiques; test d'injection de gaz; gonflement; rétention d'eau; écoulement diphasique; perméabilité à l'eau et au gaz; pression d'ouverture; microstructure

List of Symbols

GREEK SYMBOLS

α	Van Genuchten coefficient	Pa
α_σ	Fraction of the total stress	-
α^b	Van Genuchten coefficient referred to the bentonite	Pa
α^M	Van Genuchten coefficient referred to the macropores	Pa
α_n	Nth solution of the eq. $a\alpha_n = \cot\alpha_n$	-
β	Coefficient in the diffusive flux formulation	-
δ_{comp}	Vertical displacement of the piston	m
δ_{el}	Elastic rebound	m
δu_w	Water pressure increment/decrement at a given step in eq: (2.24)	Pa
$\Delta M^i_{w,fp}$	Mass of adsorbed water by the filter paper at the ith step	g
ΔM^i_g	Mass the gas or water vapour that are coming from diffusion /evaporation processes	g
$\Delta M^i_{w,Tot}$	Mass of adsorbed water by the specimen and filter paper at the ith step	g
ε_0	Permittivity of vacuum	C^2/Jm
$\underline{\varepsilon}_\delta$	Error in the calculation of the dry density	kg/m^3
ε_a	Axial strain	-
$\underline{\varepsilon}_{M_s}$	Error in the calculation of the mass of the specimen	kg
$\underline{\varepsilon}_h$	Error in the calculation of the height of the specimen	m
$\underline{\varepsilon}_r$	Error in the calculation of the radius of the specimen	m
ε_{sw}	Swelling strain	-
$\varepsilon_{sw,\max}$	Maximum swelling strain	-
$\varepsilon_{sw,DW}, \varepsilon_{sw,SW}$	Maximum free swelling strain of a mixture wetted with distilled water and synthetic water, respectively	-
$\underline{\varepsilon}_V$	Error in the calculation of the volume of the specimen	m^3
ε_v	Volumetric deformation	-
ε^{el}	Elastic component of the deformation	-
ε^{pl}	Plastic component of the deformation	-
μ_g	Nitrogen's dynamic viscosity	Pa·s
μ_w	Water's dynamic viscosity	Pa·s

ϕ	Porosity	-
π	Osmotic suction	Pa
ϑ_{Hg}	Mercury-clay contact angle	rad
ϑ_w	Wetting fluid contact angle	rad
ρ	Density of a solution	kg/m^3
ρ_α	Density of a α specie	kg/m^3
ρ_d	Dry density	kg/m^3
$\rho_{d,0}$	Reference dry density	kg/m^3
$\rho_{d,Opt}$	Dry density at the optimum	kg/m^3
ρ_g	Gas density	kg/m^3
ρ_d^b	Dry density of the bentonite in the S/B mixture	kg/m^3
$\rho_d^{b,rel}$	Relative bentonite dry density	kg/m^3
ρ_d^S	Dry density of the sand in the S/B mixture	kg/m^3
ρ_{N_2}	Nitrogen density	kg/m^3
ρ_s^b	Bentonite particle density	kg/m^3
ρ_s^{Mix}	Mixture particle density	kg/m^3
ρ_s^s	Sand particle density	kg/m^3
ρ_w	Water density	kg/m^3
ϕ^b	Ratio of the bentonite void ratio to the total void ratio	-
ϕ^M	Ratio of the macro void ratio to the total void ratio	-
$\Gamma_{f,i}, \Gamma_{b,i}$	Parameters for the correction of the laser's values	-
κ	Boltzmann's constant	J/K
Π_D	Disjoining pressure	Pa
Π_e	Osmotic pressure	Pa
σ	Total stress	Pa
σ'	Effective stress	Pa
σ_{Hg}	Mercury's surface tension	N/m
σ_{nel}	Net vertical stress	Pa
σ_v	Total vertical stress	Pa
$\sigma_{v,max}, \sigma_{v,min}$	Maximum and minimum applied vertical pressure during specimen compaction	Pa
σ_w	Wetting fluid surface tension	N/m
τ	Tortuosity	-
Ω	Flow domain for the analyses of the fluid transport	m^2

Ω^b	Area of the bentonite aggregates within the sand	m^2
Ω^m	Area of the micropores within the bentonite aggregates	m^2
Ω^n	Area of the nanopores within the bentonite aggregates	m^2
Ω^b_v	Area of the voids within the bentonite aggregates	m^2
Ω^S_v	Area of the voids within the sand skeleton	m^2
ω_α	Mass fraction of an α specie	-
ω_w	Molecular mass of the water vapour	Kg/mol
ψ	Total suction	Pa
$\zeta_{f,i}, \zeta_{b,i}$	Parameters for the correction of the laser's values	m

LATIN SYMBOLS

a,b,c	Length, width and height of the elementary crystal of smectite	m
a_{sw}, b_{sw}	Fitting parameters in eq. (2.6)	-
a_w, b_w, c_w	Fitting parameters in eq. (2.21)	-
$\hat{a}, \hat{b}$	Fitting parameters in eq. (2.28)	
$\tilde{a}, \hat{a}$	Slopes of the line y^{KC} and y^{LC}, respectively	1/m
$\tilde{b}, \hat{b}$	Shifting coefficient of the line y^{KC} and y^{LC}	m
A_{sp}	Cross sectional area of the specimen	m^2
A_p	Cross sectional area of the piston	m^2
b_k	Klinkenberg parameter	Pa
B	B- Skempton's coefficient	-
Bo	Bond number	-
c	Molar concentration	Mol/m^3
Ca	Capillarity number	-
C_c	Distortion number	-
C_{K-C}	Kozeny-Carman constant	-
C_U	Curvature number	-
d_i	Interlayer distance	m
d	Thickness of the electrostatic double layer	m
dx, dy, dz	Incremental distance along x, y or z	m
dt	Time interval	s
D	Dielectric constant	
$D_{\alpha\beta}$	Diffusion coefficient	m^2/s

D_w	Capillary diffusivity	m^2/s
e	Electronic charge	
e	Void ratio	-
e^b	Bentonite void ratio relative to the total solid fraction	-
$e_0^{b,rel}$	Reference relative bentonite void ratio	-
$e^{b,rel}$	Relative bentonite void ratio	-
e_{Hg}	Cumulative intruded void ratio	-
$e_{Hg,max}$	Maximum cumulative intruded void ratio	-
e_{fin}	Final void ratio reached after specimen compaction	-
e^i	Interlayer void ratio	-
e^m	Micro void ratio relative to the total solid fraction	-
e^M	Macro void ratio	-
$e^{M,rel}$	Relative macro void ratio	-
e^n	Nano void ratio relative to the total solid fraction	-
F_v	Vertical force applied to the specimen	N
$\mathbf{g}$	Gravity	m/s^2
H_0	Initial height of the specimen in the free swelling tests	m
H_{sp}	Height of the specimen	m
$H_{sp,i}$	Initial height of the specimen (before compaction)	m
$H_{sp,T}$	Target height of the specimen (after compaction)	m
$H_{1,0}$	Surplus height of the piston when the sample is not in the cell for compaction	m
$H_{1,in}$	Initial surplus height of the piston	m
$H_{1,fin}$	Final surplus height of the piston	m
i	Hydraulic gradient	-
I_P	Plasticity index	-
J_α^*	Diffusive mass flux	Kg/s
J_x	Mass flux of a fluid	kg/s
$k_{\alpha,eff}$	Effective permeability of a generic α phase	m^2
$k_{g,a}$	Apparent gas permeability	m^2
$k_{eff,g}$	Darcy's permeability at a given degree of saturation	m^2
$k_{eff,w}$	Darcy's permeability at a given degree of saturation	m^2
$\mathbf{k}_{gw}, \mathbf{k}_{wg}$	Viscous drag tensors for the gaseous and liquid phase in a	-

	two phase flow	
k_H	Henry's constant	Pa×m^3/mol
k_i	Intrinsic permeability	m^2
$k_{r,\alpha}$	Relative permeability of a generic α phase	-
k_∞	Absolute permeability	m^2
K	Hydraulic conductivity	m/s
L	Distance between the emission point of the laser and the origin	m
m_{N_2}	Nitrogen's molar mass	kg/mol
$m_{ref,i}$	Distance between the reference cylinder for the ith-laser	m
M_s^b	Solid mass of the bentonite	kg
M_s^{Mix}	Solid mass of the mixture	kg
M_s^s	Solid mass of the dry sand	kg
$M_{s,sp}$	Dry mass of the specimen	g
MW	Molar mass of montmorillonite	kg/mol
n_0	Electrolyte concentration	mol/l
n	Porosity	-
n_a, n_b, n_c	Number of smectite elementary units repeated along the a-axis, b-axis and c-axis	-
$n_{f,i}$	Corrected distance between the emission point of the laser and the surface of the specimen for the laser moving backward	m
$n_{f,i}$	Corrected distance between the emission point of the laser and the surface of the specimen for the laser moving forward	m
n_g	Porosity occupied by the gaseous phase	-
n_i	Rough distance between the emission point of the laser and the surface of the specimen	m
N_i	Coordinates of the ith-hitting point on the specimen surface	m
G_s	Specific gravity	-
N_A	Avogadro number	Molecule/mol
p	Vapour pressure in the air	Pa
p_0	Saturation vapour pressure	Pa
$\overline{P}$	Absolute pressure	Pa
P_a	Air pressure	Pa

P_{break}	Breakthrough pressure	Pa
P_{dw}	Downstream pressure	Pa
$\overline{P_g}$	Absolute gas pressure	Pa
P_g	Partial gas pressure	Pa
P_{Hg}	Mercury's pressure	Pa
P_{N_2}	Nitrogen pressure	Pa
P_{up}	Upstream pressure	Pa
P_w	Water pressure	Pa
P_{sw}	Swelling pressure	Pa
P_{sw}^i	Swelling pressure at the ith step	Pa
q_g	Gas flux	m/s
q_w	Water flux	m/s
Q_s	Volumetric flux	m^3/s
r	Reference cylinder's radius	m
R	Universal gas constant	J/(mol×K)
R_1, R_2, R_3	Coordinates of the three hitting points of the reference cylinder	m
R^b	Ratio of bentonite in the sand/bentonite mixture	%
R^s	Ratio of sand in the sand/bentonite mixture	%
R_{sp}	Specimens radius	m
$R\varepsilon_{sw}$	Swelling strain reduction factor	-
$RP_{sw,\alpha}$	Swelling pressure reduction factor	-
s	Matric suction	Pa
s_0	Reference suction	Pa
S_e	Effective degree of saturation	-
$S_{r,res}$	Residual degree of saturation	-
S_{rg}	Gas degree of saturation	-
S_r	Degree of saturation	-
S_r^b	Degree of saturation of the bentonite fraction	-
$S_r^{b,L}$	Local degree of saturation of the bentonite	-
S_r^M	Degree of saturation of the macropores	-
$S_r^{M,L}$	Local degree of saturation of the macropores	-

$S_{r,nw}$	Non wetting fluid degree of saturation	-
S_s	Specific surface area	m^2/g
t	time	s
t_c	Thickness of the ceramic disk	m
T	Temperature	°K
T_s	Surface tension	Pa/m
T_p	Tangential force arising from the friction between the piston and the o-ring	N
t_{fp}	Thickness of the filter paper	m
u_a	Air gauge pressure	Pa
u_{atm}	Absolut atmospheric pressure	Pa
v	Electronic valence	-
v	Macroscopic flow velocity	m/s
v_v^S	Velocity of the flow within the sand pores	m/s
V	Volume of the specimen in eq. (2.24)	m^3
V_{Hg}	Cumulative intruded volume	m^3
V_0	Total outflow/inflow volume of water for a given matric suction increment in eq. (2.23)	m^3
V_s	Solid volume	m^3
V_s^b	Bentonite solid volume	m^3
$V^{D/E}$	Volume of diffusive or evaporative flux	m^3
V_s^{Mix}	Total solid volume of the mixture	m^3
V_s^s	Solid volume of the sand fraction	m^3
V_v	Total voids volume	m^3
V_v^b	Bentonite voids volume	m^3
V_v^M	Macropores volume	m^3
V_w	Volume of water	m^3
V_w^b	Volume of water stored in the bentonite's pores	m^3
V_w^M	Volume of water stored in the macropores	m^3
w	Water content	-
w^b	Water content of the bentonite fraction in the mixture	-
w^i	Water content at the ith time step	-
w^{i-1}	Water content at the ith-1 time step	-
w_L	Liquid limit	%

w_M	Water content of the macropores	-
w_{Mix}	Water content of the mixture	-
w_{nw}	Non wetting fluid content	-
w_{opt}	Optimum water content	-
w_P	Plastic limit	%
w_w	Wetting fluid content	-
x	Apparent pore diameter	m
x_c, y_c	Coordinate of a generic point for the radius calculations	m
x_i, y_i	Coordinate of the centre of the reference system for the radius calculations	m
x_{max}	Larger pore diameter detected with the MIP	m
x_{min}	Smaller pore diameter detected with the MIP	m
x_t	Delimiting apparent pore diameter	m
y^{KC}	Bisector line passing through the points K and C	m
y^{LC}	Bisector line passing through the points L and C	m
z_m	Impedance of the ceramic disk	-
z_s	Impedance of the soil	-

ABBREVIATIONS

a.e.v.	Air entry value
cec	Cation exchange capacity
EDL	Electrostatic double layer
EGTS	Engineered gas transport system
LVDT	Linear variable differential transducer
MIP	Mercury intrusion porosimetry
PSD	Pore size density function
XRD	X-ray diffraction

1 Introduction

1.1 DISPOSAL OF LOW AND INTERMEDIATE LEVEL NUCLEAR WASTE (L/ILW)

In the context of nuclear wastes disposal, engineered barriers (multi-barrier concept) were proposed as a safety solution for the disposal of this type of wastes. These barriers consist of a series of components (i.e., metal canisters, bentonite-based buffer and backfilling materials, and low permeable host rocks) that will provide the proper isolation of the wastes from the human environment.

According to the Swiss regulations, the nuclear wastes can be divided into two main categories (Nagra, 2009):

1) **High-Level Wastes (HLW):** Spent Fuel (SF) not destined for reprocessing, or vitrified fission product solutions from reprocessing of spent fuel;
2) **Low and Intermediate-level Wastes (L/ILW)**; which include all other radioactive wastes; e.g., metals, organic and inorganic matters which stayed in contact with other radioactive sources.

Nagra (2008) estimated that the volume of L/ILW produced in about 50 years, can reach 93'000 m^3 (60'000 m^3 coming from operation and dismantling of the five Nuclear Power Plants, and 33'000 m^3 from research, industry and medicine).

The toxicity of any type of nuclear wastes decreases with time and they have to be isolated from the human environment. As far as the storage of L/ILW is concerned, Nagra (2010) proposed to store the wastes in deep geological repositories, excavated 300-700 meters below the ground surface, in suitable rock formation (e.g., Opalinus Clay). These hard rock formations are characterised by a very low hydraulic conductivity, good retention and self-sealing capacities (Ferrari and Laloui, 2013).

Figure 1.1-(a) shows a schematic representation of a repository for L/ILW disposal in Switzerland. The repository consists of: (1) repository caverns, (2) operational tunnels, (3) access tunnel, (4) test area and (5) ventilation tunnel. The disposal containers are placed in repository caverns of approximately 200 m in length, which are spaced 80 m apart. The containers in the cavern are supported by concrete. The space between the containers is filled with low viscosity mortar while all the remaining space between the wastes and the caverns is filled with high viscosity mortar. Finally, each cavern is closed with a concrete plug.
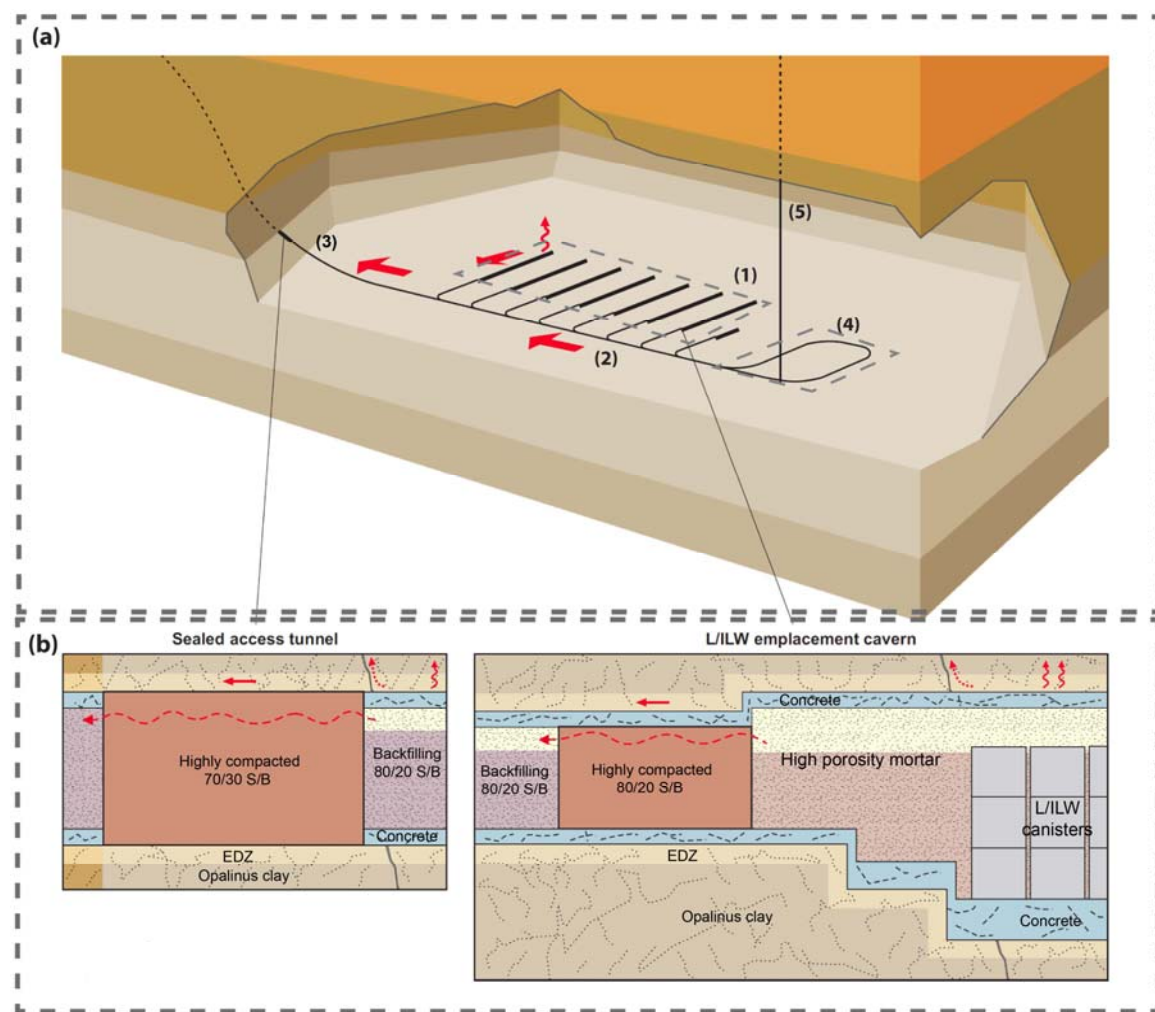
Figure 1.1: Schematic representation of a L/ILW repository (a). View of the preferential paths for the evacuation of gases (red arrows) (b); (after Nagra, 2008).

The emplacement caverns are connected to the operational tunnel through the so-called "branch tunnels". These branch tunnels, as well as the operational tunnels and all the other underground structures, will be filled with bentonite-based materials prepared at different mixing ratios and compacted to different dry densities depending on the zone of the repository in order to avoid the escape of contaminated pore water to the geosphere (Figure 1.1 (b)).

1.1.1 The issue of gas generation in the waste repositories

In the post closure phase, during all the service life of a repository, a large amount of gases, mainly hydrogen, will be produced, from the anaerobic corrosion of the canisters, the radiolysis of water and the radioactive decay of the wastes. Large amount of methane (and carbon dioxide) can also result from chemical and biological degradation of organic substances in the underground repositories (Nagra, 2008). In the Swiss waste programme, the anaerobic corrosion of the steel components can be considered as the dominant source of gas production.

The chemical reaction can be described as follows (Gallé, 2000):

$$3Fe + 4H_2O \leftrightarrow Fe_3O_4 + 4H_2 \qquad (1.1)$$
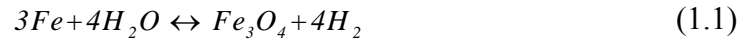
Calculations conducted by Nagra (2008) indicate that a total volume of about 20 to $30 \cdot 10^{-6}$ m^3 of gases will be produced for a L/ILW repository layout showed in Figure 1.1 in which the pore space is about 58000 m^3. The rate of gas production for a hypothetical L/ILW repository was calculated accounting for all the possible sources of gas production, based on two different waste inventories, the MIRAM 2005 and MIRAM 2008. These two inventories are based on the assumption of 50 years of operation of a nuclear power plant and the collection of waste from medical activities until 2050 (Nagra, 2008). The results revealed that the larger amount of gases is produced at the beginning of the repository life, followed by a monotonic decrease of the production rate (Figure 1.2).
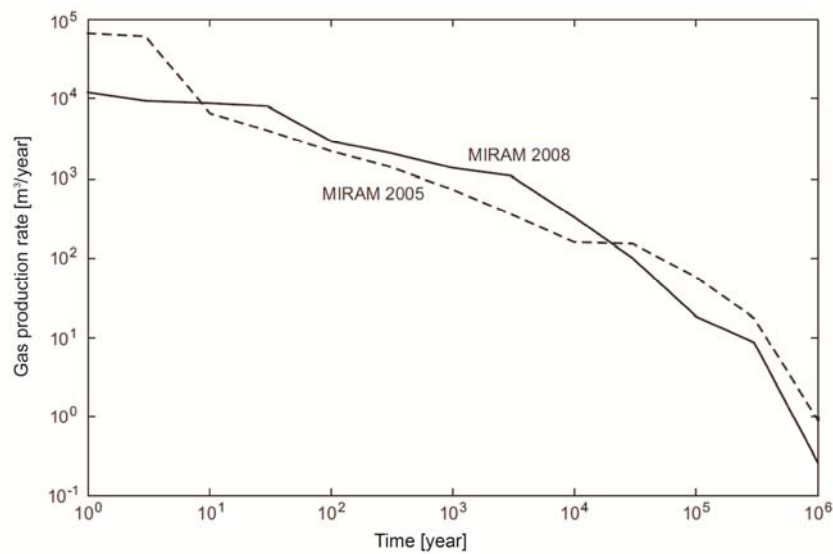

Figure 1.2: Estimated gas production rate in time (Nagra, 2008).

1.2 THE SAND/BENTONITE MIXTURE AS BACKFILLING MATERIAL FOR UNDERGROUND STRUCTURES

As previously mentioned, the gas production is a critical issue with regard to the long term safety of repositories. As a matter of fact, the formation of volatile radionuclides which can migrate into the geosphere, as well as the increase of interior gas pressure, might damage the engineered and geological barrier system (Pusch et al., 1985, e.g., Horseman et al., 1996a, Gallé, 2000, Villar et al., 2013), modifying the hydraulic and mechanical properties of the repository components (Nagra, 2008)

In order to avoid the build-up of gas pressure in the repository, Nagra (2008) proposed an engineered gas transport system (EGTS) for evacuating the produced gases. With this system, a high porosity mortar (n= 0.2 to 0.3) will be used as backfilling material for the emplacement cavern while sand/bentonite (S/B) mixtures (e.g., with a bentonite content which varies from 20 to 30 %), will be used as backfilling materials for the underground structures.

In this framework, the design of backfilling and sealing materials needs to be optimised in order to allow a controlled gas transport without compromising the radio-nuclide retention capacity. To this purpose, S/B mixtures at low bentonite content can be considered as very suitable materials. Indeed, experimental investigations performed by Romero et al. (2002) on an 80/20 S/B mixture revealed that, because of the large amount of sand in the mixture which yields to a low air entry value (a.e.v.), this kind of material is characterised by good gas transport capacity. Moreover, the presence of the bentonite (a highly swelling clay) in the mixture decreases its hydraulic conductivity and enhances its retention capacity (e.g., Abichou et al., 2002, Romero et al., 2002, Komine, 2004, Puma et al., 2013). As a consequence, gas will preferably flow through the backfilling material and the built-up of gas pressure will remains below the breakthrough pressure of the host rock.

1.2.1 Hydro-chemo-mechanical coupled processes in bentonite-based materials

Bentonite-based materials were selected as buffer and backfilling materials because of the presence of a large amount of smectite minerals. Smectite is a very active clay that has the capacity to adsorb water and hold it tightly both in its interlayer pores and on its external surface. Thanks to this mechanism, its volume can increase dozen times upon wetting so that all the voids characterising the underground structures (e.g., technological gaps, preferential flow paths, voids between the sand grains in S/B mixtures) can be easily sealed. However, the swelling capacity of the smectite at the particle level, as well as the related swelling capacity at the macroscopic level, are affected by the environmental conditions in which the bentonite is emplaced. A schematic representation of the couplings between the different types of loading is given in Figure 1.3.
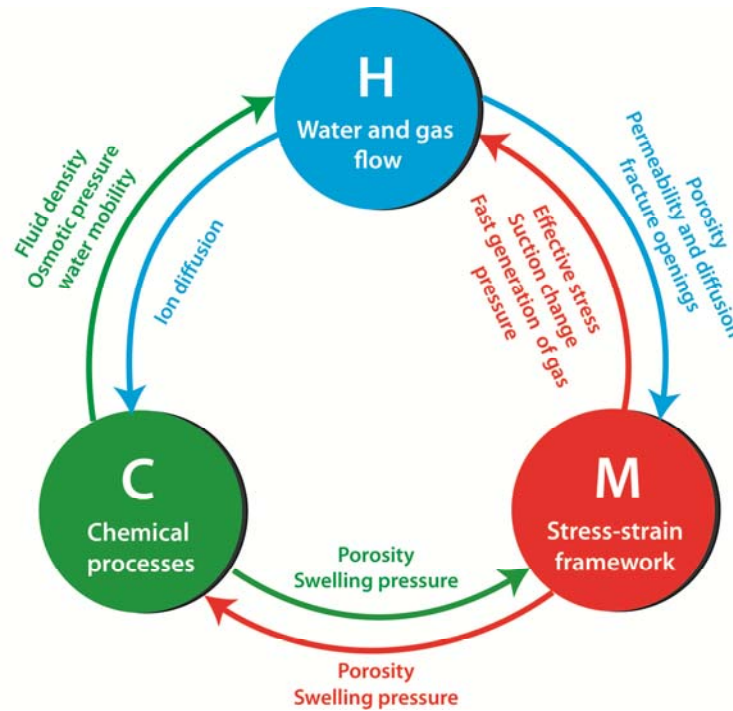
Figure 1.3: Coupled hydro-chemo-mechanical processes.

In the case of L/ILW repositories, the S/B mixture will be emplaced directly in contact with the host rock (Nagra, 2008) or, in some cases, a layer of shot clay bentonite will used to cover the host rock (Ferrari et al., 2014b). As a consequence, the S/B mixture will be saturated with water coming from the host rock. This water can contain a high amount of dissolved salts which may interact with the bentonite affecting its swelling properties. Indeed, many studies revealed that, the contact of bentonite-based materials with salty solutions can cause a decrease, or even total loss of their swelling capacity, and an increase of the hydraulic conductivity and gas transport capacity (Castellanos et al., 2008, Baille et al., 2010, Dominijanni et al., 2013, Romero, 2013); thus, compromising long term safety of the repository.

The S/B mixture for the backfilling will be prepared at water content which allows achieving the highest compaction density (the optimum water content). In order to achieve dry densities that range between 1.88 and 2.10 Mg/m^3 this water content varies from 7.5 to 12%, depending on the compaction energy (Nagra, 2008, Minon et al., 2010, Rüedi et al., 2013). This means that in situ, the mixture will be emplaced in the tunnels under unsaturated conditions.

Subsequently, this unsaturated mixture will tend to adsorb water coming from the host rock. At the beginning, the water adsorption will make the mixture swell, under free volume conditions to fill up the small technological gaps (Villar, 2007, Ferrari et al., 2014b). Once this phase is completed, the adsorption of water will continue under constant volume conditions generating swelling pressure.

Oxygen consumption in the caverns is expected starting right after the closure of the repository (within decades) so that the gases will be produced immediately after closure

(Vaughn, 2006). If the amount of the produced gas remains below the limit of gas solubility, the gases will dissolve into the pore water. Otherwise, if the gas production exceeds the gas solubility, it will flow through the mixture as separate phase, establishing a two phase flow of both water and gas. A complete saturation of the bentonite-based material, with a consequent reduction of its gas transport capacity, can be expected in the long term. As a consequence, a build-up of the pressure in the repository can be expected since the gas cannot be any longer properly evacuated. This pressure can cause either the displacement of the pore water and the consequent desaturation of the mixture, or the creation of localised preferential flow paths associated to the fast build-up of gas pressure: the so-called "breakthrough" phenomenon.

Because of the environmental conditions in which the mixture will be emplaced, (e.g., gas production and water from the host rock) the two-phase flow in the S/B mixture will likely established. Under conditions of partial saturation, water and gas will flow simultaneously, each one following its own path. However, because the two fluids are immiscible a fluid-fluid interface will establish generating a capillary pressure, thus affecting the transport capacity of the mixture.

During the service life of a repository, some convergences of the excavated tunnels can be expected. These wall displacements can cause the compression of the backfilling material, with a consequent reduction of its porosity. This also affects the swelling capacity, the retention and transport properties of the mixture. Liu et al. (2015) observed that the gas permeability of bentonite-based materials can be strongly dependent on changing confining pressure; in particular this effect was more pronounced at high degree of saturation because of the enhanced compressibility of the mixture.

1.2.1.1 *Micro and macro scale interactions*

Because of the presence of two solid components, S/B mixtures are characterised by a multi-modal pore size distributions (Romero et al., 2011). Two main levels of porosity can be identified: the macropores located between the aggregates and the intra-aggregates pores. These two levels of porosity interact with each other and change continuously upon hydro-chemo-mechanical loadings (Figure 1.4). Several Authors (e.g., Koliji et al., 2010b, Musso et al., 2013, Seiphoori et al., 2014) demonstrated that the change in microstructure can be linked with the macroscopic behaviour of double structure porous media. Moreover, investigations at the microscopic scale are of particular interest for the development and use of constitutive models for multi-structured geomaterials (e.g., Gens and Alonso, 1992, Koliji et al., 2010a, Mašín, 2013, Wang et al., 2013).
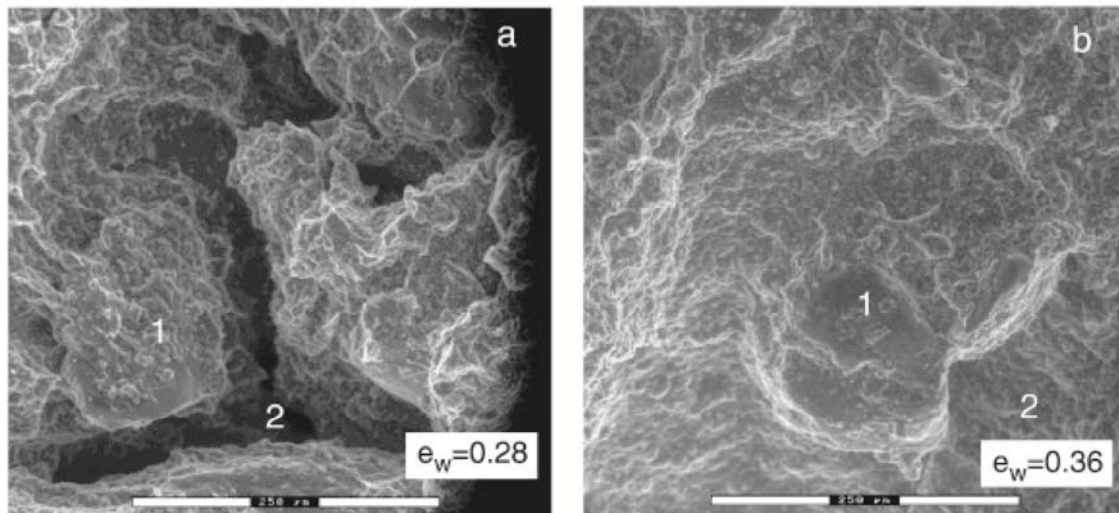
Figure 1.4: SEM photomicrographs of a compacted S/B mixture. As-compacted (a) and saturated (b) (Romero et al., 2011).

1.3 OBJECTIVES AND OUTLINE OF THE THESIS

In this framework, a systematic approach is used to analyse the hydro-chemo-mechanical (HCM) behaviour of the 80/20 sand/bentonite mixture. In particular, this research aims at:

1) Providing a better understanding of the main mechanisms of liquid and gas transport through a targeted S/B mixture in both saturated and unsaturated conditions, with a focus on the determination of the driving mechanisms behind the gas transport;
2) Linking the macroscopic behaviour of the S/B mixture to its microscopic features;
3) Comparing the features characterising the 80/20 S/B mixture with the ones of other bentonite-based materials (e.g., prepared at different mixing ratio);
4) Providing a broad collection of material properties for S/B seals;
5) Investigating the influence of changing boundary conditions at both macroscopic and microscopic level (e.g., compaction density and pore water chemistry).

In order to deeply investigate and analyse the hydro-chemo-mechanical behaviour of the 80/20 S/B mixture, this research work is organised as follows:

Chapter 2 summarises the experimental characterisation of the mixture in term of swelling capacity, retention properties and water transport under saturated and unsaturated conditions. All the investigations are performed on a mixture composed by 80 % of quartz sand and 20% of MX-80 granular bentonite type "E". A new methodology for the preparation of specimens is proposed, increasing the reproducibility and allowing obtaining a good distribution of the two solid fractions. The response of the material is

analysed upon different hydro-chemo-mechanical loadings. The water retention properties are investigated for two different target dry densities and for a wide range of suctions. The influence of the dry density variation and composition of the pore fluid on the saturated hydraulic conductivity of the mixture is analysed. Moreover, the influence of the void ratio on the unsaturated hydraulic conductivity is studied.

Chapter 3 presents the experimental characterisation of the gas transport capacity of the mixture under saturated and unsaturated conditions. To this purpose, different experimental setups are implemented and a gas injection system is designed for the measurements of the gas permeability. The concept of "geometrical permeability" is introduced to replace the concept of "intrinsic permeability". The effects of the dry density changes on the gas permeability and breakthrough pressure are investigated. Gas permeability is measured under a variety of degrees of saturation. The Klinkenberg effect on the gas permeability of the S/B mixture is also taken into account.

Chapter 4 is devoted to the characterisation of the hydro-chemo-mechanical behaviour at the microscopic level of the S/B mixture upon different loadings. The first part of the chapter reviews the swelling mechanisms of the smectite clay at the particle level as well as the impact of different HCM loads on these mechanisms. The second part is devoted to the microscopic analyses on the mixture, performed by coupling two experimental techniques: the Mercury Intrusion Porosimetry (MIP) and the Scanning Electron Microscopy (SEM). The results are analysed focusing on the swelling mechanisms acting at the particle level. Based on the results obtained at the microscopic level, the last part of the chapter gives an insight on the hydro-chemo-mechanical behaviour at the macroscopic scale. The macroscopic behaviour of the mixture is compared with the behaviour of other bentonite-based materials only considering their relative bentonite dry density.

Finally, *Chapter 5* presents the conclusions and the main achievements of this work. Suggestions for future works on experimental characterisation and modelling of tested S/B mixture are also provided.

2 Experimental characterisation of the swelling capacity, hydraulic conductivity and water retention behaviour of the sand/bentonite mixture

2.1 INTRODUCTION

This chapter is dedicated to the experimental characterisation of the swelling capacity, water retention behaviour and water permeability in saturated and unsaturated conditions of the 80/20 sand/bentonite (80/20 S/B) mixture subjected to different hydro-chemo-mechanical (HCM) loadings.

The tested material is described in terms of mineralogical composition, index properties and grain size distribution. The procedure adopted for the preparation of the mixture is introduced together with the procedure for the preparation of the specimens. The effect of compaction velocity during the sample preparation is analysed. The described procedure was respected for the preparation of all the specimens except some of those used for gas permeability tests carried out under triaxial conditions.

The HCM of the 80/20 S/B mixture is analysed in terms of single wetting swelling pressure under constant volume conditions, single wetting swelling deformation under free volume conditions, swelling pressure under different applied matric suctions, water retention capacity and water permeability under saturated and unsaturated conditions.

Swelling pressure and swelling deformation are determined for mixture compacted to different dry densities and wetted with different pore waters. The retention capacity is determined for two different dry densities under a wide range of suction using three different experimental techniques: axis translation technique, filter paper method and microcell technique. Saturated hydraulic conductivity was measured for different compaction densities and with different percolating fluids. Finally, the generated swelling pressure and unsaturated water permeability were measured during the determination of the water retention properties.

2.2 TESTED MATERIAL

2.2.1 The sand/bentonite mixture

The investigated material is a mixture of grey quartz sand and MX-80 bentonite (Wyoming) in proportion 80/20 in dry mass.

The MX-80 is a sodium granular bentonite, type 'E' (Teodori et al., 2011). The MX-80 bentonite is mainly composed of 84.9 ± 1.2 % montmorillonite, 4.8 ± 0.8 % muscovite, 3.7 ± 0.5 quartz, 5.2 ± 0.8 % feldspar and 1.3 ± 0.2 % calcite. MX-80 mixture 'E' bentonite has an exchangeable cations capacity of 52.4 meq/100 g Na, 13.2 meq/100 g Mg and 1.4 meq/100 g K (Nagra, 2007). MX-80 is the commercial name of the Wyoming bentonite that, as for other smectite enriched materials, was originated from the weathering of volcanic ashes in arid or semiarid zones where there is poor leaching and drainage, and the rate of evaporation exceeds the rate of precipitation (Mitchell and Soga, 2005).

With its high swelling and sealing capacity the role of bentonite is to reduce the hydraulic conductivity of the mixture thanks to the capacity of the smectite minerals to adsorb and stock water in their interlayers and on their external surface. More details about the mechanism of smectite-water interaction will be given in Chapter 4.

The quartz sand, which has been used for all experiments, is a grey quartz sand from Carlo Bernasconi AG (carloag.ch). Its specific gravity is 2.65. The mineralogy of this quartz sand consists mainly of silicon dioxide (97.40%), alumina (1.35%), potassium and sodium oxides (0.8%), small amounts of titanium dioxide, periclase and lime. Quartz sand has been selected for this study due to its high chemical stability. Indeed, it has limited chemical interactions with the pore water and the bentonite.

The presence of sand in mixtures prepared at low bentonite content provides a load-support enhancing the macroscopic mechanical stability (Kenney et al., 1992). It also, reduces the shrinkage of the mixture when the water content decreases and thus reduces the risk of cracking (Dixon et al., 1985). This risk is much more present in a pure bentonite (Graham et al., 2002).

2.2.2 Water used in the experiments

Deep repositories are foreseen to be excavated well below the ground water table in suitable natural rock formations such as Opalinus Clay or Brown Dogger (Swiss concept), Granite (Swedish concept) or Boom Clay (Belgium concept). Thus, under repository conditions the S/B mixture could be saturated with different types of water such as the formation water coming directly from the surrounding host rock or the water that reaches

the S/B mixture after flowing through other elements of the repository (e.g., the concrete plugs).

The capacity of the bentonite to adsorb water is strongly influenced by the ionic strength of the pore water in contact with the minerals. In general, the higher the ionic concentration in the pore water the lower the capacity of bentonite to attract water molecules and consequently to swell. Herbert and Kasbohm (2009) and Herbert et al. (2004) performed short and long term swelling tests on MX-80 bentonite specimen using waters with different compositions in order to reproduce the real repository conditions. In these studies, it was found that montmorillonite minerals in contact with alkaline and salty water can undergo changes in morphology, crystallinity, particle surface, interlayer charge and chemistry of the octahedral layers. Besides, the bentonite can be subjected to a total loss of the swelling capacity due to the transformation of a certain percentage of the montmorillonite in kaolinites.

Another example on how the pore water salinity alters the behaviour of bentonite-based materials is offered by Romero (2013). The author found that wetting bentonite-based materials under constant volume conditions with distilled water produced the occlusion of the macropores and the increase of the micropores and leaded to an increase of the unsaturated water permeability and the reduction of the gas permeability. When the same material was initially mixed with 1% of lead nitrate powder, the swelling capacity of the bentonite was inhibited and the gas permeability of the mixture was increased.

In order to study the effect of pore water salinity on the hydro-mechanical behaviour of the 80/20 S/B mixture, four different types of waters were used for the mixture preparation and for the subsequent wetting of the as-compacted specimens. Distilled water (DW) is used to allow the development of the maximum swelling of the bentonite grains. A synthetic water named Schlattingen water (SW), having the same composition of the in situ pore water that can be found in an Opalinus Clay formation, in the northern part of Switzerland (Table 2.1), is used to reproduce the real conditions of a repository in northern Switzerland. The two other fluids are sodium chloride solutions prepared at 1 mol/l (1M NaCl) and 4 mol/l (4M NaCl) concentration, respectively. These solutions were selected for comparison with the synthetic pore water because the predominant salt in the synthetic water is NaCl. With these waters the swelling capacity of bentonite is strongly limited. The osmotic suctions of the three mentioned salty waters were taken from literature and are listed in Table 2.2. In the table, also the density and dynamic viscosity of the sodium chloride solutions, whose values are taken from Romankiw and Chou (1983) and Kestin et al. (1981), respectively, are presented. In the case of synthetic water, the same values as for distilled water are considered for the density and the dynamic viscosity, due to the low percentage of salt dissolved.

Table 2.1: Composition of the synthetic water (Traber, 2011)

Compound	mmol/kg$_{H2O}$	mg/kg$_{H2O}$
Na	163.8	3765.7
K	2.551	99.75
Ca	11.91	477.4
Mg	9.166	222.8
Cl	169.0	5672.5
SO$_4$	24.00	2305.5
HCO$_3$	0.5431	33.14

Table 2.2: Osmotic suction and salinity of the pore waters used for testing

Water type	π_w [MPa]	Salinity [g/l]	μ [Pa·s]	ρ_w [Mg/m^3]
DW, distilled water	~ 0	~ 0	0.0010	1.00
SW, synthetic water	0.9[†]	12.58	0.0010	1.00
1M NaCl	4.9[*]	58.44	0.0011	1.04
4M NaCl	22.6[*]	233.78	0.0015	1.14

[†](Ferrari et al., 2014a)

[*](Witteveen et al., 2013)

2.2.3 Index properties

The cone fall method (BS 1377-2, 1990) was adopted to measure the liquid limit of the mixture. The ASTM D4318-10 standard was followed to obtain the plastic limit. The liquid limit and the plastic limit were determined with the four waters used for the other experiments. The liquid limit has a maximum value of 89% with distilled water and it decreases with the increasing of the osmotic suction of the water implemented for testing (Figure 2.1-left) whereas the plastic limit results only slightly altered by the composition of the pore water (Figure 2.1- right). Similar results were obtained for pure bentonite by Shirazi et al. (2011) and for soil/bentonite mixture by Mishra et al. (2009). The obtained values of the Atterberg limits for the different pore waters are listed in Table 2.3 and indicated in the plasticity chart in Figure 2.2. A substantial reduction of the mixture activity is observed with increasing pore water salinity, providing an initial indication on the swelling capacity reduction of the bentonite fraction. This result is explained with the reduction of the swelling capacity of the smectite minerals at the particle level. The relatively low values of liquid and plastic limits are attributed to the presence of the sand grains in the mixture.

The index properties of the S/B mixture are listed in Table 2.4 together with the index properties of the MX-80 bentonite and the quartz sand.

The specific gravity of the sand and bentonite fractions were estimated with the fluid displacement method. For the bentonite, a non-polar fluid (Kerdane) was used instead of water to avoid the development of the diffuse double layer (Seiphoori et al., 2014).

Specific surface of the sand was estimated from mercury intrusion porosimetry (MIP) analysis, whereas the specific surface of the mixture was estimated by weighted average of the specific surfaces of the two solid fractions. The particle density of the mixture was obtained as weighed average of the particle densities of the sand and bentonite as follows:

$$\rho_{s,mix} = \frac{1}{\dfrac{R_S}{\rho_{s,S}} + \dfrac{R_B}{\rho_{s,B}}} = 2.67 \ \text{Mg/m}^3 \tag{2.1}$$
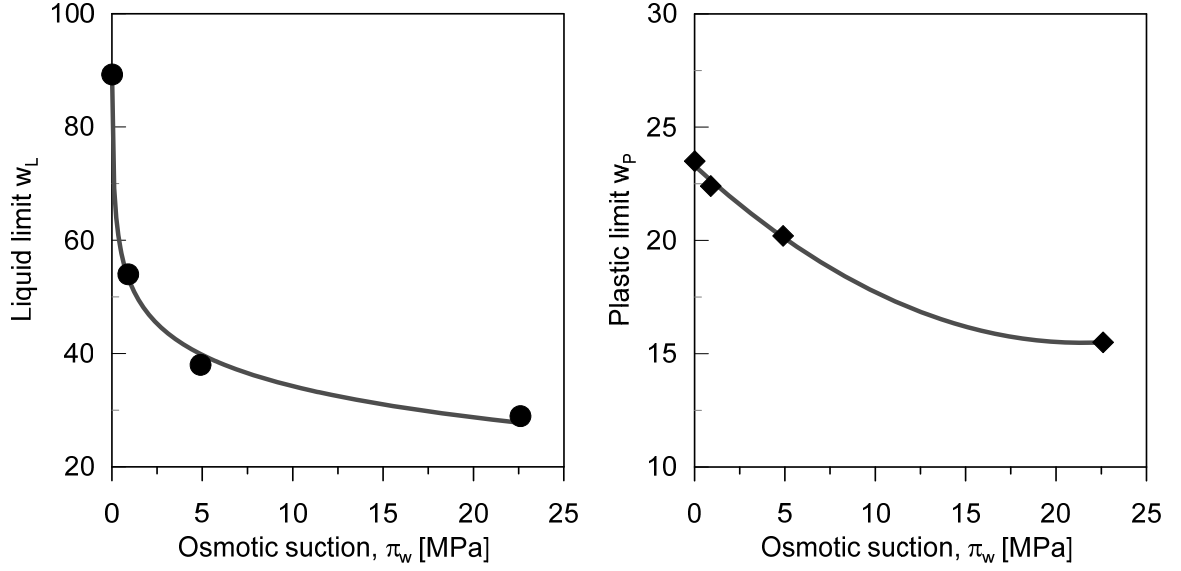
Figure 2.1: Evolution of the liquid limit and the plastic limit with the increase of osmotic suction of the pore water.

Table 2.3: Liquid limit, plastic limit and plasticity index of the mixture wetted with the four different waters.

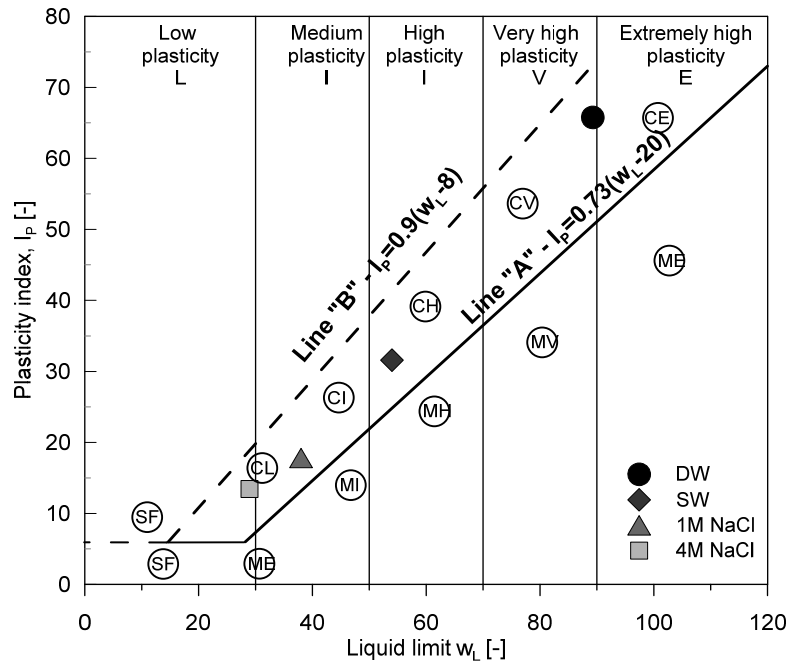| Water type	w_L [%]	w_P [%]	I_P [%]
DW, distilled water	89	23.5	65.5
SW, synthetic water	54	22.4	31.6
1M NaCl	40	20.2	19.8
4M NaCl	29	18	11

Figure 2.2: Activity of the sand/bentonite mixture prepared with different pore waters.

Table 2.4: Index properties of the tested material.

Properties	Sand	MX-80	80/20 S/B
Specific gravity, G_s [-]	2.65	2.74[*]	2.67
Liquid limit, w_L [%]	-	420[*]	89[‡]
Plastic limit, w_P [%]	-	65[*]	23.5[‡]
Smectite content [%]	-	85	17
Specific surface area, S_s [m^2/g]	0.003	523[†]	105

‡ This study – measured with distilled water
*Seiphoori (2014)
†(Plötze and Weber, 2007b)

2.2.4 Grain size distribution

For the preparation of the mixture, the sand and the bentonite were sieved through a 0.5 mm sieve. This procedure implies the elimination of the biggest bentonite pellets, which are present in the as-delivered MX-80 bentonite. It also ensures to obtain a homogeneous mixture with an even grain distribution. The grain size distributions of the tested materials are presented in Figure 2.3. Grain size distributions of the MX-80 granular bentonite (as-delivered and after sieving), the sand and the 80/20 S/B mixture were determined by dry sieving at the hygroscopic water content (w^b =5% and w^s =0%). The calculated distortion number (CU) and curvature number (CC) are listed in Table 2.5. Figure 2.4 shows an image, taken with a scanning electron microscope (SEM), of the grains of the sand and the bentonite after sieving. The grains of sand have similar size. The surface of the sand grains is characterised by the presence of several nooks and

14

crannies and is coated with some impurities. The bentonite is a mix of grains of various sizes that appear coated with some bentonite powder (finest bentonite fraction).

2.2.5 Dynamic compaction tests

Dynamic compaction tests were performed on a mixture prepared according to the procedure described in paragraph 2.2.6 to determine the maximum achievable compaction density that could be obtained for a specific compaction energy. The test was carried out following the SN 670 330 b. The results of the test are presented in Figure 2.5. An optimum water content of 0.11% and a corresponding maximum dry density of 1.88 Mg/m^3 were obtained for a compaction energy of 3.4 J/cm^3. These results are referred to a mixture wetted with distilled water.
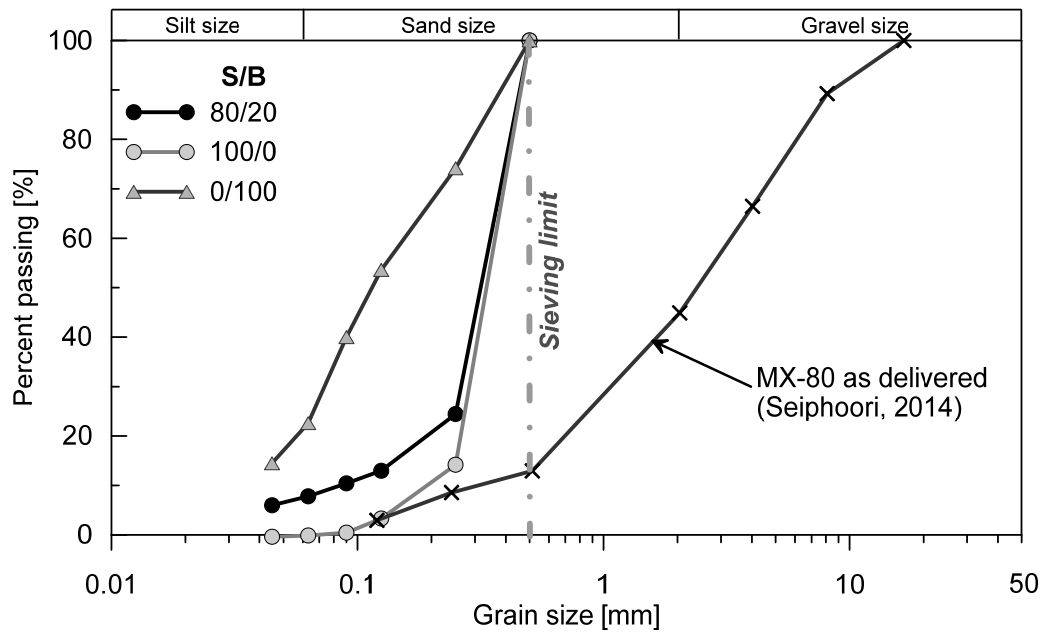

Figure 2.3: Apparent grains size distribution of the tested material and its two solid components.

Table 2.5: Uniformity coefficients and curvature numbers of the pure bentonite, the 80/20 S/B mixture and the pure sand.

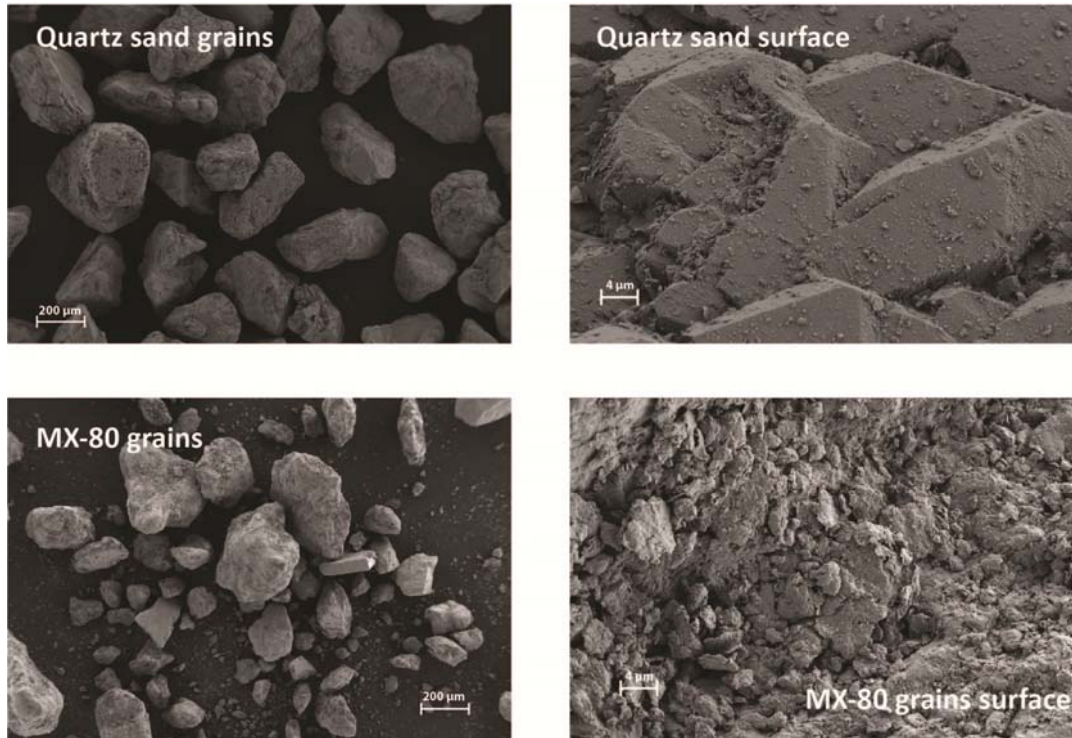|	100B	80/20 S/B	100S
Distortion number, C_U [-]	4.16	4.24	1.99
Curvature number, C_C [-]	0.88	2.54	1.19

Figure 2.4: SEM photomicrographs of the quartz and the MX-80 bentonite grains and observation of the surface of the grains at the hygroscopic water content.

2.2.6 Sample preparation

The tests described in the following sections were performed on an 80/20 S/B mixture reconstituted in the laboratory. The procedure adopted for the preparation of the specimens was established in house. It enables to obtain a uniform distribution of the bentonite and sand grains, as well as a homogeneous dry density, water content and porosity distribution. The MIP analyses presented by Manca et al. (2015) showed that the proposed procedure ensures reproducibility of the specimen characteristics and thus the consistency of the results.

To prepare the mixture, the dry sand and the granular bentonite (hygroscopic water content of 5-6% at a temperature of 21°C and relative humidity of 35-45%) were sieved at 0.5 mm and then mixed manually. When a uniform distribution of the grains was obtained, water was gently added with a spry gun with continuous mixing to reach a water content of 0.11, corresponding to the optimum water content for a dry density of 1.88 Mg/m^3, determined using a dynamic compaction test (compaction energy of 3.4 J/cm^3). Finally, the mixture was stored in hermetic containers for at least 3 days to ensure moisture equalisation. To assess the homogenisation of the water content after the selected curing time random samples were extracted from a wet mixture and the water content was measured. The measurements showed that the same water content was obtained for all the samples. This result also indicates a good distribution of the two solid fractions through the whole mass of wetted mixture.

The wet mixture was then poured in the cell used for the experiment and then compacted to the target density. To help this procedure, special moulds (hollow cylinders made of aluminium) that fit in each of the cell-rings were designed.

At the optimum water content, the risk of particle segregation is unlikely due to the fact that the finest moist particles of bentonite are coating the grain of sand and the larger grains of bentonite so that the grains movements is limited.

Two different presses were used for the compaction. The first one, from Wikeham Farrance Eng. LTD, was equipped with a load cell (maximum vertical force of 22 kN, accuracy of 0.1% of the full range) and an LVDT (accuracy of 1 μm), which serves to monitor the piston's displacements (Figure 2.6). The second one is a Walter & Bai type press instrumented with a load cell (maximum vertical force of 100 kN, accuracy of 0.1 of the full range) and a LVDT (range of 20 mm and accuracy of 0.2%). The second press was used to compact specimens when high vertical stresses were required. Specimens were prepared by static compaction performed at a constant rate of 0.5 mm/min. Compaction velocity was proven to be slow enough to prevent generation of the excess of pore water pressure (see paragraph 2.2.6.1).
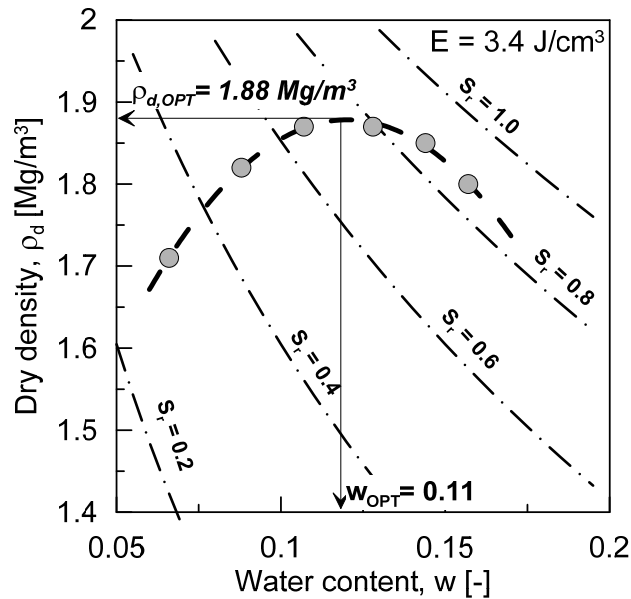

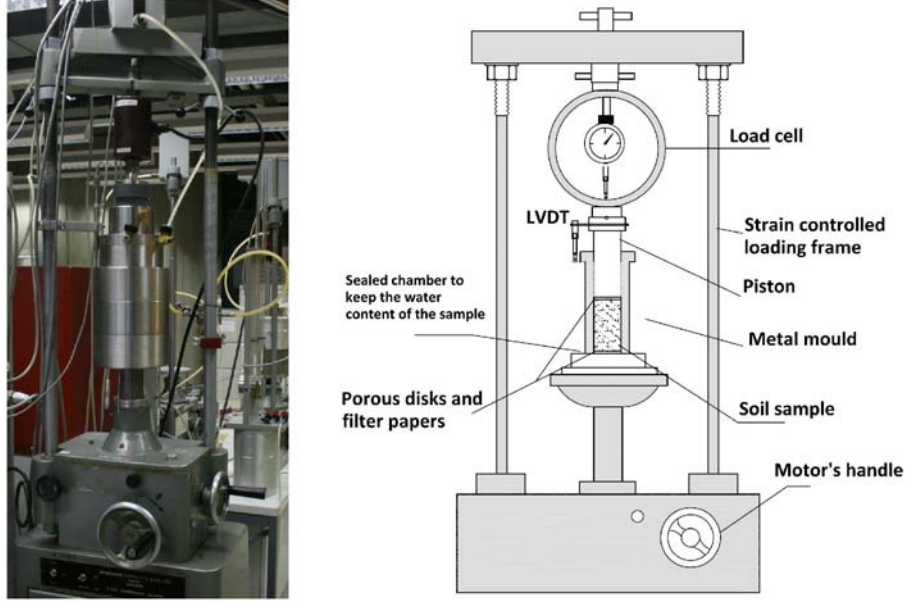**Figure 2.5: Dynamic compaction test on the 80/20 S/B mixture.**

Figure 2.6: Schematic representation of the press used for the specimen compaction (right) and compaction of a specimen inside the oedometric ring (left).

Referring to Figure 2.7, the vertical displacement of the piston (δ_{comp}) required to obtain the target dry density was determined as follows:

$$\delta_{comp} = H_{1,IN} - H_{1,FIN} - \delta_{el} \tag{2.2}$$

where $H_{1,IN}$ is the initial height of the piston, carefully measured with a calliper when the mixture is non-compacted, $H_{1,FIN}$ is the final surplus height of the piston (final target height), and δ_{el} is the elastic rebound that the material exhibits when the vertical stress is released.

$H_{1,IN}$ is obtained as:

$$H_{1,FIN} = H_{1,0} + H_{sp,T} + t_{fp} \tag{2.3}$$

where $H_{1,0}$ is the height of the piston in phase 1 when the cell is empty, $H_{sp,T}$ is the target specimen height, and t_{fp} is the thickness of the filter papers.

Knowing the height of the not-compacted specimen ($H_{sp,i} = H_{1,IN} - H_{1,0}$), the dry mass of the mixture (M_s^{Mix}) which is poured inside the cell and the initial dry density ($\rho_{d,i}$) of the specimen before compaction, the evolution of the specimen height ($H_{sp}(\sigma_v)$) and its dry density can be computed from the linear differential transducer (LVDT) readings ($\Delta H(\sigma_v)$) as follows:

18

$$\rho_d\left(\sigma_v\right) = \frac{M_s^{Mix}}{A_{sp} \cdot H_{sp}\left(\sigma_v\right)} \tag{2.4}$$

where A_{sp} is the cross-sectional area of the specimen.

The compaction is carried out until the target displacement of the piston δ_{comp} is reached.

Typical curves obtained during specimen compaction are showed in Figure 2.8. The figure depicts the variation of the specimen height, axial strain ($\varepsilon_a = \Delta H(\sigma_v)/H_{sp,i}$), considered positive for compression, dry density, and corresponding void ratio, with the applied vertical stress. The curves were obtained for a specimen that was compacted to a target dry density of 1.5 Mg/m³ and were used to quantify the elastic rebound associated to the vertical stress release. The maximum vertical pressure (σ_v^{max}) experienced by the specimen resulted equal to 1000 kPa and the final void ratio (e_{fin}) was equal to 0.82.

Measurement of the total and matric suction of the as-compacted specimen proved that, for a water content of 11%, the suction is independent on the compaction density (paragraph 2.4.3.1). This implies that the preparation of the specimen is an iso-suction process. Under this condition, the coefficient of compressibility (C_C) at the as-compacted state is equal to 0.45 and the swelling coefficient (C_S) is equal to 0.01 (Figure 2.8.d).

It was found that this technique allowed the good reproducibility of the specimens.
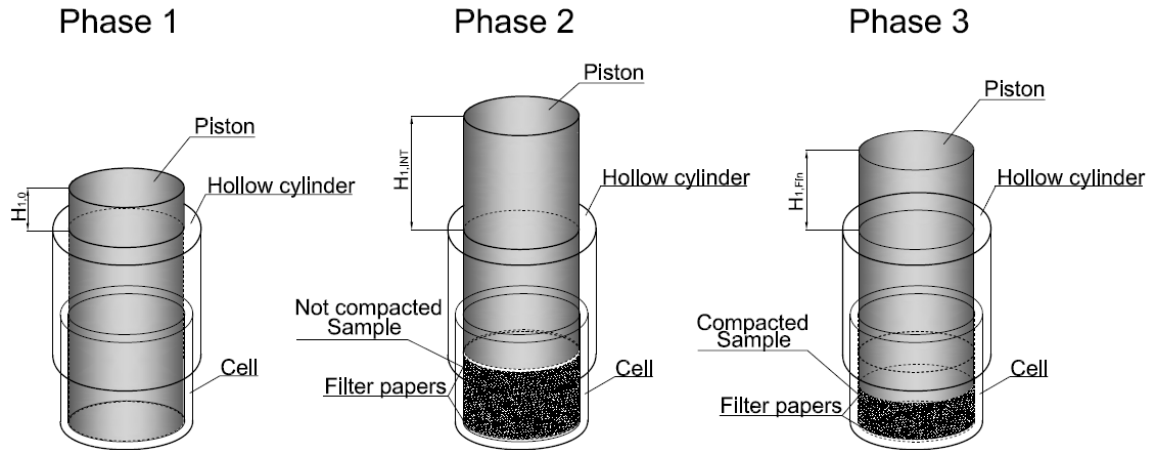

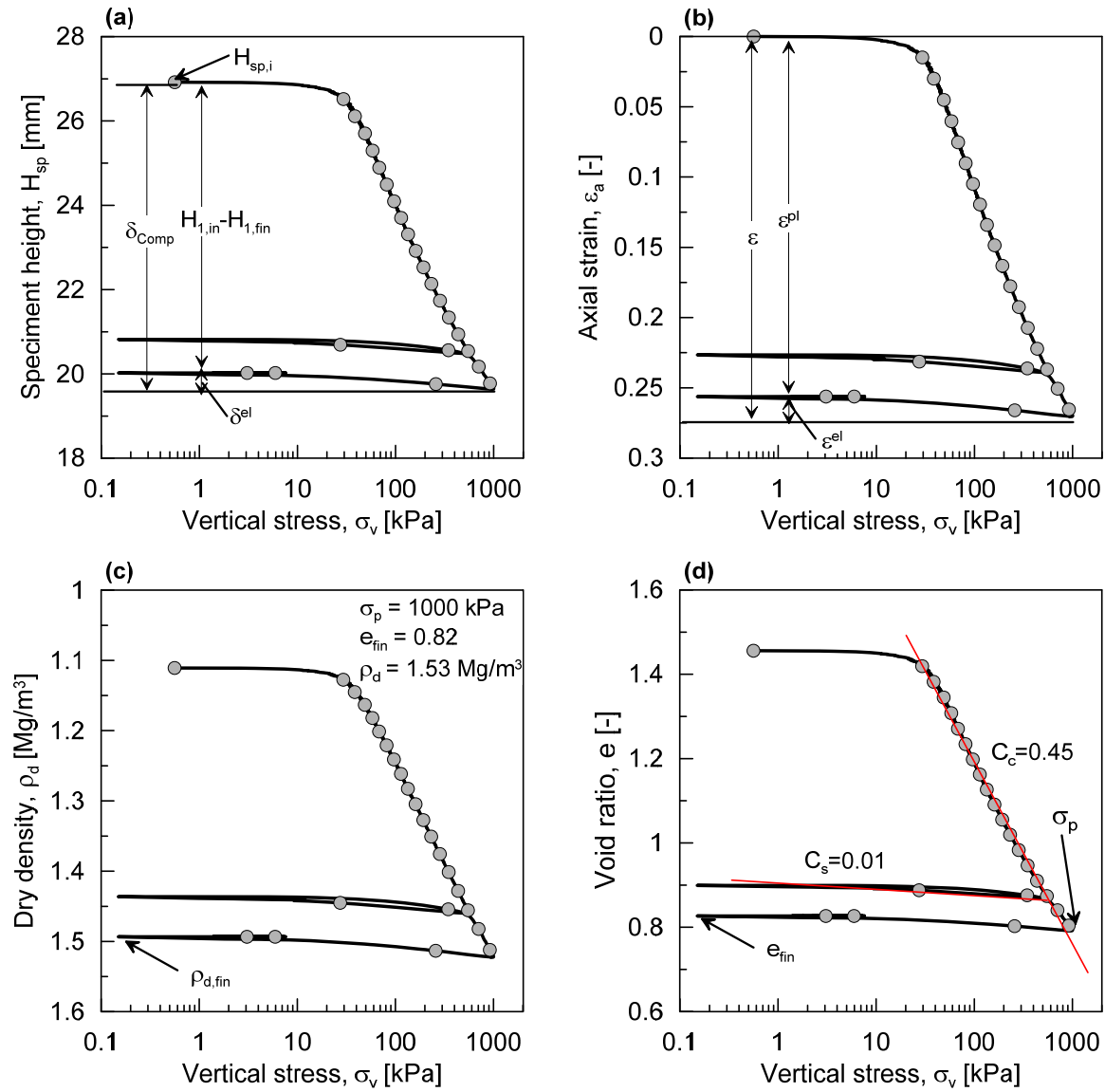Figure 2.7: Specimen compaction phases.

Figure 2.8: Evolution of the specimen height (a), axial strain (b), dry density (c) and void ratio (d) with the applied vertical stress during compaction.

2.2.6.1 *Evaluation of the compaction velocity and compaction stresses*

The tested specimens are brought to the desired dry density by means of static compaction tests. For this procedure the lateral deformations of the specimen are impeded so that the target density is achieved by progressive reduction of the specimen height. The cells implemented for all the tests are designed to maintain constant water content during compaction so that this phase corresponds to a compression process of a partially saturated specimen under undrained conditions. This implies that the compaction velocity mush be kept low enough to avoid the generation of excess pore pressure.

To select the maximum applicable velocity for specimen preparation, static compaction tests were carried out at the different compaction velocities of 0.5, 0.225, 0.100 and 0.05 mm/min, on mixtures prepared with distilled and synthetic water to the 11% of water content. Specimens of 51 mm in diameter and 40 mm in height were

compacted to a maximum dry density that ranges from 1.8 to 1.9 Mg/m^3. During these tests, the material followed the same stress path regardless the compaction velocity (Figure 2.9) ensuring that 0.5 mm/min was an appropriate velocity. When the mixture was prepared with distilled water the vertical stress applied to obtain specimens with a dry density in the range of 1.5 - 1.8 Mg/m^3 ranged between 1 MPa to 25 MPa. Higher vertical stresses ($\sigma_{v,min}$ = 3.6 MPa; $\sigma_{v,max}$ = 30 MPa) were required for compacting a mixture wetted with synthetic water to the same dry density range.

2.3 SWELLING CAPACITY

In a L/ILW repository, the S/B mixture will be emplaced with dynamic compaction technique at its optimum water content and thus in unsaturated conditions. This implies that after the emplacement, the unsaturated mixture in contact with water will swell under free volume conditions until all the technological gaps in the repository system will be sealed. After this first phase, the mixture will continue to adsorb water, and will generate swelling pressure as the volumetric deformations are impeded (Villar, 2007).

Water in the repository environment contains salts which interact with the bentonite-enriched materials and alter theirs hydro-mechanical properties (e.g. swelling and retention properties). In the most critical situation, high salinity water may inhibit the capacity of the materials to swell and to seal technological voids, which may represent preferential paths for the escape of hazardous fluids, compromising the safety of the repository.

The hydro-chemo-mechanical behaviour of bentonite enriched material was investigated in the past years by several authors. With regard to the swelling characteristics of bentonite enriched materials, and the parameters influencing their maximum swelling pressure or swelling deformation, some common conclusions were derived.

The initial dry density controls the magnitude of the swelling pressure and the swelling deformation of compacted bentonite and sand bentonites mixtures. Most of the authors report an exponential increasing of the generated swelling pressure with the compaction density regardless the type of bentonite tested (e.g. Lloret and Villar, 2007, Seiphoori, 2014). In the case of S/B mixtures the swelling capacity of these materials is also controlled by the percentage of bentonite (Komine and Ogata, 1999, Muntohar, 2003).

Swelling behaviour of bentonite was also found susceptible to the initial water content. The influence of the initial water content was more noticeable for higher dry densities but its effect vanished for high applied vertical stress (Villar and Lloret, 2008). At given dry density, the swelling capacity decreased with the increase of the initial water content (Villar and Lloret, 2008, Baille et al., 2010).
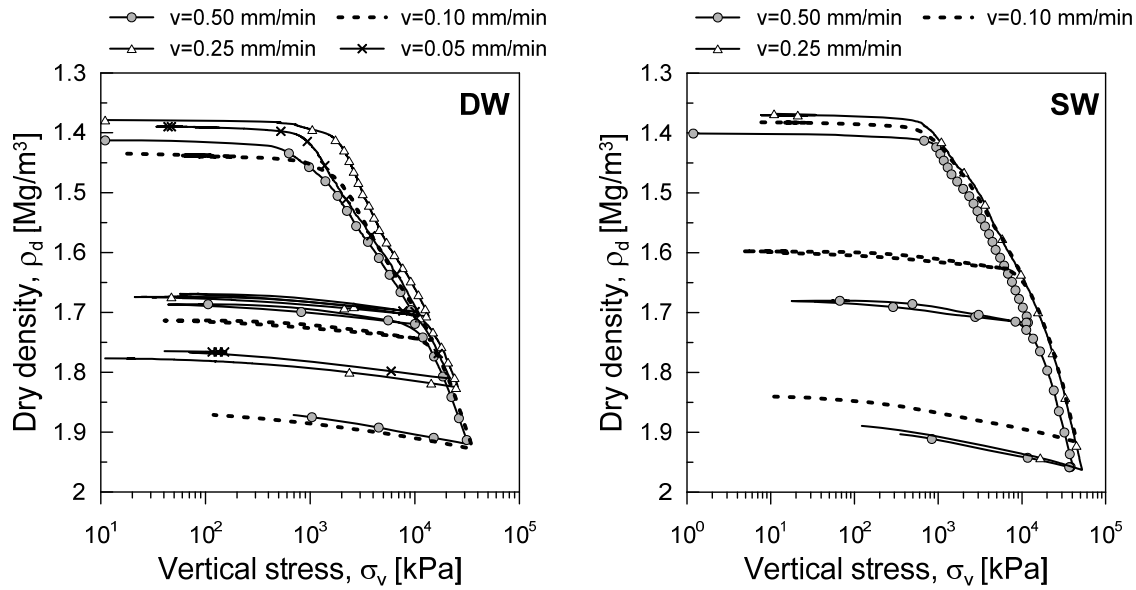
Figure 2.9: Static compaction tests at different strain rate. Mixture wetted with distilled water (left) and synthetic water (right).

A reduction of the swelling capacity of different bentonites after wetting with sea water was measured by Komine et al. (2009), showing that the swelling capacity reduction was always lower for bentonites compacted at higher dry densities. Swelling tests performed under applied axial stress also revealed that the swelling strain reduction was larger for lower axial stresses (Studds et al., 1998, Pusch, 2001a, Castellanos et al., 2008, Komine et al., 2009). The swelling capacity of bentonite decreased with the increasing the salinity of the solutions, although the effect was less significant for high vertical loads and high dry densities. Komine et al. (2009) and Dixon (2000) attributed these results to the fact that at the higher dry densities, the distance between the smectite particles was reduced; thus, the ions contained in the pore water could not infiltrate the smectite quasicrystals.

Information on the swelling behaviour of S/B mixtures at low bentonite content are limited compared to the available results for pure bentonite. Aiming at collecting new experimental evidences on the swelling capacity of the 80/20 S/B mixture this section presents the results of:

1) Swelling deformation tests carried out under zero applied axial stress;
2) Single wetting phase swelling pressure tests under isochoric conditions;
3) Controlled suction swelling pressure tests under isochoric conditions.

Initial compaction density, pore water salinity and applied matric suction were the variable changed during the tests.

2.3.1 Experimental equipment and layout

The apparatus used for the single wetting phase swelling tests consists of a thick-walled stainless steel cylinder of 79 mm in internal diameter and 110 mm in external diameter. This rigid cell ensured the oedometric condition during the test. The base of the cell was connected to a flushing line, allowing the elimination of entrapped air bubbles. Inside the cell, a specimen of 15 mm in height was placed between two filter papers and two coarse porous stones.

For the constrained swelling tests the oedometric cell was positioned inside a rigid frame in order to maintain the constant volume conditions during the test (Figure 2.10). Three screws were used to compress the rubber O-ring placed between the oedometric ring and the bottom plate; hence, leakage was prevented. A load cell in contact with a stainless steel loading ram, installed at the top of the specimen was used to measure the swelling pressure developed during the test. An initial vertical pressure of 10 kPa was applied to the specimen to ensure good contact between the various elements of the apparatus. The vertical pressure was intentionally kept low to avoid wetting collapse phenomenon which can occur when a low swelling pressure was expected. The water in the apparatus was injected at a maximum of 10 kPa of pressure using a pressure-volume (PV) controller connected to the base of the cell. The test was stopped when the swelling pressure stabilised. A PVC lid on the top of the cell prevented the evaporation of the water from the upper base of the specimen. The unwanted change in volume of the specimen during the swelling was monitored by means of a LVDT; the maximum registered volumetric strain was less than 0.1%.

The set-up used for the free swelling tests is showed in Figure 2.11. In this configuration, the upper part of cell was closed with a stainless steel lid. The specimen deformation was measured by a LVDT placed at the top of a movable rod in contact with the specimen. The upper base of the specimen was covered with a plastic foil to limit water evaporation.
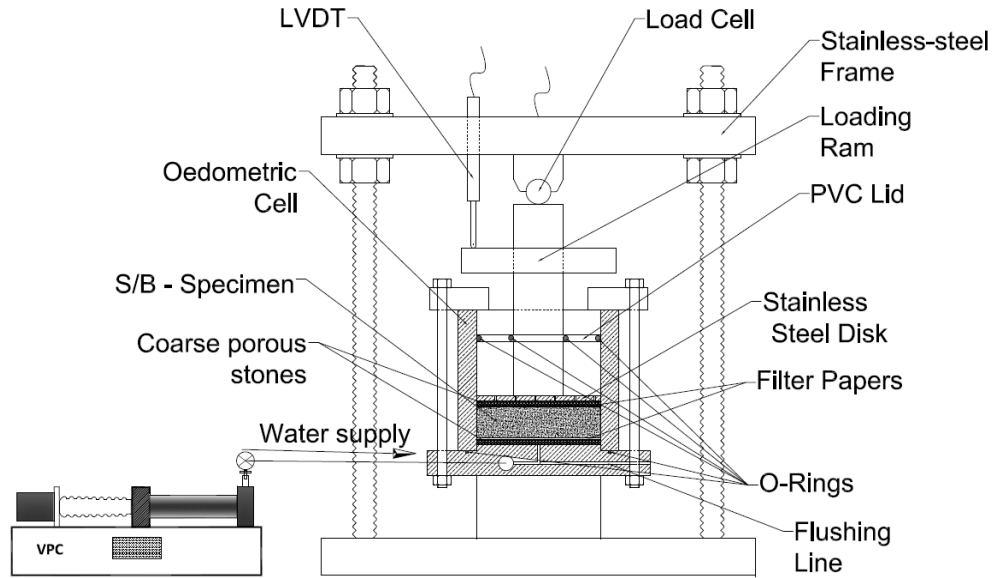
Figure 2.10 : Scheme of the apparatus for constrained swelling tests.
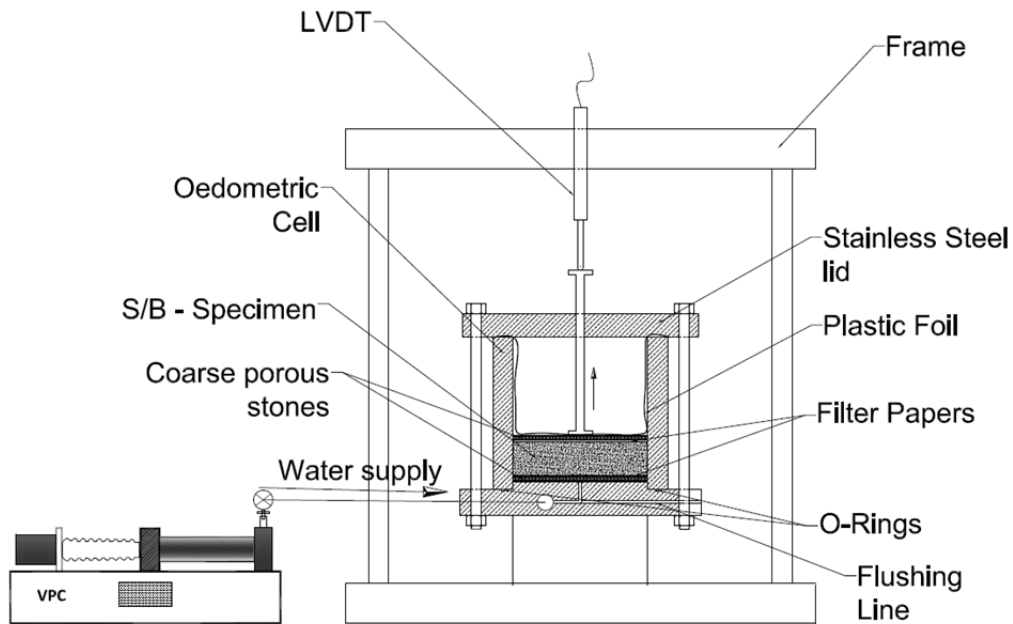
Figure 2.11 : Experimental setup for the free swelling tests.

Controlled suction constrained swelling tests were carried out on specimens of 16 mm in height and 60 mm in diameter, compacted to 1.5 and 1.8 Mg/m³ dry density for determining the relationship between swelling pressure and matric suction. The apparatus allows imposing the matric suction by the axis translation technique (Romero, 1999) while measuring the water volume exchange through the specimen. A high air entry value ceramic disk (a.e.v. 500 kPa) was mounted at the bottom of the cell for this purpose. The wetting path was done holding the gas pressure constant (600kPa) while the water pressure was increased in steps, from 100 kPa to 597 kPa, with a water PV controller.

Similar to the conventional swelling cell, the cell was placed inside a rigid frame to maintain the isochoric conditions and the swelling pressure was measured with a load cell placed at the top of the specimen. A more detailed description of this cell will be given in paragraph 2.4.2.3.

For all these tests, the transducers and the controllers were connected to a HBM data acquisition system, model QuantumX MX840A, allowing a continuous record of the measurements.

2.3.2 Free swelling tests

Figure 2.12 presents the results of the free swelling tests in terms of the change in swelling strain over time. Regardless of the type of water used as the saturating fluid, the final swelling strain increased with the initial dry density. The maximum swelling strain of the mixture wetted with synthetic pore water is significantly lower and also develops faster compared with distilled water.

The swelling strain in these experiments was defined as:

$$\varepsilon_{sw}(t) = \frac{H(t) - H_0}{H_0} \tag{2.5}$$

where $H(t)$ is the specimen height measured in time with the differential transducer, and H_0 is the initial height of the specimen.

The evolution of the measured swelling strain with time can be fitted by a hyperbolic function (Komine and Ogata, 1999, Muntohar, 2003):

$$\varepsilon_{sw}(t) = \frac{t}{a_{sw} + b_{sw}t} \tag{2.6}$$

where a_{sw} and b_{sw} are curve fitting parameters.

The asymptote of the hyperbola represents the maximum swelling strain of the material reached at the end of the saturation process, and it is calculated as follows:

$$\varepsilon_{sw,max} = \lim_{t \to \infty} \frac{t}{a_{sw} + b_{sw}t} = \frac{1}{b_{sw}} \tag{2.7}$$

The values of the curve fitting parameters a_{sw} and b_{sw}, and the maximum swelling strain for the presented experiments, are reported in Table 2.6 for distilled and synthetic water.

In order to evaluate the impact of the composition of the pore fluid on the generated swelling strain the rate of reduction of the free swelling deformation ($R\varepsilon_{sw}$) with dry density was calculated as follows (Komine et al., 2009):

$$R\varepsilon_{sw} = \frac{\varepsilon_{sw,DW} - \varepsilon_{sw,SW}}{\varepsilon_{sw,DW}} \qquad (2.8)$$

where $\varepsilon_{sw,DW}$ is the maximum free swelling strain in distilled water and $\varepsilon_{sw,SW}$ is the maximum free swelling strain in synthetic water. The rate of reduction of free swelling in the considered range of dry densities was calculated from the values of the free swelling taken from the curve fittings of the experimental data for both distilled and synthetic water Figure 2.13. A hyperbolic trend of the rate of reduction is observed with the obtained experimental data.

The swelling strain versus dry density data were fitted using a linear function as suggested by Komine and Ogata (1999) and Zhang et al. (2012). The assumed linear trend between swelling strain and dry density would suggest that the minimum dry density required to have an observable macroscopic swelling deformation of the mixture is approximately 1.3 Mg/m³ when distilled water is used and approximately 1.4 Mg/m³ when synthetic water is used. This latter observation is in agreement with the results of the constrained swelling tests in which no remarkable swelling pressure was observed for the sample with a dry density of 1.3 Mg/m³ saturated with synthetic water, and a swelling pressure of 30 kPa was observed for the sample with the dry density of 1.3 Mg/m³ saturated with distilled water (see next section, Figure 2.15).
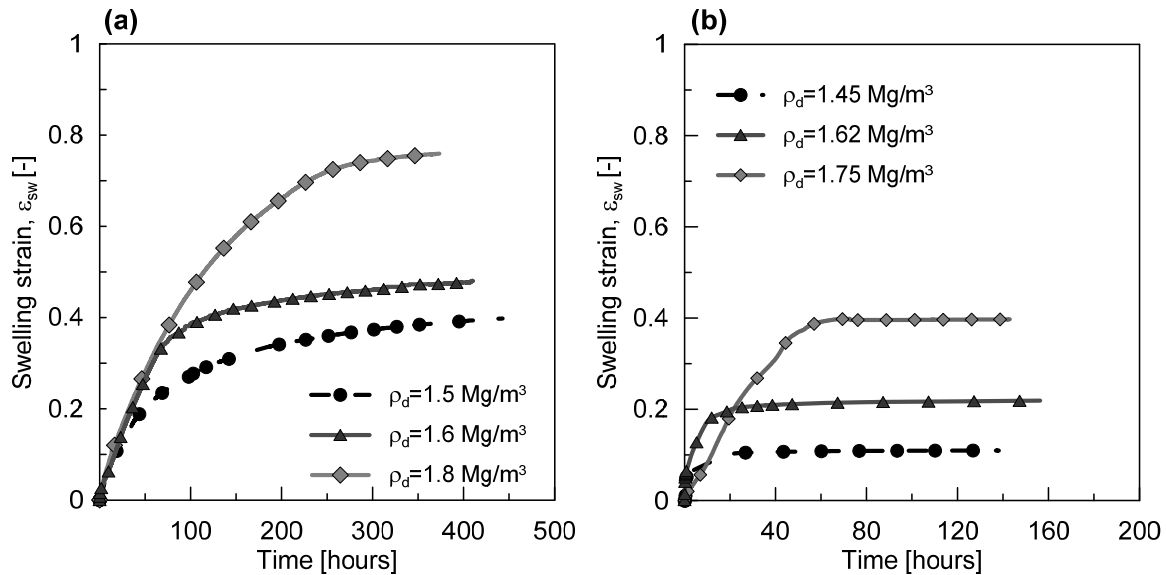

Figure 2.12: Change in swelling strain with the elapsed time for specimens saturated with distilled water (a) and synthetic water (b).

Table 2.6: Curve fitting parameters calculated from the free swelling experiments.

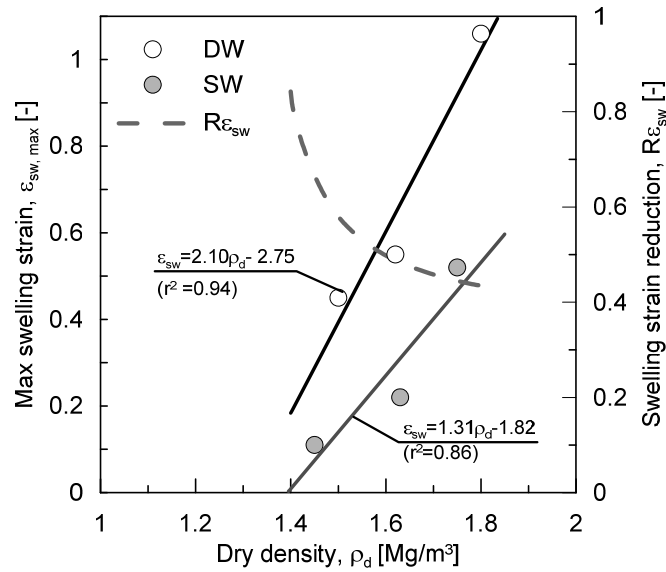| Water type	ρ_d [Mg/m^3]	a_{sw} [-]	b_{sw} [-]	$\varepsilon_{sw, max}$ [-]
	1.50	141.61	2.20	0.45
Distilled	1.60	93.82	1.83	0.55
	1.8	121.02	0.94	1.06
	1.45	1.67	8.89	0.11
Synthetic	1.62	8.93	4.59	0.22
	1.75	55.04	1.94	0.52

Figure 2.13: Comparison between the maximum swelling deformations of the S/B mixture wetted with distilled water and synthetic water as a function of dry density.

2.3.3 Standard constrained swelling tests

The results of the swelling pressure tests performed on the S/B mixture using distilled, synthetic water, and 1 M and 4M sodium chloride solutions are reported as a function of time in Figure 2.14. The data presented in the figure were treated with a moving average function in order to minimise the fluctuation due to the accuracy of the instruments and small temperature variations.

The results reveal that the swelling pressure increases quickly in the early stage of the tests (up to 50 hours for distilled water, up to 25 hours for synthetic water and less than 10 hours for sodium chloride solutions). After this stage the swelling pressure increasing rate reduces significantly. The stabilisation of the swelling pressure occurs earlier in specimen saturated with synthetic water and sodium chloride compared with distilled water. This behaviour is attributed to the higher hydraulic conductivity of bentonite-based materials in contact with saline solutions compared with the sample in contact with distilled water (Studds et al., 1998, Castellanos et al., 2008). The test

performed using synthetic water, on the specimen compacted to 1.3 Mg/m^3 of dry density, was stopped after 17 hours because no swelling pressure was generated.

To highlight the role played by the initial dry density and by the composition of the pore water, the values of the final swelling pressure as function of the initial dry density are reported in Figure 2.15. The reported values of the swelling pressure correspond to the weighted average of the swelling pressures measured after 50 hours for distilled water and after 25 hours for the other waters. An exponential relationship between the final swelling pressure P_{sw} and the dry density ρ_d was observed for three permeants:

$$P_{sw}(kPa) = \beta e^{(\beta \rho_d)} \tag{2.9}$$

where α and β are two material parameters which are listed in Table 2.7 and can be related to the osmotic suction of the pore water (Figure 2.16).
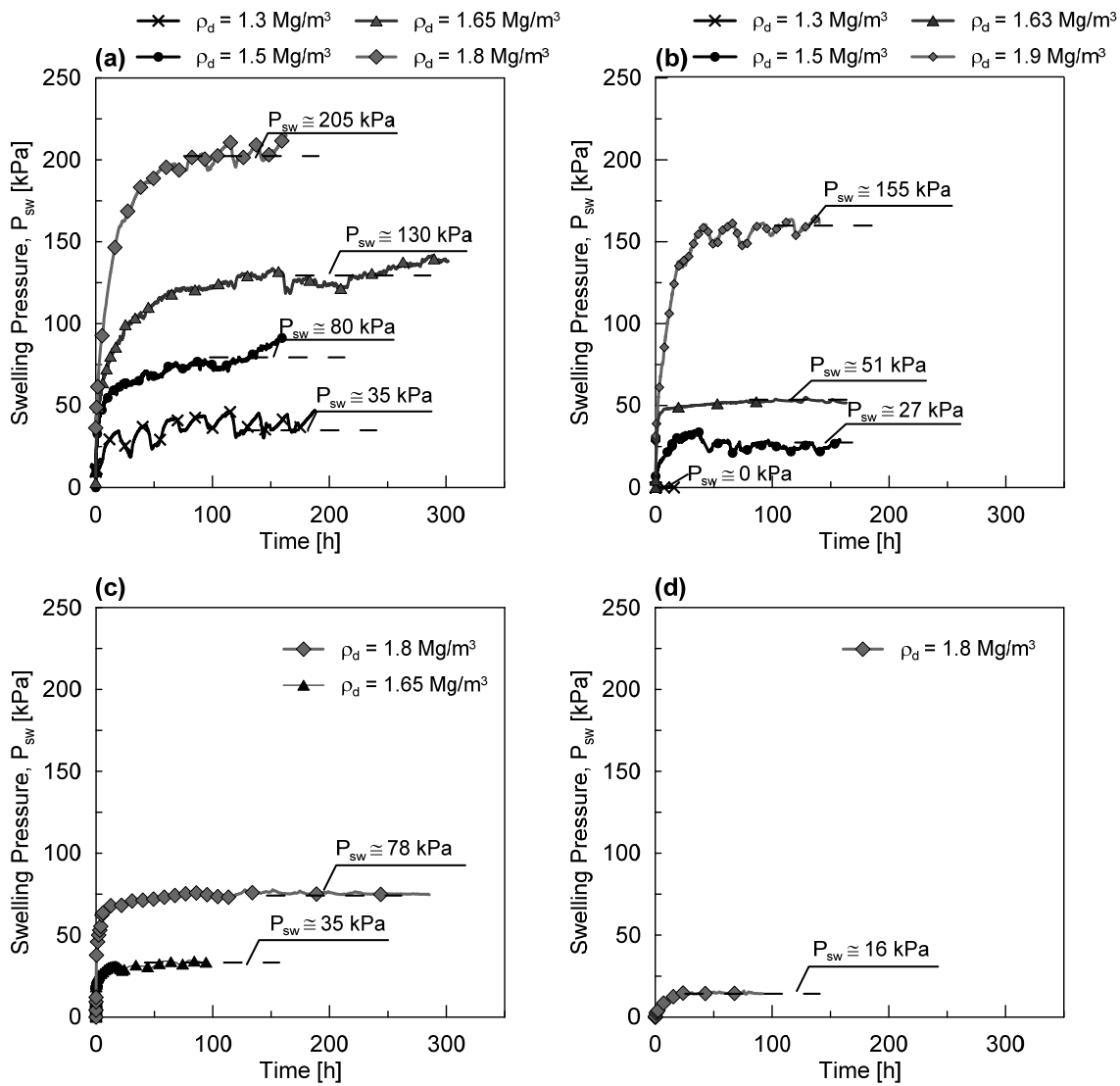

Figure 2.14: Swelling pressure development with time for distilled water (a), synthetic water (b) 1M sodium chloride solution (c) and at 4 M sodium chloride.

Table 2.7: Curve fitting parameters calculated from the constrained swelling experiments.

Water type	α [kPa]	β [m^3/Mg]
Distilled	0.27	3.74
Synthetic	3.36	4.47
1M NaCl	5.92	5.71
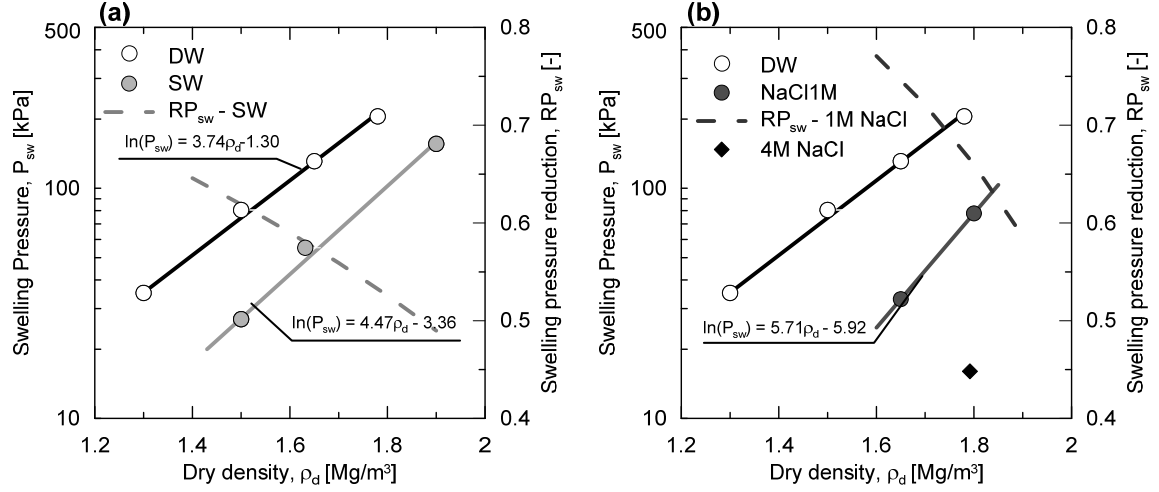
Figure 2.15: Swelling pressures developed with distilled water, synthetic water and 1M NaCl pore water as a function of the dry density.
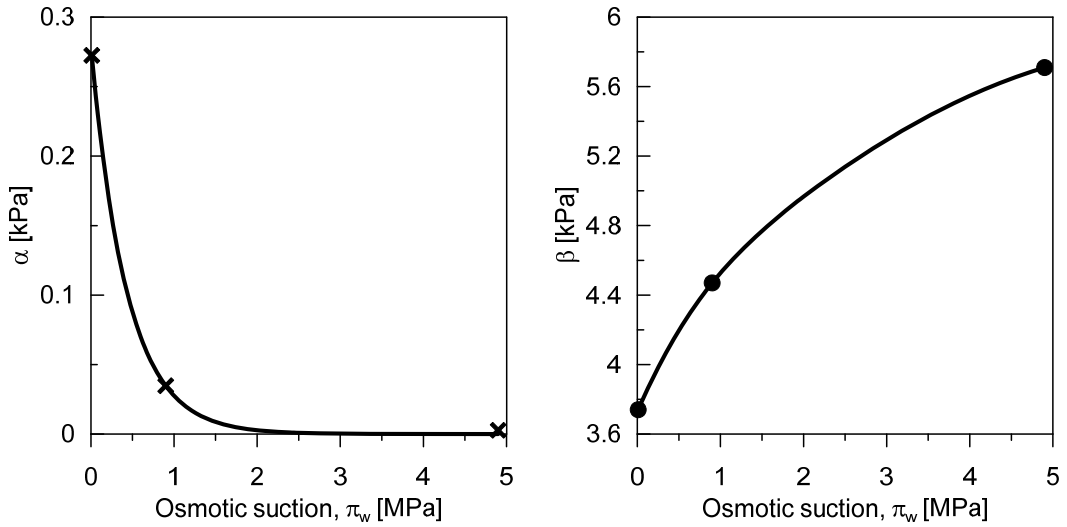
Figure 2.16: Swelling pressure fitting parameters vs suction of the pore fluid.

Similar to the free swelling tests, the effect of the chemical composition of the pore water on the swelling pressure is quantified through the rate of reduction of the swelling pressure ($RP_{sw,\alpha}$) for both synthetic water and 1M NaCl solution, as follows:

$$RP_{sw,\alpha} = \frac{P_{sw,DW} - P_{sw,\alpha}}{P_{sw,DW}} \qquad (2.10)$$

29

where $P_{sw,DW}$ is the swelling pressure in distilled water and $P_{sw,\alpha}$ is the maximum swelling pressure in the considered salty water (SW or 1M NaCl).

As shown in Figure 2.15, the swelling pressure reduction factor is larger for lower dry densities than for higher dry densities, with a maximum value of 62 % at ρ_d=1.5 Mg/m^3. The increase of the dry density leads to the decrease of the reduction factor which reaches a minimum value of 45% for the specimens with dry densities of 1.87 Mg/m^3. A similar trend is detected when NaCl solution is used. In this case, the reduction factor displays a minimum value of 59% at the highest dry density and a maximum value 77% at the lowest dry density (ρ_d=1.6 Mg/m^3). These tendencies were previously observed for pure bentonite (e.g., Dixon, 2000, Castellanos et al., 2008, Komine et al., 2009), and it is proved in this study that they also apply to S/B mixtures. Further discussions on the meaning of the reduction factor and its correlation with the microscopic features of the S/B mixture are provided in the section 4.6.4.1.

2.3.4 Controlled suction swelling tests

The evolution of the swelling pressure with the applied matric suction (s) (see section 2.4.1 for more details) for two specimens initially compacted to 1.49 Mg/m^3 (e=0.78) and 1.79 Mg/m^3 (e=0.49) and wetted with distilled water is presented in Figure 2.17. The initial matric suction of the mixture at the as-compacted state is approximately 280 kPa (measured with the filter paper method (Fredlund and Rahardjo, 1993)), regardless of the compaction density. This indicates that, at the as-compacted state, water is mainly stored in the pores located within the bentonite fraction (Romero et al., 2011). The results show that the swelling pressure is immediately generated with the decrease in matric suction following a non-linear trend in the semi-logarithmic plane. The maximum swelling pressure attained in the test is 59 kPa for the low compacted specimen and 167 kPa for the more compacted specimen. The expected maximum swelling pressures are determined from the results of the conventional swelling test (at the 0 kPa matric suction) for the final dry density of the tested specimens. The results were in good agreement with the final swelling pressure generated at a 10 kPa suction, confirming the consistency of the obtained data.

Once the state of full saturation was reached, the specimens were subjected to a monotonic drying. Similar to the water retention curve, the suction-swelling pressure curve shows hysteresis. It appears that the hysteresis is larger for the highest dry density, while it is almost negligible for the lowest dry density. This result indicates different microstructural behaviour of the material when subjected to a wetting and drying cycle.

During the monotonic drying of the specimen, a sudden drop of the swelling pressure was observed at a matric suction of 250 kPa for the mixture compacted to a dry density of 1.5 Mg/m^3. This suggests an important shrinkage of the specimen which leads to the loss of lateral contact between the specimen and the oedometric ring. This affirmation was

also confirmed by visual observation of the specimen after testing where a large gap between the oedometric ring and the specimen was detected.

A hyperbolic shape function was used to satisfactory describe the swelling pressure-matric suction relationship along the monotonic wetting:

$$P_{sw}(s) = P_{max}^0 \left[\frac{1}{1 + \left(\dfrac{s}{A} \right)^N} \right]^M \tag{2.11}$$

where, P_{max}^0 is the maximum swelling pressure at 0 kPa matric suction which can be calculated from eq. (2.9) and A, M, and N are the fitting parameters. The fitting values are reported in Table 2.8 for the two tested specimens.
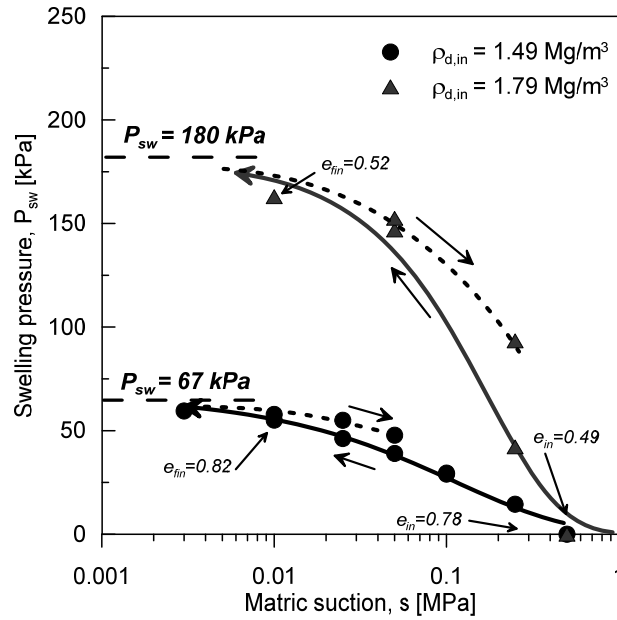
Figure 2.17: Evolution of the swelling pressure of the S/B mixture during a wetting-drying cycle under constant volume conditions for specimen compacted to two different dry densities.

Table 2.8: Fitting parameters for the swelling pressure-suction relationship in the main wetting branch.

Parameter	$\rho_{d,in}$=1.49 Mg/m^3	$\rho_{d,in}$=1.79 Mg/m^3
P_{max}^0 [kPa]	67	180
A [kPa]	42836	10771
N [-]	0.81	1.04
M [-]	103	80

2.4 WATER RETENTION BEHAVIOUR

The sand/bentonite mixture used as backfilling material might be subjected to wetting and drying processes during the working life of the repository. Wetting occurs as a consequence of the water adsorption from the host rock; drying may occur as a consequence of gas generation due to the anaerobic corrosion of the canister.

This section is devoted to the determination of the water retention capacity of the 80/20 mixture. The effect of the void ratio on the water retention behaviour of the S/B mixture is analysed along a wide range of suctions. Due to the very low unsaturated water permeability of the material, which implies long time for testing, the water retention curve is determined for two different dry densities (1.49 Mg/m^3 and 1.79 Mg/m^3) only. The main retention features of the S/B mixture are discussed here.

2.4.1 Concept of soil suction

The water retention capacity of a soil expresses its ability to adsorb and retain water into its pores. The water retention curve represents the relationship between soil suction and the amount of water stored in the soil, expressed in terms of water content, degree of saturation or water ratio.

The soil suction consists of two components: the matric suction and the osmotic suction. The matric suction is generated by the solid phase and is associated to the capillary forces, the osmotic and the electrostatic mechanisms. The osmotic suction is related to the dissolved salts of the pore water system. The sum of the osmotic suction (π) and matric suction (s) is called total suction (Tarantino, 2010):

$$\psi = s + \pi \tag{2.12}$$

The total suction is related to the relative humidity through the Kelvin's equation (Figure 2.18):

$$\psi = -\frac{RT\rho_w}{\omega_w} ln\left(\frac{p}{p_0}\right) \tag{2.13}$$

where p is the vapour pressure in the air, p_0 is the saturation vapour pressure at same temperature, R is the universal gas constant (8.31 J/mol K), T is the temperature of the sample in Kelvin degrees, ρ_w is the density of water (i.e. 0.997 kg/m^3 at 25° C), ω_w is the molecular mass of the water vapour (18,016 kg/kmol).
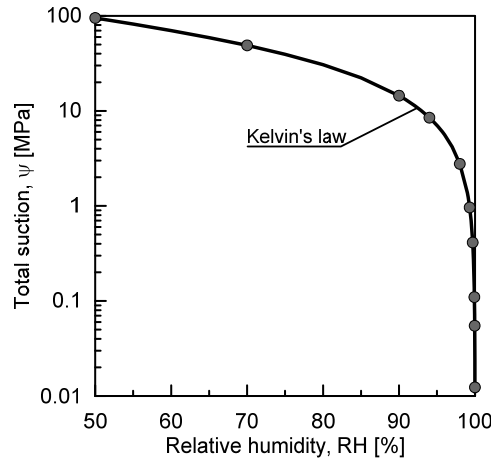
Figure 2.18: Relative humidity versus total suction according to Kelvin's law.

The matric suction is defined as the difference between the pressure of the wetting fluid and that of the non-wetting fluid and it can be expressed by the Laplace equation as:

$$s = p_a - p_w = \frac{4T_s \cos \vartheta_w}{x} \tag{2.14}$$

where T_s is the surface tension, ϑ_w is the contact angle between the wetting phase and the solid phase and x is the apparent pore diameter.

The water retention behaviour of a soil is non-linear, hysteretic and history dependent (Figure 2.19). Because of its hysteretic nature the water retention exhibits a main wetting path and a main drying path. Following the main wetting, the material goes from the residual saturation ($S_{r,res}$) up to the full saturation ($S_r = 1$). The main drying goes from the conditions of full saturation down to the residual state. All possible hydraulic states are enclosed into the main drying and the main wetting curves.

The hysteresis of the water retention curve of a soil is related to the difference of the contact angle during wetting and drying and to the bottle necks effect (Tarantino, 2010). However, the radius of the hysteresis of the water retention curve of an MX-80 granular bentonite was found to be dependent also on the nature of the volumetric deformations of the aggregates. In particular, the radius reduces after a wetting-drying cycle as a consequence of the irreversible deformations of the pore structure (Seiphoori et al., 2014).
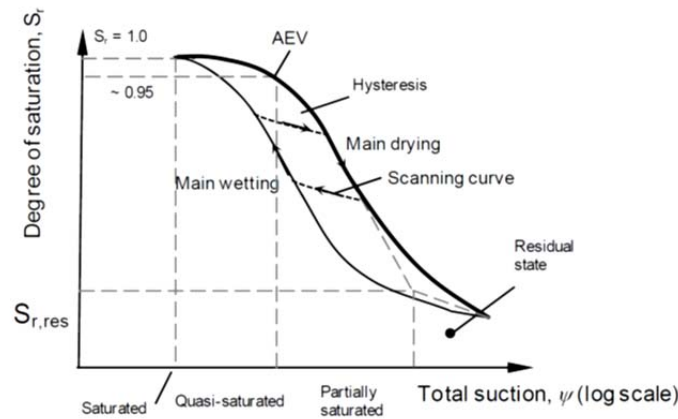
Figure 2.19: Typical water retention curve for geomaterials (from Seiphoori (2014))

The mechanisms that govern the water storage in geomaterials may differ significantly depending on the nature of the soil. For example, in sandy soils the dominant mechanism for retention is capillarity and water is retained at the contact between the particles or on the surface of the particles when very low degrees of saturation (residual state) are attained. The retention capacity of these types of soils is usually sensitive to the mechanical loads all along the water retention domain. Clayey soils, because of their structured nature as well as the strong physico-chemical interaction between the particles and the pore water system (water + ions), are characterised by two retention mechanisms: the adsorption mechanism and the capillary mechanism.

The water retention curve of deformable soils (Figure 2.20) usually presents a delimiting zone separating the capillary-dominated retention region from the adsorption-dominated retention region (Romero, 1999, Romero and Vaunat, 2000). At high suction values, water is preferably attracted within the intra-aggregate pores and tends to neutralise the negative charge in the clay particles and to hydrate the exchangeable cations on the interlayers. The shape of the water retention curve in the intra-aggregate region does not depend on the variation of the void ratio and, in the plane water content vs suction, the drying and the wetting branches of a soil compacted to two different void ratios follow the same path. At low suction, the water stored in the soil is sufficient to fully saturate the intra-aggregate pores and also to partially fill the pores within the clay aggregates (inter-aggregate pores). This region of the water retention is capillary dominated and appears very sensitive to the change in void ratio caused by hydro-mechanical actions (e.g. volume variations due to mechanical loadings or swelling and shrinkage due to wetting and drying cycles) (e.g. Romero et al., 2011, Salager et al., 2013). The air entry value (a.e.v), defined as the value of matric suction above which the gas starts to invade the larger pores of the soil, is usually higher for the specimen compacted to lower void ratio.
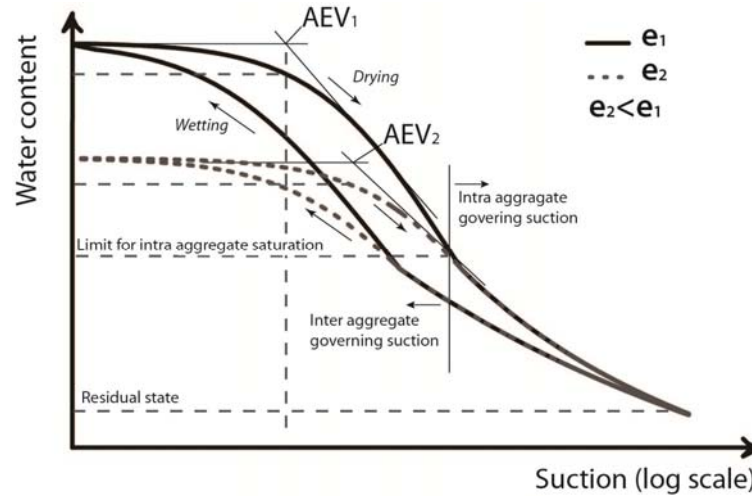
Figure 2.20: Effect of void ratio change on the water retention curve of deformable soils.

The water retention behaviour is a key point to understand the flow mechanism of wetting and non-wetting fluids through the tested sand/bentonite mixture, or any soil in general, under unsaturated conditions as it gives information on the storage mechanisms. For the specific case of a non-aggregated and non-active soil (e.g. only sand or gravel), depending on the degree of saturation the wetting fluids may occur in different forms. Referring to Figure 2.19, at very low degree of (water) saturation, usually called residual saturation state, water forms pendular rings on the grains surface and practically no water pressure can be transmitted. As the wetting-phase saturation rises above the residual state, the water occurs in a funicular form and becomes a continuous phase so that the flow of the wetting phase is possible. When the water degree of saturation increases more, the non-wetting fluid (air) became non-continuous and it drops in individual droplets allocated in the larger pores (Bear, 1972).

In the case of aggregated multi-structured soils (e.g. silty and clayey soils), depending on the degree of saturation and the fluid wettability, flows can occur through the aggregates or through the large pores. Usually, the wetting phase fills the intra-aggregate pores at low degree of saturation due to their higher retention capacity. Under such condition, and in case of capillary dominated flow, water flow occurs between the aggregates and is controlled by the aggregates contact area (Carminati et al., 2007, Carminati et al., 2008). At larger degree of saturation, the wetting fluid starts to invade the larger pores. The gaseous phase (the non-wetting fluid) has the tendency to occupy the larger pores. In an initially fully saturated soil, the drying process is initiated once the capillary pressure equals or surpasses the air entry value. After this threshold value, the advective gas transport initiates.

2.4.2 Methodologies

The determination of the water retention properties of the 80/20 S/B mixture in a wide range of suction required the combination of different techniques. For this study the following methods were used:

1. Filter paper method, for determining both total and matric suction at the as-compacted state.
2. Microcell technique, which allows the measurement of the total suction at low water content.
3. Axis translation technique, for imposing matric suction under constant volume condition.

2.4.2.1   Filter paper method

The filter paper method is an indirect method for measuring both total (filter paper not in contact) and matric suction (filter paper in contact). According to Fredlund and Rahardjo (1993), any value of suction could be measured with this technique, nevertheless the technique appears to have many sources of error; e.g., it is very sensitive to the operator and temperature variations.

Filter paper disks type Schleicher and Schuell No. 589 (SS589) were used to measure the total and matric suction of the soil at the as-compacted state. The suction versus water content calibration curves of the filter paper adopted for the measurements are presented in Figure 2.21 and were determined by Ferrari et al. (2011). The ASTM D5298-10 standard was followed to determine the initial total and matric suction of the mixture compacted to different dry densities.

To prepare suitable specimens for the filter paper method, two cylindrical specimens having similar characteristics (i.e., dry density as close as possible) were prepared for each target dry density following the procedure presented in paragraph 2.2.6. After static compaction the specimens were extracted from the oedometric ring and immediately stored in a sealed chamber for all the time required for setting up the test. This procedure limits the undesired water content loss which can occur during the test preparation. As suggested by Bulut et al. (2001), all the items related to the filter paper method were carefully washed before using them and were managed using latex glows because oily hands may cause the filter paper to adsorb more water.
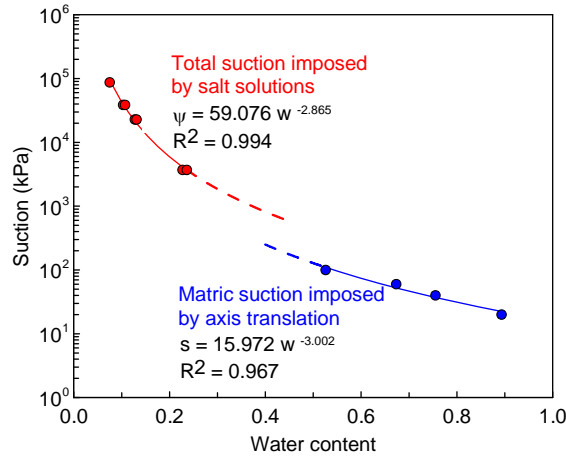
Figure 2.21: Calibration curves for total and matric suction obtained on Schleicher and Schuell No. 589 filter paper (Ferrari et al., 2011).

For the contact suction measurements, a sandwich filter paper was placed between the two specimens and the intimate contact between the soil and the filters was ensured. The sandwich filter paper consists of one filter paper type SS589 having diameter of 45 mm protected by two standard filters paper having diameter of 50 mm. These two filter papers prevent the contamination of the filter paper SS589. The contact interphase between the two specimens was sealed with electrical tape ensuring proper isolation from the surrounding atmosphere. For the total suction measurements, a third filter paper was mounted on a plastic ring which was placed on the upper surface of the specimens. The whole assembly (two specimens and the filter papers) was placed inside a glass jar that was wrapped in a plastic foil and in a paraffin tape to guarantee the perfect air-tightness of the system. Finally, the jar was placed inside an isolated box to maintain the constant temperature during equilibration time. The filter papers were extracted after two weeks equilibration time and their water content was immediately measured by oven drying them for 24 hours at 105 °C.

2.4.2.2 The microcell technique

The microcell technique is a technique developed at the Laboratory for Soil Mechanics of EPFL for measuring the retention properties of swelling soils under isochoric condition and in high suction range (total suction higher than 3 MPa). This technique provides a more precise estimation of the water retention curve, with respect to the vapour equilibrium technique, due to the possibility of including a large number of experimental points (Seiphoori et al., 2014). It also avoids the effect of dry density fluctuation as the retention curve is determined using only one specimen. This effect is usually unavoidable when the determination of the water retention capacity of a soil requires the preparation of several specimens.

This technique couples an isochoric cell, the so called "microcell" that hosts the specimen, with a chilled mirror dew point psychrometer for measurements of the total soil suction, the WP4c from Decagon (Figure 2.22).
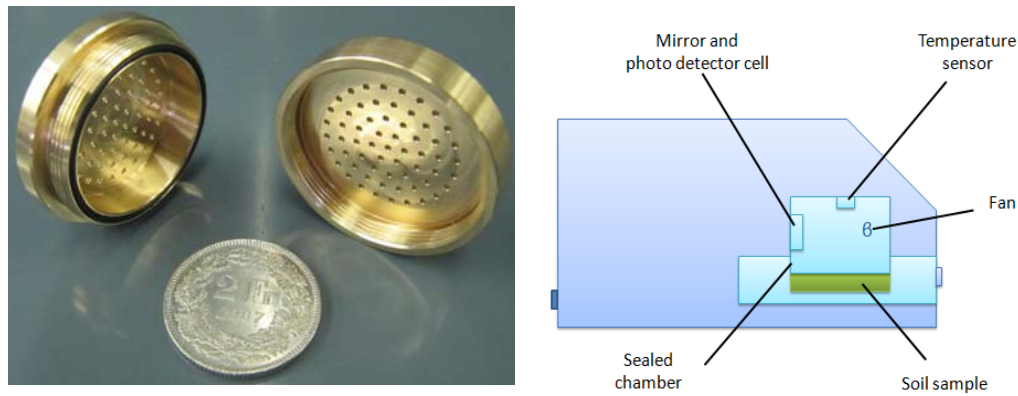
Figure 2.22: The microcell (left). Schematic representation of the WP4c device (right).

The microcell is a cylindrical shaped-cell made of brass which has been designed and manufactured at the Laboratory for Soil Mechanics of the EPFL. The cell dimensions were fixed in order to allow the cell to be positioned directly inside the WP4c chamber. In this way suction measurements can be carried out without opening the cell, maintaining the constant volume condition, and preserving the swelling pressure inside the cell.

The cell hosts a specimen of 7 mm of height and 30 mm of diameter. This small specimen was proven to be big enough to ensure obtaining a uniform distribution of the sand and bentonite fractions (Manca et al., 2015).

The cell is composed of two threatened lids that can be tightened together. The sealing of the cell is provided by an O-ring placed between the two lids. The top and the bottom of the cell are perforated to allow the water/vapour circulation. To avoid particles escape through the microcell holes during the hydration process two filter papers type Schleicher and Schuell No. 589 were placed on the top and the bottom of the specimen.

The WP4c is a dewpoint psychrometer manufactured by Decagon Devices (US) which enables to measure the total suction of a specimen in the range of 3 - 300 MPa, in a relatively short time (about 1 hour for each measurement) (Leong et al., 2003, Cardoso et al., 2007). Chilled mirror hygrometer technique was found to be one most precise total suction measurements technique when compared with other methods (Agus and Schanz, 2005a). It allows measuring the total suction of the specimen with a good accuracy (< 10%) until a minimum value of 4 MPa total suction (Arifin, 2008). For that reason the suction measurement where stopped at this limit and the retention curve for a low suction range was obtained with the axis translation technique.

The device is equipped with a sealed chamber where the following components are located (Figure 2.22, right):

- a mirror, whose temperature is precisely controlled by a thermoelectric (Peltier) cooler;
- a photoelectric cell, which detects the exact point at which the condensation first appears in the mirror;

- an infrared thermometer, which detects the specimen temperature;
- a fan, whose purpose is to allow reaching the equilibrium more quickly and to control the boundary layer conductance of the dew point sensor.

For this test, the mixture was prepared to a minimum water content of approximately 4% to avoid the segregation of the two components during the pouring phase. After preparation the mixture was compacted to the target dry density and then the cell was closed and sealed in a hermetic container for 1 day to allow moisture redistribution inside the specimen. After that, the initial suction was measured with the WP4c.

For the wetting path (Figure 2.23), the material was saturated in steps by putting the microcell in an ambient at 100% of relative humidity (zero total suction). Inside the chamber the material tended to equilibrate with the imposed relative humidity through the adsorption of water in the vapour phase. After a certain time that varies from 12 to 24 hours for each step the saturation process was interrupted. Then, the cell was sealed with paraffin tape for 1 day in order to let the adsorbed moisture to redistribute along the different pore families. After the equalisation, the suction was measured with the WP4c. The total weigh of the cell was continuously monitored in order to compute the evolution of the water content and degree of saturation.

For the drying path, a similar procedure as for the wetting path was adopted. In this case, once the material reached the minimum suction value of 4 MPa, the cell was exposed to the laboratory ambient, in which the temperature is kept at 22°C (±1°C) and the relative humidity is 41 % (corresponding total suction of 120 MPa). During the drying process the weight of the cell was monitored in order to compute the evolution of the water content. The process was stopped after a certain time that varies from 1 to 24 hours, depending on the reached water content, by sealing the microcell with the paraffin tape. As the water evaporation occurred from the holes of the microcell, so it started from the external surface of the specimen, the cell was sealed in paraffin for at least one day in order to let the total suction to homogenise inside the specimen. The drying process was stopped once the suction reached the initial suction value obtained after compaction. The microcell was opened at the end of test and the contact of the specimen with the cell was assessed. Experimental data were corrected to consider the contribution of the filter papers to the water retention.
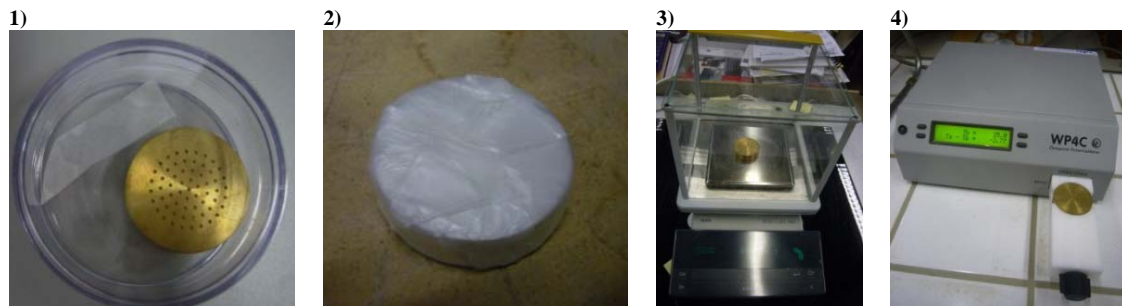

Figure 2.23: Phases of the wetting path: 1) Saturation; 2) Sealing; 3) weight measurement; 4) Suction measurement.

The water content of the specimen at each step (w^i) was calculated as follows:

$$w^i = w^{i-1} \pm \frac{\Delta M^i_{w,Tot} - \Delta M^i_{w,fp}}{M_{s,sp}} \qquad (2.15)$$

where w^{i-1} is the water content at the step before, $M_{s,sp}$ is the dry mass of the specimen, $\Delta M^i_{w,Tot}$ is the total mass of adsorbed water, by the specimen and the filter paper, at the considered step and, $\Delta M^i_{w,fp}$ is the mass of water adsorbed by the filter paper only. $\Delta M^i_{w,fp}$ is calculated as a function of the measured total suction using the water content versus suction calibration curve presented in Figure 2.21.

Once the correct water content is known the degree of saturation is calculated as follows:

$$S^i_r = \frac{w^i G_s}{e} \qquad (2.16)$$

where, G_s is the specific gravity of the mixture and e is the void ratio of the specimen considered as constant during the experiments.

For this test, the water content variation experienced by the mixture was relatively small ($\Delta w \cong 6\%$) and the mixture did not reach the condition of full saturation as the wetting was interrupted at a total suction of 4 MPa. Under such conditions, none of the tested specimens showed a significant volume reduction.

2.4.2.3 *Controlled suction oedometric cell - axis translation technique*

The axis-translation technique can be classified as a direct method for matric suction measurements. This technique allows the measurements or the application of matric suction up to 1500 kPa by using high air entry value ceramic disc available in commerce (Fredlund and Rahardjo, 1993).

In this technique, the specimen is placed in a sealed chamber where the air pressure is artificially risen up to a constant gauge pressure. In this way, the atmospheric pressure in the chamber is translated to a higher value. As a consequence, the water gauge pressure becomes positive and moves away from the metastable state limiting the risk of cavitation (Marinho et al., 2008). The advantage of maintain the gas pressure constant lies on avoiding the air-water interface bridging microvoids and limiting the pore water volume change associated to the presence of air bubbles into the water phase (Romero, 1999).

Axis-translation technique is suitable when the pores within the soil are interconnected. With this regard, the tested specimens of S/B mixture at the as compacted state (w_{mix}=0.11) have a degree of saturation of 0.38 at the low density packing (ρ_d=1.5

Mg/m^3, e =0.78) and 0.61 at the high density packing (ρ_d =1.8 Mg/m^3, e =0.48). Under such conditions, water and gas in the mixture are continuous phases and the pressures are properly transmitted.

A controlled suction oedometric cell was used in this study to determine the water retention capacity of the S/B mixture under suctions lower than 500 kPa. The schematic layout of the oedometric cell is presented in Figure 2.24. The cell consists of an oedometric ring that hosts a specimen of 16 mm in height and 64 mm in diameter. The upper surface of the specimen was in contact with a top cup where a coarse porous stone was installed. A high air entry value (HAEV) ceramic disk was installed at the bottom of the specimen. The characteristics of the ceramic disc are listed in Table 2.9. The disk was fully saturated before setting up the experiment. The ceramic disk was installed on a stainless steel cylindrical support. The support has two holes connected with a spiral grove cut that are connected to the water supply system. The spiral grove ensures the proper distribution of water at the bottom of the ceramic and allowed the periodical flushing operations required to eliminate air bubbles diffusing through the ceramic. Two O-rings were placed at the bottom of the ceramic disk support where the two holes were connected to the water supply system, to ensure that the gas flows toward the water compartment only by diffusion through the ceramic.
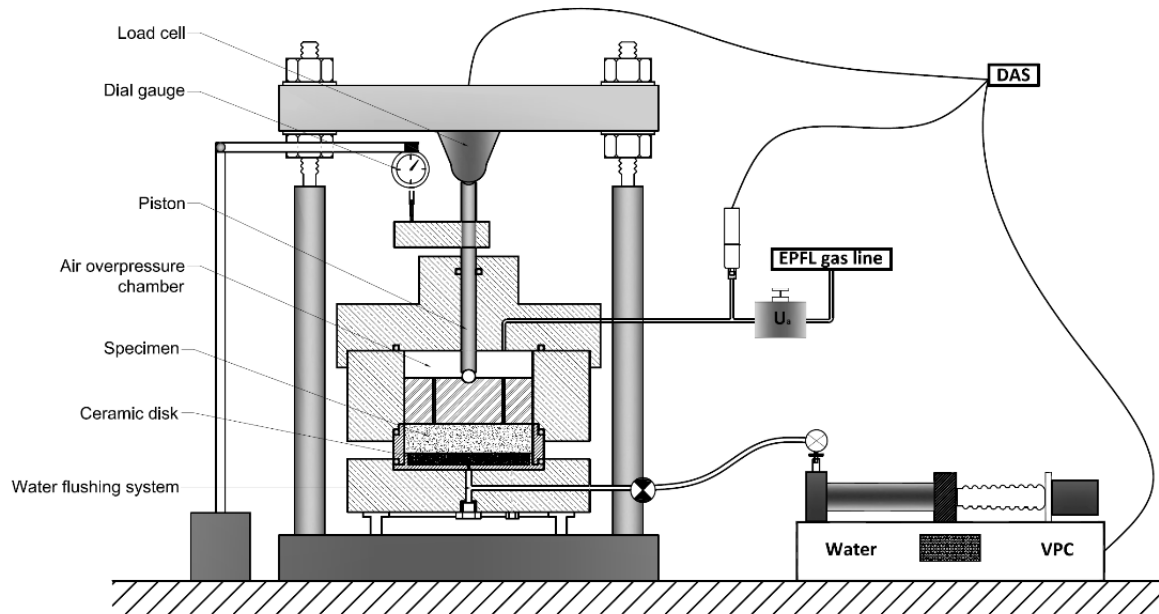

Figure 2.24: Layout for the experimental characterisation of the water retention capacity of the S/B mixture.

Table 2.9: Characteristics of the ceramic disk.

Diameter, D_c [mm]	55
Thickness, t_c [mm]	7.84
Hydraulic conductivity, k_c [m/s]	$1.93 \cdot 10^{-10}$
Nominal air entry value, AEV [MPa]	0.5

The loading system consisted of a piston which connected the top cup to a load cell mounted on a rigid frame. The load cell allowed measuring a maximum vertical force of 2 kN, with an accuracy of 0.1% of the full range, corresponding to a maximum pressure of 628 kPa. Upward vertical deformations of the piston were limited by docking the two upper bolt of the rigid frame. A small rod was connected to the piston and a LVDT was placed on the top of it for monitoring the vertical displacements of the piston. The support of the LVDT is placed outside the cell to avoid any disturbance of the vertical measurements.

Water pressure in the specimen was applied by means of a water PV controller while the gas pressure was applied directly from the main EPFL line. The gas pressure was regulated using a pressure manometer. A pressure transducer was inserted in the gas line to register the gas pressure in the overpressure chamber with an accuracy of ± 1 kPa. The load cell, the water PV controller and the gas pressure transducer were connected to the data acquisition system Quantum-X whereas the data of piston displacements were collected manually.

For the controlled suction oedometric tests the mixture was initially wetted at 11% of water content with distilled water and then compacted inside the oedometer ring to the target dry densities of 1.50 Mg/m^3, 1.70 Mg/m^3 and 1.80 Mg/m^3. After setting up the experiment, a matric suction of 500 kPa was imposed to the specimens. This suction is higher than the suction of the mixture at the as-compacted state; consequently, at the beginning of the test, the specimen experienced a drying process. Once the suction was equalised to 500 kPa, a main wetting path was initiated by reducing the matric suction stepwise up to 3 kPa.

The main drying path was initiated after the specimen was equalised to the minimum matric suction. Then the suction was increased stepwise until 500 kPa was reached.

The water content of the specimen at equilibrium, for each applied matric suction step is calculated as follows:

$$w^i = w^{i-1} \pm \frac{\Delta M^i_{w,Tot} - \Delta M^i_g}{M_{s,sp}} \tag{2.17}$$

where ΔM^i_g is the mass accounting for the gases/water vapour which are coming from diffusion/evaporation processes. More details about the issue of diffusion/evaporation happening when using the axis translation technique are given later in this paragraph.

Knowing the corrected water content, the degree of saturation is calculated with eq. (2.16), accounting for the slight variation of the void ratio of the specimen that occurs for each matric suction step.

The evolution of the void ratio with suction is depicted in Figure 2.25. Despite the precautions that were taken to maintain the isochoric conditions, the void ratio of the specimens increased due to the generation of swelling pressure upon wetting. As a

consequence, the dry density reduced of 0.02 Mg/m^3 for the lowest dry density and 0.04 Mg/m^3 for the highest dry density. Volumetric deformations of the specimen were much larger for the highest dry density due to the higher swelling pressure generated during hydration. Regarding the specimen compacted to 1.70 Mg/m^3, during the test the LVDT broke and for that reasons it was not possible to track its volumetric deformations. Visual observation of the specimen compacted to 1.70 Mg/m^3, at the end of the test, showed that the height of the specimen increased of approximately 1mm. As a consequence, the results of this test were rejected.

Test preparation, determination of the net vertical stress and swelling pressure generated

The successful or failure of the axis translation technique is strictly related to the preliminary preparation phases of the test as discussed by Marinho et al. (2008) and Vanapalli et al. (2008).

The first step for the test preparation consists on the saturation of the ceramic disk. This passage is essential to achieve the required bubbling pressure. The ceramic disk acts as a separator between water compartment and the air chamber and avoids the advective migration of gas through the water compartment (water PV controller). Advective gas migration can lead to an incorrect measurement of the water pressure and to the wrong evaluation of the water volume exchange from the specimen to the water compartment and vice versa. To saturate the ceramic, the oedometer cell was set-up and filled with de-aired water. The water inside the cell was pressurised up to a constant pressure of 1000 kPa, which is twice the air entry value of the ceramic. The pressure was maintained constant for several hours to dissolve the air present in the cervices of the ceramic. The ceramic was then subjected to several flushing cycles by opening the drainage lines at the bottom of the ceramic disk. The hydraulic conductivity of the HAEV disk was measured through a steady state permeability test performed at high pressure gradient after each flushing cycle. The saturation procedure of the ceramic disk was stopped when the hydraulic conductivity of the ceramic resulted equal or higher than 1.93·10^{-9} m/s.
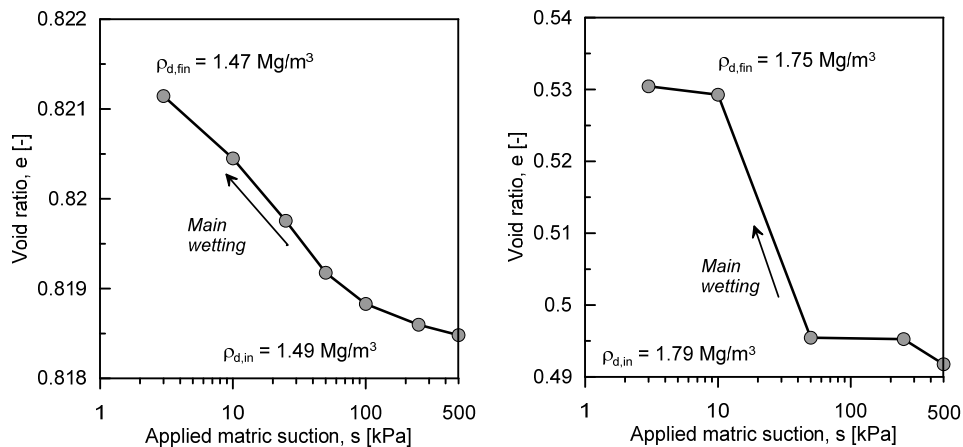

Figure 2.25: Void ratio evolution of the two tested specimen during the determination of the water retention properties.

43

The tested specimens were compacted directly into the oedometric ring following the procedure presented in paragraph 2.2.6. Immediately after compaction the specimen was wrapped with paraffin tape to avoid any water content loss during the set-up of the experiment. While compacting the specimen, the ceramic was submerged in a bath of de-aired water to avoid its desaturation that may occur when it is exposed to laboratory environment (T=22°C and RH = 41%).

For the test set-up, the saturated ceramic disk was mounted on the pedestal of the oedometric cell and the water line was flushed to eliminate the air entrapped in the drainage ducts. Prior to installing the specimen, all the parts of the oedometric apparatus were carefully dried-out to limit any alteration of the initial water content of the specimen. This procedure was very important to limit undesired swelling deformation/pressure of the specimen during the first stages of the test. Also, right before emplacing the specimen on the cell, the excess of water on the top of the ceramic was removed. Only a humid filter paper was left on the top of the ceramic. This filter paper was placed inside the jar containing the S/B mixture wetted to the initial water content so that its suction was equalised with the initial suction of the specimen. Once the specimen was placed in the oedometer, the gas pressure and the vertical stress were increased stepwise so that the net vertical stress applied to the specimen remained positive and oscillated between two fixed values (Airò Farulla and Ferrari, 2005). In this manner the undesirable volumetric deformations of the specimen were minimised.

At the beginning of the test, a net stress higher than 20 kPa was applied to the tested specimens (Figure 2.26). This initial stress, which is between 2 and 3 orders of magnitude lower than the initial stress applied to the specimen during static compaction, causes negligible variations of its initial dry density. The application of a certain net vertical stress is essential to ensure an intimate contact between the sample surface, the loading system on the top and the ceramic disk at the bottom. This ensures the transfer of water through a continuous water film and guaranties the reliable measurement of the matric suction (Marinho et al., 2008). Measurements of the initial matric suction vs dry density proved that for the S/B mixture the application of this initial vertical stress produces negligible variations of the initial matric suction (see section 2.4.3.1).

Flushing cycles of the water drainage system were performed on a regular basis for the whole duration of the test, to eliminate the volume of diffused gases occluded in the water compartment. This procedure ensures the continuity of water between the water supply and the specimen.

The net stress applied to the specimen (σ_{net}) at the beginning of the test is determined by considering the free body diagram of the system load cell-piston-specimen and solving the equilibrium to vertical displacements, as follows:

$$\sigma_{net} = \frac{F_v - T_p - \left(u_a A_p\right)}{A_{sp}} \qquad (2.18)$$

where F_v is the vertical force applied to the specimen, and registered with the load cell, T_p is the tangential force arising from the friction between the piston and the o-ring, which is measured in the laboratory by applying an increasing fluid pressure in the overpressure chamber until the displacement of the piston in detected, and, A_p and A_{sp} are the cross-sectional areas of the piston and the specimen, respectively. The tangential force was measured in the laboratory and results equal to 0.05 kN.

Swelling pressure at each suction step (P_{sw}^i) was determined as:

$$P_{sw}^i = P_{sw}^{i-1} + \frac{\Delta F_v^i}{A_{sp}} \qquad (2.19)$$

where P_{sw}^{i-1} is the swelling pressure at the step before and ΔF_v^i is the increment of the vertical force at the current step.
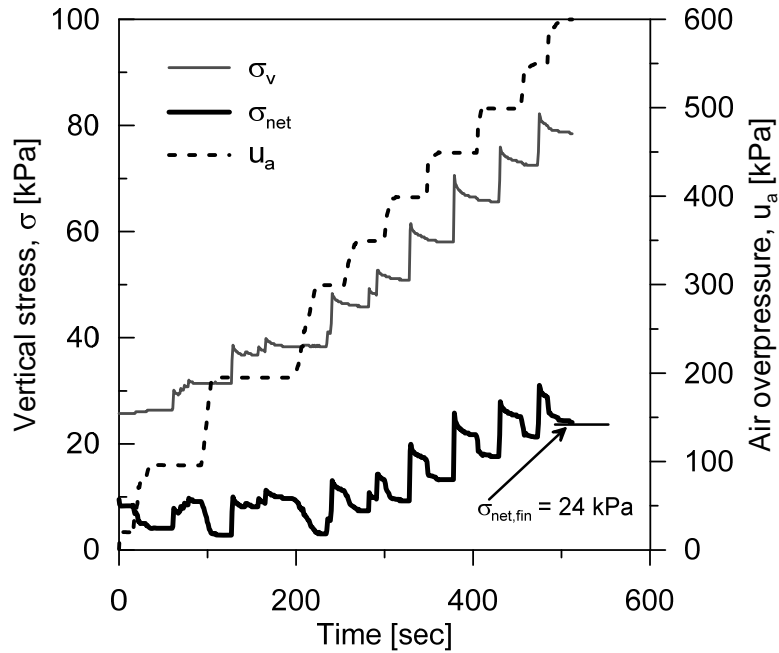

Figure 2.26: Axis translation procedure.

Water volume exchanges correction accounting the diffusion and evaporation processes

Water content changes in the soil specimen are calculated knowing the volume of water flowing from the specimen to the water supply or vice versa. Direct measurements of this volume are affected by the evaporation of water vapour toward the air supply and by diffusion of air through the ceramic disk toward the water compartment.

When the air-water interphase is established through the ceramic, a given amount air can dissolve into the water according to the Henry's law. In case of air, the volumetric coefficient of solubility in clear water is equal to 0.0178 at a temperature of 25°C (Fredlund and Rahardjo, 1993). Then, because a gas concentration gradient exists between the water in the ceramic and the water in the water supply, gases will diffuse through water according to the Fick's law. These gases will then come out and dissolve in the water drainage lines beneath the ceramic disk. The accumulation of these gases in the drainage lines is highly undesirable as may cause the discontinuity the pore water and the water in the water supply system and the poor transfer of the pore water pressure. Evaporation of the specimen pore water originates from the vapour pressure difference between the soil pore water and the air overpressure chamber and may cause the shrinkage of specimen (Romero, 2001).

Volumetric diffusion and evaporative fluxes can be detected in the water volume PV controller under steady state conditions (Romero, 1999, Airò Farulla and Ferrari, 2005). For example, when following the main wetting path, because of the diffusion of air toward the water compartment, the amount of water adsorbed by the specimen will result

lower than the true value. On the other hand, the evaporation will appear as an excessive water adsorption in steady state conditions during the wetting process and may cause the excessive desaturation and shrinkage of the specimen. Overall, this phenomenon may lead to the wrong estimation of the water content as well as the degree of saturation of the specimen.

Figure 2.27 shows the water volume exchanges occurring between the specimen and the water supplier during a wetting and a drying step. Steady state was attained after about 1200 hours in the main wetting path and after about 400 hour in the main drying path because of the very low unsaturated permeability of the mixture. Measured water volume was corrected by subtracting the measured flow rate at the steady state to the raw data. Under wetting and drying paths, the adsorbed (or expelled) volume of water versus time curve shows at steady state a positive slop indicating that water evaporation was exceeding diffusion. For this experimental setup this tendency was observed almost at any matric suction mainly because the air was injected in the air overpressure chamber directly from the main EPFL line which is an open system of infinite volume.
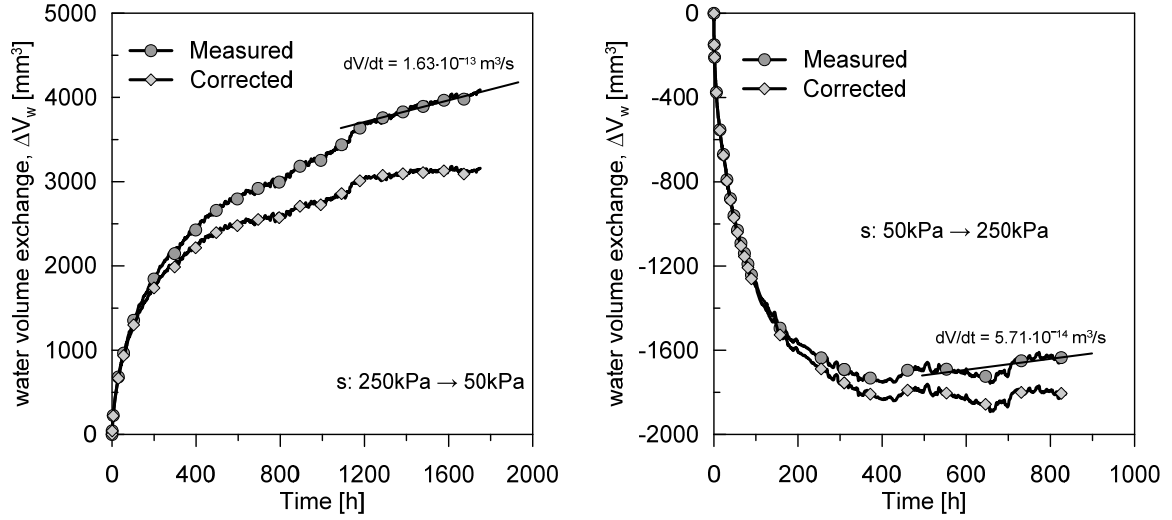
Figure 2.27: Water volume exchange versus time during one equalisation step along the main wetting (left) and along the main drying path for the specimen compacted to an initial density of 1.8 Mg/m³.
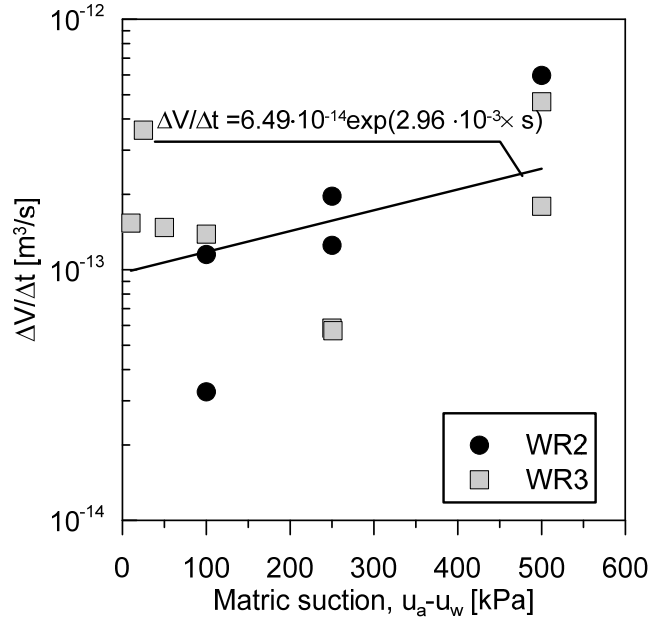

Figure 2.28: Volumetric flux at the steady state conditions detected for two different dry densities; ρ$_d$=1.70 Mg/m³ (WR2) and ρ$_d$=1.79 Mg/m³ (WR3).

Figure 2.28 reports the values of the fluxes that were measured in steady state condition during two of the three tests. These values are the result of the contribution of the evaporative and diffusive fluxes. The resultant flux decreases with the decrease of the matric suction. The volumetric fluxes (Q_s) measured under steady state condition were fitted with the following expression:

$$Q_s = \Delta V/\Delta t = 6.49 \times 10^{-14} e^{\left(2.96 \times 10^{-3} s\right)} \tag{2.20}$$

The determination of the water retention curve of the S/B mixture required approximately 9 to 13 months depending on the number of matric suction steps applied

and compaction density. In order to speed up the experiment, for the specimen compacted to a target density of 1.5 Mg/m³ it was decided to change the suction when the swelling pressure stabilised and the water content had a variation lower than 0.2% per day.

To compute the error that this procedure produced on the final results the water volume adsorbed or expelled by the specimen with time ($V_w^{sp}(t)$) is expressed as follows:

$$V_w^{sp}(t) = c_w \left(\frac{t}{b_w + a_w t} \right) \tag{2.21}$$

where a_w, b_w and c_w are fitting parameters.

The water volume exchange measured by the PV controller $V_w(t)$ is the sum of the volume adsorbed/expelled by the specimen and the additional flux that arises from diffusion/evaporation ($V^{D/E}(t)$):

$$V_w(t) = V_w^{sp}(t) + V^{D/E}(t) = c_w \left(\frac{t}{b_w + a_w t} \right) + Q_s t \tag{2.22}$$

The coefficient Q_s in equation (2.22) is known for each applied suction step from equation (2.20) making the assumption that it depends only on the experimental setup, which was always the same for all the tests.

The raw data of the water volume exchange obtained for each suction step are fitted with equation (2.22) to obtain the fitting parameters for equation (2.21). Then, the water volume that the specimen would have adsorbed after 1000 h (41.6 days) was calculated. With this procedure it was verified that, even if the suction step was changed before the steady state was achieved, the specimen adsorbed for each step more than 92 % of the final water content.

2.4.3 Results

2.4.3.1 *Initial suction measurements*

Initial suction measurements were carried out on specimens compacted to a target dry density of 1.5 Mg/m³, 1.65 Mg/m³ and 1.8 Mg/m³. Each of the specimens had a diameter of 51 mm and a height of 20 mm. Distilled water, synthetic water from Schlattingen and 1M-NaCl solution were used for this purpose. The characteristic of the tested specimens are listed in Table 2.10.

The values of the initial suction of the specimens measured for different compaction densities and for different permeants are presented in Figure 2.29.

The obtained results show some fluctuations in terms of total suction. These fluctuations are related to the variation of the water content of the specimens, to the precision of the balance used for measuring the water content of the filter papers and to the fact that the measured suction are often lower than the limit value given by the calibration curve in Figure 2.21.

Despite the fluctuation of the results, the initial suction was found to be only slightly dependent from the initial compaction density. For example, the matric suction of the mixture wetted with distilled water slightly decreases with the increase of the dry density. It is possible to state that at the as-compacted conditions, the mixture is in a sort of hydraulic transition state in which neither the mechanism of adsorption nor the mechanism of capillary dominates in the water retention mechanism.

Table 2.10: Physical properties of the specimens used for the measurement of the filter paper measurements and related suction values.

| Type of water	ρ_d [Mg/m³]	w [-]	e [-]	S_r [-]	s [kPa]	ψ [kPa]	π [kPa]
DW	1.50	10.1%	0.78	34.4%	285	1122	837
	1.53	10.1%	0.74	36.0%			
DW	1.64	10.5%	0.63	44.4%	195	1278	1083
	1.62	10.5%	0.65	43.2%			
DW	1.83	10.4%	0.46	60.2%	247	1172	925
	1.80	10.4%	0.48	57.8%			
SW	1.57	10.47%	0.70	40.1%	150	-	-
	1.55	10.47%	0.73	38.5%			
SW	1.64	10.40%	0.62	44.5%	222	2558	2336
	1.65	10.40%	0.62	44.7%			
SW	1.80	10.92%	0.48	60.5%	173	2236	2063
	1.78	10.92%	0.50	58.1%			
SW	1.49	10.79%	0.79	36.5%	212	-	-
	1.49	10.79%	0.80	36.2%			
NaCl1M	1.48	11.7%	0.80	38.9%	188	2312	2124
	1.48	11.7%	0.80	38.9%			
NaCl1M	1.75	10.2%	0.53	52.0%	211	2854	2643
	1.77	10.2%	0.51	53.8%			
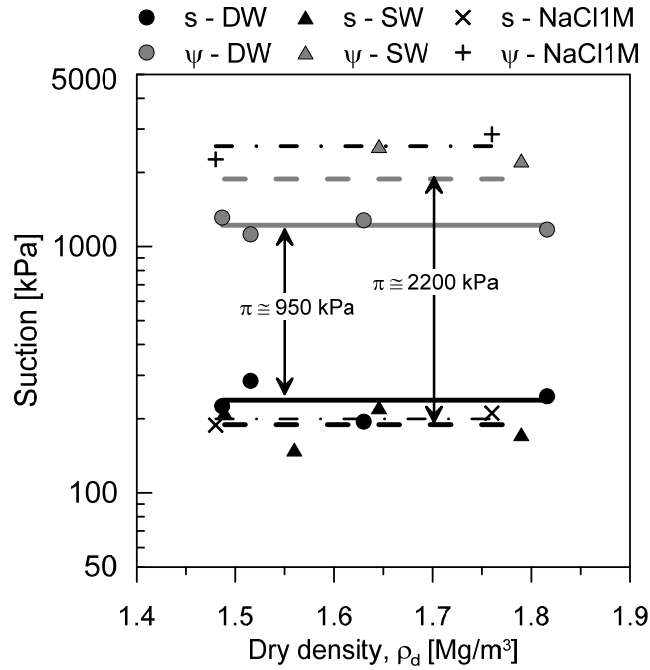
Figure 2.29: Initial suction of the mixture at different dry density and wetted with two types of water.

2.4.3.2 *Water retention behaviour of the 80/20 S/B mixture*

Figure 2.30 presents the water retention curves of the tested S/B mixture compacted to the target dry densities of 1.50 and 1.80 Mg/m^3 and obtained from the combination of the three suction techniques as explained in section 2.4.2. The water retention curve is presented both in terms of water content versus suction and degree of saturation versus suction. In the figure, the data obtained from the filter paper method are denoted as FPM, the ones coming from the axis translation technique as ATT and the micro cell technique is abbreviated with MCT.

The initial characteristics of the tested specimens are listed in Table 2.11. Variations of the initial water content from the target water content are attributed to the preparation method.

The points on the water retention curve obtained with the microcell technique started from a total suction of 10 MPa, corresponding to a water content of 4%. Then the material was wetted through the vapour phase until a suction of 4 MPa was reached. After this point the material was air dried following the main drying path.

The mixture tested with the axis translation technique was prepared to the optimum water content and then wetted to a suction value of 3 kPa. The drying path was initiated once the full saturation was achieved. Then the material was dried until a matric suction value of 500 kPa was attained. No scanning curves were determined within the framework of this study because of time constrains.

Table 2.11: Initial characteristic of the specimens used to determine the water retention curve. Distilled water was used to wet the mixture.

Suction method	ρ_d [Mg/m³]	e [-]	w [-]	S_r [-]
Filter paper	1.50	0.78	0.10	0.34
	1.53	0.74	0.10	0.36
Filter paper	1.83	0.46	0.10	0.60
	1.80	0.48	0.10	0.58
Microcell technique	1.57	0.70	0.04	0.08
Microcell technique	1.80	0.48	0.04	0.23
Axis translation	1.49	0.79	0.10	0.33
Axis translation	1.78	0.50	0.11	0.58

The S/B mixture has a relatively low retention capacity when compared to the one of pure bentonite (e.g., Villar and Lloret, 2004, Seiphoori et al., 2014). This characteristic is attributed to the large amount of sand in the mixture and to the microstructural features of the bentonite fraction. The results of the water retention curves show that the data obtained with the combination of the different techniques are in good agreement despite the dry density fluctuations.

In the water content versus suction plane, for total suctions higher than 3 MPa (w=0.09 %), the experimental data lay on the same curve showing that the effect of compaction density on the water retention behaviour of the 80/20 S/B mixture is negligible. This result suggests that the water is mainly stored in the pores belonging to the bentonite fraction, that are believed not to be affected by the compaction effort, and that the dominant retention mechanism is adsorption (Romero and Vaunat, 2000, Romero et al., 2011).

In a suction range which varies from 3 to 0.5 MPa the water retention shows a sort of transitional zone. In this region, the wetting and the drying branches of the water retention curves obtained for the two target dry density are extremely close and neither the mechanism of adsorption, not the mechanism of capillary, dominate in the water retention behaviour. This explains the very low dependency of the initial matric and total suction of the mixture on the dry density variations (Figure 2.29).
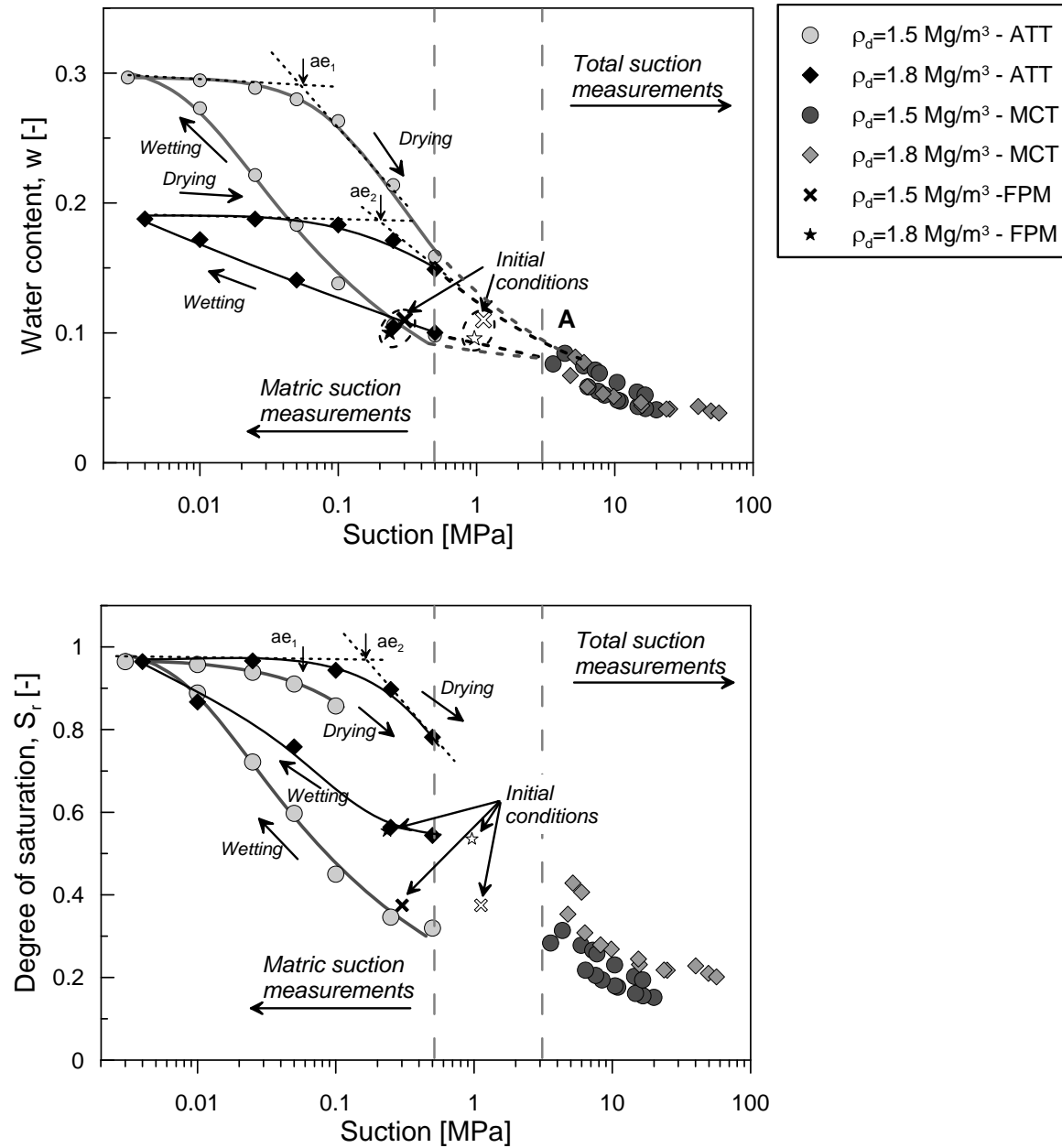
Figure 2.30: Full range water retention curve of the 80/20 S/B mixture at two different dry densities.

The effect of the dry density variation of the shape of the water retention curve is very pronounced for suction lower than 0.5 MPa. Below this threshold, the specimen compacted at lower dry density tends to retain more water as the volume of the pores is larger. When moving to the higher dry density, in the plane water content versus suction, it is observed the rotation of the drying and wetting branches of the curve around the point A (s=3 MPa, indicated in Figure 2.30). This feature is common for deformable soils (e.g., Romero et al., 2011, Salager et al., 2013) and is related to the different water retention mechanisms of the mixture under different hydraulic state.

The hysteretic behaviour in the water retention curve is also well observable. The radius of hysteresis is larger at lower suction and it narrows when the suction increases. The radius of hysteresis is also density dependent and appears larger for the lower dry

density. Similar behaviour was observed also for Boom Clay and compacted Scaly Clay by Romero (1999) and Airò Farulla et al. (2010a), respectively. In particular, Airò Farulla et al. (2010a) showed that the dominium of the attainable hydraulic state of a material enlarged with the increase of the void ratio because of the double porosity feature of the material. However, the radius of hysteresis of the mixture is very large; this result is attributed to swelling capacity of the bentonite fraction and the consequent the reversibility/non-reversibility of the volumetric deformations along a wetting and drying cycle.

In the plane suction-versus degree of saturation, the experimental data are reported until a positive swelling pressure was register. Because visual observations of the specimen were not possible until the end of the test, positive swelling pressure is considered as a necessary, although non-sufficient, indication of the lateral contact between the specimen and the ring. Pictures of the two specimens were taken at the end of the test (Figure 2.31). The specimen compacted to 1.49 Mg/m^3 of initial dry density underwent to a large shrinkage upon drying (matric suction increase) and the lateral contact was lost. For the specimen compacted to an initial dry density 1.79 Mg/m^3, the lateral contact was preserved.

The air entry value of the mixture was identified as the point of intersection of a line parallel to the suction axes placed at $S_r=1$ and the tangent to the main drying path. The air entry value is clearly density dependent. For the mixture compacted to the initial dry density of 1.49 Mg/m^3 it is equal to 53 kPa, for the mixture compacted to an initial dry density equal to 1.79 Mg/m^3 it is equal to 167 kPa.
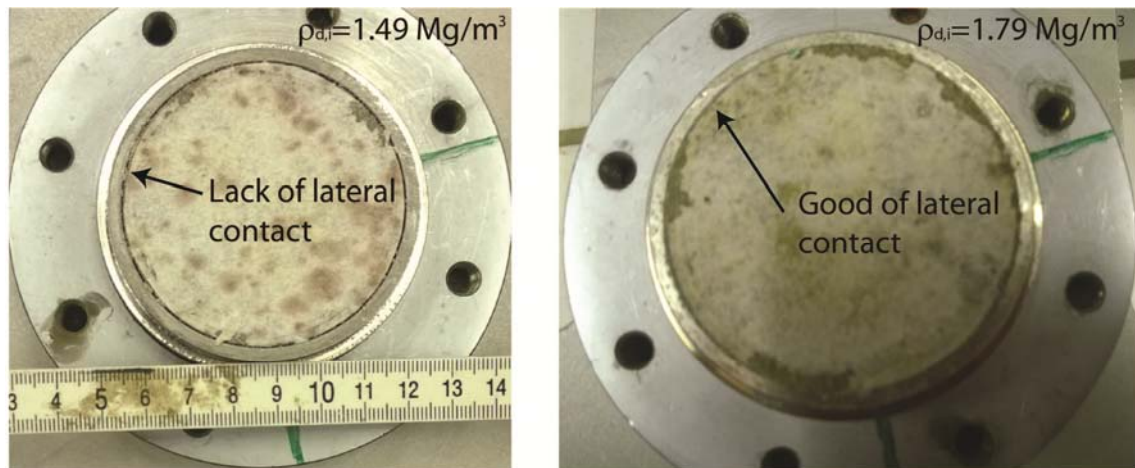

Figure 2.31: Specimens used for the determination of the WRC after extraction from the controlled suction oedometer. Low compaction density (left); high compaction density (right).

2.5 WATER PERMEABILITY TESTS

The sand/bentonite mixtures at low bentonite content have been selected as backfilling materials in L/ILW repository with the purpose of being a preferential path for gas migration. This low bentonite content enhances the gas transport capacity of the mixture and thus limits the generation of gas overpressure which is due to the production of gases during the repository life (Nagra, 2008). Nevertheless, one of the risks of having such low bentonite content is that the material will not show enough low hydraulic conductivity to prevent the migration of radionuclides to the geosphere.

Numerous investigators reported that the hydraulic conductivity of bentonite-based materials is affected by several parameters such as the mixing ratio as well as by the chemical composition of the permeant and the grain size distribution of the bentonite.

Abichou et al. (2002) found that 5 % of SS-100 bentonite powder added to a simulated S/B mixture was sufficient to achieve a hydraulic conductivity lower than $2 \cdot 10^{-10}$ m/s. For the same bentonite ratio the mixture prepared with powder bentonite showed a different hydraulic conductivity than mixtures prepared with granular bentonite.

Experimental investigations carried out by Komine (2004) showed that a hydraulic conductivity lower than $1 \cdot 10^{-11}$ m/s was attainable adding at least 15 % of Kunigel-V1 bentonite in the mixture. This low hydraulic conductivity depends on the ability of the bentonite to seal the voids within the grains of sand. Visual observation carried out with an environmental scanning electron microscope showed that 20 % of bentonite was sufficient to fill up all the pores within the sand grains under condition of full saturation with distilled water (Komine, 2004).

Chemistry of the pore fluid has a great impact on the hydraulic conductivity of bentonite-based materials. An increase of the chemical concentration of the permeant produces an increase of its hydraulic conductivity (Studds et al., 1998). When salty water is added, the swelling and sealing capacity of the bentonite is compromised (Romero, 2013).

The saturation state is also an important variable affecting the permeability of soils. The presence of other fluids in the pore space (e.g. air and water vapour) reduced the space in the pore volume which is devoted to the water flow and changes the tortuosity of the flow path; as a consequence, the water permeability is reduced. In case of multi-structure soils such as clayey soils, depending on the hydraulic state of the material, water is preferably flowing through different levels of porosity. In particular, through the aggregates at high suction values, or between the aggregates, at low suction values (Romero, 1999, Carminati et al., 2008, Romero, 2013).

This section is devoted to the experimental characterisation of the hydraulic properties of the mixture in saturated and unsaturated conditions. The effect of the variation of compaction density and pore water salinity on the saturated permeability will

be analysed. The unsaturated hydraulic conductivity is measured for a mixture compacted at two different dry densities and wetted with distilled water.

2.5.1 Methodology

2.5.1.1 *Measurement under saturated conditions*

Measurements of the hydraulic conductivity of the 80/20 S/B mixture were carried out on specimens compacted to a dry density that was ranging between 1.5 Mg/m^3 and 1.8 Mg/m^3 and fully saturated with four different pore fluids (section 2.2.2).

For these tests, a special permeameter cell was designed in house (Figure 2.32). The permeameter cell consists of thick-walled stainless steel ring of 51 mm in internal diameter and 40 mm in height situated between two plates that were fixed together with four screws. The screws allowed the compression of two O-rings that ensured the water tightness of the cell. The oedometric ring has internal threaded walls. This solution, together with the swelling of the saturated mixture, ensured that during compaction and upon saturation the grains (of sand and bentonite) well filled the interstices of the oedometric ring ensuring the elimination of preferential flow paths along the specimen/ring interface. Water in the permeameter was injected with PV controllers which allowed applying a maximum water pressure of 2 MPa, with an accuracy of 0.001 MPa, and monitoring the water volume with an accuracy of 1 mm^3. The water injection and the extraction lines had a central duck and a circular (spiral) grove cut on the surface allowing the water to sweep radially through the sintered porous disk during the preliminary flushing operations and allowing a homogeneous distribution of the injection pressure during the tests. Inside the cell, the specimen was sandwiched between two sintered brass porous disks and two filter papers which enabled a good distribution of the water along the specimen surface.

The tested specimens were compacted directly inside the permeameter ring following the standard procedure illustrated in section 2.2.6. Once the cell was set-up, both the upper and the lower bases of the permeameter were connected to the PV controllers. The injection ducts were flushed with water to remove the air entrapped in the sintered porous disks and in the drainage lines. Then, the specimen was saturated maintaining a low pressure difference to allow the evacuation of the air bubble within the specimen but preventing the transport of the fine smectite particles. The migration of fines is likely for mixture at this low bentonite content which are compacted to the low dry density but it is highly undesirable as it can led to the pore clogging, the internal erosion of specimen and to a non-homogeneous distribution of the bentonite in the mixture (see section 3.5.1). All this phenomena can produce irreversible variations of the hydraulic conductivity (Dunn, 1985). The hydraulic conductivity tests were performed in steady state conditions by applying pressure gradients between two specimen ends. As suggested by Villar (2000) the pressure difference applied during the tests was maintained lower than the swelling pressure of the specimen. The inlet and outlet water fluxes were measured with time with

the two PV controllers. The saturation of the specimens required a time that varies from 2 weeks to few months depending on the dry density, and on the chemistry of the permeant. In some cases, especially when distilled water was used as permeant, the specimens were prepared at initial water content higher than 11% to speed up the saturation. Microstructural analysis evidenced that this procedure did not alter the final pore structure of the mixture at the full saturation and thus should not alter the experimental results. The specimen was considered fully saturated when the measured inflow and outflow matched. The final water content of the specimen was measured post-mortem to verify that the condition of full saturation was achieved during the test.

When the specimen were tested using NaCl solutions, in order to prevent the corrosion of the PV controllers it was required to use a toxic interface form GDS instrument that was placed between the specimen and the controller. For the special case of the specimen testes with NaCl solutions at 1 and 4 mol/L, due to the low swelling capacity of the mixture it was necessary add a layer of resin in the cell-specimen interface to avoid the generation of preferential flow paths and the consequent false increase of the hydraulic conductivity.

The interface cell from GDS instrument consists of two chambers, separated by an impermeable membrane. The upper chamber, made of Plexiglas, was filled with "clean" water (distilled water) and it was connected to a PV controller. The lower chamber, made of stainless steel, was filled with the "highly corrosive" water and was connected to the sample. Each chamber is equipped with a two-ways valve. The cell was filled following a procedure that ensures minimising the quantity of air entrapped in each chambers. It was verified that the pressure and the fluxes were properly transmitted by the interface cell.
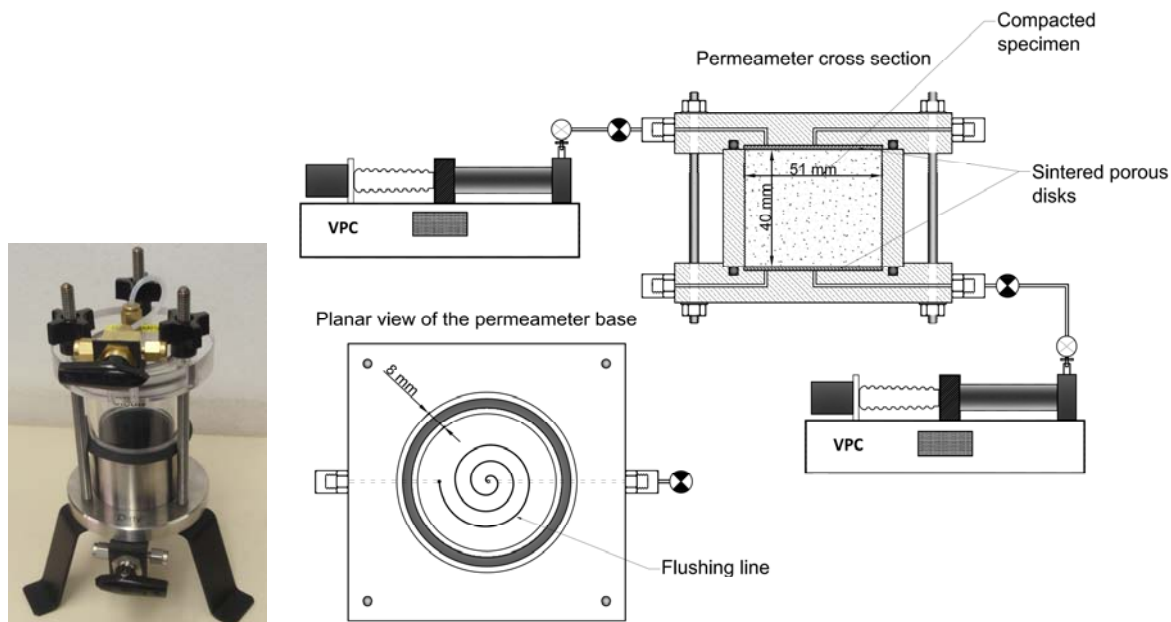

Figure 2.32 : Interface cell (left). Experimental setup for water permeability test with the permeameter cell (right).

2.5.1.2 Measurements under unsaturated conditions

Data on the permeability of the 80/20 S/B mixture under unsaturated condition, both along the main wetting and the main drying path, were obtained during the determination of the water retention capacity. The transient inflow and outflow data measured for each matric suction step applied to the specimens were back analysed using the formulation proposed by Kunze and Kirkham (1962) which account also for the non-negligible impedance of the ceramic disk:

$$\frac{V_w}{V_0} = 1 - \sum_{n=1}^{\infty} \frac{2 \cdot exp\left(-\alpha_n D_w t \Big/ H_{sp}^2\right)}{\alpha_n^2 \left(a + csc^2 \alpha_n\right)} \tag{2.23}$$

where V_0 is the total outflow/inflow volume for a given matric suction increment, V_w is the outflow in time, α_n is the nth solution of the equation $a\alpha_n = \cot\alpha_n$; D_w is the capillary diffusivity, t is time, H_{sp} is the length of the specimen, a is the ratio of impedance of the ceramic disk to the impedance of the soil ($a = z_m / z_s = K_w(s)t_d / LK_d$). Inflow and outflow data in the analysis are the one corrected to account for steady state evaporation as explained in sections 2.4.2.3.

Equation (2.23) was derived under the assumptions of a rigid soil matrix, isothermal and one-dimensional inflow, incompressible and homogeneous fluid, constant water pressure head along the specimen height, negligible air flow and constant permeability over each suction steps. To take into account the presence of the ceramic disk, the equality of the flow through the ceramic disk and the soil is added as boundary condition of the problem.

Knowing the capillary diffusivity of water at each suction step the corresponding hydraulic conductivity is calculated as follows:

$$K_w(s) = \frac{D_w \gamma_w V_0}{V \delta P_w} \tag{2.24}$$

where V is the volume of the specimen and δP_w is the water pressure increment/decrement at a given step.

The assumption that the permeability of the soil is constant, over a small step change of matric suction (or water pressure), is generally not correct; however, it simplifies a lot the calculations. Due to this restriction the effective permeability is determined using the inflow/outflow data that do not exceed 30% of the total change associated with each matric suction step (Romero, 1999). The corresponding degree of saturations were calculated in the main wetting path as a weighted value which is tending to the previous equalisation value and in the main drying path as the average between the previous and the final degree of saturation, as follows (Romero, 1999):

$$S_r = 0.85 \times S_r^i + 0.15 \times S_r^{i+1} \quad (\text{ wetting })$$
$$S_r = \frac{S_r^i + S_r^{i+1}}{2} \qquad (\text{ drying })$$

(2.25)

For further details about the determination of the unsaturated permeability using axis translation technique see Romero (1999).

2.5.2 Tests results

2.5.2.1 *Saturated hydraulic conductivity*

Hydraulic conductivity was computed assuming laminar flow, by applying the Darcy's law for incompressible fluids and neglecting the difference in elevation:

$$Q = -KA_{sp} \frac{P_{up} - P_{dw}}{\gamma_w H_{sp}}$$

(2.26)

where Q is the volumetric flux measured at the inlet or at the outlet (normally the two values should coincide), A_{sp} is the cross-sectional area of the specimen, P_{up} and P_{dw} are the upstream and downstream pressure applied, $\gamma_w = \rho_w g$ is the specific weight of water, H_{sp} is the height of the specimen (corresponding to the drainage length). The quantity $\frac{P_{up} - P_{dw}}{\gamma_w H_{sp}} = i$ is the so called linear hydraulic gradient established along the specimen.

Knowing the hydraulic conductivity (K), the intrinsic permeability of the medium (k) is calculated as follows:

$$k = \frac{K\mu}{\rho_w g}$$

(2.27)

where μ is the dynamic viscosity of the water, ρ_w is the density of water, whose values are listed in Table 2.2 for the different permeants, and g is the gravity.

The tests were performed at constant laboratory temperature of 21 ±1 °C.

The experimental values of the hydraulic conductivity, and permeability, obtained for this study for the different specimens are reported in Table 2.12 to 2.15 , together with the values of the dry density, the water contents and degrees of saturation at preparation, and the final degrees of saturation.

Table 2.12 : Results of the permeability with distilled water.

ρ_d [Mg/m^3]	e [-]	w_i [-]	$S_{r,i}$ [-]	K [m/s]	k [m^2]	w_f [-]	$S_{r,f}$ [-]
1.46	0.83	0.14	0.45	$1.89 \cdot 10^{-11}$	$1.68 \cdot 10^{-18}$	0.31	1.01
1.50	0.78	0.12	0.41	$4.84 \cdot 10^{-11}$	$4.30 \cdot 10^{-18}$	0.30	1.03
1.50	0.78	0.16	0.53	$2.32 \cdot 10^{-11}$	$2.07 \cdot 10^{-18}$	0.29	0.99
1.49	0.79	0.11	0.37	$3.77 \cdot 10^{-11}$	$3.35 \cdot 10^{-18}$	0.28	0.96
1.59	0.68	0.12	0.47	$2.11 \cdot 10^{-11}$	$1.88 \cdot 10^{-18}$	0.26	1.02
1.70	0.57	0.12	0.56	$1.43 \cdot 10^{-11}$	$1.27 \cdot 10^{-18}$	0.21	0.97
1.80	0.48	0.11	0.60	$7.46 \cdot 10^{-12}$	$6.64 \cdot 10^{-19}$	0.20	1.10

Table 2.13 : Results of the permeability with synthetic water.

ρ_d [Mg/m^3]	e [-]	w_i [-]	$S_{r,i}$ [-]	K [m/s]	k [m^2]	w_f [-]	$S_{r,f}$ [-]
1.50	0.78	0.10	0.35	$1.46 \cdot 10^{-9}$	$1.49 \cdot 10^{-16}$	0.27	0.91
1.50	0.78	0.11	0.38	$6.99 \cdot 10^{-9}$	$7.11 \cdot 10^{-16}$	0.28	0.98
1.51	0.77	0.11	0.37	$5.43 \cdot 10^{-9}$	$4.83 \cdot 10^{-16}$	0.27	0.94
1.59	0.68	0.11	0.42	$1.48 \cdot 10^{-9}$	$1.66 \cdot 10^{-16}$	0.23	0.91
1.65	0.62	0.11	0.44	$4.22 \cdot 10^{-10}$	$4.31 \cdot 10^{-17}$	0.23	1.01
1.70	0.57	0.11	0.51	$3.18 \cdot 10^{-10}$	$3.33 \cdot 10^{-17}$	0.20	0.93

Table 2.14 : Results of the permeability with 1M-NaCl.

ρ_d [Mg/m^3]	e [-]	w_i [-]	$S_{r,i}$ [-]	K [m/s]	k [m^2]	w_f [-]	$S_{r,f}$ [-]
1.56	0.71	0.09	0.34	$6.97 \cdot 10^{-08}$	$7.44 \cdot 10^{-15}$	0.26	0.96
1.65	0.62	0.11	0.44	$2.18 \cdot 10^{-08}$	$2.31 \cdot 10^{-15}$	0.22	0.96

Table 2.15 : Results of the permeability with 4M-NaCl.

ρ_d [Mg/m^3]	e [-]	w_i [-]	$S_{r,i}$ [-]	K [m/s]	k [m^2]	w_f [-]	$S_{r,f}$ [-]
1.5	0.78	0.10	0.34	$1.62 \cdot 10^{-07}$	$2. \cdot 10^{-14}$	0.25	0.93

Figure 2.33 presents the results of the water permeability test carried out on the 80/20 S/B mixture specimens. Regardless of the type pore fluid, the hydraulic conductivity decreases as the dry density of the specimen increases. In agreement with the results of hydraulic conductivity versus dry density (or void ratio) that were obtained for different soils (e.g., Komine, 2004, Karnland et al., 2008) an exponential trend was found to best fit the experimental data.

$$K_w = \hat{a} \, exp\left(\hat{b}\rho_d\right) \tag{2.28}$$

with $\hat{a}$ and $\hat{b}$ fitting parameters which depends on the different pore fluids and are listed in Table 2.16.

The results suggest that the volume of the voids devoted to water transport (effective porosity) increases with the concentration of the salt solution and decreases with the dry density. Also, the sensibility of the water permeability on the changes of dry density seems more pronounced with the increase of the pore water salinity. Similar to the swelling pressure trend, it appears that at higher dry density the S/B mixture increases its capacity to sustain chemical loadings.

2.5.2.2 *Unsaturated hydraulic conductivity*

The data of the water permeability under conditions of partial saturation, for the two specimens compacted to an initial dry density of 1.49 Mg/m^3 and 1.79 Mg/m^3, are presented in Figure 2.34. The obtained values are also reported in Table 2.17 and 2.18. Regardless of the initial dry density, the effective permeability of the mixture to the water phase increases monotonically with the degree of saturation. This behaviour is a consequence of the increase of the fraction of the pore volume devoted to the water flow and the enlargement of the bentonite pores due to the internal swelling of the bentonite aggregates. The data obtained at nearly saturated conditions are in good agreement with those obtained by measuring the saturated permeability to water under steady state conditions in the permeameter cell. This confirms the validity of the method used for estimation the unsaturated permeability.
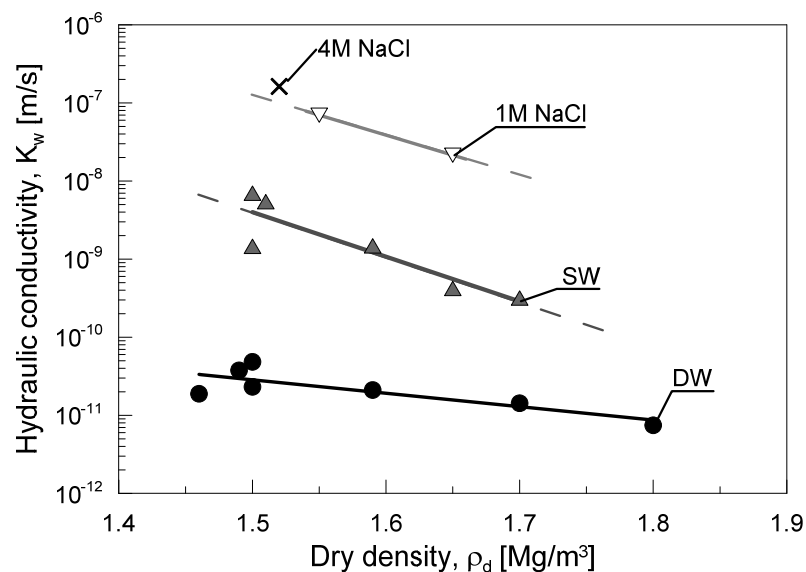

Figure 2.33: Measurements of the hydraulic conductivity of the S/B mixture using different pore fluids.

Table 2.16: Fitting parameters calculated from the hydraulic conductivity tests.

Water type	$\hat{a}$ [m/s]	$\hat{b}$ [m^3/Mg]
Distilled	$1.08 \cdot 10^{-8}$	-3.96
Synthetic	1.50	-13.16
1M NaCl	6.00	-11.79

At low degrees of saturation (S_r = 0.37 for ρ_d =1.49 Mg/m³ and S_r = 0.52 for ρ_d =1.79 Mg/m³) the effective permeability become very small because the water occupies the smallest pores belonging to the bentonite, where adsorption forces are the greater. This saturation state is called irreducible or connate-water saturation and indicated that the water is quasi-immobile.

In the plane hydraulic conductivity versus degree of saturation, the unsaturated hydraulic conductivity curve obtained with the applied hydraulic path show hysteresis for the two dry densities. However the higher hysteresis is detected for the specimen compacted to the higher dry density and lower void ratio. In the plane hydraulic conductivity versus suction, the curve shows hysteresis along a wetting and drying cycle. This hysteresis is related to the irreversible deformation of the internal structure of the bentonite along a wetting- drying cycle.
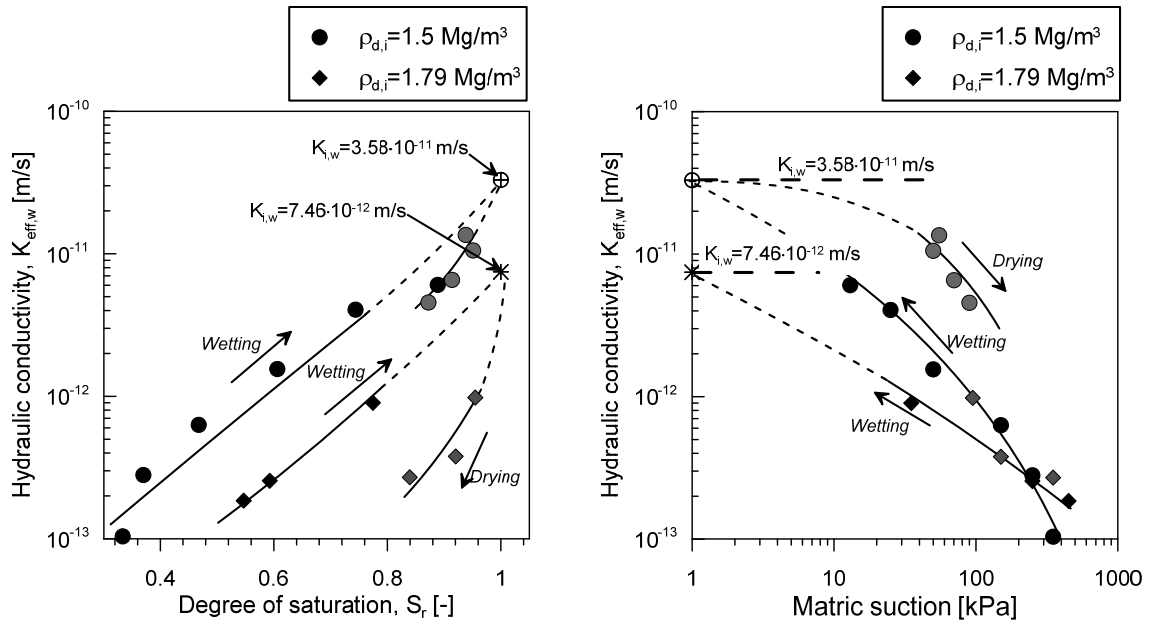
Figure 2.34: Unsaturated hydraulic conductivity of the S/B mixture compacted to two different dry densities.

Table 2.17 : Results of the hydraulic conductivity tests in unsaturated conditions, along a wetting-drying cycle, for a target initial density of 1.5 Mg/m³.

S_r	s	K	k
[-]	[kPa]	[m/s]	[m²]
0.33	350	$1.04 \cdot 10^{-13}$	$1.06 \cdot 10^{-20}$
0.37	250	$2.8 \cdot 10^{-13}$	$2.86 \cdot 10^{-20}$
0.47	150	$6.30 \cdot 10^{-13}$	$6.43 \cdot 10^{-20}$
0.61	50	$1.55 \cdot 10^{-12}$	$1.59 \cdot 10^{-19}$
0.74	25	$4.05 \cdot 10^{-12}$	$4.14 \cdot 10^{-19}$
0.89	13	$6.05 \cdot 10^{-12}$	$6.18 \cdot 10^{-19}$
0.95	50	$1.06 \cdot 10^{-11}$	$1.08 \cdot 10^{-18}$
0.94	55	$1.36 \cdot 10^{-11}$	$1.38 \cdot 10^{-18}$
0.91	70	$6.55 \cdot 10^{-12}$	$6.69 \cdot 10^{-19}$
0.87	90	$4.55 \cdot 10^{-12}$	$4.65 \cdot 10^{-19}$

Table 2.18 : Results of the hydraulic conductivity tests in unsaturated conditions, along a wetting-drying cycle, for a target initial density of 1.8 Mg/m³.

S_r	s	K	k
[-]	[kPa]	[m/s]	[m²]
0.55	450	$1.85 \cdot 10^{-13}$	$1.89 \cdot 10^{-20}$
0.59	250	$2.55 \cdot 10^{-13}$	$2.60 \cdot 10^{-20}$
0.77	35	$9.00 \cdot 10^{-13}$	$9.19 \cdot 10^{-20}$
0.95	95	$9.79 \cdot 10^{-13}$	$1.00 \cdot 10^{-19}$
0.92	150	$3.78 \cdot 10^{-13}$	$3.86 \cdot 10^{-20}$
0.84	350	$2.70 \cdot 10^{-13}$	$2.76 \cdot 10^{-20}$

2.6   SUMMARY AND CONCLUSIONS

This chapter presented the results of an investigation on the effect of different hydro-chemo-mechanical loadings on the swelling behaviour, retention properties and hydraulic conductivity in saturated and unsaturated conditions of the 80/20 sand/bentonite mixture.

A first evaluation of the response of the mixture to chemical loadings is given by means of the determination of the index properties. The results revealed the strong dependency of the plastic limit to the salinity of the pore water.

The tested mixture exhibits a relatively low swelling capacity when compared with other bentonite-based materials prepared with higher bentonite contents. Swelling pressure is found to be suction dependent and very sensitive to chemical loadings. In the swelling pressure versus dry density the data results satisfactory fittings exponential function regardless the type of water used in the experiments. The maximum swelling strain of the mixture hydrated under free volume condition is linearly dependent on the initial dry density. The swelling pressure suction curve shows hysteresis. The radius of

hysteresis is smaller for the lowest dry density whereas it becomes larger for the highest dry density.

The determination of the water retention curve of the 80/20 S/B mixture required the use of three different experimental techniques to cover a wide suction range. The water retention curve of the S/B mixture presents common features with the water retention behaviour of double structure soils. For suctions lower than 3 MPa, the water retention curve is independent from the compaction density suggesting that the mechanism of water adsorption is the dominant mechanism of retention. For matric suctions lower than 0.5 MPa water is held in the mixture by capillary forces and the effect of dry density change becomes very pronounced. The region between 0.5 MPa and 3 MPa is considered as a transitional zone. The air entry value and the radius of the hysteresis are density dependent.

The relationship between saturated hydraulic conductivity and dry density is determined using different pore fluids. An exponential function is used to fit the data. The results suggest a strong increase of the channels devoted to the water transport with the decrease of the dry density and increase of the salinity of the pore water.

The unsaturated hydraulic conductivity is very sensitive to the changes in degree of saturation and dry density. Indeed, it increases as the degree of saturation increases and it reduces when the dry density decreases. This last result is in contrast with the result obtained for materials which are characterised by double-structure porosity with non-deformable aggregates. The curves also show hysteresis in both planes hydraulic conductivity vs degree of saturation and hydraulic conductivity vs suction.

The extremely low unsaturated hydraulic conductivity that the mixture exhibits when distilled water was used as permeant, leads to long time for testing; e.g., more than 1 year is required to obtain each water retention curves, and few months to achieve the full saturation.

The sensitivity of the mixture, in terms of reduction of the swelling pressure and free swelling deformation, or increase of the hydraulic conductivity, to chemical loadings was more pronounced for lower dry densities. At a higher dry density, the swelling capacity of the mixture in contact with aqueous solutions is better preserved.

3   Gas testing in the 80/20 sand/bentonite mixture

3.1 INTRODUCTION

This chapter is devoted to the experimental characterisation of the gas transport capacity of the 80/20 sand/bentonite mixture under saturated and unsaturated conditions.

The first part of the chapter discusses the basic concepts of gas transport in porous media with the specific focus on a swelling porous media, which are characterised by an evolving pore structure under different hydro-mechanical loadings. The concept of saturated and unsaturated permeability is introduced for a mixture under conditions of partial saturation. The concept of breakthrough pressure is discussed for materials under conditions of full saturation.

The experimental setups and procedures developed for the gas testing are described in the second part of the chapter. In particular, two set-ups were investigated, the gas injection under constant volume conditions and the gas injections under triaxial conditions, thus with the specimen subjected to a given confining pressure. The advantages and limits of the two methods are also discussed based on the obtained results. The design and calibration of the different instruments used in the experiments are also detailed.

The final part of the chapter discusses the results of gas permeability and breakthrough pressure obtained at the laboratory scale for the tested mixture. All the tests presented in this chapter are performed under constant laboratory temperature and using distilled water as wetting fluid.

3.2 BASIC CONCEPTS ON GAS TRANSPORT IN GEOMATERIALS

As it was mentioned in the introduction of this thesis, during the post closure phase of the waste repository, a large amount of gas will be generated mainly as a consequence of the anaerobic corrosion of the metal canisters. As the gas starts to be generated in the repository it will dissolve in the pore water of the backfilling material and then will be release by diffusion. Considering that a large amount of gas will be produced during the repository life and, that the amount of gas that can be evacuated by diffusion is limited, the gas concentration will exceed the gas solubility leading the gas pressure to increase. From this moment on, other transport mechanisms will appear and become predominant (i.e., two phase flow and gas breakthrough depending on the degree of saturation). The two phase flow may take place when the gas pressure overcomes the so called "air entry value" of the fully saturated material and a continuous gas phase is formed. In this condition the gas is mainly transported away by advective flow and some water can be expelled, leading to a partial desaturation of the porous medium. In a fully saturated mixture, if the gas pressure continues to increase, other mechanisms may appear such as dilatancy-controlled gas flow, and gas flow along macroscopic tensile fractures (Nagra, 2008, Horseman et al., 1996b). The aforementioned processes are synthetises in Table 3.1.

Table 3.1: Processes of gas migration in porous media.

Stage	Gas migration process	State of gas species	Conditions
1	Gas dissolution and diffusion in the pore water	Gas dissolved in the pore water	$P_g < P_{entry}$
2	Two phase flow of immiscible fluids	Continuous gas phase; gas dissolved in the pore water; water vapour in the dry air	$P_{entry} < P_g < P_{break}$
3	Gas breakthrough - Non-darcian flow through preferential pathways	Continuous air phase; Gas dissolved in the pore water;	$P_g > P_{break}$

3.2.1 Gas solubility and diffusion

The dissolution and diffusion of a gaseous species into the pore water is controlled by two fundamental laws: the Hanry's law and the Fick's law.

The Henry's law states that, at constant temperature, the solubility of a gas in a liquid is directly proportional to the partial pressure (P_g) of the gas:

$$P_g = k_H c \tag{3.1}$$

with k_H, the solubility coefficient or Hanry's constant (Pa/mol/m^3) and c, the molar concentration of gas (mol/m^3).

The diffusive mass flux (J_α^* in kg/s), for a binary system (only two species are considered) is calculates as follows (Bear, 1972, Webb, 2006):

$$J_\alpha^* = -\rho D_{\alpha\beta} \nabla \omega_\alpha \tag{3.2}$$

$\omega_a = \rho_\alpha / \rho$ is the mass fraction of a specie α in a solution of density ρ and $D_{\alpha\beta}$ is the binary diffusion coefficient. The above form of the Fick's law is modified for a porous media by introducing a coefficient β to take into account the effective path of the gas through the pore water of the medium as follows:

$$J_\alpha^* = -\rho\beta D_{\alpha\beta} \nabla \omega_\alpha = -\rho D_{\alpha\beta}^* \nabla \omega_\alpha \tag{3.3}$$

$$\beta = nS_g \tau \tag{3.4}$$

where n is the porosity, S_g is the degree of saturation of the medium with respect to the gas phase and τ is the tortuosity.

The phenomenon of gas diffusion will not be further discussed as it is not the focus of this thesis.

3.2.2 Two phase flow of immiscible fluids – phenomenological aspect

In unsaturated conditions, water and gas flow simultaneously through the medium and each fluid establishes its own tortuous path, which forms very stable channels (Bear, 1972). In the case of simultaneous flow of water and gas (immiscible fluids), the interfacial tension is not zero and a fluid-fluid interface separates the two fluids in each pore.

The complex movement of water and gas through a porous media is driven by capillarity forces, viscous forces and gravity. Depending on the relevance of one of these forces difference flow regimes can occur: viscous fingering, capillary fingering or stable displacement (Méheust et al., 2002, Chau and Or, 2006, Lenormand et al., 1988 from

Senger et al., 2013). In order to identify the flow regime in a porous media one can refer to different dimensionless numbers: the capillary number (Ca), which quantifies the relative importance of the capillarity and viscous forces, the bond number (Bo) quantifies the relative values of the gravity forces over the capillary at the pore scale, and the viscosity ratio (M):

$$Ca = \frac{\mu_w V r^2}{\sigma k} \qquad (3.5)$$

$$Bo = \frac{\Delta \rho g r^2}{\sigma} \qquad (3.6)$$

$$M = \frac{\mu_{nw}}{\mu_w} \qquad (3.7)$$

where μ_w and μ_{nw} are the viscosity of the wetting and non-wetting fluid, respectively, V is Darcy's velocity the fluid, r is the pore radius, σ is the surface tension between the two fluids, k is the intrinsic permeability of the porous medium, $\Delta \rho$ is the difference in the two fluids and g is gravity.

For example, if gravity is neglected and small pores are considered, capillary fingering occurs at low flow rate as capillary forces dominates the flow process ($Ca \ll 1$). At high flow rate the viscous forces dominated the flow and viscous fingering regime can occur ($Ca \gg 1$). In case of viscous fingering, the displacement front tends to be stabilised (stable displacement) if the contribution of the gravity increases (Méheust et al., 2002). The displacement front tends to stabilise also for high viscosity ratio and high capillary number. Because of the complexity to measure the capillary number and the bond number in a multi-structure porous media such as the tested mixture the flow regime will not by analysed in the rest of the thesis.

3.2.2.1   *The concept of effective, intrinsic and relative permeability*

The advective transport of water and gas within a porous medium obeys to the Darcy's law, once the steady state has been established. From a rigorous point of view, the equation for computing the fluxes in m/s, in two phase flow regime, in a rigid porous media are written as follows (Whitaker, 1986):

$$\begin{cases} \boldsymbol{q}_w = -\dfrac{\boldsymbol{k}_{eff,w}}{\mu_w} \cdot \left(\nabla P_w - \rho_w \boldsymbol{g} \right) + \boldsymbol{k}_{wg} \boldsymbol{q}_g \\[3mm] \boldsymbol{q}_g = -\dfrac{\boldsymbol{k}_{eff,g}}{\mu_g} \cdot \left(\nabla P_g - \rho_g \boldsymbol{g} \right) + \boldsymbol{k}_{gw} \boldsymbol{q}_w \end{cases} \qquad (3.8)$$

where $\boldsymbol{q}_w$ and $\boldsymbol{q}_g$ are the water and gas fluxes, respectively, expressed in m/s, $\boldsymbol{k}_{eff,w}$ and $\boldsymbol{k}_{eff,g}$ are the Darcy's permeability tensors at a given degree of saturation, μ_w and μ_g are

the dynamic viscosity ∇P_w and ∇P_g are the pressure gradients of water and gas, respectively, $\boldsymbol{k}_{wg}$ is the viscous drag tensor for the wetting phase and $\boldsymbol{k}_{gw}$ is the viscous drag tensor for the gaseous phase and $\boldsymbol{g}$ is gravity. In the present study, the second terms of equation (3.8) can be neglected as the ratio between the viscosity of the gas and the viscosity of the water is 0.018; thus much lower than 1 (Whitaker, 1986, Dana and Skoczylas, 1999).

In a porous media, at a given void ratio, the coefficient of permeability for a given phase depends on the degree of saturation of the considered phase; i.e., the amount of the void space devoted to the flow. To consider this aspect, the concepts of intrinsic and relative permeabilities are introduced:

$$\boldsymbol{k}_{eff,\alpha} = k_i \cdot k_{r,\alpha} \qquad (3.9)$$

where k_i is the intrinsic permeability of the medium, which corresponds to the permeability of the medium fully saturated with one phase (either water or gas) and $k_{r,\alpha}$ is the relative permeability, a dimensionless number which varies from 0 to 1.

For a rigid porous medium, the coefficient of intrinsic permeability (m^2) depends solely on the properties of the solid matrix and on the configuration of the void space. According to this definition, water and gas permeability of a rigid porous media should coincide; except for the Klinkenberg effect (see section 3.2.2.3 for a deeper discussion on this effect). However, if the pore structure of the medium changes, depending on the dry density, hydraulic state and pore water chemistry, this affirmation is not valid anymore.

The relative permeability is the ratio of the effective permeability (permeability of the porous medium to a particular phase under unsaturated condition) to the intrinsic permeability. In unsaturated condition, the liquid and the gas phases have different pressure due to capillary forces and interfacial curvature. The difference between the gas and the water pressure is the capillary pressure and it is related to the degree of saturation by means of the water retention curve.

An example of typical relative permeability curves, obtained for two different fluids (e.g., a non-wetting and a wetting fluid), is given in Figure 3.1. The figure presents the ideal case of relative permeability curves obtained for a non-hysteretic and non-active material. In this particular case, because the intrinsic permeability is independent from the type of fluid, the relative permeability to water at $S_r = 1$ coincides with the relative permeability to gas at $S_{rg} = 1$. The non-wetting relative permeability curve is characterised by an S-shape whereas the wetting relative permeability curve is usually concave upward (Ahmed, 2010). At low degree of wetting-phase saturation, lower than the irreducible degree of saturation, the $k_{r,g}$ variation is quite small. A sharp decrease of $k_{r,g}$ with the increase of the water degree of saturation is observed for high S_r. This results indicates that the large pores are occupied first by the non-wetting phase (Bear,

1972, Ahmed, 2010). At approximately $S_r = 0.85$, the gas phase is not continuous and its relative permeability become zero. Regarding the relative water permeability, it is equal to one at $S_r = 1$ and decreases with the decreases of the water saturation indicating the reduction of the void space dedicated to the water flow. At the residual degree of saturation, the water phase can be considered as immobile and the water flow ceases.

3.2.2.2   Concept of intrinsic permeability for an active porous medium

Experimental investigation carried out on different porous media proved that the concept of intrinsic permeability and relative permeability cannot be applied to active porous media, or to any other porous media whose pore structure evolves under certain loadings, in a straight-forward manner.

Loosveldt et al. (2002) measured the permeability of a mortar to water and argon. Their results showed that the intrinsic water permeability was systematically lower than the gas permeability (one or two order of magnitude), despite the experimental data of gas permeability were corrected for the Klinkenberg effect. The Authors suggested that this difference may be attributed to the chemical activities of pure water in concrete that may lead to rehydration of non-reacted cement, dissolution/precipitation, migration of fine elements and water adsorption in the smallest pores of the cement matrix, so to a change in the pore structure.

A difference of several orders of magnitude in the intrinsic permeability to water and gas was also detected by Tanai et al. (1996), Villar and Lloret (2001), Romero (2013) and Villar et al. (2013) for different types of bentonite and sand/bentonite mixtures compacted to different dry densities. The difference in the intrinsic permeabilities was strongly reduced when the swelling of the bentonite was inhibited by chemical agents so that the pore structure was "fixed"; e.g. when a 80/20 S/B mixture was mixed with lead nitrate, this different was only of two orders of magnitude (Romero, 2013). Deep investigation performed on the microstructure of these material suggested that this large difference is originated from the pore structure change due to bentonite swelling (Villar and Lloret, 2001, Romero, 2013).

In the light of the reported results, it is clear that the concept of intrinsic permeability cannot be applied to an active soil, and thus not to the tested S/B mixture, as this value is strongly related to the pore structure arrangement at the different hydro-chemo-mechanical state. As a consequence, in the next part of the thesis the term intrinsic permeability will be substituted with the term geometric permeability. The geometric permeability will be used to define the fraction of the permeability which solely depends on the pore structure. The term effective permeability, to a given phase, will be used to refer to the permeability of the mixture under unsaturated conditions. In chapter 4 an attempt to derive the geometric permeability for different hydraulic states will be presented based on the microstructural characterisation.
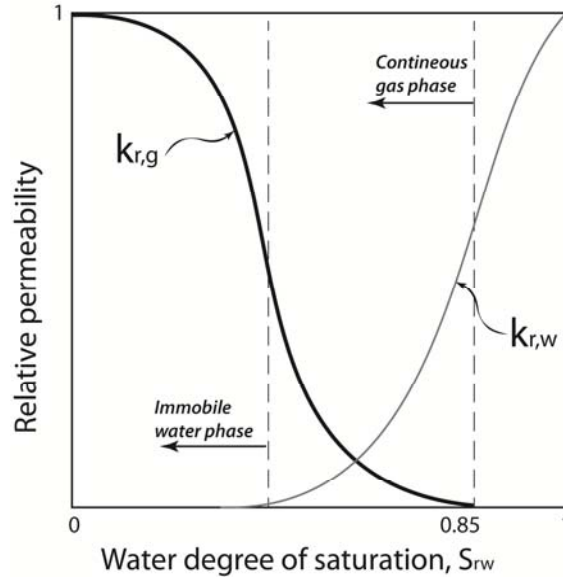
Figure 3.1: Typical non-hysteretic relative gas permeability curves for a non-active porous media (modified from Ahmed (2010)).

3.2.2.3   The Klinkenberg effect

The Klinkenberg effect takes into account the pressure dependence of the effective permeability to gas. This additional term comes from the fact that, when the size of the pore approaches the mean free path of the gas molecules, the velocity of the flowing molecules on the walls of the channels is not zero (slip flow), as it was the case for water. As a consequence of this phenomena, the gas permeability results higher than the water permeability.

Klinkenberg (1941) showed that, in a steady state test, the apparent gas permeability $k_{g,a}$ is a linear function of the reciprocal of the (absolute) gas pressure ($\overline{P_g}$):

$$k_{g,a} = k_\infty \left(1 + \frac{b_k}{\overline{P_g}} \right)$$

$$b_k = \frac{c\kappa}{\sqrt{2}\pi r^3}$$

(3.10)

with k_∞ the geometrical (gas/water) permeability, which is solely dependent on the pore structure, b_k the Klinkenberg coefficient, κ the Boltzmann's constant, r the pore radius and c is a constant.

The Klinkenberg effect can be important when the intrinsic permeability is lower than 10^{-18} m^2 and at low gas pressure. For specimen of sandstone, Tanikawa and Shimamoto (2006) found that b_k increases with the decrease of the water permeability, and its variation can be described with the following equation:

71

$$b_k = Bk_i^{-C} \tag{3.11}$$

where B and C are constants equals to $1.5 \pm 0.6 \cdot 10^{-7}$ and 0.37 ± 0.038, respectively. Typical values of the Klinkenberg parameter, for different intrinsic permeability, are also listed in Table 3.2.

The influence of the Klinkenberg effect on the estimation of the gas permeability of Febex bentonite was investigated by Villar et al. (2013). Despite the very low intrinsic permeability to water and the extremely narrow pore size, the Authors reported that this effect was negligible in the range of gas pressure applied.

The experimental determination of the intrinsic gas permeability and the b_k parameter requires performing gas permeability tests under steady state conditions, by applying different gas pressure gradients to the specimen. The permeability resulting from these tests are then plotted against the invers of the mean gas pressure to determine the intrinsic permeability and the b_k parameter. In case of a non-active porous media, whose pore structure and thus intrinsic permeability remain stable, this test can be performed at one degree of saturation only; e.g., on a dry material. Because of the swelling capacity of the tested S/B mixture, its pore structure, and thus the associated geometrical permeability, is continuously evolving (see section 4.6.4.3). As a consequence, the Klinkenberg parameter should dependent on the hydro-mechanical state of the mixture.

Table 3.2: Typical Klinkenberg parameters for different intrinsic permeabilities (Wu et al., 1998).

k_i [m^2]	b_k[Pa]
10^{-12}	$3.95 \cdot 10^3$
10^{-15}	$4.75 \cdot 10^4$
10^{-18}	$7.60 \cdot 10^5$

3.2.3 Breakthrough pressure

The breakthrough is a phenomenon which is in general associated to the formation of preferential flow paths through the porous medium. The breakthrough phenomenon in clayey soils has being investigated by several authors aiming at understanding the hydro-mechanical (e.g., stress state and saturation) conditions under which the process occurs. Two main mechanisms were proposed for gas breakthrough in clayey soils: dilatancy controlled gas flow and gas flow along macroscopic tensile fractures (Horseman et al., 1996b).

The dilatancy-controlled gas flow, also called pathway dilation (after Horseman et al. (1996b), is a phenomenon which leads to the increase of the pore space to accommodate the high pressurised gases. It is related to the creation of a pressure-induced network pathways which dilates and propagates in the material when the gas pressure P_g is higher than a fraction of the total stress (σ) (Horseman et al., 1996b):

$$P_g > \alpha\sigma \tag{3.12}$$

where α is a fraction of the total stress transmitted between clay particles in equilibrium. It is expressed as follows:

$$\alpha = \frac{\Pi_D - \Pi_e + P_w}{\sigma} \tag{3.13}$$

with Π_D the disjoining pressure (which can be equated with the local value of the swelling pressure (De Derjaguin and Churaev (1987) from Horseman et al. (1996b)), Π_e is the osmotic pressure and P_w is the hydrostatic pressure.

This gas-driven microfracture process is characterised by an increase in the pore space, associated to a detectable increase in the intrinsic permeability and a change in the capillary pressure-saturation curve. In low permeability claystones, the gas flow is still controlled by the visco-capillary forces but the transport properties of the solid matric are changed with respect to the intact porous media and are coupled with the matric deformation; e.g., it is accompanied by an increase of the intrinsic permeability and by a permanent modification of the water retention curve (Nagra, 2008). The created pathways are highly instable and close as soon as the pressure is released.

According to the classic theory of hydro-fracturing, the gas flow along macroscopic tensile fractures occurs when the gas pressure is higher than the sum of the minimum principal stress (σ'_{min}) and the tensile strength of the material (σ_t) (Nagra, 2008):

$$P_g > \sigma_t + \sigma'_{min} \tag{3.14}$$

The gas transport along tensile fracture is typical of clay stones and is associated to an increase of many order of magnitude of the bulk permeability of the medium. It can be seen as single gas flow and it does not produce any water displacement.

Bentonite-based materials, such as the tested S/B mixture, in principle, do not exhibit any tensile strength. As a consequence, the literature review and the experimental work performed in this thesis were focus on collecting evidences for verifying the so called dilatancy-controlled gas flow.

3.2.3.1 *Breakthrough experiments on bentonite-based materials*

The breakthrough experiments on fully saturated MX-80 bentonite were performed by several authors. In all these tests, the injection conditions (e.g., constant flow rate or constant gas pressure) and the mechanical boundary conditions (constant volume, radially confined or isotropically confined) were different which makes difficult to give a general interpretation of the breakthrough phenomenon.

Pusch et al. (1985), Tanai et al. (1996) and Gallé and Tanai (1998) performed gas migration tests on fully saturated bentonite, maintained under constant volume conditions. In these tests, the breakthrough pressure, or critical pressure, was defined as the pressure that produces a steep increase of the outflow. Pusch et al. (1985) observed that the critical pressure was generally lower than the swelling pressure. Microstructural observations showed that gas penetrates from the larger voids which were created because the high gas pressure displaced the compressible clay matrix. Horseman et al. (1996a) and Horseman and Harrington (1997) ran a series of breakthrough tests on fully saturated MX-80 bentonite subjected to an isotropic state of stress. The Authors reported that, when gas was injected at a constant flow rate, the gas pressure rose up to a peak value which was higher than the sum of the swelling pressure and the back pressure. According to Horseman and Harrington (1997), the gas breakthrough event was accompanied by the creation of preferential pressure-induced pathways that were characterised by a high conductivity. A spontaneous decrease of the gas pressure was observed after the peak, suggesting the achievement of a steady state conditions. In 100% bentonite specimen, a rapid drop of the gas pressure (shut-in) was observed when the gas injection was ceased, suggesting the closure of preferential flow paths (Harrington and Horseman, 2003).

Gas permeability of Febex bentonite and MX-80 bentonite, after the breakthrough event, have been computed by Villar et al. (2013) and Horseman et al. (1999), respectively. Villar et al. (2013) report values of gas permeability in the range between $6.4 \cdot 10^{-19}$ m^2 and $4.8 \cdot 10^{-22}$ m^2. Horseman et al. (1999) found similar values of gas permeability for highly compacted MX-80 bentonite. The increase of gas permeability after the breakthrough event was always observed, suggesting the dilation of some pressure induced pathways. A decrease of gas permeability was observed after the gas injection was stopped. In Febex bentonite, the post-breakthrough gas permeability values appeared independent from the dry density and water content of the specimen, suggesting

that the flow, after the breakthrough event, took place along some preferential pathways (Villar et al., 2013).

Cyclic breakthrough tests revealed that, after the first breakthrough event, the gas flowed through the bentonite without the gas pressure versus time curve presented a clear peak, because some gas bubbles remained trapped in the created preferential flow paths (Horseman et al., 1996a). However, when water was re-injected into the material after the first breakthrough event, all the preferential flow paths were sealed and the peak pressure was regained (Tanai et al., 1996, Harrington and Horseman, 2003).

In a fully saturated 30/70 S/B mixture, subjected to isotropic confinement, the continuous passage of gas was detected when the gas pressure was equal or slightly higher than the generated swelling pressure, however a discontinuous passage of gas was detected at a much lower gas pressure (Liu, 2013).

In bentonite-based materials, the peak breakthrough pressure and time for the breakthrough depends on the saturation of the specimen, the injection rate, the percentage of bentonite and the dry density of the clay (e.g., Gallé, 2000, Graham et al., 2002, Liu, 2013, Villar et al., 2013). According to Graham et al. (2002), at the degree of saturation lower than 93%, the gas pressure built up is not possible because of the presence of open highly-conductive channels (large inter-aggregate pores) in the bentonite. After this threshold value, the peak pressure increases exponentially with the degree of saturation.

Harrington and Horseman (2003) studied the influence of the boundary conditions in the breakthrough pressure. They observed that, when the specimen was kept under constant volume conditions, the increase in gas pressure was associated to an increase on the pore water pressure and the total stress. These observations were a clear indication of the penetration of the gas in the material and the tendency of the clay to delate. Harrington and Horseman (2003) postulated two mechanism for displacing water by means of gas injection. The first mechanism obeys to the conventional two-phase flow mechanism and implies the drainage of the water from the pore space. This first mechanism implies the global desaturation of the specimen subjected to a given imposed matric suction (P_g-P_w) and the consequent volume reduction (shrinkage) of the specimen during gas injection. The second mechanism considers that the gas pressure acts as a total stress on the fully saturated clay, causing its consolidation and the expulsion of the water from the pressure-induced flow paths.

Overall, breakthrough tests in bentonite indicate that the gas does not flow through the original pore space of the fully saturated material but through pressure-induced preferential pathways which are created because the gas is able to displace the clay particles (Pusch and Hökmark, 1990).

The most important findings of all the aforementioned Authors was that the gas breakthrough occurs at a pressure much higher than the gas entry and that no water was displaced during the test. In general, all the tests carried out in compacted bentonite showed that the passage of gas occurred without any appreciable desaturation of the

specimen. This result can be explained by the extreme narrowest of the inter-particles space and the strong chemo-physical interaction of the water in the interlayer particles (Horseman et al., 1999). Under this condition the gas migration was only possible if some channels were opened in the material.

3.3   EXPERIMENTAL SETUPS

In this study two different experimental setups for the injection of gas were implemented.

3.3.1   Gas injection tests under constant volume conditions

The measurement of gas effective permeability and breakthrough under constant volume conditions were performed using the permeameter cell described in section 2.5.1.1.

All the tested specimens were initially prepared under the as-compacted conditions (w=11% and given dry density) and then wetted inside the cell.

For the gas permeability tests, a given amount of water was immediately injected after compaction from both sides of the cell. Water was injected with a water PV controller at a pressure of 20 kPa. Because the mixture at the as-compacted state has very large macropores (Manca et al., 2015), the injected water is expected initially to flow preferentially through those pores so that the wetting front can advance for some millimetres along the specimen height. After this first injection, the permeameter cell is sealed in order to allow the moisture redistribution through the entire volume. Because of the very low unsaturated hydraulic conductivity of the mixture, this operation requires from 12 to more than 60 days depending on the dry density. During moisture equalisation, the gas permeability was measured on a regular basis. It was observed that the value of the permeability decreased during time suggesting that the water was redistributing along the specimen height. The test was considered as concluded once a stable value of gas permeability was obtained. To verify the hypothesis of homogenous moisture redistributions, at the end of the test the specimen was divided in three parts and the water content of each sub-specimen was measured by oven drying.

For the gas breakthrough tests the specimens were fully saturated following the same procedure adopted for the water permeability tests.

3.3.2   Gas injection test under triaxial condition

There is not a unique standard procedure for performing gas injection tests in porous material. For highly expansive soils, such as pure bentonite, the gas injection tests can be performed either in constant volume conditions or in triaxial conditions (Horseman et al., 1996a, e.g., Gallé and Tanai, 1998, Romero, 2013, Villar et al., 2013). One of the most

delicate aspects to take into account, in order to obtain reliable results, is to avoid the development of preferential flow paths that may form between the external surface of the specimen and the walls of the cell hosting it. Generation of preferential flow path in the specimen-cell interface is unlikely in case of a fully saturated bentonite because the high swelling pressure provides a good sealing of the interface (Villar and Lloret, 2001). For the specific case of the tested S/B mixture, the generated swelling pressure is relatively low (max 200 kPa under full saturation and for the high dry density) and the risk of having preferential gas flow during the test performed under constant volume conditions is likely. To avoid this problem, it was decided to carry out all the gas testing in a special triaxial cell available at EPFL. The use of the triaxial cell enables to apply a certain confining pressure to the specimen which is maintained higher than the gas injection pressure. This solution ensures a good adhesion of the membrane to the specimen and avoiding the creation of those preferential paths; in addition, the major advantage of this cell is that it is equipped with a contactless system for the measurements of radial deformations of the specimen.

3.3.2.1 *Description of the triaxial apparatus*

The triaxial apparatus used in the experiments consists of five main parts (Figure 3.2): (1) the triaxial cell, (2) a system of PV controllers to apply the water back pressure, the confining pressure and the gas pressure in case of breakthrough test, (3) the loading system for the application of the axial loading which is equipped with and internal LVDT for controlling the axial displacement, (4) the laser-based measurements system for measurement of the radial deformation, (5) the Fast Track control system to acquire the data.
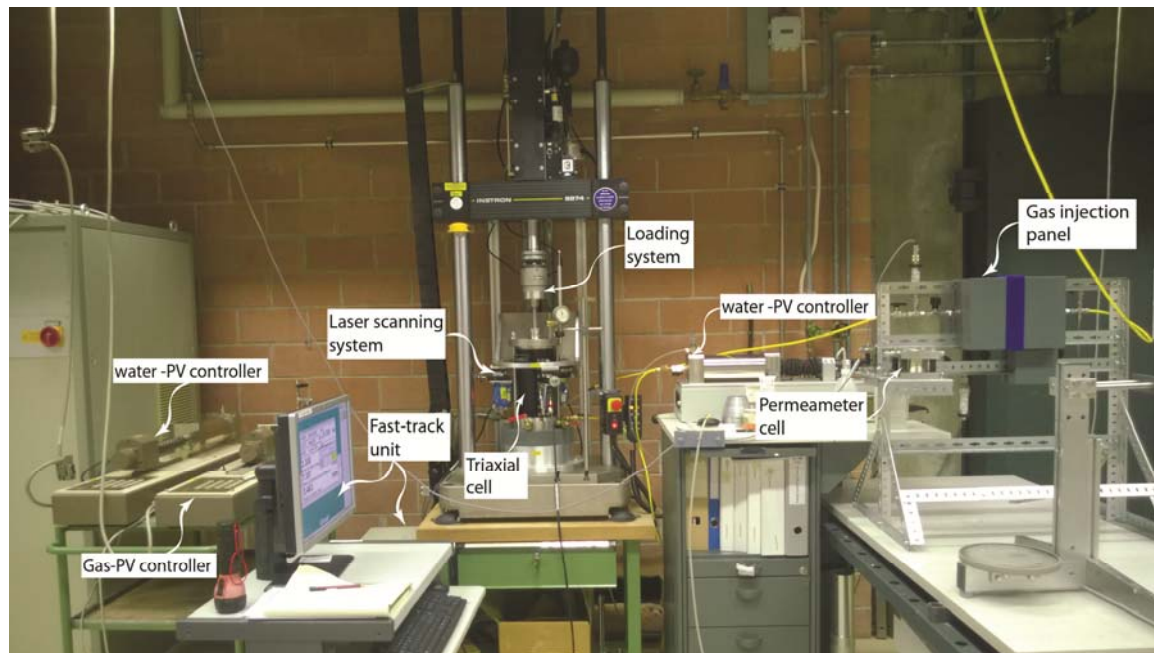
Figure 3.2: View of the triaxial apparatus.

(1) The triaxial cell

The triaxial cell was previously used by Rascol (2009) in the framework of a study related to soil liquefaction. The cell consists of a thick walled cylinder made of Certal aluminium which results stiffer and lighter than normal aluminium. The cylinder has an internal diameter of 100 mm and hosts a specimen of 80 mm of diameter and a height of 180 mm. However, for the gas injection test the specimen height was reduced to maximum 90 mm to accelerate the saturation process in case of breakthrough tests. The cell has three flat glass windows positioned at 120° from each other which allow taking the measurement of the radial deformation of the specimen. According to Rascol (2009) the cell can sustain a confining pressure of 2 MPa without having considerable radial deformations. At this pressure, a maximum displacement of 0.2 μm was predicted at the centre of the glass windows using a FEM calculation. The base of the cell and the top cup were modified in this study to allow performing gas testing. The base of the cell has 5 ways out. One way is connected to a pressure-volume controller whose purpose is to apply the confining pressure. Two of them are connected to the pedestal; one serves to apply pressure (water or gas) at the bottom of the specimen and the second one is connected to a pressure transducer that serves to monitor the pore water pressure. The last two ways out are connected to the top cup and serve to apply the pressure to the top of the specimen (either water or gas). Both the pedestal and the top cup have two holes connected through a circular (spiral) grove cut on the surface allowing the preliminary flushing operations and the homogeneous distribution of the injection fluid during the tests.

(2) System of PV controllers

The system of PV controllers consist of one water PV controller for applying the confining pressure, one water PV controller for applying the water pressure at the bottom of the specimen and one last gas PV controller which is used to apply the gas pressure during the gas breakthrough test. When needed, another PV controller can be connected to the top cup to enable the saturation of the specimen from top and bottom, or the application of a hydraulic gradient to gently flush away the air from the pore space.

(3) The axial loading system

The axial load is applied to the specimen with a hydraulic pump which provides 207 bar oil operative pressure to the system. The loading system consists of a piston whose movements are controlled by an external unit call Fast track. The vertical displacements of the piston are controlled with an internal LVDT. A load cell is installed at the end of the piston. The transfer of the load to the specimen is performed with a stainless steel road which was specifically designed to facilitate the perfect alignment of the system piston-road-top cup.

(4) Laser sensors

The measurements of the volume change after the application of the confining pressure are mandatory for determining the actual dry density at which the gas permeability or gas breakthrough tests are performed. In the case of saturated soil, the volume variation are derived from the measurements of the water volume exchange during sample testing, considering water as incompressible, and are performed using a graduated burette or a PV controller. However, when dealing with unsaturated soil, the pore space is occupied by water and air simultaneously and other techniques are required for estimating the volumetric deformation of the specimen. Also, for special test condition, like dynamic loading and or breakthrough the classical method for volumetric strain estimation fails so other methods are required. As Geiser (1999) states "*the choice of the method is influenced by the type of test, cost, available equipment, stress and stress strain level, necessity for continuous data acquisition, acquisition frequency*". For this thesis, it was required to have a method which avoids any disturbance of the specimen during the gas injection. For this reason, the measurements of the specimen volume have been performed using a laser scanning system which allows sweeping the sample surface in three different lines allowing the detection and identification of non-uniformities and localised deformation. The system was already available at LMS and well documented by a former PhD student (Rascol, 2009).

The system for measuring the radial displacements is a laser based measurements system. The lasers uses in this study are the optoNCLD ILD1700-10 from MICRO-EPSILON MESSTECHNIK. These sensors utilise the principle of optical triangulation as a measurement method. The laser produces and emits a laser light beam which hit a target inside the measuring range. Then the light is reflected diffusively and is adsorbed by the receiver. The measuring range, defined as the space interval in which the target occurs, is equal 10 mm in case the laser beam travels only through air. For the specific case of our experimental setup the laser beam travels through three difference media (water-glass-air). As a consequence, the optical path is changed with respect to the one of air and the measuring range increases; at the same time, the distance between the emission point and the starting of the measuring range is reduced (Rascol, 2009).

The three lasers are mounted on a frame which is independent from the triaxial cell. The plate where the lasers are fixed is perfectly horizontal and can translate vertically. The relative position of the lasers is fixed to 120°. However, the rotation and the translation in horizontal plane are allowed to facilitate the good positioning of the lasers against the cell's windows. The vertical position of the lasers is manually monitored with a 10 mm dial gauge. It is worth to mention that, due to cell design, the scanning of the specimen is allowed only starting from 3 cm from the specimen base.

The uncertainties of this type of measurements were deeply discussed in the PhD thesis of Romero (1999) and Rascol (2009) and will not be further discussed here. However, because the use of this apparatus requires a very precise calibration and a good capacity to handle the system, the calibration was entirely repeated. To minimise the error

in the measurement of the radial deformations, the calibration was performed using the same setup as the one used for all the gas injection tests.

(5) The fast track

The fast track is an external unit that allows controlling the loading system and acquires the data. It also allows setting some limits, for example on the piston displacement and force to avoid any damage of the sensors. For data acquisition the signal coming for each of the sensor is filtered using some specific algorithms programed in the system. The user should only pay attention to set an acquisition frequency (in Hz) which is lower than the frequency for the data filtering (fixed at 25 Hz).

Note that the cell cannot be turn on unless the fast track system is on.

3.3.2.2   Calculation of the radius, radial deformations and volumetric deformations

Thanks to the continuous measurements of the three lasers the value of the radius and the coordinates of the centre of the circular cross-section can be track all along the specimen height. The procedure elaborated by Rascol (2009) is here used for the computation of the radius and the coordinates of the centre of the specimen.

For this calculation the radius of the specimen is calculated knowing the value of the radius (r =39.79±0.01 mm) of a reference cylinder. Referring to Figure 3.3, it is assumed that the three laser beams intersect in the same point. This strong hypothesis required a very precise positioning of the lasers. The origin of the reference system (X, Y) is placed at the intersection of the three lasers beam and the X axis is aligned with laser n°1. Considering the reference cylinder centred, the coordinate of the three hitting points are the following:

$$R_1 = \begin{bmatrix} -1 \\ 0 \end{bmatrix} R_{ref} \qquad R_2 = \begin{bmatrix} 1/2 \\ -\sqrt{3}/2 \end{bmatrix} R_{ref} \qquad R_3 = \begin{bmatrix} 1/2 \\ \sqrt{3}/2 \end{bmatrix} R_{ref} \qquad (3.15)$$

The distance (L_i) between the emission point of the ith-laser and the origin reference system can be calculated according to the following equations:

$$L_i = m_{ref,i} + R_{ref} \qquad (3.16)$$

$$L_i = n_i(z) + \varepsilon + r_{sp,i} \qquad (3.17)$$

where $m_{ref,i}$ is the distance between the emission point and the reference cylinder, $n_i(z)$ is the distance between the emission point and the surface of the specimen, ε is the thickness of the painted membrane which isolate the specimen from the confining fluid and $r_{sp,i}$ is the distance between the origin of the reference system and specimen surface.

The parameter $m_{ref,i}$ is considered as fixed. This implies that the lasers must be carefully positioned always at the same relative distance from the cell every time that a new experiment is set up. The parameter ε represents the thickness of the layer that covers the specimen. This layer is made of two membranes, one layer of silicon grease and one layer of white paint.

Combining equations (3.15), (3.16) and (3.17) is now possible to calculate the coordinates of the three points where the lasers hit the specimen, N_1, N_2 and N_3, as follows:

$$N_1(z) = \begin{bmatrix} x_1 \\ y_1 \end{bmatrix} = \left[R_{ref} - m_{ref,1} + n_1(z) - \varepsilon \right] \begin{bmatrix} -1 \\ 0 \end{bmatrix}$$

$$N_2(z) = \begin{bmatrix} x_2 \\ y_2 \end{bmatrix} = \left[R_{ref} - m_{ref,2} + n_2(z) - \varepsilon \right] \begin{bmatrix} \dfrac{1}{2} \\ -\dfrac{\sqrt{3}}{2} \end{bmatrix} \qquad (3.18)$$

$$N_3(z) = \begin{bmatrix} x_3 \\ y_3 \end{bmatrix} = \left[R_{ref} - m_{ref,3} + n_3(z) - \varepsilon \right] \begin{bmatrix} \dfrac{1}{2} \\ \dfrac{\sqrt{3}}{2} \end{bmatrix}$$

The centre of the circular cross-section of the specimen is defined as the intersection of two perpendicular bisectors lines, KC and LC, passing through $N_1 N_2$ and $N_2 N_3$, respectively.

$$
\begin{aligned}
y^{KC} &= \tilde{a}x + \tilde{b} & y^{LC} &= \hat{a}x + \hat{b} \\
\tilde{a} &= -\frac{(x_2 - x_1)}{(y_2 - y_1)} & \hat{a} &= -\frac{(x_3 - x_2)}{(y_3 - y_2)} & (3.19) \\
\tilde{b} &= \frac{x_2^2 - x_1^2 + y_2^2 - y_1^2}{2(y_2 - y_1)} & \hat{b} &= \frac{x_3^2 - x_2^2 + y_3^2 - y_2^2}{2(y_3 - y_2)}
\end{aligned}
$$

The coordinate of the centre are then calculated as follows:

$$X(z) = \frac{\left(\tilde{b} - \hat{b} \right)}{\left(\hat{a} - \tilde{a} \right)} \qquad (3.20)$$

$$Y(z) = \tilde{a}X(z) + \tilde{b}$$

Finally the radius can be calculated as the distance between the centre and any point on the circumference:

$$R_{sp}(z) = \sqrt{\left(X_2(z) - X_c(z) \right)^2 + \left(Y_2(z) - Y_c(z) \right)^2} \qquad (3.21)$$
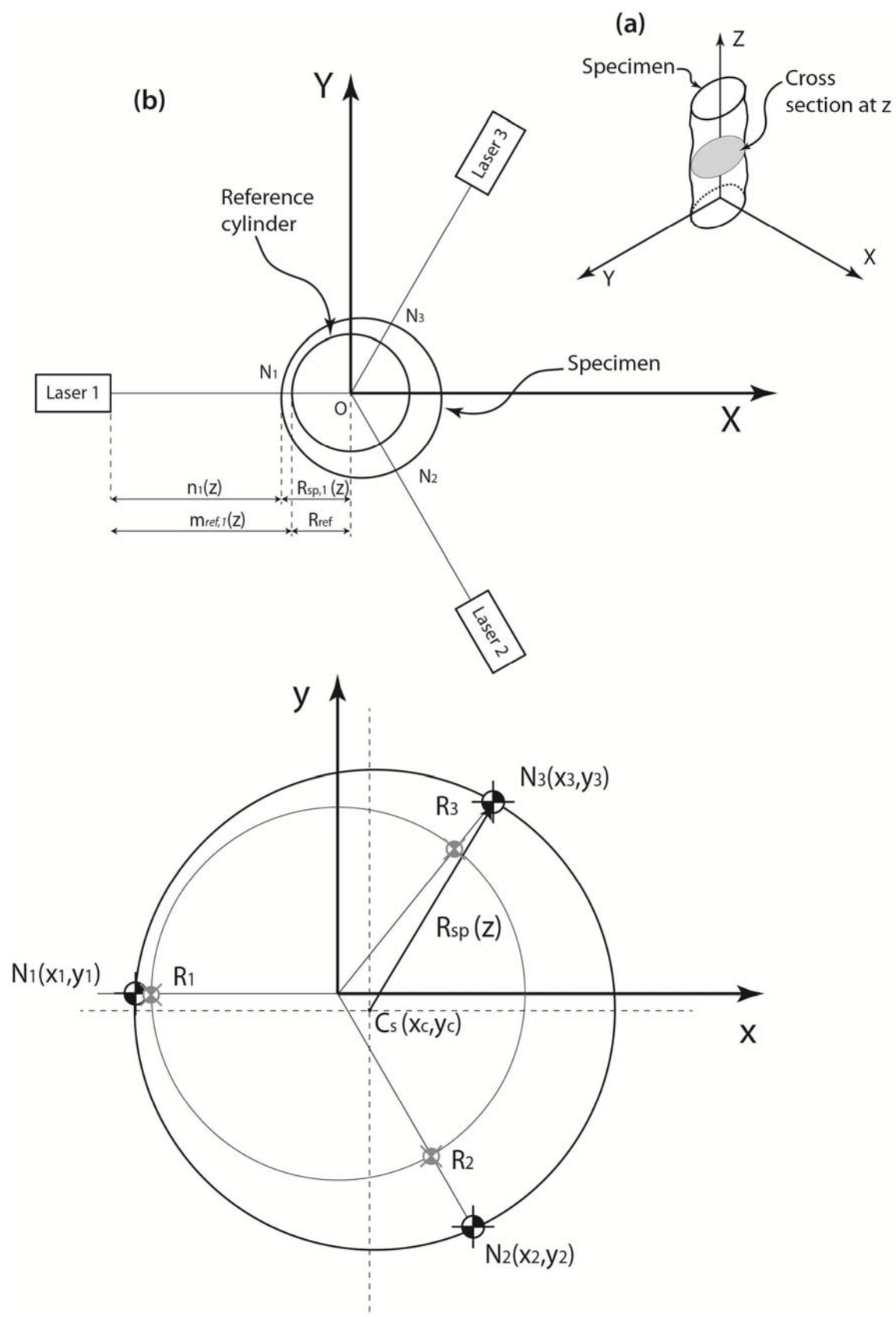
Figure 3.3: Parameters for the calculation of the specimen radius (modified from Rascol (2009)).

3.3.2.3 Calibration procedure

1) Scaling coefficients for the lasers

A special calibration tool was constructed by Rascol (2009) to obtain the relationship between the rough data values and the real measurements of the distance between the laser and the target surface. The calibration tool consists of a cup, which fits on the top of the triaxial cell, where a moving target is attached (Figure 3.4). During the calibration the target was moved back and forth and the measurements of the laser were taken. This procedure also allowed capturing the hysteresis in the measurements of the distance and it was repeated for each of the three laser sensors. A linear regression was obtained for each of the laser sensors (Figure 3.5):

$$\begin{cases} n_{f,i} = \Gamma_{f,i} x_i + \zeta_{f,i} \\ n_{b,i} = \Gamma_{b,i} x_i + \zeta_{b,i} \end{cases} , i = 1, 2, 3 \tag{3.22}$$

with x_i the distance measured by the ith laser, $\Gamma_{f,i}$ the scaling coefficient for a target moving forward, $\Gamma_{b,i}$ the scaling coefficient for a target moving backward and $\zeta_{f,i}$ and $\zeta_{b,i}$ the two coefficients which account for the hysteresis. When this calibration is applied, the maximum relative error committed on the measurement of the distance between the lasers and the target is 6 % (Figure 3.6).

2) Radius measurements

In order to verify the scanning procedure, the first scan is performed with the cylinder used for the calibration procedure. This cylinder is painted with a homogeneous layer of white paint to enhance the performance of the lasers. The results of this firs scan are presented in Figure 3.7. The measured radius was found slightly smaller than the actual radius of the cylinder (39.70 mm measured with the lasers against 39.79 mm of real value).

The same procedure is repeated with the reference cylinder covered with one latex membrane and then covered with two membranes (Butyl and Latex), in which a layer of silicon grease in interposed in between, to measure the thickness of membranes. In both cases a thin layer of plastic white paint was painted where the lasers hit the target. Note that the last configuration, with two membranes, is the one that is used for all the gas injection tests. The thickness of one painted membrane resulted equal to 0.49 mm (± 0.15 mm), whereas the thickness of two membranes, plus grease and white paint, resulted equal to 1.21 mm (± 0.23 mm). A compression of 0.01 mm each 200 kPa of the membrane was recorded with the lasers.
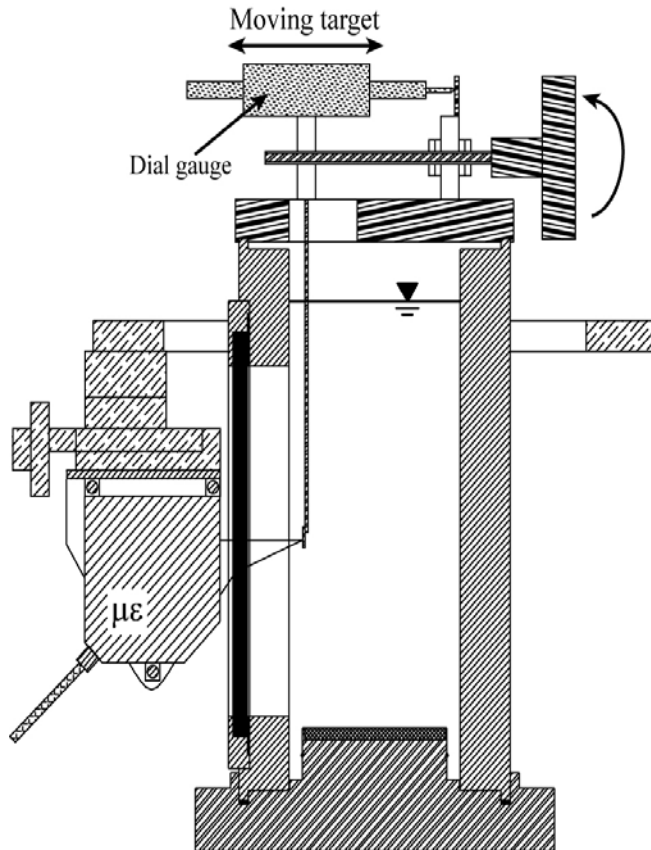
Figure 3.4 : Experimental setup for the calibration of the laser sensors (from Rascol (2009).
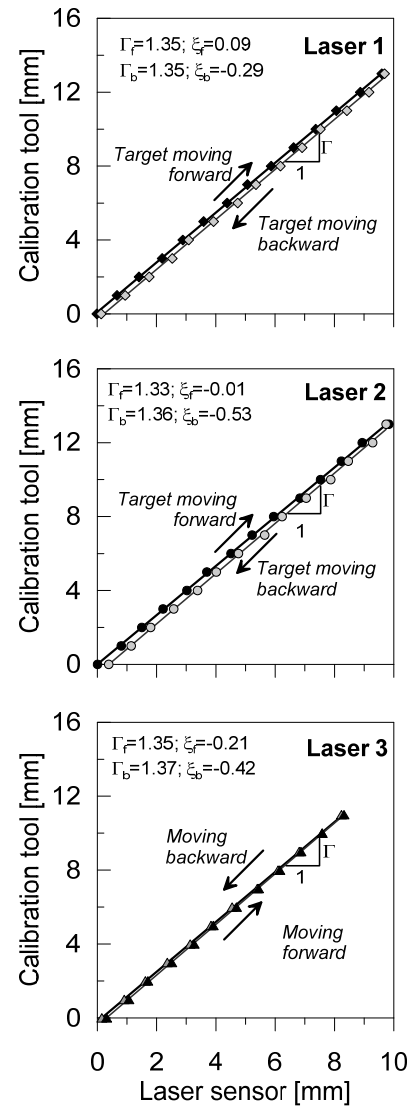
Figure 3.5: Results of the calibration for the three lasers.
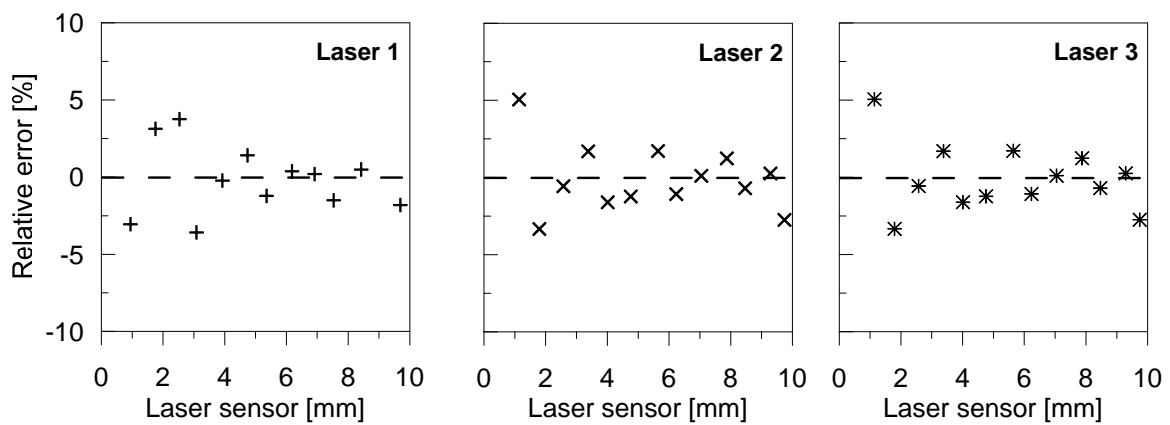
Figure 3.6: Relative errors.

The error in the estimation of the dry density ($\underline{\varepsilon}_\rho$) of an 80×80 mm cylindrical specimen, with a fluctuation of $\underline{\varepsilon}_r \pm 0.23$ mm on the measurement of the radius, is calculated as follows:

$$\underline{\varepsilon}_\rho = \frac{1}{V}\underline{\varepsilon}_{M_s} - \frac{M_s}{V^2}\underline{\varepsilon}_V \qquad (3.23)$$

where V is the volume of the specimen, M_s is the dry mass, $\underline{\varepsilon}_{M_s}$ is the error in the measured dry mass ($\pm$ 0.01 g) and $\underline{\varepsilon}_V$ is the error in the volume calculated as follows:

$$\underline{\varepsilon}_V = \pi R^2 \underline{\varepsilon}_h + \pi R H_{sp}\underline{\varepsilon}_r \qquad (3.24)$$

with R and H_{sp} radius and height of the specimen, $\underline{\varepsilon}_h$ the error in the measurement of the height ($\pm$ 0.01 mm). A maximum error of $\pm$ 0.01 Mg/cm^3 on the dry density was obtained for the specimen used for the testing under triaxial conditions.

In all the tested configurations it was found a high fluctuation of the measurements which is probably related to the fluctuations of the n-values which are not filtered when the measurement of the radius are taken manually (as in this case). Much stable value of the radius was obtained when the measurements of the lasers was recorded with the automatic data acquisition system, the Fast Track.
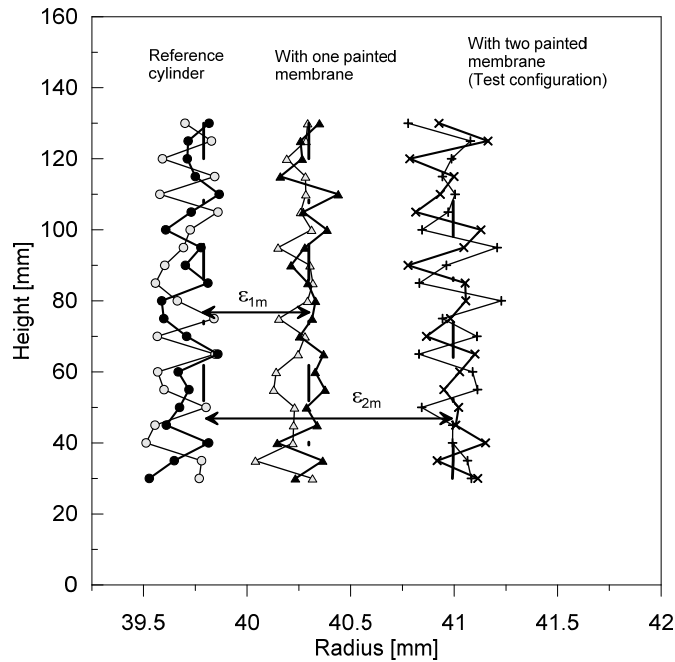
Figure 3.7: Measurements of the radius of the reference cylinder along its height. Comparison of the radius of the reference cylinder in different configurations.

3) *Radius correction for accounting the variation of confining pressure*

In order to capture the effect of the confining pressure on the variation of the radius, the reference cylinder was subjected to a cycle of monotonic increase and decrease of the confining pressure. During this cycle, the evolution of the radius at the middle height of the specimen ($z=80$ mm) was automatically recorded with the available data acquisition system (DAS). The elastic deformations of the reference cylinder were subtracted to the measured ones. The results show that the radius of the reference cylinder falsely increases with the increase of the confining pressure (Figure 3.8). This source of error can be considered as negligible with respect to the one obtained when the measurement of the n-values are recorded manually.
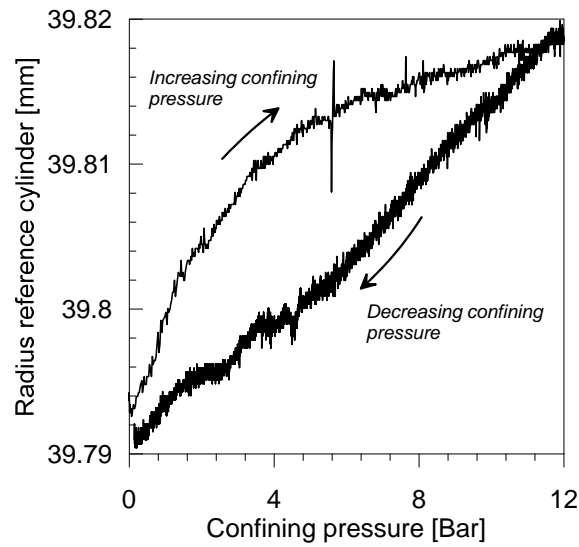
Figure 3.8: Evolution of the radius of the reference cylinder with the variation of the confining pressure.

3.3.3 The gas injection system

A "flexible" gas injection system was designed in house to allow performing gas permeability tests and gas breakthrough tests on the tested S/B mixture. The term flexible is used in this framework because the system was designed having the purpose to perform gas breakthrough test, with the constant gas pressure method (e.g., Villar et al., 2013), and gas permeability tests, with a low pressure gradient in transient conditions, on specimens whose gas permeability is lower than $1 \cdot 10^{-12}$ m^2. The system consists of (Figure 3.9): (1) the Nitrogen supply reservoir maintained at an initial pressure of 20 Bar; (2) the pressure regulator for adjusting the upstream pressure from 0 to 300 kPa; (3) two stainless-steel cylinders of 75cm^3 and 1000 cm^3, respectively, connected to the main source of Nitrogen, (4) an intermediate chamber for the saturation of the gas, (5) a gas and a water PV controllers which are connected to the cell, when gas breakthrough tests are performed, (6) three pressure transducers to control the pressure in different parts of the system. The two stainless steel reservoirs and all the valves are selected to sustain a maximum pressure of 12 MPa. However, the gas pressure in the system must be limited to 1MPa to avoid the damage of the pressure probes. The dimension of the two gas reservoir was selected following the criteria explained in section 3.4.1.2. The gas injection panel is depicted in Figure 3.10.
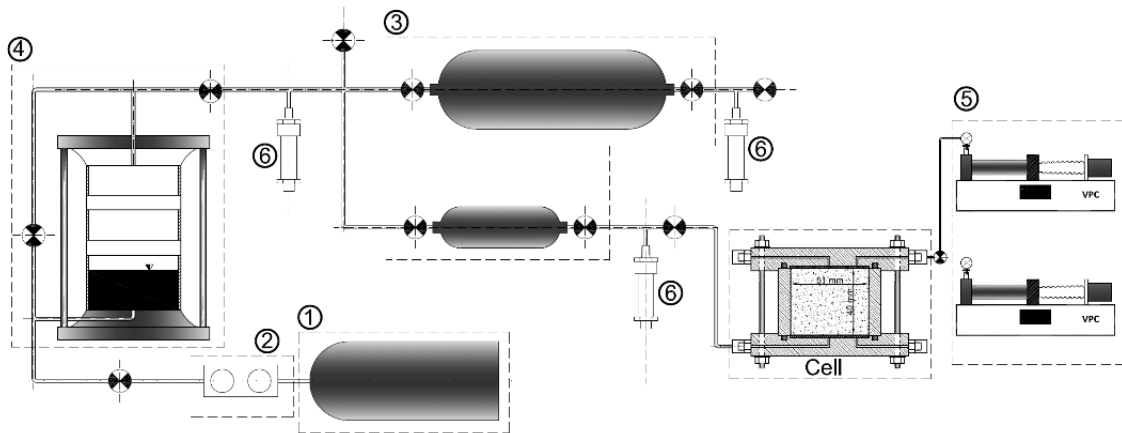
Figure 3.9: Schematic representation of the gas injection system connected to a permeameter cell.
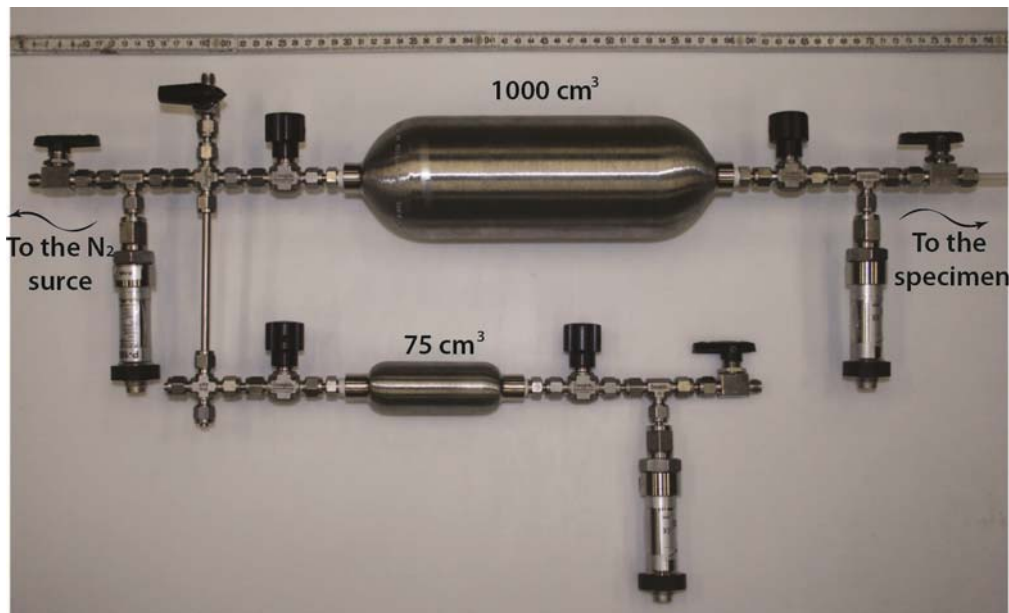
Figure 3.10: Gas injection panel.

3.4 GAS PERMEABILITY TEST ON THE 80/20 SAND/BENTONITE MIXTURE

3.4.1 Test procedure

The gas permeability of the partially saturated S/B mixture was obtained through a pulse-decay method (e.g., Brace et al., 1968, Dana and Skoczylas, 1999) based on the analysis of a transient pressure-dissipation process using the fundamental equations, such as the Darcy's law, the mass conservation equation and the constitutive equation of the fluid.

For this method, the cylindrical specimen, whose degree of saturation was assumed as homogeneous, was initially subjected to atmospheric pressure (e.g., the valve at the outlet is kept open). The inlet of the cell (permeameter or triaxial cell) was connected to one of the two airtight gas reservoirs of known volume. The selection of the reservoir depends on the expected degree of saturation of the specimen. For all these experiments, nitrogen (N_2) of above 99% purity was selected as safety replacement of hydrogen as suggested by Villar et al. (2013). The gas reservoir was initially filled with gas at a known pressure. The upstream line was instrumented with a pressure probe which recorded the pressure decay in the reservoir with time.

One of the main assumptions of the measurements of gas permeability with the pulse decay method is the uniform saturation of the specimen. In order to meet this requirement the gas pressure in the upstream gas reservoir was maintained quite low; e.g., lower than 60 kPa. In this way, the desaturation of the specimen, which would be provoked by the

injection of the non-wetting fluid, was limited. Another precaution to avoid the desaturation of the specimen was to limit the duration of the test by selecting the right gas reservoir. The downstream side of the gas circuit was indeed open to the atmosphere laboratory, thus subjected to a relative humidity of 41 %. Because this relative humidity was much lower than the one of the specimen, its desaturation was likely in case the test was too long.

3.4.1.1 *Mathematical formulation for the measurement of gas permeability*

For the analysis of the pulse-decay test, isochoric conditions were considered and the compressibility of the grains was neglected.

Referring to Figure 3.11, the excess of inflow over outflow during a short time interval (dt) through the surface of the control volume, that is perpendicular to the x direction is expressed as follows:

$$J_x dx\, dy\, dz\, dt - \left(J_x dx\, dy\, dz\, dt + \frac{\partial J_x}{\partial x} dx\, dy\, dz\, dt \right) \qquad (3.25)$$

where J_x is the mass flux of the fluid.

For the principle of mass conservation, the excess of flow is balanced by the variation of mass with time within the control volume:

$$n_g \frac{\partial \rho_g}{\partial t} dx\, dy\, dz\, dt = -\frac{\partial J_x}{\partial x} dx\, dy\, dz\, dt$$

$$n_g \frac{\partial \rho_g}{\partial t} = -\frac{\partial J_x}{\partial x} \qquad (3.26)$$

where $n_g = n(1 - S_r)$ is the porosity occupied by the gaseous phase, and ρ_g is the gas density.
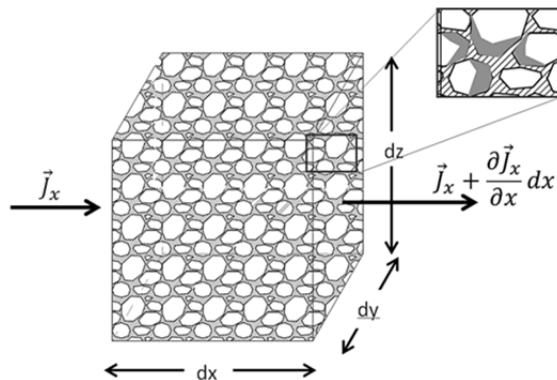
Figure 3.11 : Cross section of model for the controlled volume.

The mass flux is expressed by:

$$J_x = \rho_g \cdot q_{g,x} \tag{3.27}$$

where $q_{g,x}$ is the Darcy's velocity of the gas, which is equal to:

$$q_{g,x} = -\frac{\rho_g \cdot k_{eff,g} \cdot g}{\mu_g} \frac{1}{\rho_g g} \frac{\partial \overline{P}}{\partial x} \tag{3.28}$$

The combination of equations (3.26), (3.27) and (3.28), considering a homogeneous and isotropic porous medium, yields to:

$$n_g \frac{\partial \rho_g}{\partial t} = +\frac{k_{eff,g}}{\mu_g} \frac{\partial}{\partial x}\left(\rho_g \frac{\partial \overline{P}}{\partial x}\right) \tag{3.29}$$

The density of ideal gas (ρ_g) is a function of its absolute pressure ($\overline{P} = P + P_{atm}$) and temperature ($T$). This relationship is expressed by the gas state equation:

$$\rho_g = \frac{m_g \overline{P}}{RT} \tag{3.30}$$

where R is the universal gas constant and m_g is the molar mass of the gas.

Introducing equation (3.30) into equation (3.29), the governing equation of gas transport in a rigid porous medium is obtained (Bear, 1972):

$$n(1-S_r)\frac{\partial \overline{P}}{\partial t} = \frac{k_{eff,g}(S_r)}{2\mu_g} \frac{\partial^2 \overline{P}^2}{\partial x^2} \tag{3.31}$$

where $k_{eff,g}$ is the effective permeability with respect to the gas phase expressed in m^2.

Equation (3.31) expresses the transient flow process only in in one direction. This expression can be written in all the directions as:

$$n(1-S_r)\frac{\partial \overline{P}}{\partial t} = \frac{k_{g,eff}(S_r)}{2\mu_g} \nabla^2 \overline{P}^2 \tag{3.32}$$

In order to include the Klinkenberg effect in the analysis, the gas permeability is expressed as a function of the gas pressure using equation (3.10). As a consequence the mass conservation is modified as follows:

$$n(1-S_r)\frac{\partial \overline{P}}{\partial t} = \frac{k_\infty}{2\mu_g} \frac{\partial^2 \overline{P}^2}{\partial x^2} + \frac{b_k k_\infty}{\mu_g} \frac{\partial^2 \overline{P}}{\partial x^2} \tag{3.33}$$

The Klinkenberg parameter (b_k) is calculated with equation (3.11) where the geometric permeability is calculated based on the microstructure of the S/B mixture at the given hydraulic state as proposed in section 4.6.4.3.

The boundary conditions for the permeability test were written considering that the pressure at the downstream was equal to the atmospheric pressure whereas the upstream side was connected to the airtight reservoir of know volume, that was initially pressurised at a known pressure. At the upper boundary, the outflowing mass from the gas reservoir ($\frac{\partial M_{g,r}}{\partial t}$) is equal to the mass flux through the specimen ($\frac{\partial M_{g,up}}{\partial t}$).

The two mass fluxes can be expressed as:

$$\frac{\partial M_{g,r}}{\partial t} = \frac{m_g V_{up}}{RT} \frac{\partial \overline{P}_{up}}{\partial t} \tag{3.34}$$

$$\frac{\partial M_{g,up}}{\partial t} = \rho_g q_{g,x} A_{sp} \tag{3.35}$$

where V_{up} and P_{up} are the volume and the pressure of the airtight reservoir, respectively, $M_{g,up}$ is the mass of the gas in the reservoir and A_{sp} is the specimen cross-sectional.

Combining equations (3.30), (3.34) and (3.35) the upper boundary condition is written as:

$$\frac{\partial \overline{P}_{up}}{\partial t} = \frac{k_{eff,g}}{\mu_g} \frac{A_{sp}}{V_{up}} \overline{P}_{up} \frac{\partial \overline{P}_{up}}{\partial x} \tag{3.36}$$

Finally, the following system must be solved in order to simulate the gas injection process:

$$\begin{cases} n(1-S_r)\dfrac{\partial \overline{P}}{\partial t} = \dfrac{k_\infty}{2\mu_g}\dfrac{\partial^2 \overline{P}^2}{\partial x^2} + \dfrac{b_k k_\infty}{\mu_g}\dfrac{\partial^2 \overline{P}}{\partial x^2} & \\[2mm] \dfrac{\partial \overline{P}_{up}}{\partial t} = \dfrac{k_{eff,g}}{\mu_g}\dfrac{A_{sp}}{V_{up}}\overline{P}\dfrac{\partial \overline{P}_{up}}{\partial x} & for : \forall t; x = 0 \\[2mm] \overline{P}_{dw} = \overline{P}_{atm} & for : \forall t, x = L \\[2mm] \overline{P} = \overline{P}_{in} = \overline{P}_{dw} & for\, t = 0; \forall x \end{cases} \tag{3.37}$$

This system was solved numerically using a finite difference scheme implemented in MATLAB. The numerical solution was then compared with the experimental data in order to find the value of the effective permeability.

3.4.1.2 Parametric analyses for the design of the gas injection system

The gas injection system was equipped with two stainless steel reservoirs of 1000 cm^3 and 75 cm^3, respectively. The gas permeability of the specimen was measured using the bigger reservoir when high values of permeability were expected; i.e., in case of low compaction density or low degrees of saturation. The small reservoir was used when low values of permeability were expected; i.e., in case of high degrees of saturation.

The dimensions of the two reservoirs were selected based on a parametric study by using the system of equations (3.37). In this study, the characteristics of the specimen, such as size, void ratio and degree of saturation, were fixed, whereas, the volume of the reservoir and the gas permeability were varied as shown in Figure 3.12. The dimension of the reservoirs was selected based on the time required for the upstream pressure to reach the atmospheric pressure. In case of specimens of high permeability, if the pressurised gas reservoir is too small, the gas flows through the specimen too fast and it would impossible to measure the permeability. In case of low permeability measurements, the goal was to perform the permeability measurements in a short time to limit the evaporation of the water from the specimen that may occurred at the downstream due to the relative humidity gradient between specimen and laboratory environment.
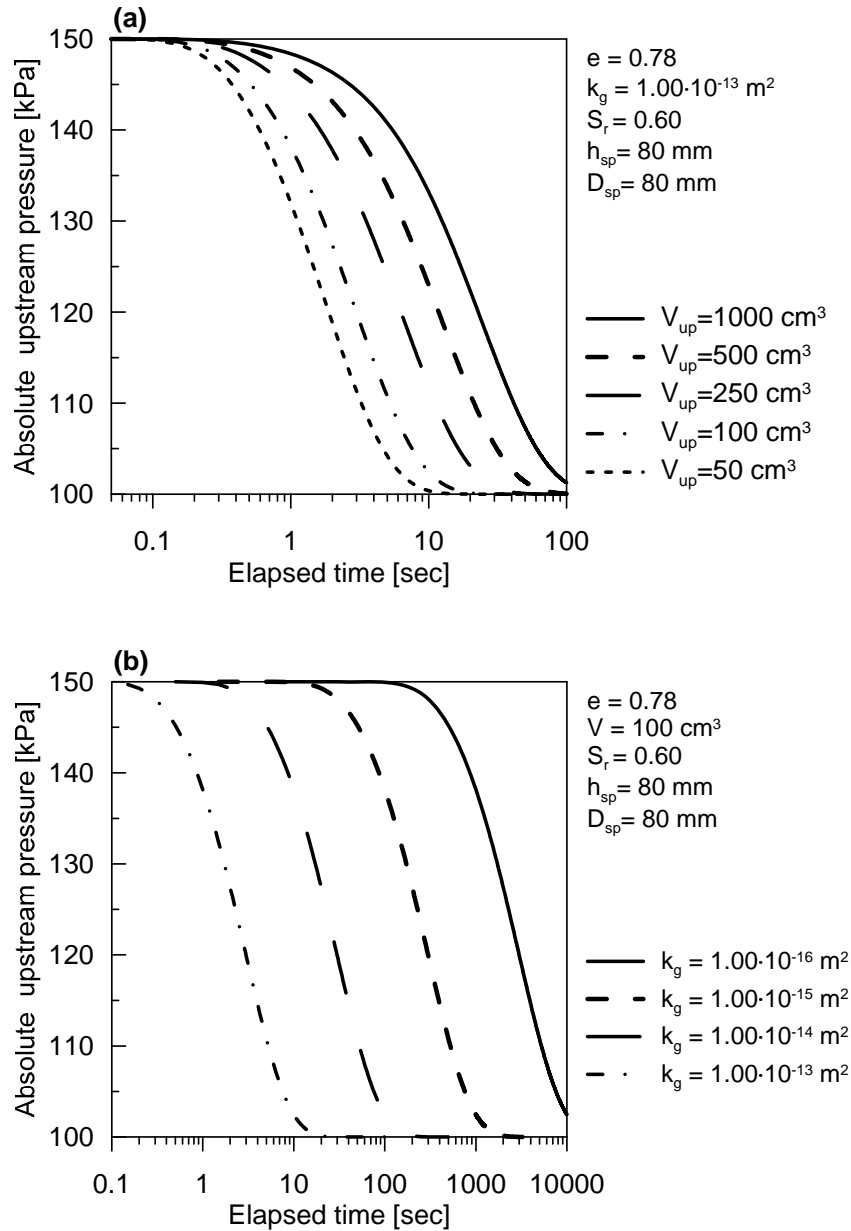
Figure 3.12: Parametric analyses for the selection of the gas reservoirs.

3.4.2 Specimen preparation

Specimen for the gas permeability tests were prepared following two different procedures depending on the applied boundary conditions; i.e., constant volume condition or isotropic confinement. The constant volume condition is a close condition to the in situ condition of the waste repository, because the S/B mixture will be emplaced in tunnels excavated in the host rock. However, because some issues were encountered during this type of tests, which will be discussed later in this chapter, it was decided to change the methodology and perform the test under isotropic confinement. In this paragraph the methodologies adopted for the specimen preparation are presented. The advantages and limitations of the two techniques are discussed in the light of the obtained results in section 3.4.3.

For all these tests, no specimens were prepared in dry conditions for several reasons. Firstly, it was impossible to produce a homogenous mixture when the sand and the bentonite were too dry because the phenomenon of particle segregation was very likely. Also, the expected gas permeability would be too high and thus not measurable with the designed gas injection system. Finally, the drying in the hoven at 105°C of the bentonite fraction of the mixture would cause irreversible microstructural modifications leading to changes in the permeability (Villar et al., 2013).

3.4.2.1 *Constant volume conditions*

For these tests, the mixture was initially prepared at the 11% of water content and then compacted to the target dry densities; 1.5 Mg/m^3 and 1.8 Mg/m^3. After compaction in the permeameter cell, the initial water content of the as-compacted specimen was increased in a controlled way by injecting a given amount of water by means of a PV controller. This preliminary phase was necessary due to the high gas permeability of the S/B mixture at the as-compacted state. Then, the permeameter was closed for several days to allow the moisture redistribution. After this curing period, the gas permeability was measured several times during a period of time which varied from 12 days to some months, until a constant value was recorded. The weight of the permeameter was measured before and after each of the gas permeability test to assess the possible change in the water content due to water displacement by gas injection. Because the gas pressure was always kept low (maximum 60 kPa), it was found that the weight of the cell remained constant. Because some of the injected water was adsorbed by the filter papers and by the porous disks in the permeameter, the exact water content of the specimen was not known a priori. As a consequence, at the end of the gas permeability test the water content of the specimen was measured by drying in an oven at 105°C for 24h, in agreement with the SN 670 3406. Water content was measured at the top, bottom and centre of the specimen to assess the moisture homogenisation.

3.4.2.2 *Triaxial conditions*

Specimens of 80 mm of diameter and 80 mm in height were prepared for the gas injection tests under triaxial conditions, form the S/B mixture wetted to different water contents in the range of 12 to 28 %. The mixture was wetted several days prior to compaction and then sealed in a hermetic container to allow moisture redistribution. Then the wetted mixture was statically compacted following the standard procedure. Because of the high water content of the mixture during preparation, the compaction velocity was reduced to 0.02 mm/min to avoid any undesired generation of excess pore water pressure, and related drainage of the specimen. Moreover, because of the large height, the specimen was compacted in two half to ensure the homogeneity of the dry density.

After compaction, the specimen mass was recorded with an accuracy of 0.01 g and the height of the specimen was measured with a calliper with a precision of 0.01 mm. Then the specimen was mounted in the triaxial apparatus and wrapped firstly in one Butyl membrane and then in one Latex membrane, between which silicon grease was interposed

(Figure 3.13). Each of the two membranes was tightened to the top cup and the pedestal with at least two pairs of O-rings to well isolate the specimen from the confining fluid. It was verified that this solution well prevent the diffusional losses of the injected gas through the membranes. The external surface of the membranes was pained with white plastic paint to enhance the performances of the laser scanning system for measuring the radial deformation of the specimen. After that, the cell was set-up following the procedure proposed by Rascol (2009) to avoid the specimen shearing which could occur when the loading piston was installed.

The triaxial cell was then filled with de-aired water and a first scan of the specimen radius along its height was taken. It was observed that the radius of the specimen measured with the laser results slightly higher than the radius of the stainless steel mould used for the compaction because of the elastic rebound that occurs during the extraction procedure. This error leaded to a reduction of the specimen dry density of maximum 0.05 Mg/m^3 which was then partially compensated when the confining pressure was applied. A confining pressure of 100 kPa was applied to ensure the good adhesion of the membranes to the specimen surface and thus to avoid the generation of preferential flow paths in the specimen-membrane interface. Finally, the gas permeability was measured by injecting the gas from the bottom to the top of the specimen.

At the end of the test the specimen was extracted from the triaxial cell and the water content was measured.

The initial characteristics of the tested specimens are reported in Table 3.3 and 3.3. In the tables, the values of the suction are derived from the main wetting branch of the water retention curve which account for the dependency of the water retention behaviour on the void ratio (section 2.4.3.2).
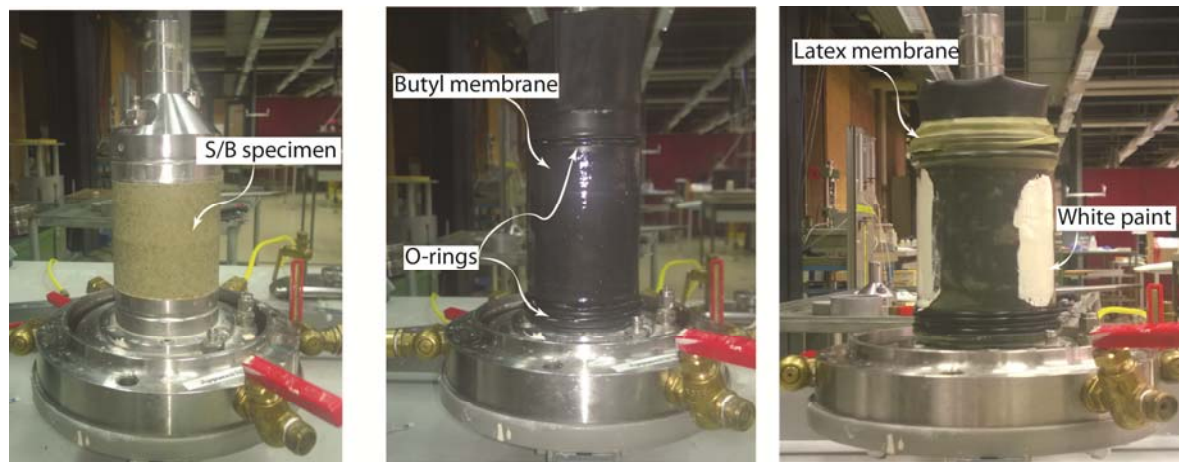
Figure 3.13: Sequences for the installation of the S/B specimen for the gas injection tests in the triaxial apparatus.

Table 3.3: Characteristics of the specimens tested under constant volume conditions.

Specimen code	e [-]	w_{av} [-]	S_r [-]	s [kPa]
GP_CV1	0.80	0.19	0.63	40
GP_CV2	0.76	0.23	0.79	16
GP_CV3	0.78	0.24	0.81	15
GP_CV4	0.76	0.19	0.66	35
GP_CV5	0.78	0.19	0.66	35
GP_CV6	0.78	0.25	0.87	10
GP_CV7	0.78	0.26	0.91	10
GP_CV8	0.78	0.25	0.87	10

Table 3.4: Initial characteristics of the specimens tested under isotropic confinement.

Specimen code	e [-]	w [-]	S_r [-]	s [kPa]
GP_dd15_TX1	0.81	0.12	0.41	200
GP_dd15_TX2	0.80	0.14	0.48	150
GP_dd15_TX3	0.80	0.15	0.49	95
GP_dd15_TX4	0.85	0.17	0.54	70
GP_dd15_TX5	0.83	0.24	0.77	18
GP_dd15_TX6	0.83	0.21	0.66	35
GP_dd15_TX7	0.81	0.28	0.92	7
GP_dd15_TX8	0.82	0.21	0.67	35
GP_dd15_TX9	0.80	0.26	0.87	10
GP_dd15_TX10	0.78	0.24	0.81	15
GP_dd18_TX2	0.52	0.13	0.69	85
GP_dd18_TX4	0.53	0.18	0.93	3
GP_dd18_TX5	0.51	0.16	0.85	16
GP_dd18_TX6	0.54	0.17	0.84	18
GP_dd18_TX7	0.49	0.12	0.65	130
GP_dd18_TX8	0.49	0.14	0.78	35

3.4.3 Results analyses

The results of gas permeability tests obtained for a dry density of 1.5 Mg/m^3, with the specimen wetted under constant volume conditions, are presented in Figure 3.14.

For each test the lowest value of the gas permeability is measured right after the water injection. Then, it tends to increase with time indicating that the water is moving through the specimen driven by suction gradients. The lower gas permeability at the beginning of the test suggests the existence of some layers of material which are strongly wetted. The results indicate that the stabilisation of the gas permeability occurs after a

time that varies between 12 to 60 days because of the extremely low permeability to water. The measurements of the water content in three sections revealed a non-homogenous distribution of the water in the specimen even if the gas permeability stabilised. The final values of the permeability measured with this method are listed in Table 3.5, together with the calculated gas accessible void ratio ($e(1-S_r)$). In the table, the values of the permeability obtained both neglecting and accounting for the Klinkenberg effect are reported. The analyses of the results revealed that the Klinkenberg effect is negligible in the tested S/B mixture. This results is related to the presence of large macropores in unsaturated conditions (Manca et al., 2015) that, according to eq. (3.11), lead to a large value of the geometrical permeability and thus to small value of the b_k parameter.

The results obtained under constant volume conditions prove that this wetting method is not ideal for obtaining a homogeneous moisture distribution on specimens of a height of 40 mm in short time. Indeed, because the of the limited water pressure used to avoid the displacement of the finest particles, the water front at the moment of the injection does not penetrate the entire volume of the specimen. Because of this issue, the tests on specimen compacted to 1.8 Mg/m^3 were not performed, as the stabilisation phase would require too long. Moreover, microstructural analysis on a cycle of wetting and drying revealed the irreversible change of microstructure after the first wetting (section 4.6.3.2) for the mixture compacted to the higher target dry density. As a consequence, an irreversible change of the gas permeability can be expected in the zones of the specimen that are wetted first. However, this is not a problem for the mixture compacted to the lower dry density as the microstructural changes due to wetting are reversible. Another issue that can arise when performing the gas permeability tests is the occurrence of preferential flow paths along the specimen-cell interphase that would results in an overestimation of the permeability. This possibility is likely when the tests performed on specimens compacted to low dry densities and relatively dry, because the generated swelling pressure is too low for sealing these paths. However, comparison of these results with the one obtained under isotropic confinement revealed that, at relatively high degree of saturation, this issue is avoided thanks to the use of a ring with threatened surface.

To overcome this issue, it was decided to wet the mixture to the desired water content prior to compaction and to perform the test under isotropic confinement.
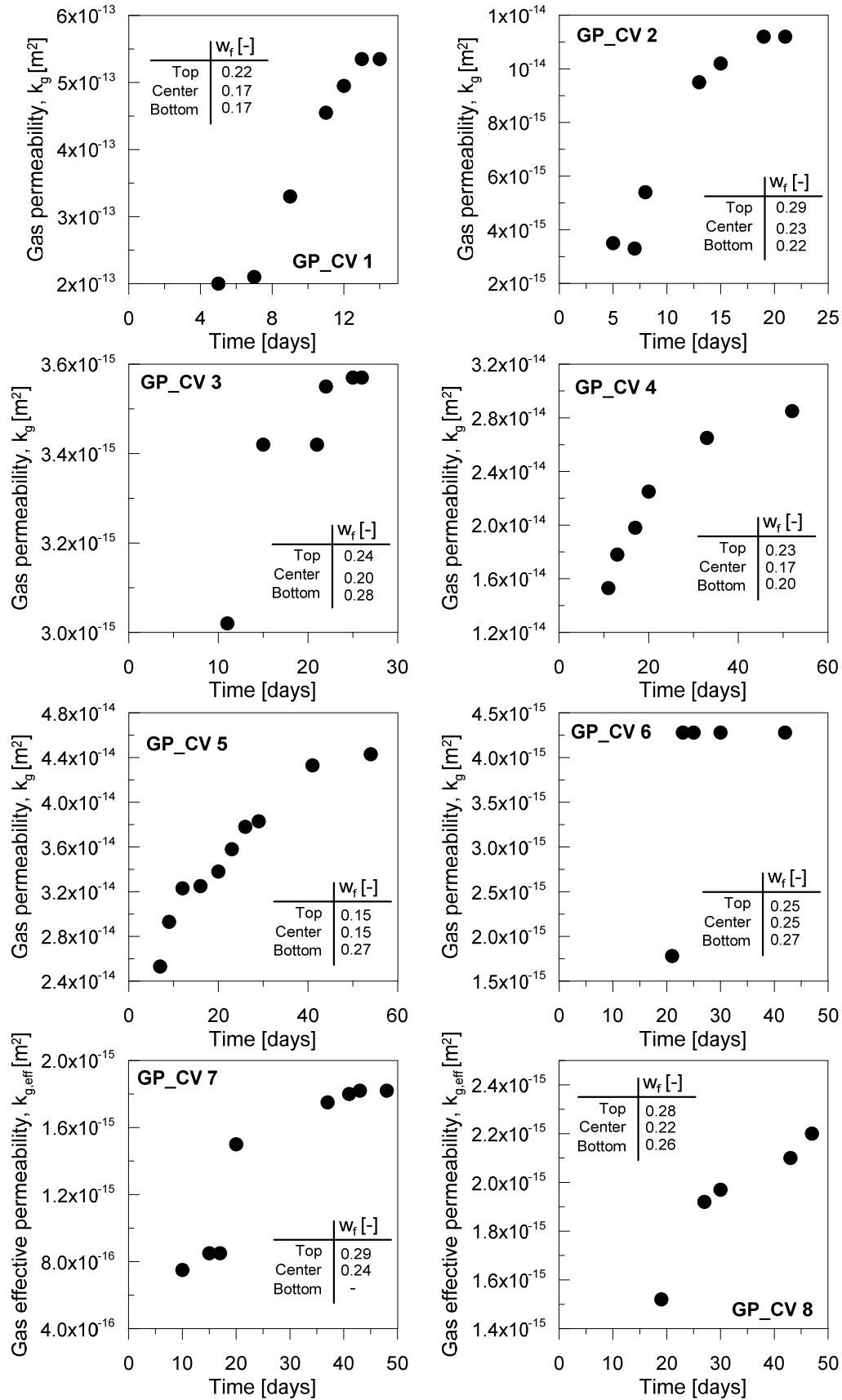
Figure 3.14: Results of the gas permeability tests under constant volume conditions on specimens compacted to 1.5 Mg/m³ dry density.

Table 3.5: Results of the gas permeability tests under constant volume conditions

Specimen code	$k_{g,eff}$ [m^2]	k_∞ [m^2]	$e(1-S_r)$ [-]
GP_CV1	$5.35 \cdot 10^{-13}$	$4.50 \cdot 10^{-13}$	0.29
GP_CV2	$1.10 \cdot 10^{-14}$	$1.00 \cdot 10^{-14}$	0.16
GP_CV3	$3.57 \cdot 10^{-15}$	$3.60 \cdot 10^{-15}$	0.15
GP_CV4	$2.85 \cdot 10^{-14}$	$3.00 \cdot 10^{-14}$	0.26
GP_CV5	$4.43 \cdot 10^{-14}$	$4.00 \cdot 10^{-14}$	0.27
GP_CV6	$4.28 \cdot 10^{-15}$	$4.28 \cdot 10^{-15}$	0.10
GP_CV7	$1.82 \cdot 10^{-15}$	$1.82 \cdot 10^{-15}$	0.10
GP_CV8	$2.20 \cdot 10^{-15}$	$2.20 \cdot 10^{-15}$	0.10

The typical results obtained when the gas was injected in the triaxial apparatus are presented in Figure 3.15. The scanning of the specimen radius along the height is always performed more than once; usually, right after installing the specimen in the triaxial apparatus, 5 hours after installation and then again after 24 hours. The application of the confining pressure of 100 kPa on the specimen causes the reduction of its void ratio. This is due to the fact that the removal of the specimen from the compaction mould leads to the increase of its volume due to the elastic rebound. These elastic deformations are partially compensated with the application of the confining pressure (Liu et al., 2015). The gas permeability is measured right after the application of the confining stress and then after the consolidation phase. The reduction of the gas permeability after the consolidation of the specimen is associated with the increase of the degree of saturation, and the associated gas accessible void ratio, caused by the reduction of the specimen volume under constant water content (Figure 3.15-right).
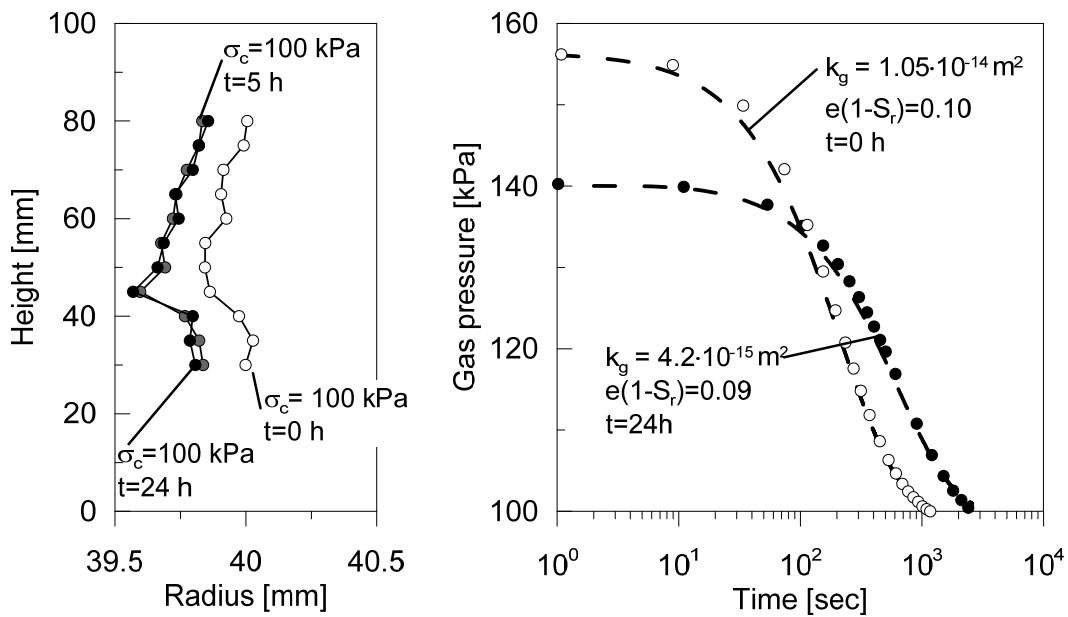
Figure 3.15: Results of the gas permeability tests performed on the specimen GP_dd15_TX9. Evolution of the radius (left) and measurement of the permeability after the emplacement of the specimen and after 24 h (right).

The evolution of gas permeability at different degrees of saturation, for the specimens compacted to two target dry densities, is presented in Figure 3.16-left. The evolution of the gas permeability with the accessible void ratio is presented in Figure 3.16-right. All the obtained results are listed in Table 3.6 together with the final values of void ratio, water content, degree of saturation and associated suction, and the gas accessible void ratio. In the figure, the results of the tests performed under 100 kPa of confining stress are plotted together with the results obtained under constant volume conditions. In most of the cases, the gas permeability obtained under constant volume conditions results two orders of magnitude lower than the ones obtained under constant confining stress. The lager discrepancies are observed in those tests where a large non-homogeneity of water distribution is detected, because of the formation of some quasi-impermeable layers of mixture, at the injection sides, which lead to a strong reduction of the permeability. Interestingly, the specimen that has a homogenous distribution of the water content (GP_CV6) has similar gas permeability than the one obtained under 100 kPa of confining pressure. This result suggests that the use of the permeameter ring, whose walls is threatened, limits the creation of preferential flow paths also for low swelling soils. However, in order to obtain reliable results when testing the specimen under constant volume conditions, it is necessary to use another wetting method; e.g., wetting through vapour circulation forced in to the specimen with a peristaltic pump or the use of the axis translation technique.

With regard to the gas permeability versus degree of saturation curve, the results lay on the same lines regardless the target dry density. Also, the mixture results permeable to gas even at high degrees of water saturation suggesting the existence gas conductive channels, most probably empty macropores, even at high degrees of saturation (see paragraph 4.6.3.2 and 4.6.4.2).

The obtained data can be divided into two different intervals. From the as-compacted state up to $S_r = 80$ % the variation on gas permeability with degree of saturation is not very pronounced. For degrees of saturation higher than 80 %, the gas permeability decreases of several orders of magnitude.

$$
\begin{aligned}
k_g &= C_1 \, exp(\, C_2 \times S_r \,); \quad 0.4 < S_r < 0.8 \\
k_g &= D_1 \, exp(\, D_2 \times S_r \,); \quad S_r > 0.8
\end{aligned}
\tag{3.38}
$$

where C_1, C_2, D_1, and D_2 are finning parameters whose values are listed in Table 3.7.

The value of the saturated permeability to gas can be extrapolated for the trend of the rest results as suggested by Villar and Lloret (2001). As a consequence, a value of $8 \cdot 10^{-12}$ m^2 is taken as the gas geometrical permeability of the fully dried 80/20 S/B mixture at any dry density. Similar to the results obtained in pure bentonite by other authors, this value is much higher than the measured saturated water permeability because of the strong microstructural modification associated to the wetting.
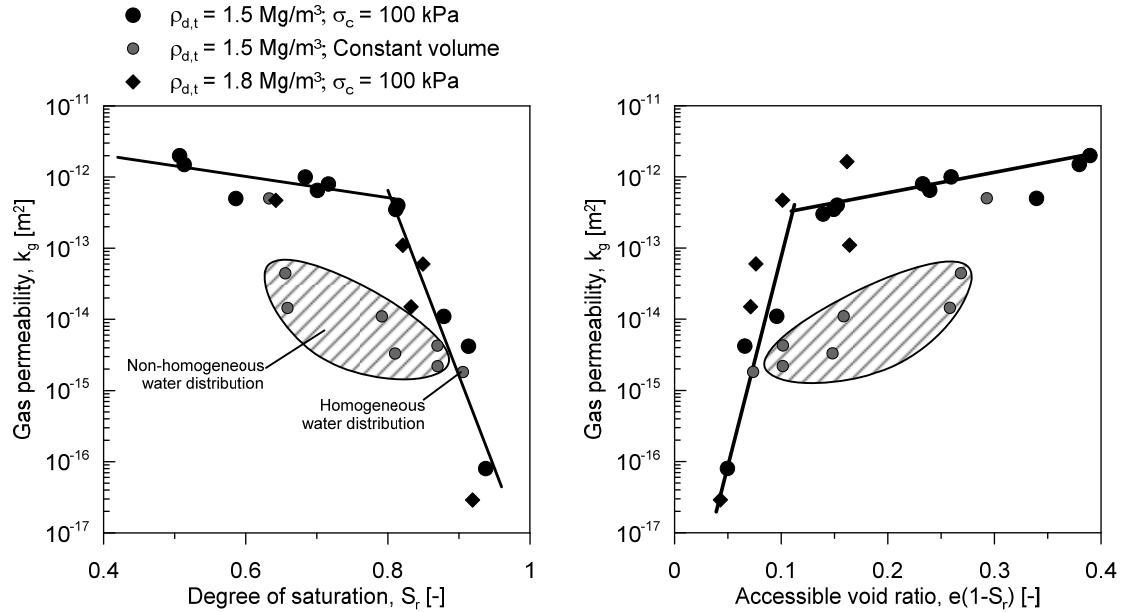
Figure 3.16: Evolution of the gas permeability vs degree of saturation (left) and versus the accessible void ratio.

Table 3.6: Results of the gas permeability tests on the S/B mixture compacted to two different dry densities.

Specimen code	e_f [-]	w_f [-]	S_r [-]	$k_{g,eff}$ [m²]	$K_{g,eff}$ [m/s]	s [kPa]	$e(1-S_r)$ [-]
GP_dd15_TX2	0.78	0.150	0.513	$1.5 \cdot 10^{-12}$	$1.04 \cdot 10^{-6}$	75	0.380
GP_dd15_TX3	0.79	0.150	0.507	$2.0 \cdot 10^{-12}$	$1.39 \cdot 10^{-6}$	100	0.390
GP_dd15_TX4	0.82	0.180	0.586	$5.0 \cdot 10^{-13}$	$3.47 \cdot 10^{-7}$	55	0.339
GP_dd15_TX5	0.82	0.250	0.814	$4.0 \cdot 10^{-13}$	$2.78 \cdot 10^{-7}$	15	0.153
GP_dd15_TX6	0.82	0.220	0.716	$8.0 \cdot 10^{-13}$	$5.55 \cdot 10^{-7}$	25	0.233
GP_dd15_TX7	0.79	0.279	0.938	$8.0 \cdot 10^{-17}$	$5.55 \cdot 10^{-11}$	6	0.050
GP_dd15_TX8	0.82	0.210	0.684	$1.0 \cdot 10^{-12}$	$6.94 \cdot 10^{-7}$	35	0.259
GP_dd15_TX8_2	0.80	0.210	0.701	$6.5 \cdot 10^{-13}$	$4.51 \cdot 10^{-7}$	30	0.239
GP_dd15_TX9	0.79	0.260	0.879	$1.1 \cdot 10^{-14}$	$7.64 \cdot 10^{-9}$	9	0.096
GP_dd15_TX9_2	0.76	0.260	0.913	$4.2 \cdot 10^{-15}$	$2.92 \cdot 10^{-9}$	7	0.066
GP_dd15_TX10	0.79	0.240	0.811	$3.5 \cdot 10^{-13}$	$2.43 \cdot 10^{-7}$	16	0.149
GP_dd15_TX10_2	0.78	0.240	0.822	$3.0 \cdot 10^{-13}$	$2.08 \cdot 10^{-7}$	15	0.139
GP_dd18_TX2	0.52	0.133	0.687	$2.7 \cdot 10^{-13}$	$1.14 \cdot 10^{-6}$	85	0.161
GP_dd18_TX4	0.50	0.183	0.919	$2.9 \cdot 10^{-17}$	$2.01 \cdot 10^{-11}$	7	0.043
GP_dd18_TX5	0.51	0.161	0.849	$6.0 \cdot 10^{-14}$	$4.17 \cdot 10^{-8}$	16	0.076
GP_dd18_TX6	0.54	0.168	0.863	$2.7 \cdot 10^{-14}$	$1.04 \cdot 10^{-8}$	19	0.071
GP_dd18_TX7	0.49	0.119	0.636	4.810^{-13}	$3.26 \cdot 10^{-7}$	140	0.018
GP_dd18_TX8	0.48	0.150	0.798	$1.1 \cdot 10^{-13}$	$7.74 \cdot 10^{-8}$	25	0.083

Table 3.7: Fitting parameters in eq. (3.38).

$C_1\ [m^2]$	8.00×10^{-12}
$C_2\ [-]$	-3.43
$D_1\ [m^2]$	4.58×10^8
$D_2\ [-]$	-60.00

3.5 BREAKTHROUGH PRESSURE OF THE 80/20 SAND BENTONITE MIXTURE

3.5.1 Specimen preparation – saturation procedure

Breakthrough tests were performed on specimens that were fully saturated prior to the gas injection. Also in this case, tests were performed in the permeameter cell and in the triaxial apparatus.

Specimens for the tests performed inside the permeameter were initially prepared at the 11% of water content and compacted to the target dry density following the procedure presented in section 2.2.6. The specimens were then saturated by applying a water pressure gradient following the procedure adopted in section 2.5.1.1.

The saturation of the specimen that was tested under triaxial conditions was performed in two stages:

1) The material at the 11 % of water content was poured in a cylindrical stainless-steel mould and compacted to the required dry density. Because the specimen has a height of 90 mm, to ensure a good dry density distribution the compaction was achieved in two time steps. Then, the obtained cylinder was extracted from the compaction mould, weighted and the height was carefully measured with a calliper. After that, the specimen was wrapped in geotextile and placed in a two-pieces mould with 80 mm of internal diameter and 120 mm of height. Two plastic cylinders of the same diameter were placed at the top and the bottom of the specimen. To provide constant volume conditions during the wetting process the mould was tightened using two hose clamps and the whole assembly was secured in a vise. The mould has a net of small holes all around the surface to facilitate the entering of the water to the specimen. The geotextile prevents the escape of the fine particles of bentonite from the specimen. Also, it does not stick to the specimen surface and it is very easy to remove. The whole assembly (specimen, mould and vise) was finally submerged in a water reservoir for at 10 days. After this period, the specimen was extracted and the weight was measured again to calculate its water content and the degree of saturation at the

end of this first phase. This method allowed reaching a degree of saturation of 80% for a specimen prepared to an initial dry density of 1.77 Mg/m^3.

2) The pre-wetted specimen was mounted into the triaxial cell and a confining pressure equal to the swelling pressure (estimated from equation (2.9) and considering distilled water as pore fluid) is applied to prevent undesirable volumetric deformations. Inside the triaxial apparatus, the specimen was saturated by applying a small hydraulic gradient (i<60). During this stage, it was always ensured that the difference between the pore water pressure and the confining pressure remained equal or slightly higher than the expected swelling pressure of the specimen.

There are many advantages on performing the specimen saturation in two time steps. First of all, it accelerate the saturation of the specimen of 90 mm of height, of very low permeable S/B mixture, which otherwise will take too long. Also, during the first saturation stage the wetting occurs without occupying any devices such as PV controllers or the triaxial cell, which can then be used for other tests.

This method allows obtaining homogenised specimen in term of water content distribution and void ratio (Seiphoori, 2014).

The saturation of the sample in the triaxial cell was controlled using the B-Skempton's criterion. Following this criterion, if a sample is fully saturated and no pore water drainage is allowed, an increase in the isotropic confining stress (σ_c) on the sample should result in an equivalent change in pore water pressure (u_w). The B-value is expressed as follows:

$$B = \frac{\Delta u_w}{\Delta \sigma_c} \tag{3.39}$$

Right after the specimen was installed in the triaxial apparatus, the cell was filled with de-aired distilled water and the first scan of the specimen radius was taken along its height.

For performing the breakthrough tests under triaxial conditions filter papers at the top and the bottom of the samples were not installed. This decision was made aiming at assessing the possibility of clay erosion as a consequence of the injection of gas and because filters paper may represent obstacles for the flow of fine particles of clays (more details about this subject are given in section 3.5.1).
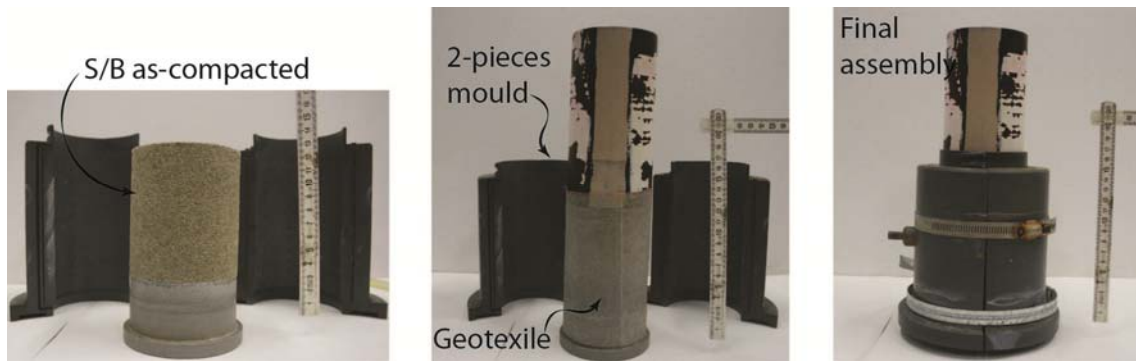
Figure 3.17: Phases of the preparation of the specimen for the breakthrough test under triaxial conditions. From left to right: as compacted specimen; specimen wrapped in geotextile; specimen tightened in the two-pieces mould.

3.5.1 Assessing erosion as a consequence of gas injection

The erosion of the finest component of the mixture poses an important problem for the assessment of short and the long term safety of the barriers because it can cause the local variation (increase or decrease) of the hydraulic conductivity, swelling pressure, retention properties and gas transport capacity. In addition, clays can act as carrier for chemicals and thus enhancing the transport of contaminants in the biosphere (Benamar et al., 2007).

According to Börgesson and Sandén (2006), the erosion of the clay particles occurs when *"the drag forces on the clay particles from the water movements is higher than the sum of the friction and attraction forces between the fine particles and the clay structure"* and it requires, locally, a very fast increase of the water pressure.

Referring to the phenomena of clay transport as a consequence of water flow, the parameters that play a major role on the transport rate are (Cerda, 1988, Börgesson and Sandén, 2006, Benamar et al., 2007, Suzuki et al., 2013):

1. The flow rate velocity. The particle concentration, and the total amount of particles recovered at the effluent, decreases with the decrease of the flow rate velocity. The size of the particles recovered with the fluid injection decreases with the decreasing of the velocity. The rate of particle deposition increases until a critical flow velocity, after that, it decreases because the magnitude of the hydrodynamic forces is enough to lift the particles. The size of the channels is also flow rate dependent.
2. Presence of macropores or large channels that enhances the faster movement of the suspended particles. Suzuki observed that in a 30/70 S/B mixture (blocks) the piping is likely in the cell sample interface because of the technological gaps. In this space it was also found an accumulation of silica sand which prevented the self-sealing process.
3. Pore size distribution. Independently from the total porosity and the flow velocity, Benamar et al. (2007) found that the particles moves easily in a soil formed by glass beats, which presented a very uniform pore size distribution and smooth surface, than in a soils formed by crushed gravel, which are characterised by the presence of

cervices and cavers in which particles can be trapped. In this sense, the presence of sand in the S/B mixture reduces the possibility to erode mass because it leads to obtain a multi-modal pore structure and the fine can remain entrapped in its nooks and crannies.

4. Swelling capacity under different hydro-mechanical conditions. The swelling capacity of the porous material influences its capacity to heal any type of preferential pathways, such as technological gaps in the repository or the pipes created by a very fast movement of water. The swelling capacity of bentonite based material depend on its hydro-mechanical (and chemical) conditions and so the clay transport. However, the possibility to develop the required swelling pressure is influenced by the flow rate.

5. The electrolyte concentration and pH. The colloidal forces, given by the sum of attraction and repulsion forces, acting between a fine particle and the rest (e.g., sand surface) are strongly influenced by the electrolyte concentration. With his experimental investigation on mobilisation of fine quartz in a fully saturated medium, Cerda (1988) evidenced the existence of a critical Na^+ concentration which depends on the pH; below this critical concentration the repulsive forces results dominant and the mobilisation occurs.

Bentonite and bentonite-based buffer materials can suffer piping and erosion during the early stage of construction if the water flow rate exceeds 0.1 l/min (Suzuki et al., 2013, Börgesson and Sandén, 2006). In long term the highly conductive channels are expected to be sealed thanks to the swelling properties of bentonite. However, if for any reason these preferential pathways remains open the risk of erosion remains important also for the long term safety assessment.

3.5.1.1 *Is clay erosion possible upon gas injection?*

To the author knowledge, the phenomena of piping and erosion as a consequence of gas injection were never investigated before. However, in the work of Arnedo et al. (2008), in which the breakthrough phenomena in a 80/20 S/B mixture was investigated, it was found that when the gas penetrated the specimen pipes were form all along the cell-specimen interface, indicating that piping can occurs also as a consequence of gas penetration.

Microstructural observations carried in this study, on the 80/20 S/B mixture, shows that under condition of full saturation the bentonite gel that is filling the voids formed by the coarse fraction (sand) consists of 1nm elementary smectite sheet forming stacks of approximately 4 – 28 nm thickness depending on the mixture dry density and pore water salinity (see section 4.6.3.2). This will occur when the mixture is compacted to the lower dry density and wetted with distilled water.

Due to the important different in size between the macropores (approximately 100 μm depending on the dry density) and the size of the clay particles, stacks that are subjected to hydrodynamic and colloidal forces, maybe torn off, individually or in large

groups, and carried away by high water or gas flow, causing an internal erosion of the mixture.

In order to analyse the phenomenon of bentonite erosion induced by the gas flow, the triaxial apparatus is adapted for assessing the erosion phenomenon. This adaptation required a special filter (trap for bentonite particles) located in between the tested specimen and the water PV controller devoted to the application of the pore water pressure. This filter allows the visual observation of the turbidity of the outflow water.

To the author understanding, critical conditions can be expected when distilled water is flowing (used as saturating fluid) because repulsive force between particles are maximised and so is easy to displace single particle. As a consequence, the first assessment on this phenomenon will be addressed using distilled water as saturating fluid.

3.5.2 Results analyses

3.5.2.1 *Constant volume conditions*

Tests were performed on cylindrical specimens compacted to dry densities in the range 1.49 to 1.8 Mg/m^3. After saturation, and before starting the injection of gas, the specimens used for these experiments were used for the estimation of the water hydraulic conductivity of the mixture (section 2.5). The physical properties of the tested specimens are listed in Table 3.8.

Pre-humidified nitrogen (N_2) was injected from the top of the specimen with a gas PV controller at a constant flow rate of $1.67 \cdot 10^{-9}$ m^3/s; only for the specimen compacted to a dry density of 1.8 Mg/m^3 the gas injection was performed at the flow rate of $3.46 \cdot 10^{-9}$ m^3/g. At the bottom of the specimen, water was supplied at constant pressure with a PV controller. No apparent gas leakage was observed during the tests.

The results of all the gas breakthrough tests are presented in Figure 3.18. The increase of the gas pressure is observed with time. The breakthrough event is defined as the moment in which the gas pressure reaches its maximum and the downstream mixed flow rate has a sharp increase. The values of the gas pressure at the breakthrough event are also listed in Table 3.9. The breakthrough event occurs after about 40 to 70 hours from the beginning of the injections. At the constant flow rate, the time for the breakthrough seem to increase with the increase of dry density, in agreement with the results of Graham et al. (2002).

Once the breakthrough event has occurred, the gas pressure spontaneously decreases until the gas, which flows through the specimen, completely filled the water PV controller at the downstream. From this moment on, the controller can no longer accommodate more gas volume and the built-up of the downstream pressure is observed. At the same time, the upstream gas pressure increases.

The results show that the gas breakthrough always occurs at a pressure higher than the sum of the water pressure and the breakthrough pressure confirming the results already observed for other bentonite based materials (e.g., Horseman and Harrington, 1997, Villar et al., 2013).

The excess gas pressure (P_{break} - P_{w}) at the breakthrough is higher than the measured air entry value of the mixture. This would suggest that normal viscous two phase flow is occurring in the S/B mixture and that the gas penetration in S/B mixture would causes the specimen desaturation. To verify this hypothesis, the water content of specimens, at the end of the tests, was measured by hoven drying the specimens at 105 °C for 24 hours, and the degree of saturation was estimated from the specimen dry density. The measured degree of saturation of all the tested specimens results close to 1. This final result would suggest that the gas migration in the S/B mixture induces the fabric deformation, and thus path ways dilation, due to the very high deformability of the bentonite fraction.

Table 3.8: Physical properties of the tested specimens.

Specimen code	ρ_d [Mg/m^3]	e [-]	w_i [-]	S_r [-]	P_{sw} [kPa]	a.e.v. [kPa]
GB_1	1.49	0.79	0.11	0.37	71	50
GB_2	1.50	0.78	0.16	0.55	74	50
GB_3	1.59	0.68	0.12	0.47	103	-
GB_4	1.70	0.57	0.12	0.56	158	-
GB_5	1.80	0.48	0.11	0.51	230	100
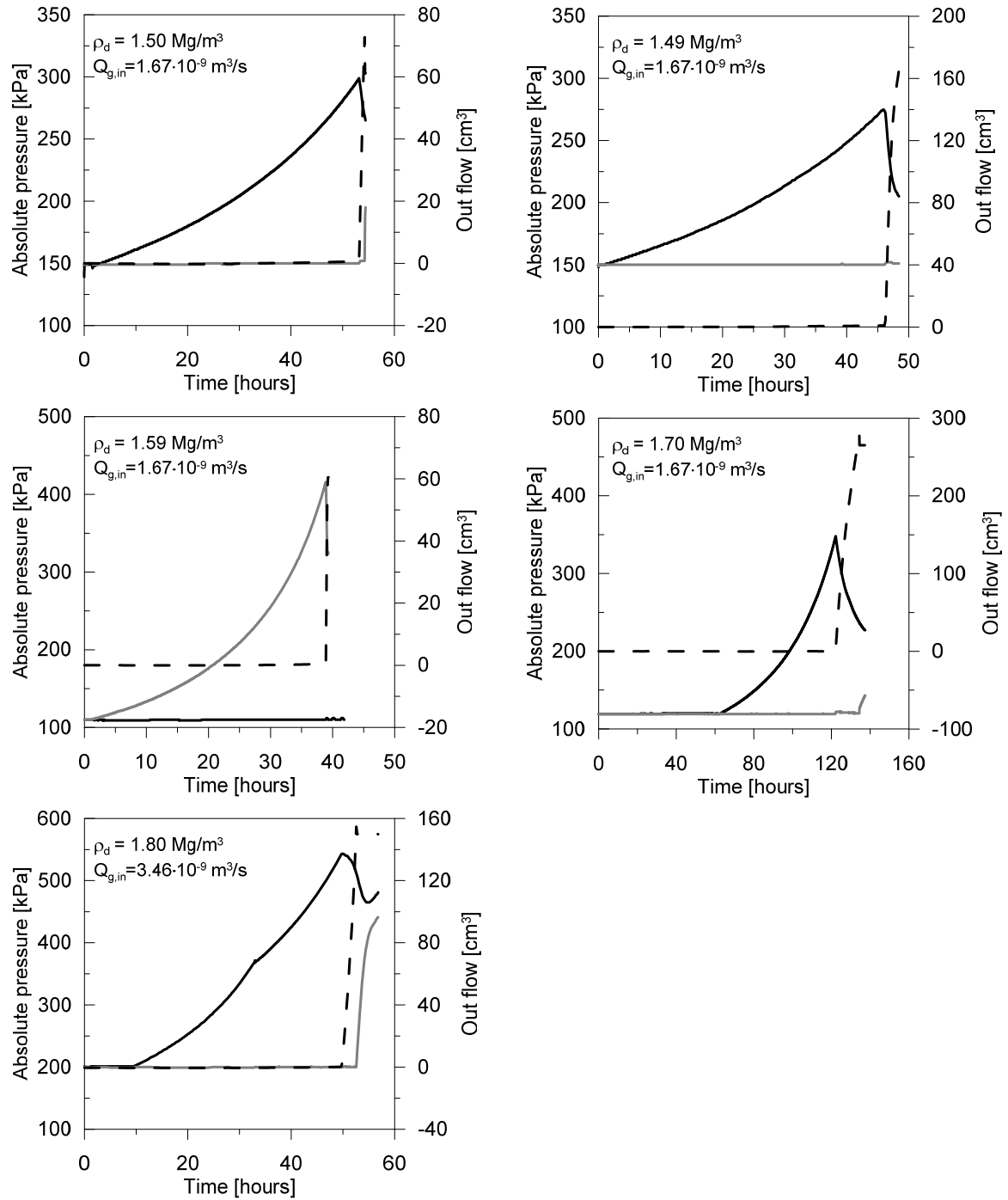
Figure 3.18: Results of the breakthrough tests on the 80/20 S/B mixture. Tests were performed under constant volume conditions and for different compaction densities.

Table 3.9: Results of the breakthrough tests.

Specimen code	P_w [kPa]	Q_g [m³/s]	$P_{g,break}$ [kPa]	$S^*_{r,fin}$ [kPa]
GB_1	150	$1.67 \cdot 10^{-9}$	299	0.96
GB_2	150	$1.67 \cdot 10^{-9}$	275	0.99
GB_3	110	$1.67 \cdot 10^{-9}$	416	>1.00
GB_4	120	$1.67 \cdot 10^{-9}$	348	0.97
GB_5	200	$3.46 \cdot 10^{-9}$	547	>1.00

[*]computed from the measurements of the final water content

3.5.2.2 Triaxial conditions

The tests under triaxial condition aimed at investigating the volumetric behaviour of the tested S/B mixture and the phenomena of clay erosion during the breakthrough event in order to provide evidenced on the possibility of the creation of pressure induced pathways.

Procedure

For this test, after the partially saturated S/B specimen ($S_r = 80\%$) was installed in the triaxial apparatus, a confining pressure of 250 kPa was applied. To complete the saturation of the specimen, the water pressure was applied at the top and bottom. Confining pressure and water pressure were raised simultaneously up 450 kPa and 250 kPa, respectively. To avoid any undesired swelling of the specimen during the final stage of the saturation, the difference between confining pressure and pore water pressure was always kept higher than swelling pressure of the specimen at full saturation, estimated knowing its dry density from eq. (2.9). Water saturation was assessed with the B-check Skempton method. A B-value of 0.95 was achieved. At the end of the saturation and B-check tests, the pore water pressure reached a valued of 465 kPa and the confining pressure reached a value of 670 kPa. Prior to start the gas injection, the confining pressure was further increased to 820 kPa and the ducts connected to the top cup were gas-flushed to remove all the water in the upstream conduits. A gas pressure of 465 kPa was applied on top of the specimen for two days. During this two days it was assessed that the volume of the gas PV controller was constant, proving that no-leak sources was present in the conduit. After this preliminary phase, a constant volumetric gas flux of $8.34 \cdot 10^{-10}$ m³/s was applied to the top of the specimen while the water pressure at the bottom was maintained constant.

During the gas injection, it was necessary to increase the confining pressure up to 1150 kPa to avoid the preferential flow of the gas in the specimen/membrane interface.

The volumetric behaviour was investigated following the evolution of the axial displacements, thanks to the LVDT installed in the axial loading system, and the variation of radius along the height, thanks to the three lasers installed outside the triaxial cell.

To monitor the clay erosion during the gas injection, the interface cell (described in section 2.5.1.1) was installed along the water injection line. Is this setup, the clean chamber (made of Plexiglas) of the interface was connected to the bottom of the specimen and the dirty chamber (made of stainless steel) was connected to the water PV-controller. The advantage of using the interface cell is that it allows collecting the water, which is pushed out from the specimen during the gas injection, in a relatively small volume (max 200 cm^3) and it also allow a visual observation of the turbidity of this water, giving a first assessment of the clay erosion. The water collected in the interface cell, was transferred in small glass cups. These cups where then placed in the oven at 105 °C to allow water evaporation. The caps were weighted before and after oven drying with a precision balance which has an accuracy of ±0.0001 g to measure the amount of eroded clay.

Because the two chambers of the interface are equipped with a 3-ways valve, it was possible to periodically empty the clean chamber every time that it was fully filled with gas without altering the pressure at the bottom of the specimen. This allowed the gas pressure to spontaneously decay after the breakthrough events, and avoid the increase of the pressure at the bottom of the specimen.

Results

The results of the tests performed on the specimen initially compacted to 1.79 Mg/m^3 are presented in Figure 3.19 and Figure 3.20. During the gas injection, the relative gas pressure increases up to a critical pressure of 1038 kPa (1138 kPa of absolute pressure) because of the isothermal compression of the mass of the gas stored in the upstream gas PV-controller. The excess gas pressure ($P_g - P_w$) equals the swelling pressure at the time step t_1. At this moment, no outflow at the downstream is detected. When the gas pressure reaches 850 kPa ($t = t_2$) the water outflow increases up to a value of $1.74 \cdot 10^{-11}$ m^3/sec. This value is smaller than the volume of gas which is injected at the top of the specimen suggesting that the gas is probably displacing some water from the larger pores of the mixtures but did not yet established its own preferential path to reach the bottom of the specimen. As a consequence, this value of gas pressure is acknowledged as the gas pressure at the entry (Horseman et al., 1996b, Harrington and Horseman, 2003). From this moment, and up to $t = t_3$, most of the emerged flux consists of water. The total volume of water expelled from the specimen during this time frame was approximately 2.5 cm^3, which corresponds to a reduction of the degree of saturation of the specimen the specimen of 1.6 %.

When the gas pressure reaches its maximum value ($t = t_3$), a very fast increasing of the outflow is observed. This result indicates that the gas has finally established its own tortuous paths until the bottom of the specimen.

The mass flux of gas at the upstream and the downstream is calculated after the breakthrough event as follows:

$$M_{N_2} = m_g n \frac{RT}{P} \tag{3.40}$$

with m_g the molar gas of nitrogen, considered dry for simplicity.

Observing the results in Figure 3.19, it is noticed that the mass flux which exits from the specimen is higher that the mass of gas that is injected at the top of the specimen suggesting that some water/clays is displaced during the gas injection.

After the breakthrough event, the gas pressure at the upstream spontaneously decreases until a stationary value of approximately 750 kPa, suggesting that this gas pressure is sufficient to maintain open and stable gas-pathways through the specimen when the gas injection pump-rate is maintained constant.

The evolution of the radius of the specimen during of the test is reported in Figure 3.20. The radial, axial and volumetric deformations of the specimen are presented in Figure 3.21 along with the variation of the specimen void ratio. The preparatory phase of the test (saturation phase) causes a reduction of the specimen volume because the applied confining pressure was slilty higher than the swelling pressure. During the phase of gas pressure increase, the specimen does not exhibit significant volumetric deformations. After the peak pressure, a reduction of the specimen volume is observed probably as a consequence of the coupled effect of the reduction of the gas pressure and the effect of the high confining pressure.

The presence of clay eroded during the process of gas migration through preferential flow path is documented in Figure 3.22. The figure shows one of the cups in which was collected the water expelled from the specimen during the gas injection phase. Some fine clay is clearly visible. Approximately, 0.1739 g of fine was collected during the gas injection test; corresponding to 0.02% of the total dry mass of the specimen (equal to 816.63 g). This result suggests that the transport of fine particles during the gas injection is possible in S/B mixture at low bentonite content and that this experimental setup allowed collecting evidences on this issue.

At the end of the test, a water content of 0.18 was measured which correspond to a degree of saturation of 1.10. This high degree of saturation (>1) indicates that a certain amount of the pore water is stored in the interlayer of smectite. This water, for MX-80 bentonite has a density which varies between 1.14 Mg/m^3 and 1.32 Mg/m^3 depending on the number of water molecules stored in the interlayer (Jacinto et al., 2012). Because the density of the water is higher in the interlayer, the calculation of the degree of saturation assuming $\rho_w = 1$ leads to its overestimation (Jacinto et al., 2012).
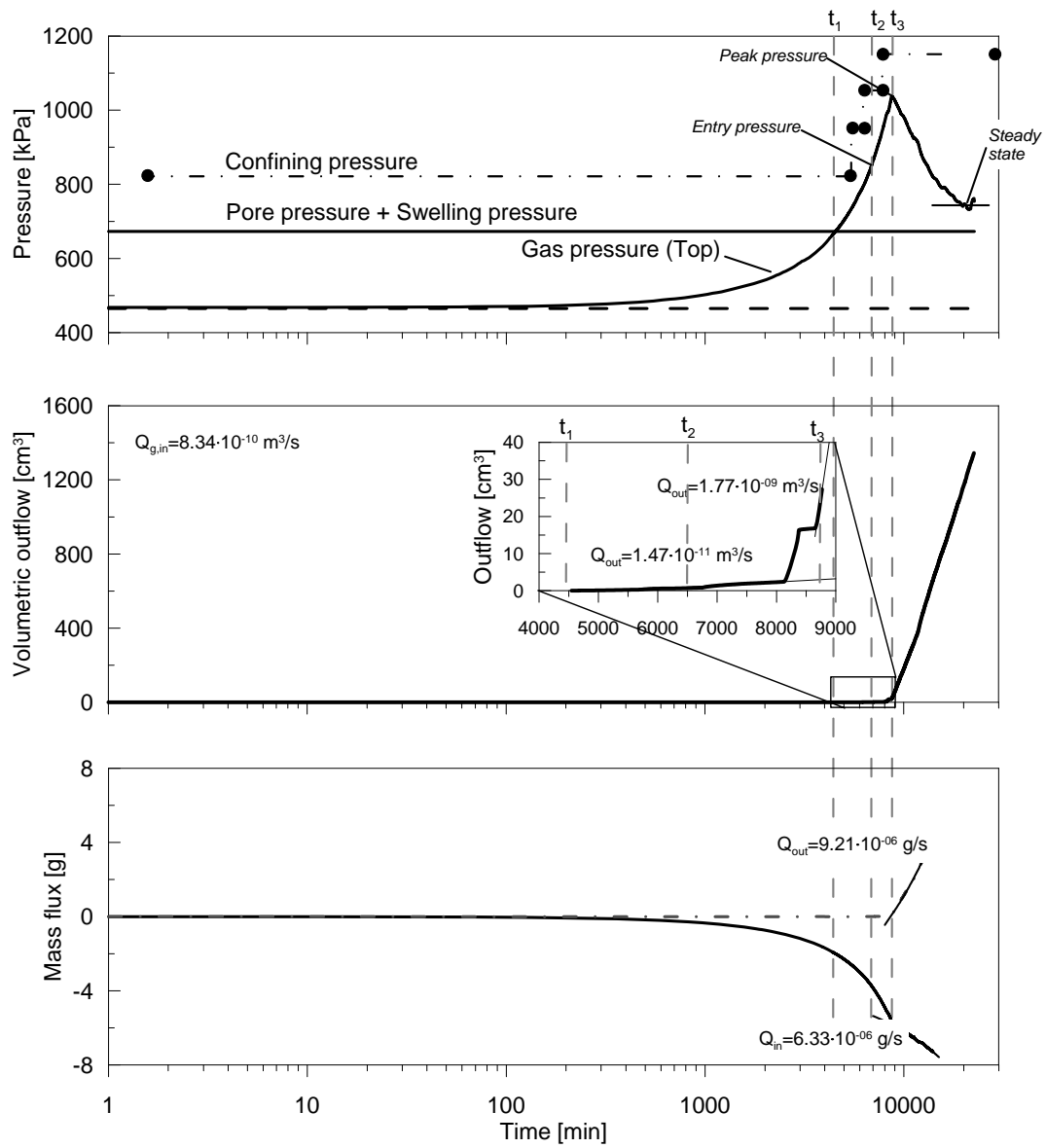
Figure 3.19: Results of the breakthrough tests on an 80/20 S/B mixture compacted to 1.8 Mg/m³. From top to bottom: evolution of the gas pressure, confining pressure and pore water pressure and evolution of the measured outflow.
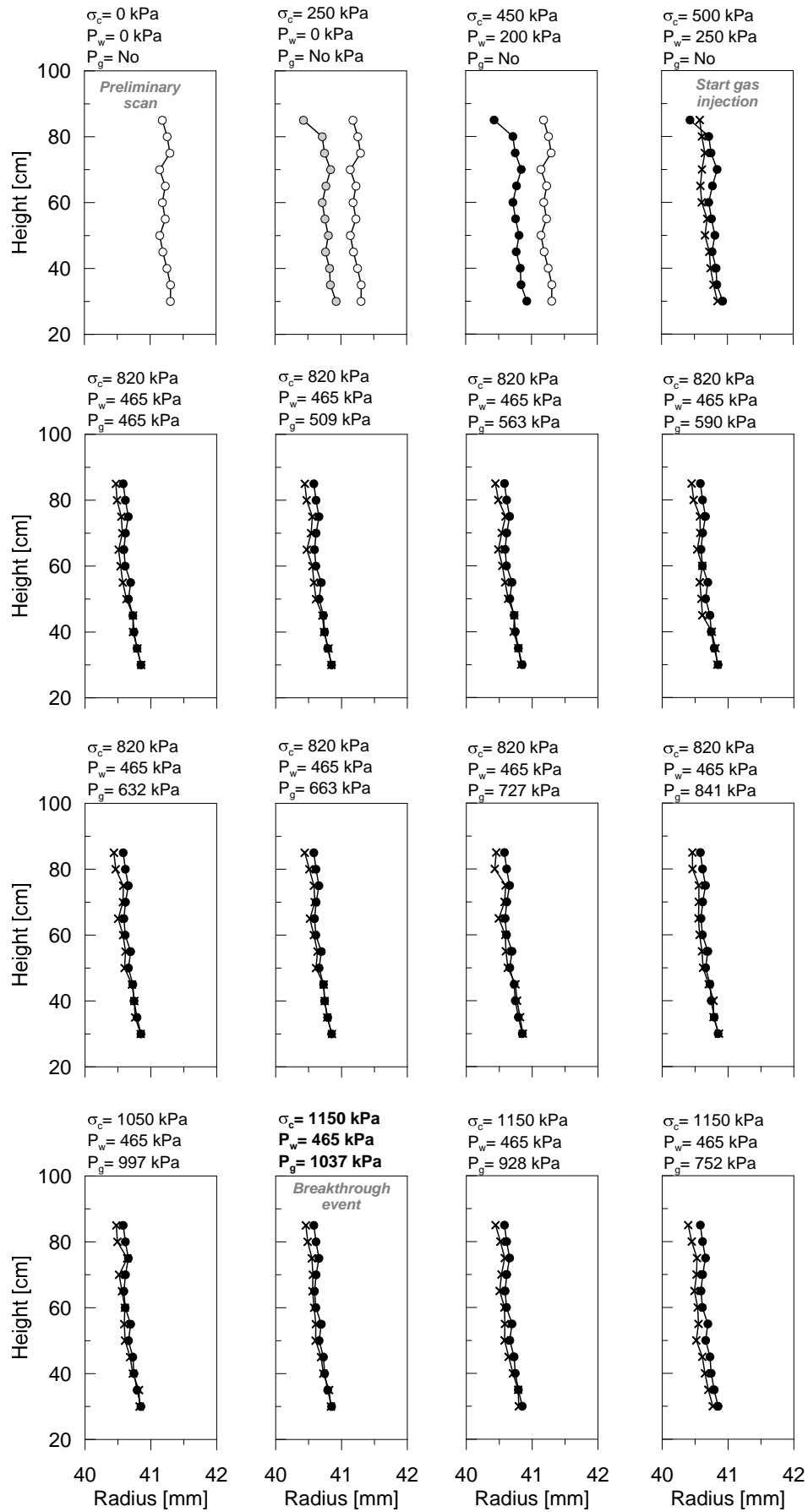
Figure 3.20: Evolution of the specimen radius along the specimen's height at different gas pressure.

113
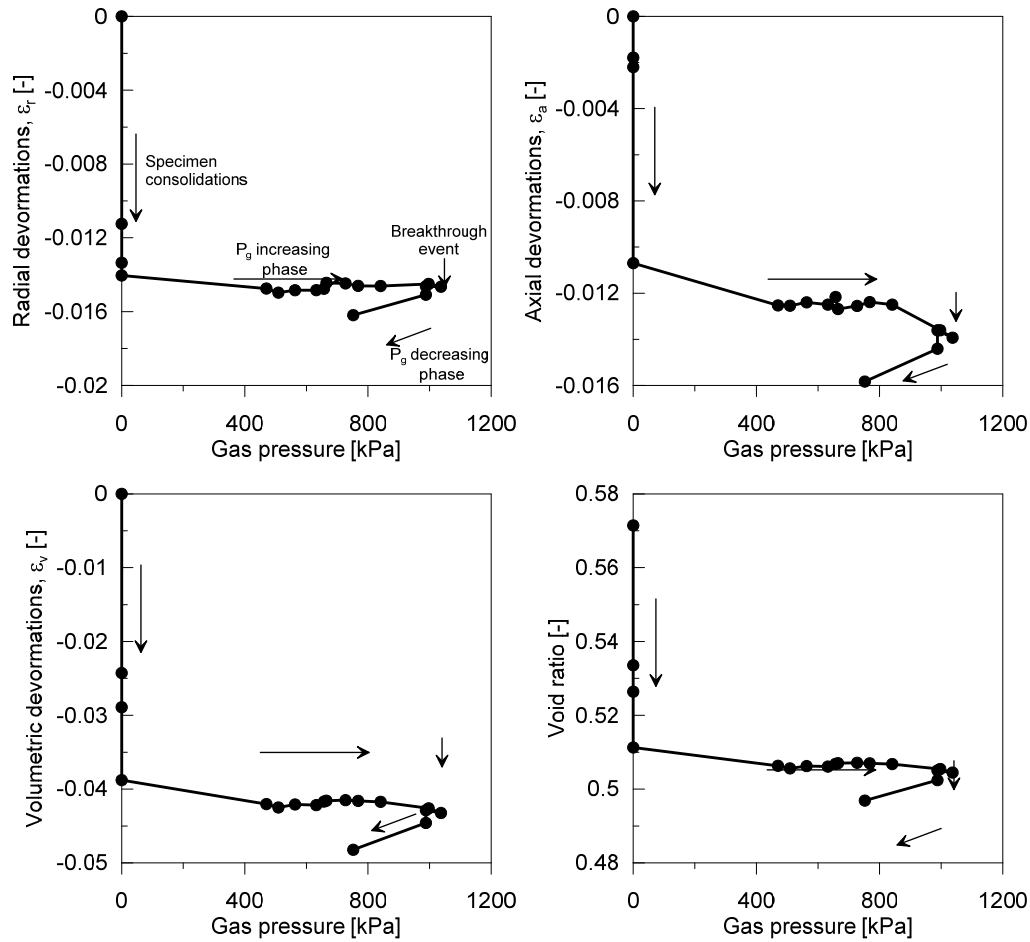
Figure 3.21: Evolution of the radial, axial and volumetric deformations and the void ratio during the gas injection process.
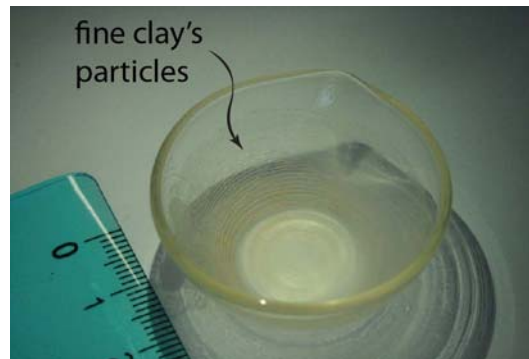
Figure 3.22: Eroded mass during the gas injection test under constant volume conditions.

3.5.3 Process understanding

The results presented in the previous section show that the breakthrough pressure (peak pressure) results always higher than the sum of the swelling pressure and the pore water pressure, regardless the dry density or the boundary conditions. The water displacement associated to the normal mechanism of two phase flow seems not possible when the fully saturated clays are subjected to a fast increase of gas injection pressure.

114

Indeed, this mechanism implies the global desaturation of the specimen subjected to a given imposed matric suction ($P_g - P_w$) and the consequent volume reduction (shrinkage) of the specimen during gas injection. In our experiments, the volume of the specimen remains practically constant during the phase of pressure increasing and the degree of saturation measured post mortem results always close or, in some cases, higher than 1.

The results presented in section 3.5.1 showed that the critical pressure is considerably higher than the sum of the swelling pressure and the pore water pressure and confirm the results observed in case of gas injection under constant volume conditions (e.g., Harrington and Horseman, 2003, Villar et al., 2013). However, the peak breakthrough pressure obtained under isotropic confinement is much higher than the one obtained under constant volume conditions. In order to better understand this result, the magnitude of the gas breakthrough pressure is compared with the magnitude of the total stress in the two different experimental setups. This comparison is also made for all the experimental data collected for bentonite-based material by other Authors (Table 3.9). For soils containing active clays, and in case of the test performed under isochoric conditions, the total stress is equal to the sum of the swelling pressure and the water pore pressure (Horseman et al., 1996b):

$$\sigma = P_{sw} + P_w \tag{3.41}$$

whereas, in case of test performed under triaxial conditions, the total stress coincides with the applied confining pressure:

$$\sigma = \sigma_c \tag{3.42}$$

In Table 3.10 are reported the values of the swelling pressure, pore water pressure, total stress, gas breakthrough pressure (peak pressure) which are collected from literature and from the tests performed in this thesis. In the table, the abbreviation CV refers to constant volume conditions, IC refers to isotropic confinement, and K0 refers to the radially confined specimen. The ratio of the peak pressure to the total stress is calculated for each of the tests.

The results of the test carried out under triaxial conditions suggest that the breakthrough in S/B mixture occurs when the gas pressure equals the total stress. When the tests are carried out under constant volume conditions, regardless the type of the percentage of bentonite used, or the dry density, the peak pressure results between 1.5 and 7 times the total stress. Only in some cases the gas breakthrough pressure results lower than the total stress (e.g., Pusch and Carlsson, 1985, Liu, 2013). However, the specimen tested by Liu (2013) were not fully saturated.

The analyses suggest that, in bentonite-base materials, as soon as the gas penetrates the material, the gas pressure act as a total stress on the clay matrix. Because the process of gas injection occurred very fast, e.g., gas was injected at high flow rate, the gas does not have the time to displace the pore water stored in the material. As a consequence, the

pore water pressure in the preferential path would rapidly increase of a quantity equals to the gas pressure minus the sum of the swelling pressure and the neutral pore pressure. From the moment of the breakthrough, the water will start to flow out to release the excess pore water pressure causing consolidation of the fully saturated bentonite, with the consequent enlargement of the preferential flow path and the decrease of the gas pressure.

Table 3.10: Results of the breakthrough tests on several types of bentonite-based materials.

Material	P_{sw} [MPa]	P_w [MPa]	P_g [MPa]	σ [MPa]	Boundary conditions	Reference	P_g/σ	Comments
MX80	26	0	5	26	CV		0.19	-
MX80	18	0	5	18	CV		0.28	-
MX80	1.8	0	1.6	1.8	CV		0.89	-
MX80	2.7	3.4	5.8	6.1	CV	Pusch et al. (1985)	1.51	-
MX80	1.5	0	3.2	1.5	CV		2.13	-
MX80	40	0	21	40	CV		0.53	-
MX80	27.5	0	11	27.5	CV		0.40	-
MX80	35	0	19	35	CV		0.54	-
MX80	6.15	1.01	15.19	16	IC	Horseman et al. (1996a)	1.01	-
80/20 S/B	0.16	0	1.876	0.16	CV	Arnedo et al. (2008)	12.04	Localised injection
30/70 S/B	7.16	0	7.1	7.16	IC		0.99	-
30/70 S/B	7.39	0	8.1	7.39	IC		1.10	-
30/70 S/B	6.86	0	2.16	6.86	IC		0.31	Unsaturated specimen
30/70 S/B	6.93	0	2.5	6.93	IC		0.36	Unsaturated specimen
30/70 S/B	4.8	0	2.49	4.8	IC	Liu (2013)	0.52	Unsaturated specimen
30/70 S/B	7.88	0	8.53	7.88	IC		1.08	Second breakthrough after re-saturation
30/70 S/B	7.4	0	9.8	7.4	IC		1.32	Second breakthrough after re-saturation
30/70 S/B	7.05	0	8.5	7.05	IC		1.21	-
MX-80	4.80	1	19.40	5.80	CV		3.52	An increase of total stress was observed
MX-80	4.62	1	9.90	10.00	K0	Harrington and Horseman (2003)	1.09	radial confined - free axial
MX-80	4.89	1	13.00	5.89	CV		2.38	An increase of total stress was observed
Febex	2.58	0	7.10	2.58	CV		2.75	-
Febex	2.77	0	7.50	2.77	CV		2.71	Second breakthrough after re-saturation
Febex	3.17	0	9.10	3.17	CV		2.87	-
Febex	3.17	0	7.00	3.17	CV		2.21	Second breakthrough after re-saturation
Febex	1.15	0	1.00	1.15	CV	Villar et al. (2013)	0.87	-
Febex	1.15	0	2.90	1.15	CV		2.53	Second breakthrough after re-saturation
Febex	1.72	0	5.20	1.72	CV		3.02	-
Febex	2.26	0	6.60	2.26	CV		2.92	Second breakthrough after re-saturation
80/20 S/B	0.07	0.15	0.30	0.22	CV		2.05	-
80/20 S/B	0.07	0.15	0.28	0.22	CV		1.95	-
80/20 S/B	0.10	0.11	0.42	0.21	CV	**This study**	2.52	-
80/20 S/B	0.15	0.12	0.35	0.27	CV		1.74	-
80/20 S/B	0.23	0.20	0.55	0.43	CV		1.74	-
80/20 S/B	0.23	0.46	1.14	1.25	TX		1.28	-

3.6 SUMMARY AND CONCLUSIONS

This chapter investigated the mechanism of gas transport through the selected S/B mixture, under condition of partial saturation and under condition of fully saturation.

From this characterisation the following achievements are highlighted:

Two methods to perform the gas injection tests were investigated, the constant volume condition tests and the controlled confining pressure tests. The tests, under constant confining pressure required the use of a triaxial apparatus which allowed monitoring the radial deformation of the specimens under unsaturated conditions. A laser scanning system was used for this purpose.

The results revealed that the method for preparing the specimen for testing under constant volume conditions would not allow reaching the moisture equilibrium, leading to obtain values of gas permeability lower than under triaxial conditions. Only one test conducted under constant volume conditions showed good moisture redistributions. The gas permeability measured with this specimen was in good agreement with the results obtained under triaxial conditions suggesting that, combination of the use of a ring with threatened walls and the generation of swelling pressure sealed the preferential flow paths which may occur at the ring-specimen interphase.

The Klinkenberg effect was accounted in the interpretation of the gas permeability tests. Despite the low pressure applied to the specimen during the gas permeability tests, this effect results negligible because of the presence of large macropores in the unsaturated mixture.

The gas permeability of the S/B mixture is independent from the compaction density in the involved range.

The breakthrough phenomenon was investigated under isochoric conditions and under triaxial conditions. The results suggest that some preferential flow paths are created during the breakthrough event. The gas passage occurred at a gas pressure which was always higher than the air entry value of the mixture. Nevertheless, any appreciable reduction of the degree of saturation occurred during the time frame of the test.

The possibility of clay transport as a consequence of the gas flow was investigated. The results revealed that a very small amount of fines was washed away during one gas tests.

4   Characterisation of the pore space morphology of the sand/bentonite and related macroscopic behaviour

4.1 INTRODUCTION

Hydro-chemo-mechanical properties of clayey soils are strongly dependent on the chemical and physical interaction between their different components (solid, liquid, and gas) and the morphology of the pore network.

In order to understand well the phenomena governing the swelling properties of the mixture as well as its transport capacity both in term of water and gas transport a broad microscopic investigation is performed.

The first part of this chapter is devoted to the definition of structure and fabric of clay minerals with a focus on the family of smectite minerals, which are the main component of the MX-80 bentonite. Then, the interaction between water and clay particles, and the effect of the hydro-chemo-mechanical loadings at the particle level are described.

The second part of the chapter presents the results of the microstructural investigation of the tested material. This study is carried out using a combination of two experimental techniques: Mercury Intrusion Porosimetry (MIP) for a quantitative analysis and, high resolution scanning electron microscopy (SEM) for a qualitative analysis. The MIP tests were carried out at the laboratory of construction material (LMC) whereas the SEM observations were performed in the interdisciplinary centre of electron microscopy (CIME), both located at the EPFL.

Finally, the macroscopic response of the tested mixture, and more generally of bentonite-based materials, subjected to different hydro-chemo-mechanical loadings is discussed. These analyses take into account the coupling phenomena occurring at the microscopic level, which are fundamental for describing the HCM behaviour of the material at the macroscopic level.

4.2 SMECTITE CLAYS: STRUCTURE, WATER INTERACTION AND SWELLING MECHANISMS

The smectite mineral (more specifically montmorillonite) is the dominant mineral in MX-80 granular bentonite used in the S/B mixture. This mineral, as all the clay minerals, belongs to the family of phyllosilicates which are made up of two simple structural units: the silicon tetrahedron (silicate sheet) and the aluminium or magnesium octahedron (Gibbsite or Brucite sheet) sheet. The basic crystalline unit cell of smectite consists of two tetrahedral silica sheets bonded together to an octahedral sheet (TOT unit). The TOT smectite unit cell has a dimension $a \times b \times c$ = 0.516×0.898×0.94 nm^3 (Figure 4.1-right). Basic units are connected together along the a and b-axis to form a single smectite sheet. The smectite sheet has a size equal to:

$$\left(a \times n_a\right) \cdot \left(b \times n_b\right) \tag{3.43}$$

with n_a and n_b being the number of TOT unit repeated along the a and b-axis, respectively. Smectite sheets are then staked together along the c-axis to form the so called smectite quasicrystal. In dry condition the bonding between elementary layers (smectite sheets) is provided by van der Waals forces and by the presence of exchangeable cations (Mitchell and Soga, 2005). The types of exchangeable cations that are more often found in montmorillonite are Na, Ca, Mg and K (Pusch et al., 1990). These cations have different affinity with clay particles and, depending on the affinity, they can replace each other. They can also be arranged in a series in term of their affinity with the clay as follows (Das, 2008):

$$Ca^{2+} > Mg^{2+} > K^+ > Na^+$$

Figure 4.1 (left) shows a high resolution transmission electron micrograph (HR-TEM) of smectite quasicrystals. The image was taken on a slice of 50 nm thickness of hydrated MX-80 bentonite by Tessier et al. (1992). In the figure, the quasicrystals appear of different thicknesses. They are mostly organised in face-to-face arrangement, but also the edge-to-face arrangement can be observed. In some cases quasicrystals tend to overlap suggesting that the smectite sheets are randomly staked. Thin quasicrystals appear curved suggesting a certain flexibility of these structural units (Laird, 2006).

Typically, a smectite flake has a diameter of about 50-200 nm (Pusch, 2001a) so that n_a and n_b are close to 200. In compacted bentonite-based materials the number of sheets per quasicrystals depends on several variables such as the type of exchangeable cations in the interlayer, water content and compaction state. Figure 4.2 illustrates a saturated and strongly compressed pellet of MX-80 taken by Pusch et al. (2003). In the picture quasicrystal are organised together mostly in a face-to-face arrangement forming bigger bentonite aggregates.
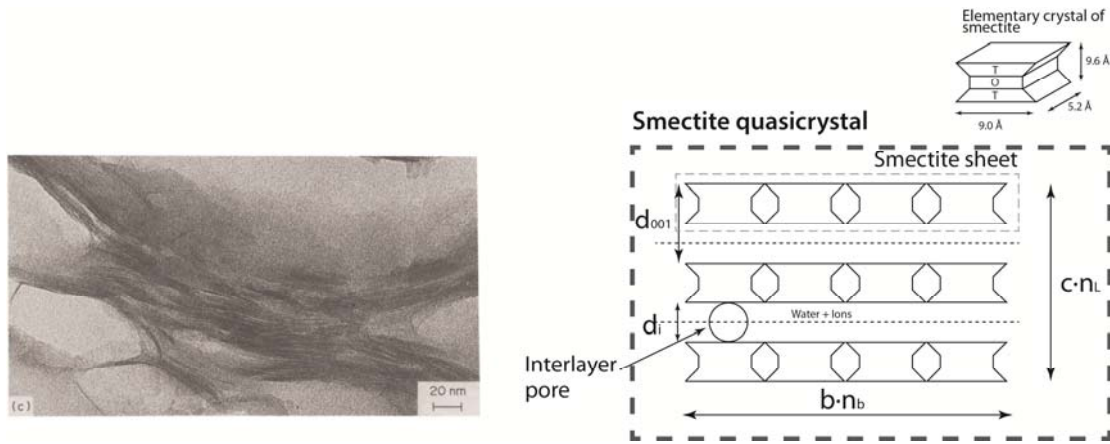
Figure 4.1: TEM observation of smectite quasicrystals at high magnification (left) (Tessier et al., 1992). Schematic representation of one smectite quasicrystal and the elementary crystal of smectite (right).

Knowing the dimensions of the smectite quasicrystals, the total specific area (S_s) and the external area (A_{ext}) of the quasicrystals can be calculated as (Tournassat and Appelo, 2011):

$$S_s = 2ab \frac{N_A}{MW} \tag{4.1}$$

$$A_{ext} = \frac{2ab}{n_c} \frac{N_A}{MW} \tag{4.2}$$

where N_A =6.022·10^{23} (molecules/mol) is the Avogadro's number and MW is the molecular weight of montmorillonite (equal to 733 g/mol).

Total specific area of 523 m^2/g and external area of 33.1 m^2/g of the MX-80 bentonite were measured by Plötze and Weber (2007a). Measurements of the external surface were carried out on the bentonite at the 16.9 % of water content and were determined using the BET method (nitrogen adsorption). Under these conditions, the average number of sheets per particle, calculated as the ratio of the total specific surface to the external specific surface (Agus and Schanz, 2008b), results equal to 15.
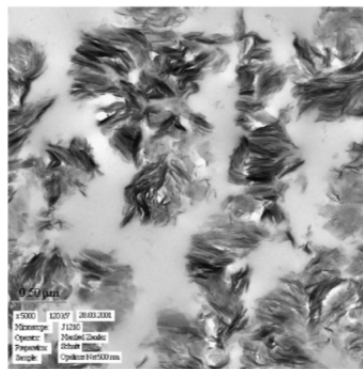
Figure 4.2: TEM photomicrograph taken on a strongly compressed MX-80 bentonite pellet; density at saturation of 1.75 Mg/m³ (Pusch et al., 2003).

4.2.1 Water and clay interaction

Four typical mechanisms characterise the clay water interaction at the particle level (Mitchell and Soga, 2005):

- Hydration of the exchangeable cations: because water is a permanent dipole is attracted by the exchangeable cations which can be located in the interlayer space or in the clay surface.
- Attraction by osmosis: cations concentration tends to be higher in the proximity of the negatively charged quasicrystal surface. In a clay-electrolyte environment water molecules tend to diffuse from a zone of low salt concentration to a zone of higher salt concentration.
- Charged surface-dipole attraction: in a similar way of the hydration of exchangeable cation the positive pole of the water dipole is attracted to the negatively charged clay surface to neutralise the charge.
- Attraction by London dispersions forces: van der Waals attractive forces that can bond water molecules to clay surface.

The nature of these interactions, together with the size of the pores, is generally considered for classifying the water in clayey soils (Hueckel, 1992, Romero, 1999) (Figure 4.3). Interlayer water consists of a mixture of exchangeable cations and water molecules which are strongly bonded to the silica surface (Pusch and Carlsson, 1985). In the case of Na-bentonite the maximum number of water molecules that can be allocated in the interlayer is four (Saiyouri et al., 1998, Bestel, 2014); however, this number may reduce if other exchangeable cations are present in the interlayer (Pusch, 2001b). Water in the diffuse double layer consists of a mixture of exchangeable cations, ions, and water molecules located on the surface of quasicrystals. This layer forms a transition zone between the clay surface and the free pore water. The remaining water consists of a charge balance solutions located far enough from the negative charged silica surface and is classified as bulk or free water. Interlayer water, together with the double layer water, can be considered as a quasi-immobile fraction of the total pore water whereas the free water can flow due to hydraulic gradient at ambient temperature (Hueckel, 1992, Romero, 1999).
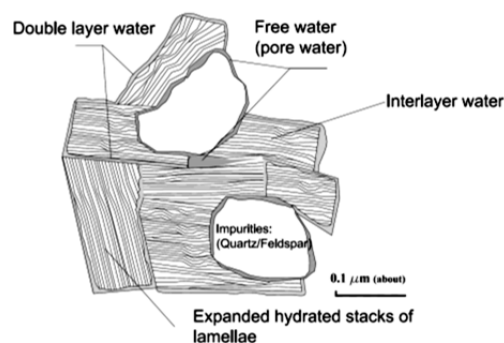
Figure 4.3: Schematic representation of an aggregate of clay for the visualisation of the interlayer water, double layer water and free water.

The state of water in compacted bentonite and the ratio of the free water to the quasi-immobile water depend on factors such as compaction state, hydration level, and chemistry of the pore fluid.

Pusch and Carlsson (1985) and Dixon (2000) discussed the influence of the clay dry density on the ratio of interlayer water to diffuse double layer concluding that at high dry density clay particles are so close that most of the water will be stored in the interlayers. The reduction of the dry density will produce separation and the reorientation of the clay particles so that diffuse double layer can develop. At very low dry density, water that is far enough from the clay surface will be likely in the "free" state. Pusch et al. (1990) estimated that under condition of full saturation, for a clay density lower than 1 Mg/m^3 the percentage of interlayer water is lower than 50 % of the total water stored in the specimen.

Information on the water localisation as a function of suction are given by Saiyouri et al. (1998). The authors analysed the hydration mechanism of two compacted bentonite (FoCa7 and MX-80) and showed that at suction higher than 10 MPa water is present only between the smectite sheets and there is nearly no external water. The amount of external water increases for low applied suction.

Regarding the effect of the chemistry of the pore water, according to the double layer theory, in a clay-electrolyte system the thickness of the electrostatic double layer water (d) covering a clay quasicrystal is a function of the electrolyte concentration and the valence of the ions (Mitchell and Soga, 2005):

$$d = \sqrt{\frac{\varepsilon_0 D \kappa T}{2 n_0 e^2 v^2}} \qquad (4.3)$$

with ε_0 the permittivity of vacuum (8.8542×10^{-12} C^2/J m), D ($\varepsilon = \varepsilon_0 D$) the dielectric constant of the medium, κ the Boltzmann's constant (1.38×10^{-23} J K^{-1}), e the electronic charge, n_0 the electrolyte concentration, T the temperature, v the cation valence. Electrostatic double layer can go up to 200 Å in distilled water; its thickness tends to reduce when increasing salt concentration in the bulk solution and the valence of the exchangeable cation. When the concentration of salts in the free water exceeds 1 M the thickness of the EDL reaches 3 Å (Tournassat and Appelo, 2011). In this sense, it is possible to conclude that the compression of the diffuse double layer will be reflected in an increase of the ratio of the free water to the total pore water.

4.2.2 Swelling mechanisms of smectite clays

Laird (2006) stated that six separate processes act simultaneously to promote the swelling of smectites in aqueous solutions, as follows: crystalline swelling, double-layer swelling, breakup or formation of quasicrystals, cations demixing, co-volume swelling and Brownian swelling. Among them, crystalline swelling, double layer swelling,

breakup of the quasicrystals, and cations demixing seem to be the dominant mechanisms in the swelling process (Suzuki et al., 2005, Laird, 2006). Co-volume swelling and Brownian swelling are more important in highly disperse solutions and will not be discussed in this context.

The crystalline swelling is a hysteretic and discrete process related to the progressive placement of layers of water molecules within the smectite sheets for neutralising the negative charge arising from isomorphous substitution in the crystal lattice. As a consequence of crystalline swelling, the distance between each smectite sheet along the c-axis (interlayer distance, d_i in Figure 4.4) varies with the progressive hydration of the bentonite from a minimum of 3 Å to a maximum of 12 Å, depending on the hydration level, the chemical potential, and type of exchangeable cations in the interlayers (Quirk et al., 1986, Pusch et al., 1990, Saiyouri et al., 1998, Tuller and Or, 2003). Analysis of this hydration mechanism showed that the number of layers of water molecules varies from a minimum of 0-1 layer at the hygroscopic water content to a maximum of 4 layers at the water content of ~30 %. After that, the interlayer distance remains fixed (Bestel, 2014). Crystalline swelling is controlled by the balance between the forces of (electrostatic) attraction that arise from the attraction between the negatively charged clay surface and the positively interlayer charged cations, and repulsion forces acting between the sheets surface that comes from the partial hydration potential energy of the interlayer cations. Crystalline swelling can be contrasted by increasing the dry density of a specimen. Pusch et al. (2003) observed that during wetting under constant volume of a highly compacted MX-80 bentonite the high compaction density helped the quasicrystal to resist to full expansion.

The double layer swelling occurs between the quasicrystals for neutralising the remaining negative charge on their external surface. Negative charge on the external surface is lower than the internal one so that the exchangeable cations are weakly bonded to the surface and they can diffuse from a region of high concentration (near the surface) to a region of lower concentration (Laird, 2006). Nevertheless, some cations are tightly held on the clay surface and create the so called Stern layer (which has approximately the thickness of the diameter of a hydrated cation).

The breakup of the quasicrystals occurs when additional water layers have the possibility to enter in the quasicrystals so that the basal spacing (d_{001} in Figure 4.4) becomes larger than 2.16 nm ($d_i > 1.2$ nm) and the diffuse double layer can fully develop. As a consequence of this last mechanism, the number of smectite sheets forming a quasicrystal reduces during water up-taking and varies from a maximum of 360 at a 60 MPa total suction to less than 10 at 3 MPa total suction (Saiyouri et al., 1998, Saiyouri et al., 2004). This mechanism of particles breakdown is strongly reduced for NaCl concentration higher than 0.3 mol/l (Suzuki et al., 2005). Under certain environmental conditions, e.g. bentonite hydrated under free volume conditions with distilled water or with a dilute electrolyte solutions, quasicrystals of low-charge Na-smectite can spontaneously break-up into individual layers. Conversely, some quasicrystals of high-

124

charge Na-smectite will remain intact, although most of them will breakup (Laird, 2006). Quasicrystals have also the possibility to fuse together if their kinetic energy is sufficient to overcome the repulsive forces arising from the diffuse double layer and enough exchangeable cations and water molecule are expulsed from the region between quasicrystals (Laird, 2006).

Cation demixing phenomenon is related to the preference of smectite for different type of cations that can be present in the aqueous smectite system. This affects both the crystalline swelling and the breakup of quasicrystals. However, crystalline swelling affects cation demixing (Laird, 2006).

The different swelling mechanisms illustrated in this section have different importance depending on the hydro-chemo-mechanical loadings applied to the tested material. In the last part of this chapter the macroscopic behaviour of the S/B mixture will be discussed in light of these swelling mechanisms.

4.3 SAND/BENTONITE MIXTURES: MICROSTRUCTURE AND IDENTIFICATION OF THE DIFFERENT PORE FAMILIES

Natural or engineered soils consist of a mixture of solid particles, water and air. The arrangement of solid particles is forming the solid skeleton. The term *"structure"* for a soil refers to the arrangement of the particles and pore space.

Structured soils compacted to the dry side of the optimum water content, which are composed of one main solid fraction, typically present an aggregated fabric, and their pore structure is characterised by bi-modal or multimodal distributions (e.g., Delage et al., 1996, Cuisinier and Laloui, 2004, Airò Farulla et al., 2010b, Koliji et al., 2010b). For these soils, the term micro-porosity refers to the intra-aggregate pores, whereas the term macro-porosity refers to the inter-aggregate pores.

Because of the presence of two solid fractions, sand grains and bentonite assemblages, the pore structure of the S/B mixture requires its own definitions. The schematic representation of a mixture at low bentonite content with its different structural levels is presented in Figure 4.4. Macro-pores refer to the pores between the sand particles and the bentonite assemblage. Bentonite assemblages (or aggregate) are an aggregation of smectite quasicrystals and some impurities. A smectite quasicrystal (or stack) is an element composed of elementary negatively charged smectite sheets that are stacked in the direction of the c-axis. In this study, all of the pores belonging to the bentonite assemblage are called bentonite pores. The bentonite pores can be further divided into micro-pores, referring to the pores between the quasicrystals of smectite and the inter-layer pores (or intra-quasicrystal pores), which are the pores between the smectite sheets within a quasicrystal.

From these definitions, the total void ratio (e) can be written as follows:

$$e = e^M + e^b \qquad (4.4)$$

where e^M is the macrostructural void ratio, e^b and is the void ratio of the bentonite assemblages, which is then expressed as follows:

$$e^b = e^m + e^i \qquad (4.5)$$

with e^m the microstructural void ratio, and e^i the interlayer void ratio.

In this study, a threshold value of $x_t = 5$ μm is used to delimit the macropore region from the bentonite pore region. Further clarifications for the selection of this limit are provided in section 4.6.1.

Due to the pressure limitation of the MIP apparatus, the interlayer pores and micropores smaller than 4 nm cannot be intruded by mercury. However, for the specific case of active clays, these pores can be computed from the MIP data as the total void ratio minus the intruded void ratio (Lloret et al., 2003, Delage et al., 2006, Nowamooz and Masrouri, 2009, Seiphoori et al., 2014).

Because of the presence of bentonite, the morphology of mixture pore system can be influenced by parameters such as the mixing ratio, the grain size distribution of the bentonite and water content, among other parameters. At low bentonite content, sands grain are in contact and form a skeleton in which the bentonite assemblages are located. With the increasing of bentonite content, the sand grains are floating in the clay matrix (Viola et al., 2005). SEM observations on simulated S/B mixtures evidenced that when the mixture is prepared with powdered bentonite the simulated sand (made of glass beats) results coated by bentonite; on the other hand, if granular bentonite is used, bentonite have the tendency to place between the voids left by glass beats (Abichou et al., 2002).
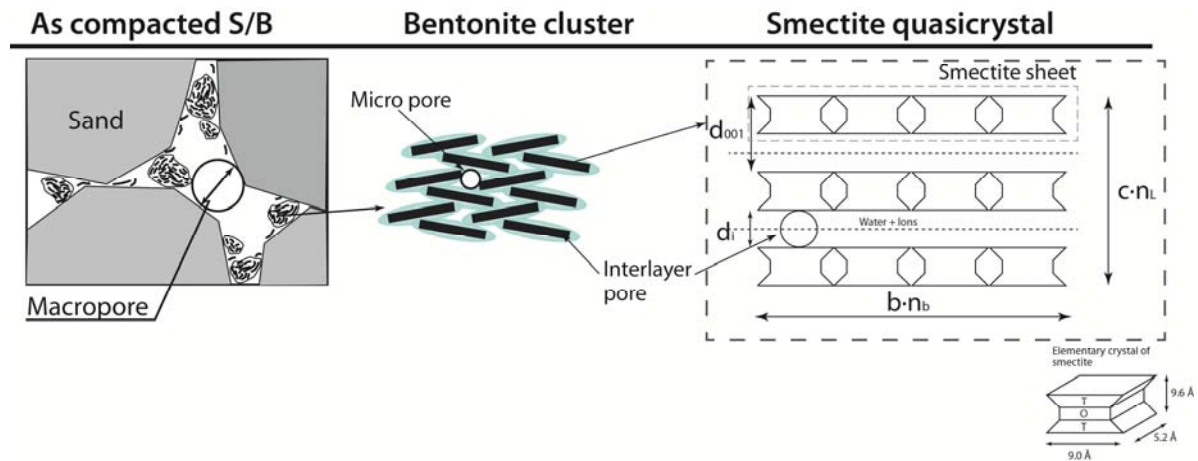
Figure 4.4: Schematic representation of the sand/bentonite mixture at low bentonite content and identification of the different pore families.

4.4 EXPERIMENTAL METHODS FOR MICROSTRUCTURAL OBSERVATIONS

Mercury Intrusion Porosimetry technique (MIP) and Scanning Electron Microscopic (SEM) observations were used in order study the evolution of the pore structure of the mixture upon saturation with different types of water.

This section contains a description of the experimental techniques used in this context and the methods adopted for the preparation of the specimens.

4.4.1 Mercury intrusion porosimetry

Mercury intrusion porosimetry is an experimental technique that provides a quantification of soil porosity within the soil mass. It was first introduced by Ritter and Drake (1945) and then extensively used for the characterisation of the pore structure of different geo-materials (Romero and Simms, 2008).

The Pascal 140+400, POROTEC, Thermo Electron Corporations porosimeter device was used for the MIP analysis. The operative range of the first unit (Pascal 140) varies from 0.1 kPa to 400 kPa (Thermo Electron, 2006). The second unit (Pascal 440) allows applying a maximum intrusion pressure of 400 MPa (Thermo scientific, 2007).

For this experiment, the tested specimen is inserted in a specimen holder (dilatometer) which is filled with mercury. The dilatometer used for testing the S/B is the type CD3P from Porotec (http://www.porotec.de/) which is specially design for testing powders. The main characteristic of this dilatometer is that the capillary tube (where the mercury is injected) has two holes at its extremity. In this way, the mercury does not fall directly on the friable specimen of S/B mixture and the alteration of its pore structure is prevented.

Since mercury does not wet the pore surface, it is required to apply a certain pressure in order for mercury to invade the pores. During the experiment the pressure of the mercury is slowly increased and the intruded volume is recorded.

A cylindrical shape of the pores is assumed for the interpretation of the test results. With this assumption, the Washburn equation (Washburn, 1921) is used to relate the pore diameter (x) to the pressure at which the mercury (Hg) intrudes the pore (P_{Hg}), as follows:

$$x = \frac{4\sigma_{Hg} \cos \vartheta_{Hg}}{P_{Hg}} \tag{4.6}$$

where σ_{Hg} and ϑ_{Hg} are the surface tension and the contact angle of the mercury, respectively. For the analysis, a value of σ_{Hg} = 0.480 N/m (at a temperature of 20 °C)

was adopted. The contact angle between mercury and clay, which usually varies between 139° and 147° (Diamond, 1970), was assumed equal to 140°.

Specimens tested with this technique are required to be firstly dried to eliminate all the water present in the pores and then putted under vacuum to eliminate air from the pores. This procedure ensures the elimination of any fluid that may obstacle the entering of the mercury.

The test is interpreted based on the assumption that the pore space consists of a system of cylindrical pores, each of which is entirely and equally accessible to the outer surface of the specimen and thus to the surrounding mercury.

The results of the MIP tests are represented in terms of cumulative intruded void ratio, defined as the ratio of the injected mercury at a given pressure to the solid volume of the tested specimen ($e_{Hg} = V_{Hg} / V_s$), and pore size density function ($PSD = -\Delta e_{Hg} / \Delta \log x$), with respect to the apparent pore diameter (x). The apparent pore diameter is defined as (Scheidegger, 1958) *"the diameter of the larger sphere which contains the pore and yet remains wholly within the pore space"*.

Details on the analytical derivation of the *PSD* can be found in Juang and Holtz (1986), Romero (1999), and Montanez (2002).

4.4.1.1 *Specimens preparation*

In order to prepare the specimens for the microstructural analyses, the mixture was initially prepared at the 11% of water content and then compacted to the target dry density inside an oedometric ring or the microcell (Chapter 2, Section 2.4.2.2).

The microcell was specifically used to prepare the specimen under condition of partial saturation. In this case, after the compaction, the cell was closed and water was injected with a syringe from the various holes of the microcell and from both sides. Inside the microcell, the S/B specimen was placed between two ASTM steel mesh number 200 (opening equal to 75 μm) to prevent the migration of fine particles during sample preparation and wetting (Figure 4.5). The advantage of using the mesh, instead of a common filter paper, is that it has no retention capacity and does not prevent the migration of liquid to the specimen.
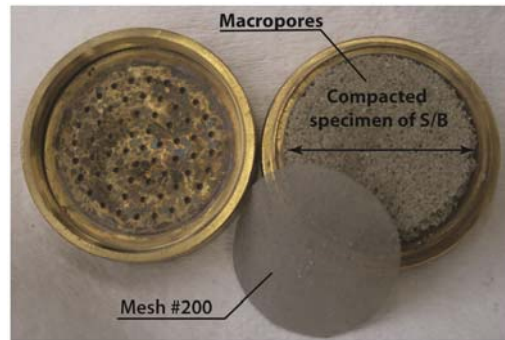
Figure 4.5: Specimen compacted into the Microcell for MIP measurements.

Because the mixture at the as-compacted state has very large macropores (Manca et al., 2015), the injected water is expected to flow preferentially through those pores. Because the water invades immediately the large macropores, and for specimens of this size, a large heterogeneity in the pore structure is not expected. This affirmation is supported by the results of Pusch and Yong (2003) where it was shown that the water front advances from the larger macropores channels and depending on the testing conditions penetrates 2-3 cm distance from the pressurised surface when pressurised water is pushed into highly compacted MX-80 bentonite.

After the water injection, the microcell is sealed in paraffin tape for 15 days to allow moisture redistribution along the different levels of pore. During this period the injected water migrates by diffusion inside the bentonite aggregates to promote the swelling of the aggregates (Delage et al., 2006, Pusch and Yong, 2003).

Cylindrical specimens of 8 mm in diameter and 6 mm height (approximately 0,6 g in dry mass) were re-cored from the bigger specimen using a steel sharp tube just before the freeze drying procedure to limit disturbances and desiccation of the specimens. A small piston was used to extract the specimen from the tube. The method allowed the production of specimens of similar mass ensuring the consistency of the results. Moreover, because of the relatively low swelling pressure generation upon wetting, the elastic rebound during swelling pressure release was small and it did not alter the pore structure of the specimens.

Prior to the tests, the specimens were dried using the freeze drying method. The method consists in the direct immersion of the specimen in liquid nitrogen (boiling point of -196°C) followed by sublimation in vacuum at 0.060 mbar and at a temperature of -52°C. The fast freezing avoids the 9% of water volume increase due to water crystallization because of the formation of a very large number of small crystals (Delage et al., 1996). Direct immersion in nitrogen can cause the formation of superficial micro-cracks on the specimen surface (Delage and Pellerin, 1984), which in the MIP analyses may alter the macropores and lead to a not-precise estimation of the intruded volume. The extraction of the pore water by sublimation process ensures minimum disturbances to the pore structure avoiding the generation of water and air menisci which cause the shrinkage

of the specimen (Penumadu and Dean, 2000). The different phases of the specimen preparation for MIP analyses are illustrated in Figure 4.6.

The characteristics of the tested specimens for the MIP analyses are listed in Table 4.1. Variations of the water content of the as-compacted specimens are attributed to some evaporation that occurred during preparation.

4.4.1.2   Repeatability of the MIP measurements

To verify the repeatability of the MIP measurements, the analyses on the as-compacted specimens prepared to two target dry densities ($\rho_d = 1.5$ Mg/m^3 and $\rho_d = 1.8$ Mg/m^3) and wetted with distilled water, were repeated twice. The results of these tests are presented Figure 4.7. Regardless of the compaction density, the PSDs curve of the specimens compacted to the same target dry density show a slight variation of the dominant modes (Figure 4.7.a and b). However, the cumulative curves appear very close (Figure 4.7, c and d) showing the consistency of the obtained results. This suggests that the peak variation is not related to the macropore closure but to some slight variations on the distribution of the sand and bentonite grains.

The quasi-equality of the cumulative curves of two different specimens prepared to the same compaction density, and water content, is an indication of the good homogenisation of the pore structure. In this sense it is possible to conclude that the procedure used for the specimen preparation (section 2.2.6) allows the production of similar specimens, which are characterised by a uniform distribution of the two fractions of the mixture over the whole volume.
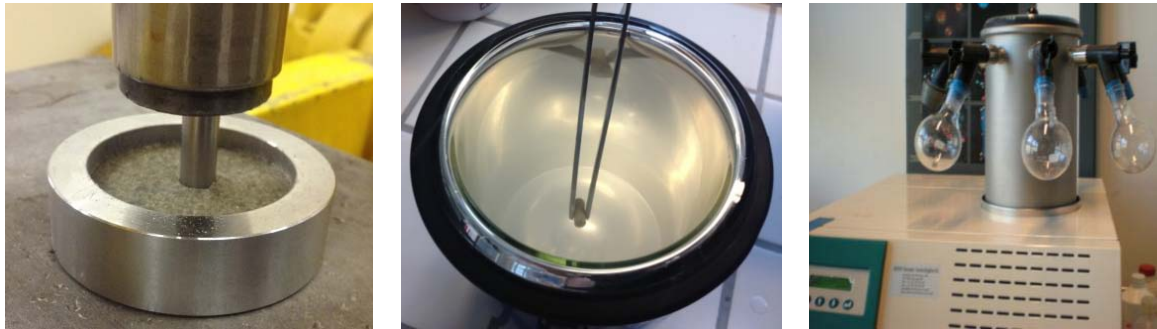
Figure 4.6: Specimen preparation for MIP analysis. From the left: 1) specimen re-coring; 2) fast freezing in nitrogen bath, 3) freeze drying.

Table 4.1: Characteristics of the specimens used for the MIP analyses.

Specimen code	ρ_d [Mg/m^3]	e [-]	w [%]	S_r [-]
DW_01w	1.43	0.87	0.12	0.35
DW_02w	1.50	0.78	0.11	0.39
DW_03w	1.51	0.77	0.11	0.38
DW_04w	1.50	0.78	0.15	0.50
DW_05w	1.49	0.79	0.25	0.85
DW_06w	1.52	0.76	0.29	1.03
DW_01w2	1.50	0.78	0.16[*]	0.56
DW_01d	1.53	0.75	0.16[**]	0.56
DW_07w	1.65	0.62	0.12	0.50
DW_08w	1.61	0.66	0.09	0.38
DW_09w	1.81	0.48	0.09	0.53
DW_10w	1.80	0.48	0.10	0.53
DW_11w	1.79	0.49	0.09	0.51
DW_11w	1.80	0.48	0.14	0.72
DW_13w	1.78	0.50	0.16	0.87
DW_14w	1.80	0.48	0.18	0.98
DW_02d	1.78	0.50	0.14[**]	0.73
SW_01	1.46	0.83	0.11	0.35
SW_02	1.50	0.78	0.28	0.95
SW_03	1.82	0.47	0.11	0.63
SW_04	1.80	0.48	0.13	0.72
SW_05	1.76	0.52	0.15	0.75
SW_06	1.84	0.45	0.17	1.01
1M NaCl_01	1.51	0.77	0.11	0.39
1M NaCl_02	1.51	0.77	0.32	0.01
4M NaCl_01	1.51	0.77	0.11	0.00
4M NaCl_02	1.50	0.78	0.29	0.01

*Specimen prepared with a mixture wetted at w=16.3 % and then compacted to the target dry density.
**Extracted from the specimen used for the determination of the WRCs after a cycle of wetting and drying.
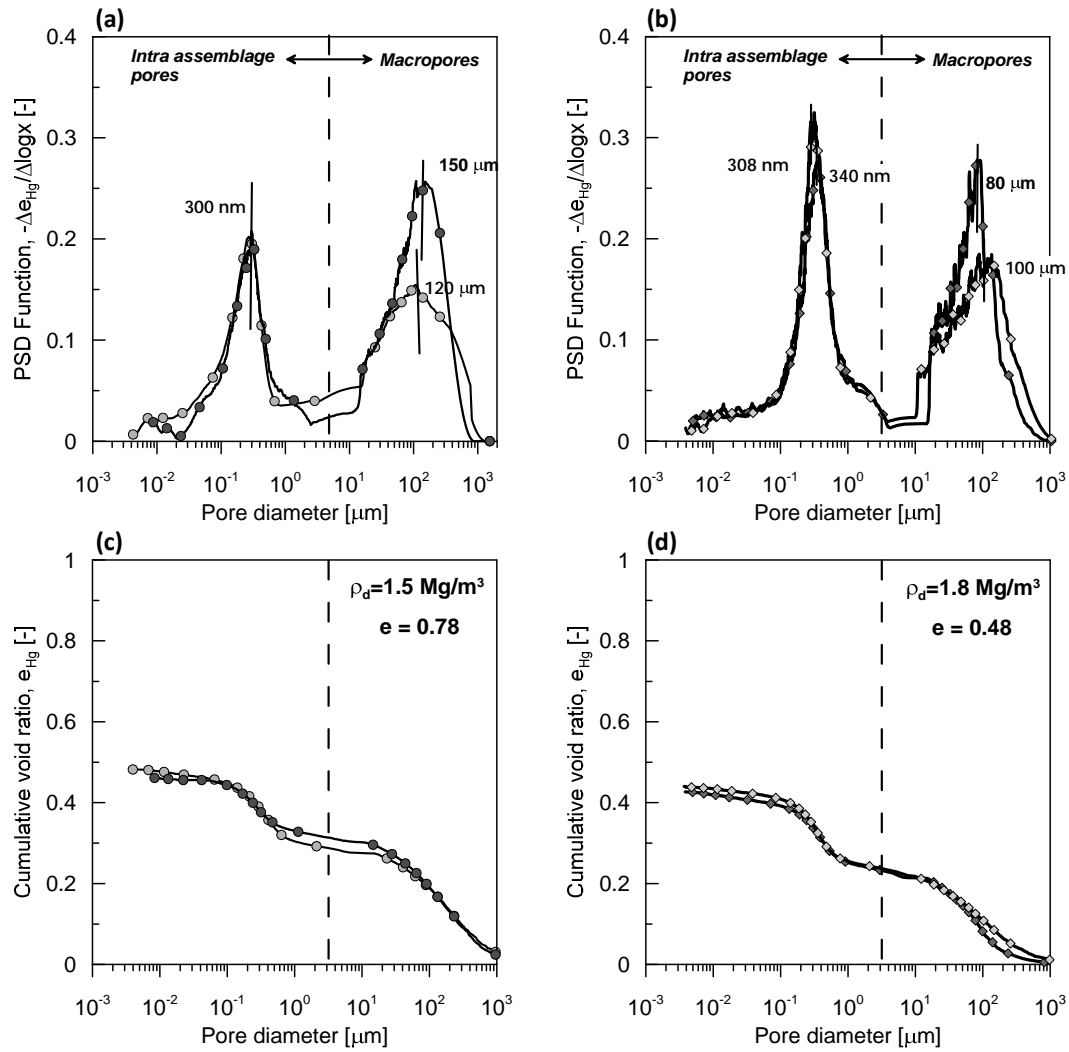
Figure 4.7: PSD function and cumulative void ratio of the S/B mixture compacted to 1.5 Mg/m³ (top) and to 1.8 Mg/m³ dry density (bottom). Tests were repeated twice for each dry density. All the specimens were wetted with distilled water.

4.4.2 Scanning electron microscopy for qualitative microstructural observation

SEM observations are used in this study as a support to the MIP measurements for the microstructural characterisation of a porous media. The list of the SEM observations performed in the study is presented in Table 4.2.

The high resolution scanning electron microscope Zeiss Merlin available at CIME, EPFL, was used for the observations. The instrument allows shooting the specimen with an electron beam at the maximum energy of 30 keV. To maximise the stability of the images, the specimens for the SEM observations were freeze dried 24 h prior to the observations. This procedure is mandatory because in presence of water in the specimen the electrons can hit the water molecules and scatter in undesirable directions creating noise in the image.

Table 4.2: Characteristics of the specimens used for the SEM analyses

Type of water	Comments
DW	As-compacted specimen; $\rho_d = 1.5$ Mg/m^3
DW	Saturated specimen under constant volume conditions; $\rho_d = 1.5$ Mg/m^3
DW	Saturated specimen under constant volume conditions; $\rho_d = 1.8$ Mg/m^3
DW	MX-80 hydrated to $w = 55\%$ to simulate the as-compacted conditions
1M NaCl	Saturated specimen under constant volume conditions; $\rho_d = 1.5$ Mg/m^3
4M NaCl	MX-80 hydrated to $w = 52\%$ to simulate the as-compacted conditions
-	MX-80 bentonite at the hygroscopic water content after sieving
-	Quartz sand at the hygroscopic water content after sieving

For these tests, the material coating was avoided to prevent any alteration to the pore structure. Due to the non-conductive nature of the S/B mixture, the specimens were shot with an electron gun at a voltage of 2 kV to limit the charging phenomena that can arise if the energy of the electron beam is too high. This low energy allows the acquisition of images that are rich in surface details because the interaction volume at which the electrons penetrate the specimen is reduced (Goldstein et al., 2007).

The HRSEM used for the microstructural observations also allows performing energy dispersive X-Ray (EDX) analyses that aided to identity the elements composing the various minerals. Thanks to this tool, it was possible to distinguish the smectite minerals from other impurities present in the MX-80. The analysis required to shoot the specimen with a beam of high voltage (10 keV). For this reason the interaction volume was considerably increased. An example of EDX results is presented in Figure 4.8. The figure shows on the upper-left of the picture a bentonite aggregate attached to a grain of sand. The related spectrum (spectrum 2) shows that elements such as Na, Al, Mg, O and Si, which are all the elements composing the sodium smectite mineral, are detected. On the upper-right side of the picture it is shown an impurity (most probably a mineral of muscovite). Despite the fact that it is not possible to exactly identify the type of mineral, this can be distinguished from the smectite because Mg and Na are missing in the spectrum (spectrum 3).
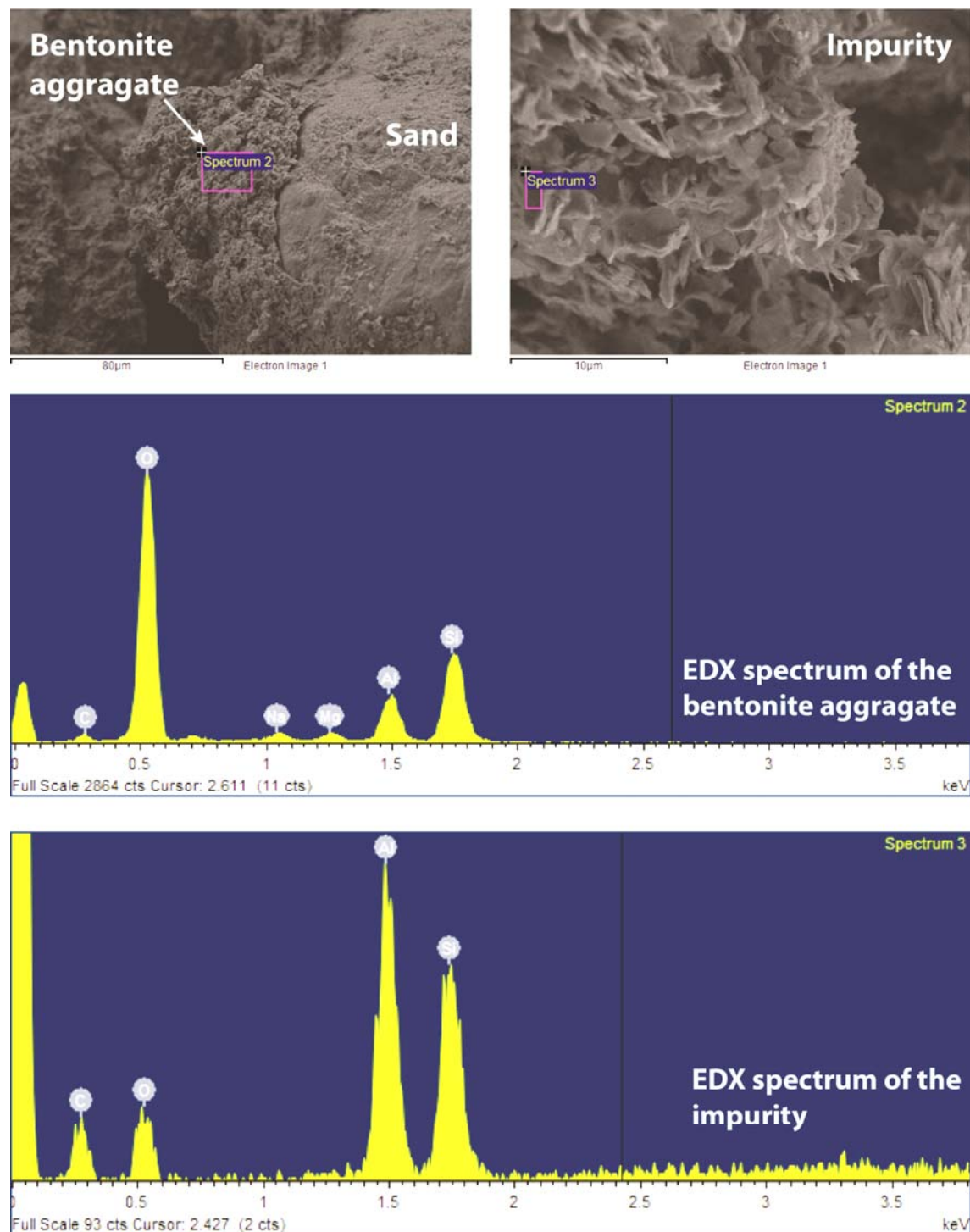
Figure 4.8: EDX analysis of a bentonite aggregate and an impurity.

4.5 PORE STRUCTURE STABILITY OF THE SAND/BENTONITE MIXTURE UNDER DIFFERENT HCM LOADINGS

4.5.1 Pore structure arrangement at the as-compacted state

The as-compacted state of the material refers to a mixture prepared with 11% water content (target water content), which is then compacted to the target dry density. The initial total suction after compaction, measured with the non-contact filter paper method, is equal to 1.1 MPa for specimens prepared with distilled water, 1.9 MPa for specimens prepared with synthetic water, and 2.3 MPa for the specimen prepared with 1 M sodium chloride solution (Chapter 2, section 2.4.3.1). These initial suction values are in the transitional zone of the water retention curve, indicating that most of the water is stored intra-assemblage pores. Consequently, the initial water content of 11% of the mixture corresponds to a water content for the bentonite fraction (w^b) of 55%.

Figure 4.9 shows a SEM photomicrograph of an as-compacted S/B mixture specimen prepared with distilled water. In the picture, the arrangements of the sand grains and the bentonite aggregates are observed, along with two different pore families, the macropores and the micropores. At this bentonite content, the sand particles are in contact with each other, creating a solid skeleton, which provides a certain mechanical stability (Viola et al., 2005). The finer fraction of bentonite coats the sand grains, whereas the larger aggregates are located in the large voids within the sandy skeleton (Zoom 2).
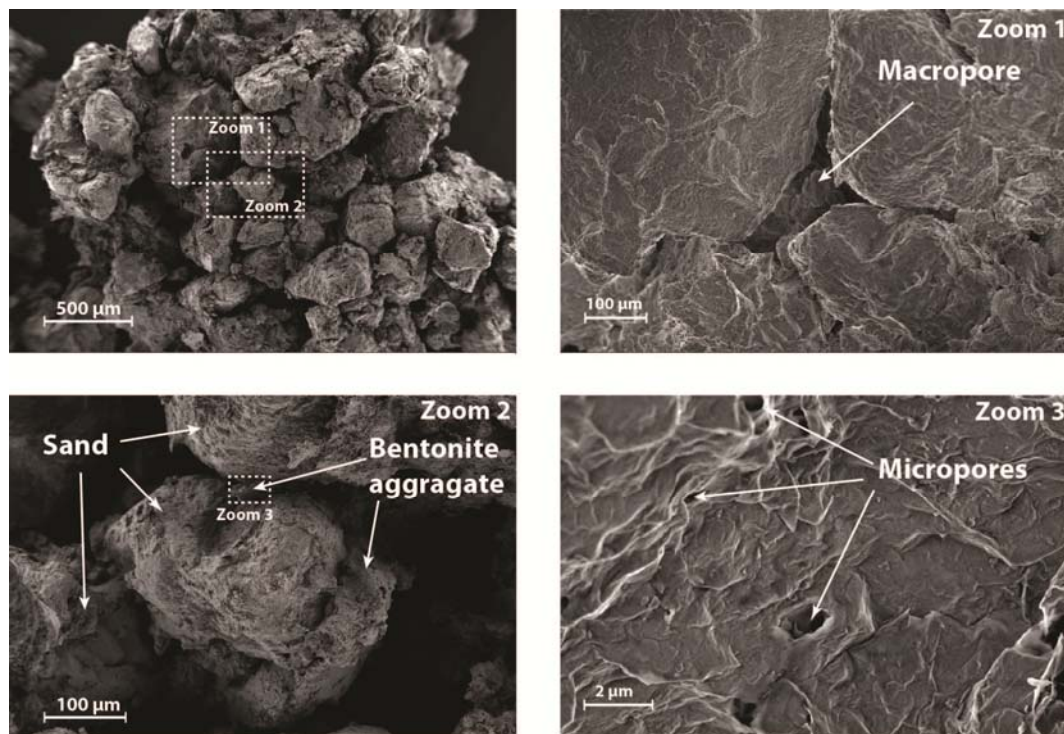
Figure 4.9: SEM photomicrograph of a S/B a specimen prepared with distilled water and competed to a dry density of 1.5 Mg/m³. View of the different structural levels.

Macropores are located between sand grains and the bentonite assemblages (Zoom 1), while micropores are visible in the clay assemblages (Zoom 3). Due to the limited resolution of the SEM apparatus, interlayer pores are not visible.

The MIP tests show that the S/B mixture in the as-compacted state presents a clear bimodal pore size distribution (PSD), regardless of the dry density or the salinity of the water used for the preparation of the mixture (Figure 4.10 and Figure 4.11). The peak for larger apparent pore diameters is associated with voids between the sand particles and at the contact zones between the bentonite assemblages (macropores). The peak for smaller apparent pore diameters is associated with the larger fraction of the pore volume within the bentonite assemblages (micropores within the quasicrystals).

When distilled water is used as the wetting fluid, the specimens compacted to a low densities (ρ_d=1.4 Mg/m^3 and ρ_d=1.5 Mg/m^3) show a dominant mode in the macroporosity region between 150 μm and 120 μm (Figure 4.10.a). At a higher compaction density (ρ_d=1.8 Mg/m^3) the dominant macropore mode moves toward a smaller pore diameter with a peak located between 100 μm and 80 μm. At higher dry densities the cumulative macrostructural void ratio decreases (Figure 4.10.b), showing closure of the largest pores due to an increase of the mechanical loading (Koliji et al., 2010b). Independent from the degree of packing, both the PSDs of the compacted specimens saturated with distilled water show a second dominant mode at approximately 0.3 μm. The cumulative curves, normalised to the void ratio presented in Figure 4.10.c show that the ratio of the maximum intruded void ($e_{Hg,max}$ for a mercury pressure of 400 MPa) to the total void ratio (e) is equal to 0.88 for the specimen compacted to the 1.80 Mg/m^3 of dry density and 0.51 for the specimen compacted to the 1.43 Mg/m^3 of dry density. This result, which was never observed for other clayey soils, indicates the reduction of the bentonite pore volume as a consequence of the specimen compression. This behaviour is attributed to the high water content (w^b = 55%), and thus high compressibility, of the bentonite fraction, and clearly evidences the irreversible mechanical behaviour of the bentonite aggregates. On the basis of these observations, the assumption that only macropores are affected by the compaction energy (e.g., Hoffmann et al., 2007, Lloret and Villar, 2007, Nowamooz and Masrouri, 2012) is not applicable for S/B mixture prepared at this high initial water content.
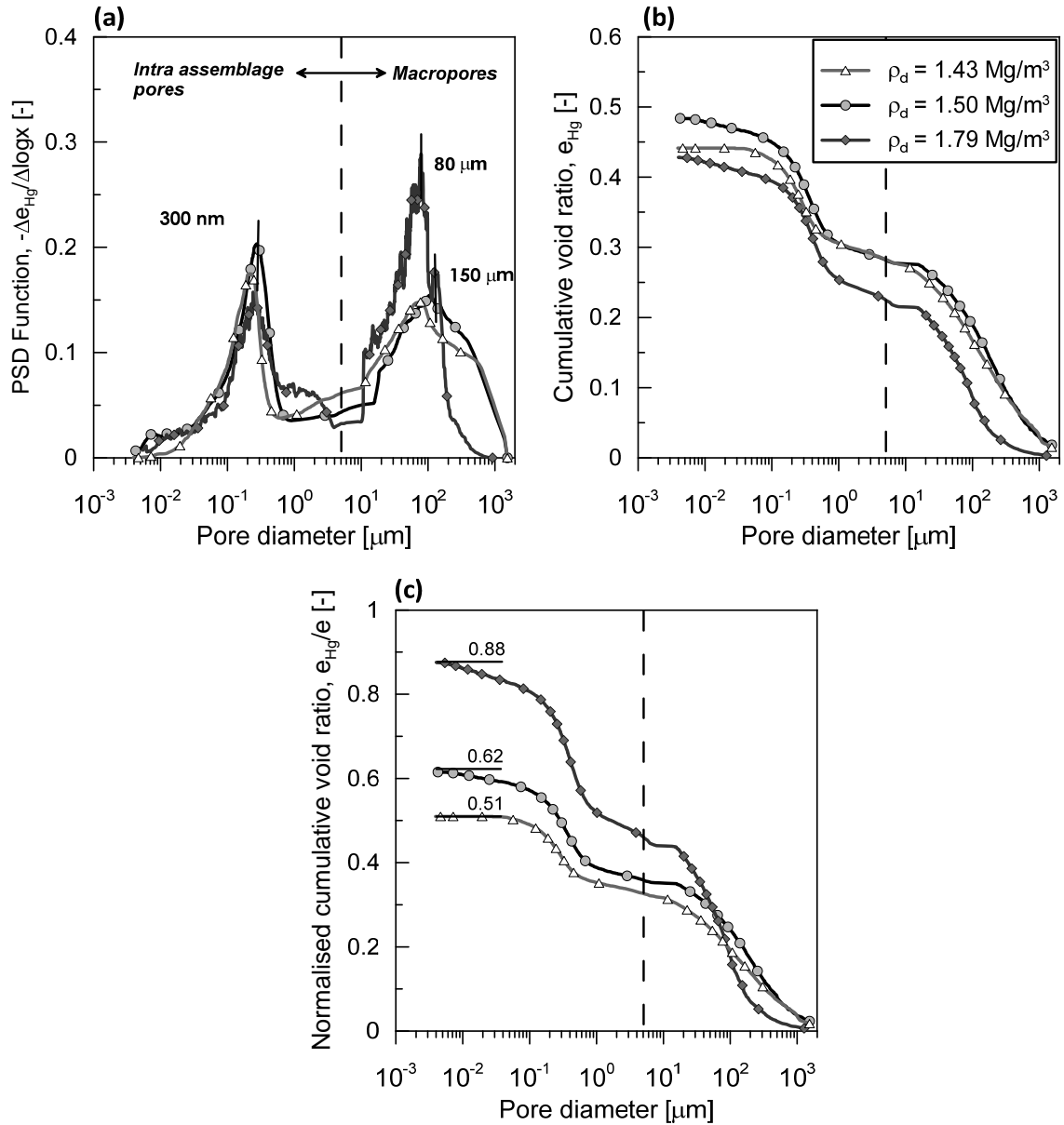
Figure 4.10: PSD functions, cumulative void ratio and a normalised cumulative void ratio of the S/B mixture compacted to three different dry densities and hydrated to *w*= 11% with distilled water.

The PSD functions of specimens compacted to the same dry density, and prepared with different pore fluids, show that the intra-assemblage pore mode moves toward smaller apparent diameters when the pore water salinity increases. The macropore mode is only slightly changed (Figure 4.10.a). The observation of the cumulative curves presented in Figure 4.11.b shows that the intruded void ratio slightly decreases with the increase of pore water salinity, indicating that the initial swelling of the bentonite assemblages is reduced during the mixture preparation.

A comparison of SEM images on pure MX-80 bentonite wetted to *w* = 55% with distilled water and 4 M NaCl supports the MIP observations (Figure 4.12). When the granular bentonite is wetted with distilled water, its structure appears very homogeneous.

Conversely, the structure of bentonite wetted with the 4 M NaCl solution appears more compacted and some intact grains are visible.

In Figure 4.13 PSD curves (for apparent diameters lower than 1 μm) of S/B mixture wetted with distilled water and 4M NaCl solution are compared with the PSD detected for a single grain of MX-80 tested at its hygroscopic water content (obtained by Seiphoori et al. (2014)). In the figure are also presented SEM images of Figure 4.12 at higher magnification. The smaller peak detected for the MX-80 wetted with 4M NaCl, at 25 nm, is similar to the one detected for the single grain of MX-80 tested at its hygroscopic water content; located at 12 nm. When the granular bentonite is wetted with distilled water, its structure appears to be formed by many flexible sheets (thin quasicrystals of smectite) arranged in a typical wave-flake-like shape; micropores of different sizes are observed among the quasicrystals (Figure 4.13.b). The structure of bentonite wetted with the 4 M NaCl solution appears very different as the quasicrystals are not visible (Figure 4.13.b). Energy dispersive X-Ray (EDX) measurements confirm that the bentonite assemblages are coated with precipitated sodium chloride, which impedes the bentonite expansion and partially compensates the volume increase of the macropores.
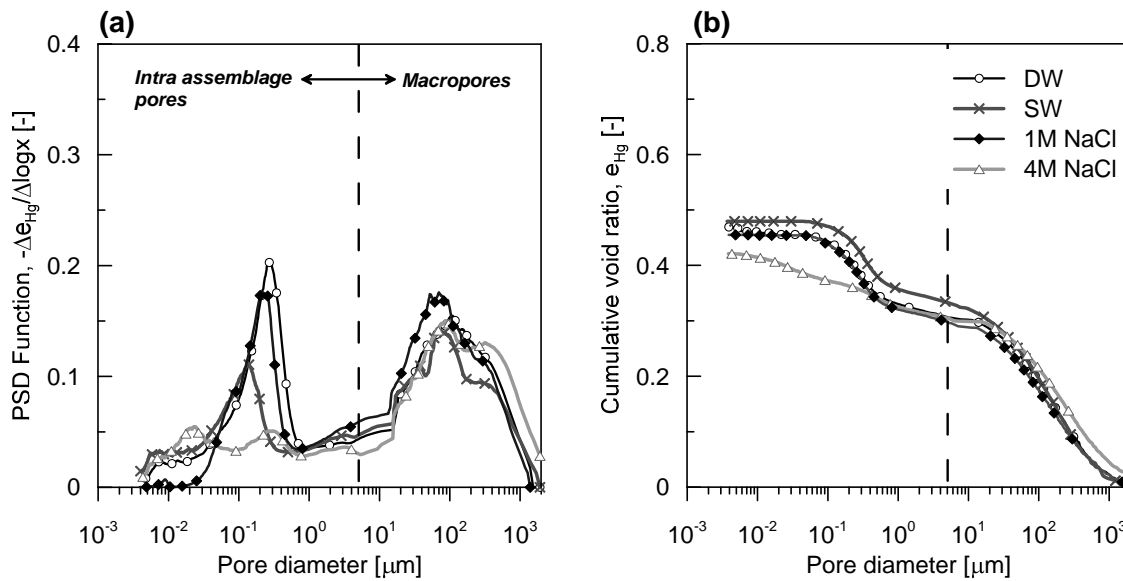
Figure 4.11: PSD function and cumulative void ratio of the S/B mixture compacted to the loose state (*e* = 0.78) and wetted with different types of water.

138
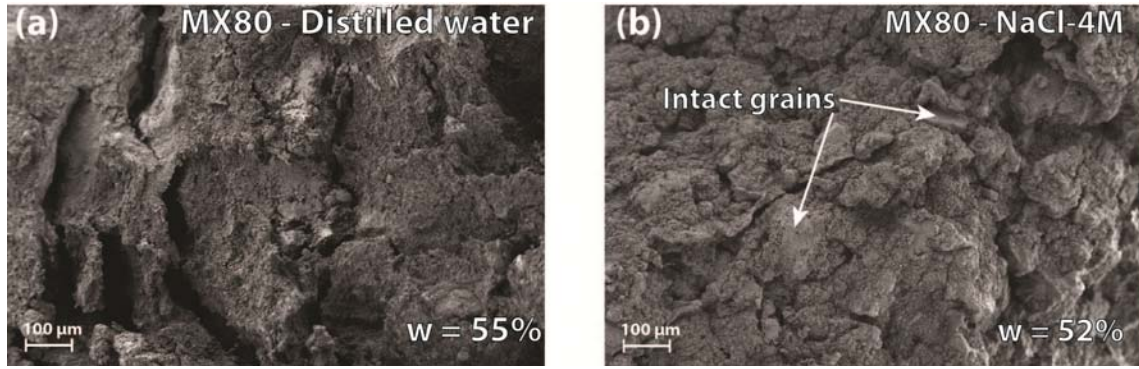
Figure 4.12: SEM image of MX-80 granular bentonite wetted to w~55% with distilled water (s) and 4M NaCl (b).
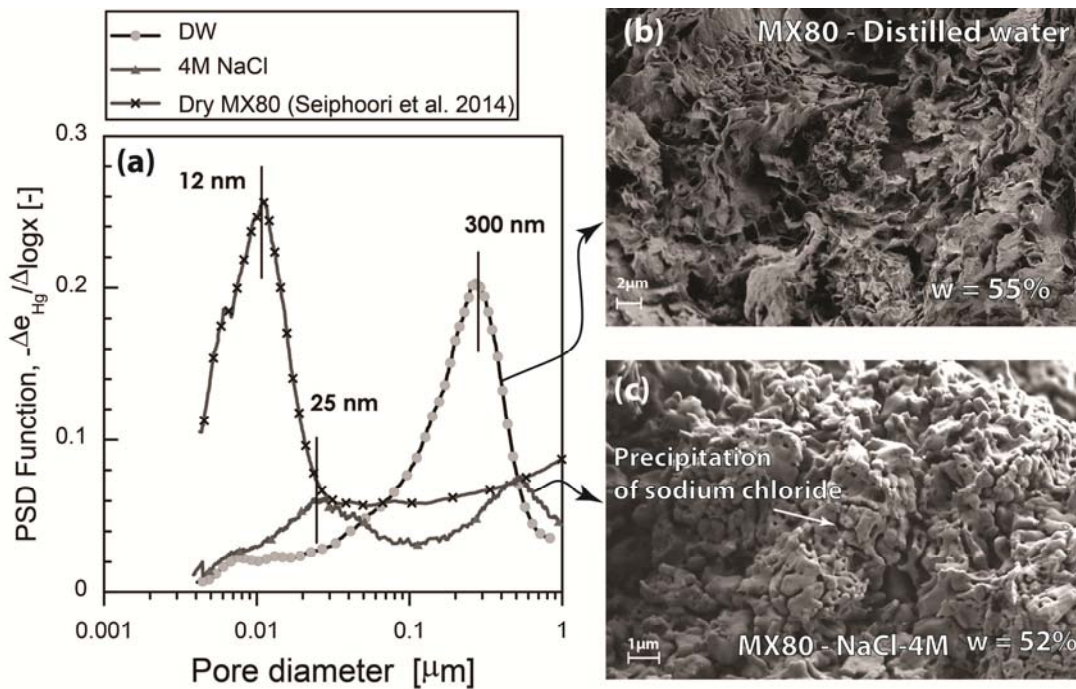
Figure 4.13: PSD observed in the bentonite region (a), SEM image of MX-80 granular bentonite wetted to w~55% with distilled water (b) and 4M NaCl (c).

4.5.2 Mechanisms of microscopic swelling under wetting-drying cycle in constant volume

This section discusses in detail the results of the MIP tests on the S/B mixture specimens subjected to a cycle of wetting and drying. Specimens that followed the main wetting path were initially compacted to two target dry densities, 1.5 and 1.8 Mg/m³ inside the microcell. Then, the specimens were wetted with distilled water under isochoric conditions to the target water content. Corresponding matric suction values are derived from the measurements of the water retention behaviour of the mixture (Chapter 2; section 2.4.3.2). The results of the MIP analysis are presented in Figure 4.14 for the

specimen compacted to the lower density and in Figure 4.15 for the specimen compacted to the higher density.

The PSD curves for both of the two dry densities show that the progressive hydration of the mixture leads to a shift of the microporosity mode towards larger apparent diameters because of the swelling of the bentonite assemblages (Figure 4.14.a and Figure 4.15.a). The macropore characteristic mode moves toward smaller apparent diameters, and the associated volume is considerably reduced. For the lower dry density, the cumulative void ratio curves show that the wetting process under a constant volume condition is characterised by an important increase of the intruded void ratio (Figure 4.14.b). Specimens compacted to the high dry density show a reduction of the intruded porosity upon wetting (Figure 4.15.b). Regardless of the dry density, at the end of the saturation process, the material presented a single mode PSD.

To visualise the wetting process, SEM photomicrographs are obtained on MX-80 bentonite wetted with distilled water at the hygroscopic water content of 5% (Figure 4.16.a) and at the as-compacted water content of 55% (Figure 4.16.b). These images are then compared with the SEM image of an S/B mixture fully saturated under the constant volume condition. In this state, assuming that all of the water is stored within the bentonite assemblages and considering that the macropores are fully invaded, the bentonite water content is equal to 120% (Figure 4.16.c).
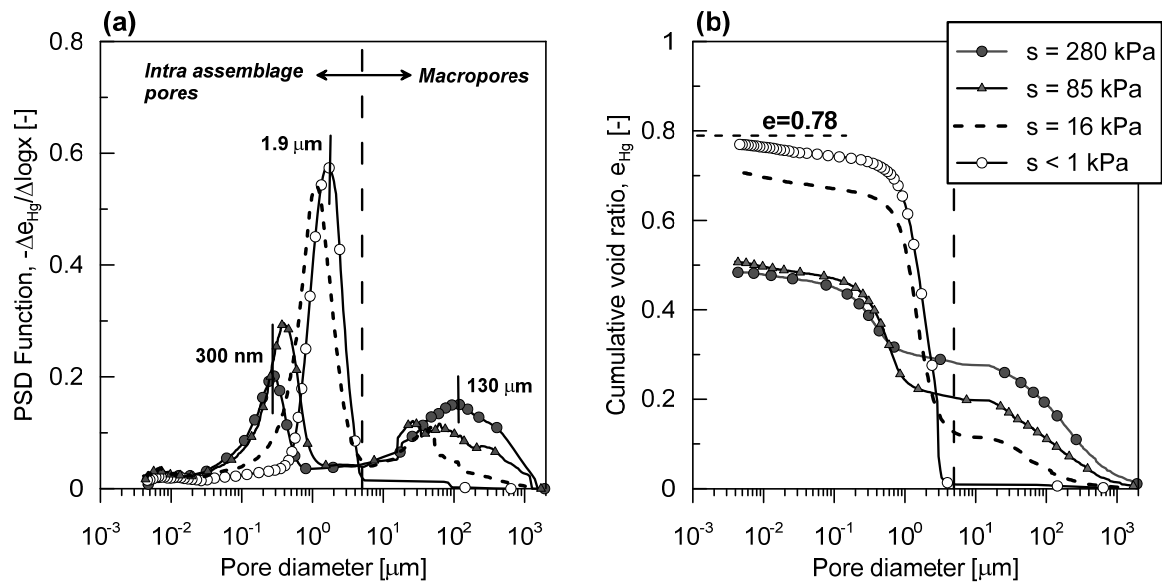
Figure 4.14: Pore structure evolution of the S/B mixture subjected to wetting process under constant volume conditions initially compacted to a dry density of 1.5 Mg/m³.
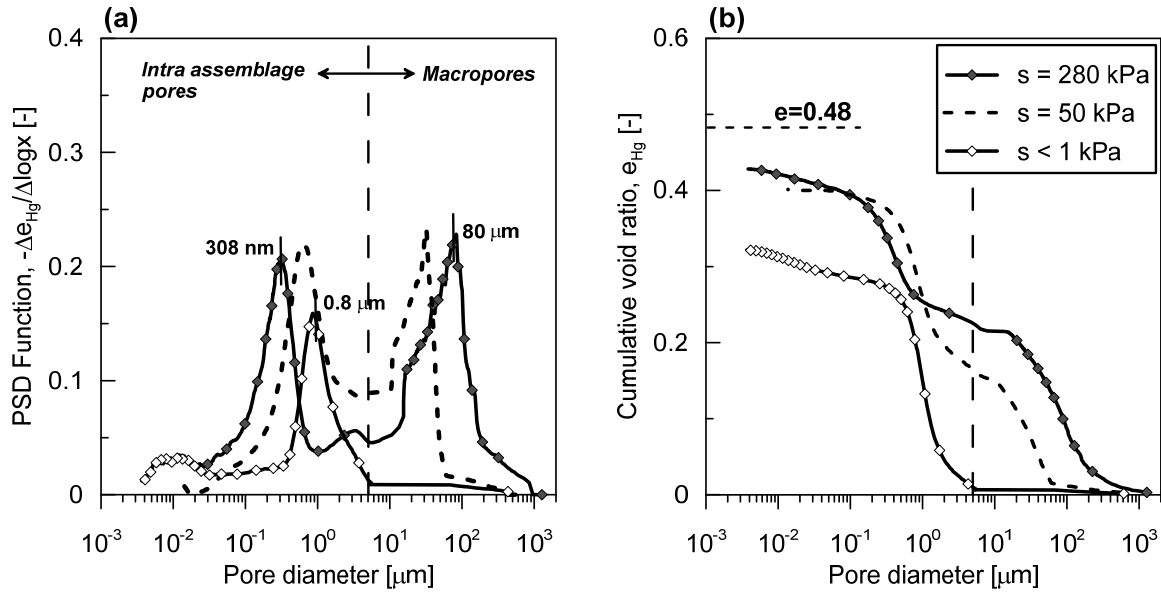
Figure 4.15: Pore structure evolution of the S/B mixture subjected to wetting process under constant volume conditions initially compacted to a dry density of 1.8 Mg/m³.

At the hygroscopic water content, the larger grains of bentonite appear to be coated by the finest bentonite fraction. At the water content of 55%, the typical wave-flake-like structure of highly hydrated smectite is visible, as the quasicrystals were oriented in an edge-to-face arrangement. At the end of the saturation process, the smectite quasicrystals appear thin and flexible, and the pores within them have the size of some micrometres, in agreement with the MIP results.
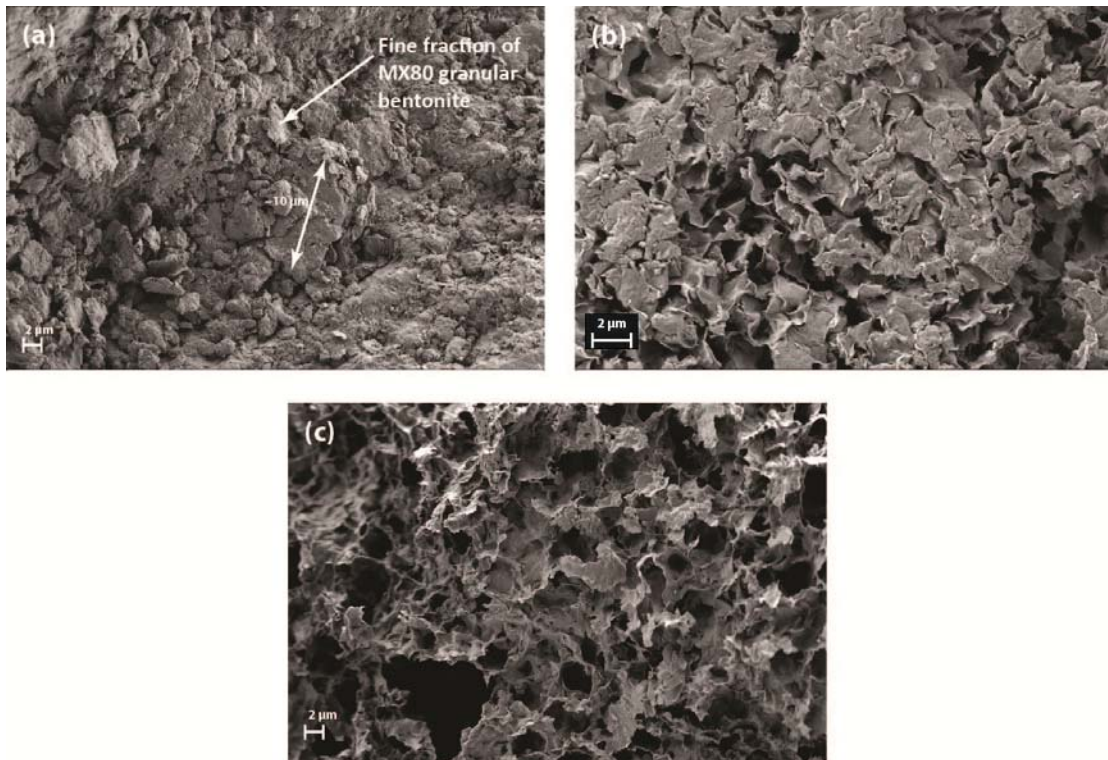
Figure 4.16: SEM photomicrographs of an aggregate of MX-80 bentonite hydrated under free volume condition. a) *w*= 5%; b) *w*>55%. c) Aggregate of MX-80 bentonite in a fully hydrated S/B mixture; *w* > 100%.

141

To have an insight on the reversibility of the pore structure of the S/B upon one drying-wetting cycle, two specimens for the MIP analyses were re-cored from the specimens used for the determination of the water retention properties of the mixture at the end of the drying process (s=500 kPa). The results of this test are presented in Figure 4.17 for the specimen compacted to the lower density and in Figure 4.18 for the specimen compacted to the higher density. PSD and cumulative curves at the end of the wetting-drying cycle are presented along with the curves at the as-compacted state and at the end of the wetting process. At the end of the drying process, the specimen compacted to the lower density shows a bi-modal PSD indicating the creation of macropores due to the shrinkage of the bentonite aggregates. The maximum intruded void ratio at the end of the drying is lower than the one at the end of the wetting and also, it does not match the maximum intruded void ratio at the as-compacted state. This result suggests the partial reversibility of the pore structure at this compaction density. It is worth to remind that the specimen extracted from the controlled suction oedometer underwent to an important shrinkage at the end of the drying process; the dry density of the specimen measured with the MIP apparatus was equal to 1.53 Mg/m^3. Global shrinkage of the specimen is indicated by the reduction of the macropore volume which results smaller than in the as-compacted state.

The S/B mixture compacted to the higher dry density shows a different behaviour. In this case, only few macropores are created at the end of the drying process and the cumulative curve appears very close to the one at the end of the wetting process suggesting that the bentonite aggregates were subjected to irreversible deformations. Similar results were only observed on highly compacted MX-80 bentonite by Seiphoori et al. (2014), where this behaviour was attributed to the irreversibility of the splitting of smectite quasicrystals when these experience a high swelling pressure.
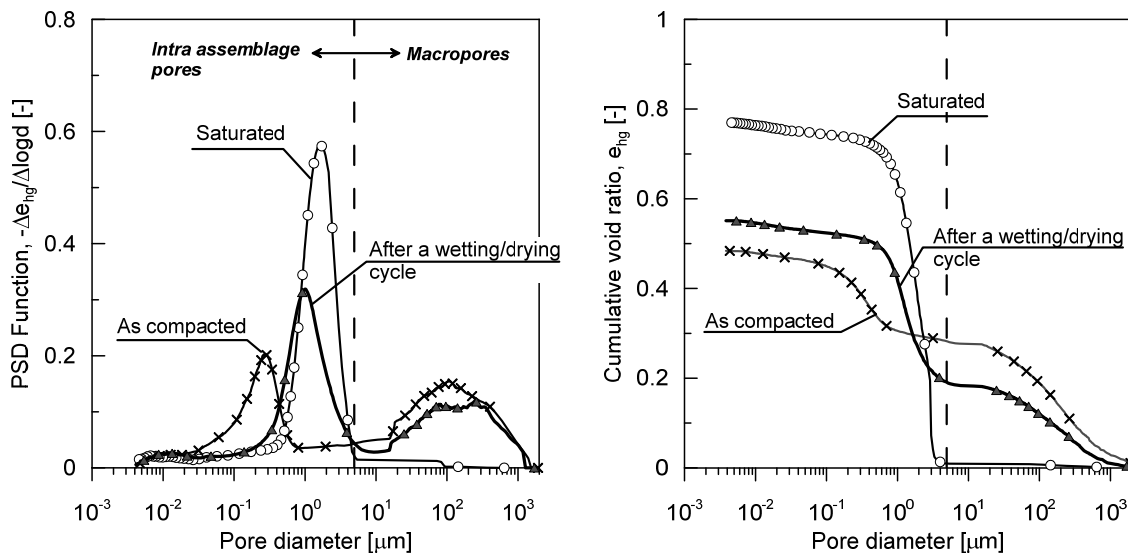
Figure 4.17: Pore structure evolution of the S/B mixture subjected to a cycle of wetting and drying under constant volume conditions. ρ_d = 1.5 Mg/m^3.
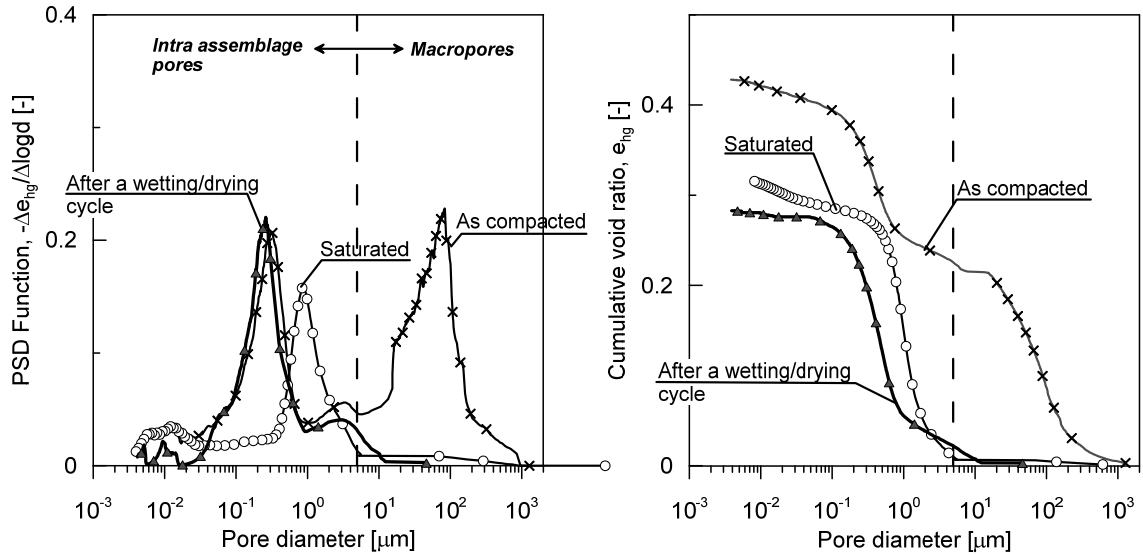
Figure 4.18: Pore structure evolution of the S/B mixture subjected to a cycle of wetting-drying under constant volume conditions. ρ_d = 1.8 Mg/m³.

4.5.3 Influence of the compaction density on the fully saturated mixture

Figure 4.19 presents the results of the MIP tests on the S/B mixture compacted to three different dry densities and wetted under constant volume conditions. To emphasise the influence of the compaction density, the cumulative void ratio is normalised by the void ratio of the mixture so that the percentages of filled voids by mercury before and after the wetting are immediately visible.

Independent from the compaction density, the PSD shifts from a bi-modal distribution at the as-compacted state to a mono-modal distribution upon saturation with distilled water. At the end of the wetting process, the single dominant apparent diameter is approximately 1.6 µm for the mixture compacted to 1.5 and 1.65 Mg/m³, and 0.8 µm for a mixture compacted to 1.8 Mg/m³.

The mixture compacted to the loosest states (ρ_d =1.5 Mg/m³; e =0.78) displays a sharp increase of the mercury-intruded voids after saturation, showing that the volume of pores intruded by the mercury tends to approach the total available pore volume (Figure 4.19.a). At an intermediate compaction state (ρ_d =1.65 Mg/m³; e =0.62), an increase of the intruded void ratio, subject to saturation, is still observed (Figure 4.19.b). However, at this compaction state, the mercury fails to fill all of the voids. At the denser state (ρ_d =1.8 Mg/m³; e =0.48), the final intruded void ratio reduces when the mixture passes from the as-compacted to the fully saturated state (Figure 4.19.c). This result was observed only in highly compacted bentonite or in sand/bentonite mixtures prepared at high bentonite contents (Agus and Schanz, 2005b, Delage et al., 2006, Seiphoori et al., 2014); in the present study, it is shown that at a high dry density, S/B mixtures prepared with a low bentonite content also have the same microscopic swelling features as the pure bentonite.
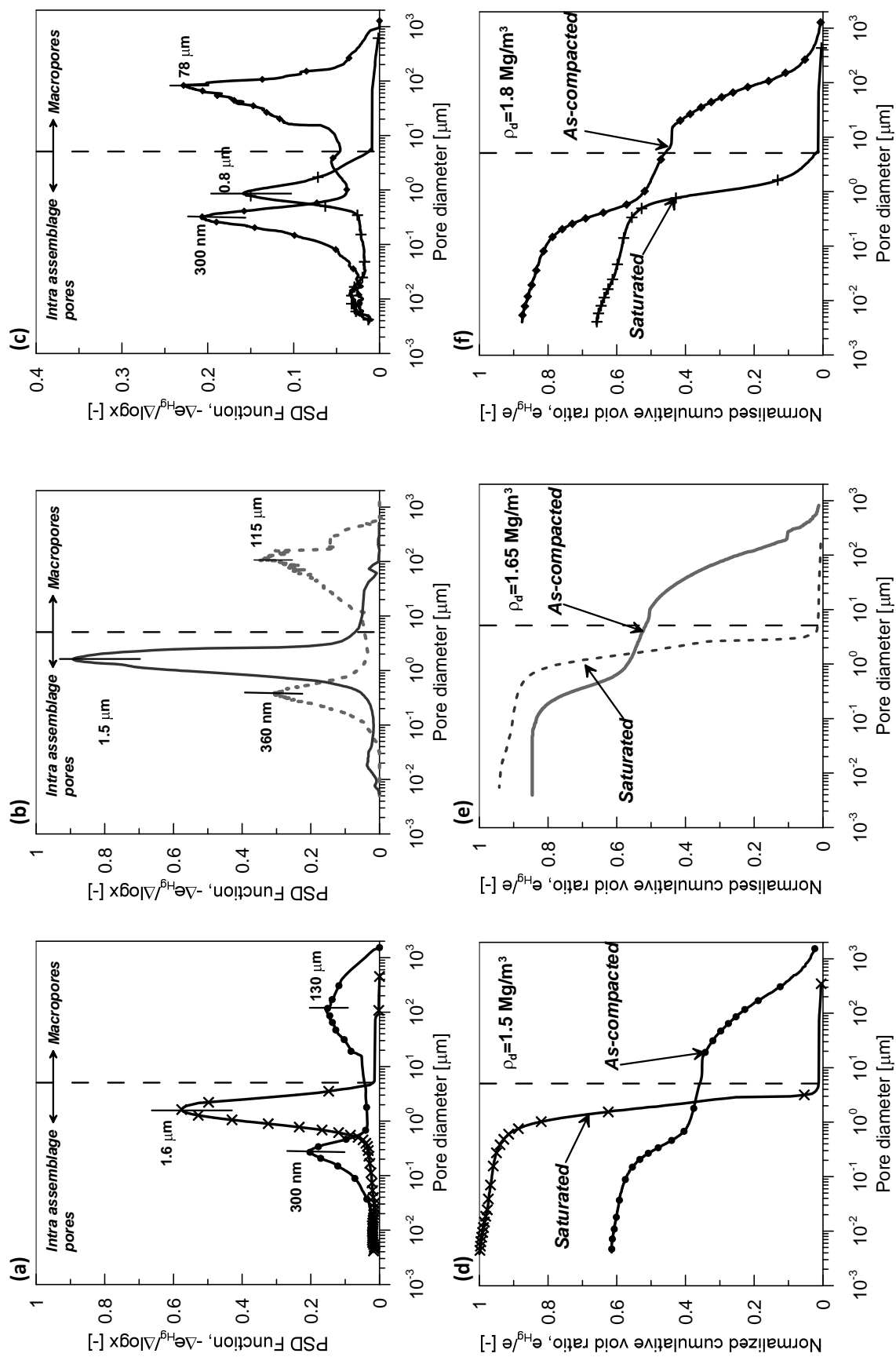
Figure 4.19: PSD function and normalised cumulative void ratio of the S/B mixture compacted at two different densities at the as-compacted state and after wetting under constant volume conditions.

4.5.4 Influence of the pore water salinity on the fully saturated mixture

The results of the MIP tests and the SEM observations on specimens compacted to ρ_d =1.5 Mg/m^3 (e =0.78) saturated under constant volume with different types of water are presented in Figure 4.20 and 4.21.

The mixture hydrated with synthetic water presents a mono-modal PSD with a mode slightly shifted toward larger apparent pore diameters (Figure 4.20.a) compared with distilled water. As the pore water salinity is increased, the PSD shows a bi-modal distribution (Figure 4.20.c). The cumulative void ratio curves show that the maximum intruded void ratio decreases as the pore water salinity increases (Figure 4.20.b and Figure 4.20.d). These observations reflect a reduction of the bentonite swelling occurring at the particle level and the inefficiency of the bentonite to properly seal the macropores.
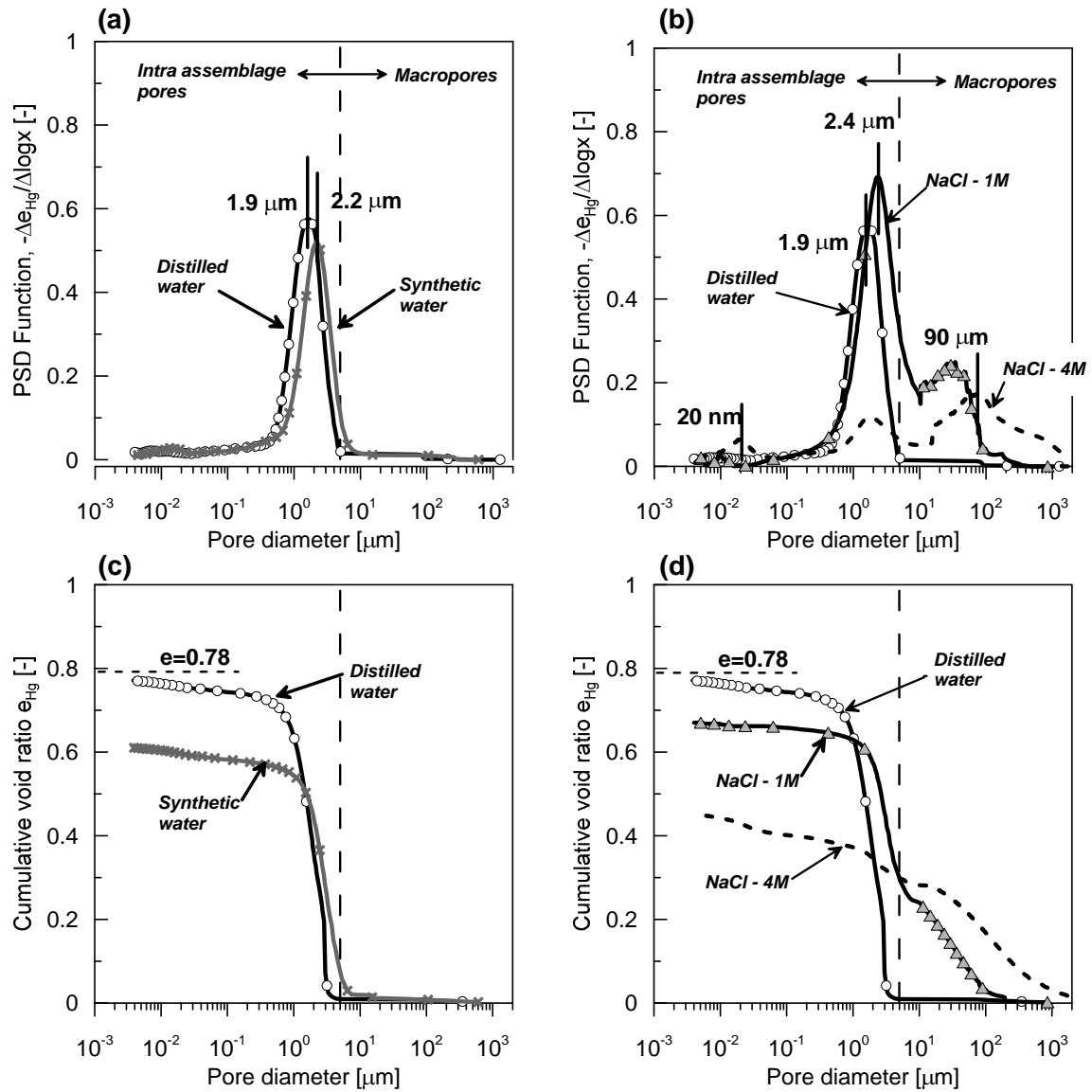
Figure 4.20: MIP test results of the S/B mixture prepared using different types of water. a) Comparison between distilled water and synthetic water. b) Comparison between distilled water and sodium chloride solutions.

The comparison of the SEM photomicrographs of the material wetted with distilled water and 1 M sodium chloride supports these conclusions (Figure 4.21). For the mixture hydrated with distilled water, the expanded bentonite fills all of the pores within the sand particles (Figure 4.21.a and b). The smectite quasicrystals appear very thin and oriented in the typical edge-to-face arrangement (Figure 4.21.c). For the mixture hydrated with the sodium chloride solution, some large pores are visible (Figure 4.21.d and e). At higher magnifications, it appears that the typical wave-flake-like structure of hydrated bentonite is maintained. However, the smectite flakes appear more compacted and thicker compared with those wetted with distilled water (Figure 4.21.f).

To complete the microstructural observations MIP tests were performed on specimens compacted to the target dry densities of 1.8 Mg/m^3 wetted with synthetic water under isochoric conditions to the target water content. The results of these analyses are presented in Figure 4.22.

Similar to the results obtained with distilled water, the shift of the micropores mode towards larger apparent diameters with the progressive hydration is observed (Figure 4.22.a). The macropore characteristic mode moves toward smaller apparent diameters and the associated volume is considerably reduced. At the end of the saturation process, the material presented a single mode PSD and the reduction of the intruded porosity upon wetting is observed (Figure 4.22.b).
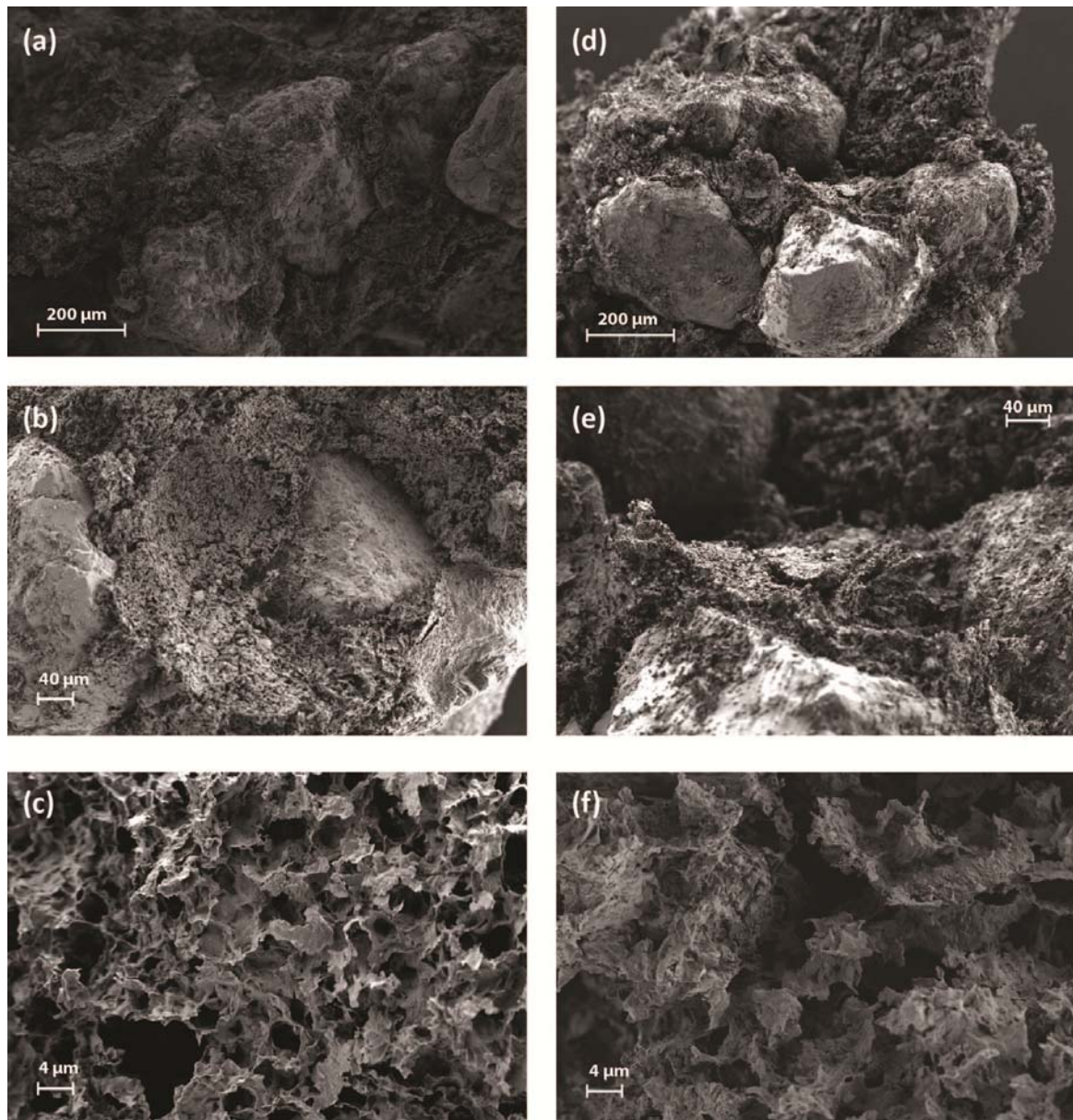
Figure 4.21: SEM images at different magnifications of the S/B mixture compacted to a dry density of 1.5 Mg/m³ and hydrated with distilled water (a) and sodium chloride solution at 1 Mol/litre concentration.
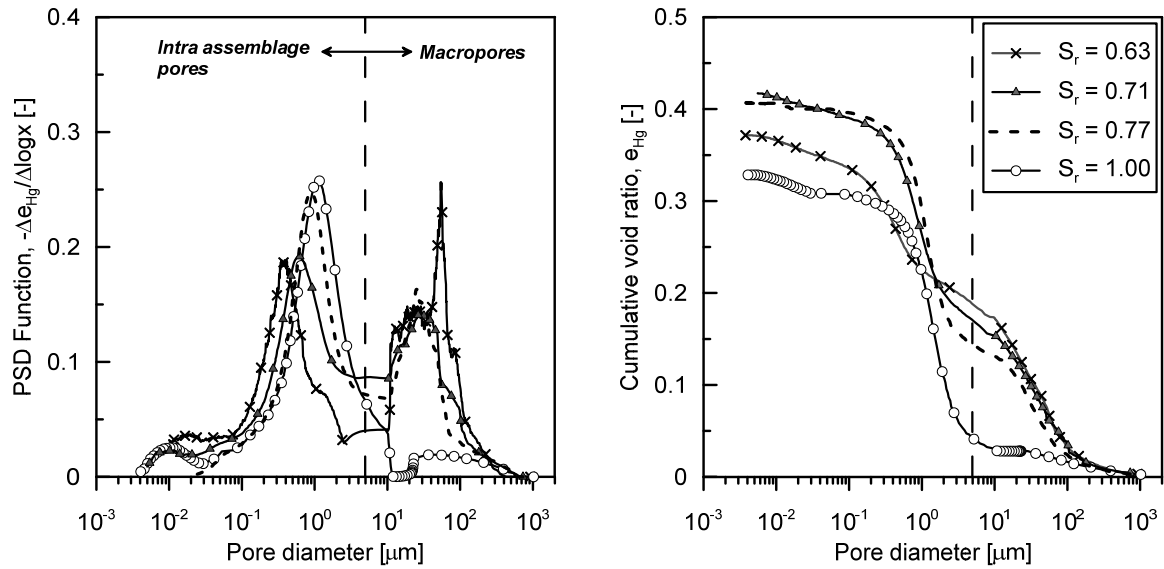
Figure 4.22: : Pore structure evolution of the S/B mixture subjected to wetting process under constant volume conditions initially compacted to a dry density of 1.8 Mg/m³ and wetted with synthetic water.

4.6 DISCUSSION: FROM THE MICROFABRIC TO THE MACROSCOPIC BEHAVIOUR

4.6.1 Quantitative evaluation of the micro, macro and nano void ratio

Quantitative evaluations of void ratios are possible with the MIP measurements upon the selection of an appropriate criterion for distinguishing the different pore regions. The position of the micro/macro pore threshold is not trivial and may change depending on the type of material that is analysed (Romero et al., 2011).

In this paragraph, a new criterion for dividing macropores from the bentonite pores, in the tested S/B mixture, is proposed. To prove its efficiency for the determination of the void ratio of the different pore families, the obtained void ratio trends are compared with three criteria proposed by other authors. The basic principles of tested criteria are briefly recalled in the following:

1) Romero et al. (2011)-a. This criterion is based on the interpretation of the water retention behaviour of the material. In this case the intra-aggregate pore region is defined as the pore domain in which the retention curve is not sensitive to the changes in total void ratio and water is mainly retained by adsorption mechanism. On the contrary, the macropore region is defined as the zone where capillary mechanism is dominant and thus is very sensitive to the change in void ratio. Once the threshold suction, which divides the macropore dominant retention region from the micropore dominant retention region, is selected, the corresponding pore radius is determined according to the Laplace equation. The

148

disadvantage of this criterion is that it requires the determination of the retention capacity of the material at least for two different void ratios and for a large suction domain. This, for the tested S/B mixtures, implies a long time for the experiments. For the tested S/B mixture wetted with distilled water, the suction threshold value is located at 3 MPa (Figure 2.30). The threshold pore diameter for the tested mixture resulted located at x_t=93 nm.

2) Delage and Lefebvre (1984) and Delage et al. (1996). This criterion is based on the assumption that the micropores are considered as non-constricted pores. Thus, all the mercury that is injected in these pores during the pressure increasing phase is recovered during the pressure decreasing phase of the MIP test. According to this criterion, the limiting pore diameter for the mixture wetted with distilled water ranges from 90 to 200 nm.

3) Romero et al. (2011)-b. This criterion is based on the assumption that, for any compacted soil, a threshold that distinguishes the intra and inter-aggregate pores must exists. This threshold is defined as an upper bound for the micropores and a lower bound for the macropores, at the same time. Following this criterion, the threshold coincides with the dominant pore diameter of the PSD of the mixture fully saturated at constant volume, equal to 1.8 μm.

The criterion proposed by the author (criterion n°4) is based on the dual observations of the MIP and SEM data. For the case under study, regardless of the compaction dry density, the MIP and SEM observations show that macropore volume strongly decreases after full saturation with distilled water (e.g., Figure 4.14 and Figure 4.21.b). This reduction is a consequence of the expansion of the bentonite assemblages, which occlude the macropores. Figure 4.14, Figure 4.18, and Figure 4.19 show that larger pores that disappear after the saturation are larger than 5 μm; in this sense, the threshold value $x_t =$ 5 μm is used to delimit the macropore region from the remainder (Figure 4.23). In this study, this value is assumed as independent from the compaction density of the material and is in very good agreement with the separation between the micropore and the macropore peaks of the PSD for the as-compacted states (Figure 4.10). Along with the maximum intruded void ratio ($e_{Hg,max}$), this threshold value allows quantification of the different void ratios for the considered testing conditions (Figure 4.23).

Following the definition of pore families given in section 4.3 and according to the MIP capabilities the different void ratios are discriminated based on their pores size and computed as follows (Figure 4.23):

$$e_{Hg,max} = \int_{x_{min}}^{x_{max}} F(x)dx \tag{4.7}$$

$$e^M = \int_{x_t}^{x_{max}} F(x)dx \tag{4.8}$$

$$e^m = \int_{x_{min}}^{x_t} F(x) \qquad (4.9)$$

$$e^n = e - e_{Hg,max} \qquad (4.10)$$

$$e^b = e^m + e^n \qquad (4.11)$$

where $F(x)$ is the PSD function at a given HCM state, x is the apparent pore diameter at a given pressure, x_{max} and x_{min} are the larger and the smaller pore diameter detected with the MIP apparatus, and e^n refers to the interlayer pores and the micro pores which are smaller than 4 nm.

The four criteria were tested to track the evolution of the pore fabric of a mixture prepared to a dry density of 1.5 Mg/m^3 and wetted to different water contents under isochoric conditions (Figure 2.25).

The evolution of the void ratios calculated for the four different partition criteria is presented in Figure 4.25. When the void ratios are calculated in agreement with criterion n° 1 and n° 2, the macro void ratio increases as the matric suction of the mixture decreases; simultaneously, the bentonite void ratio is decreasing showing a contraction of the bentonite clusters during wetting. If the void ratios are calculated in agreement with criterion n° 3, after an initial decrease of the macropores volume and an initial increase of the bentonite volume along wetting, it appears that the wetting is associated to increase of the macro voids and a reduction of the bentonite volume. These results are clearly not compatible with the SEM observations presented in Figure 4.16 where it is shown that the wetting under constant volume condition of the mixture produces an occlusion of the macropores due to the expansion of the bentonite. This demonstrates that criterion n° 1, n° 2 and n° 3 are not appropriate to separate the different pore families of the tested S/B mixture.

When the void ratios are calculated with the criterion proposed in this study, the process of water uptake under constant volume conditions leads to the reduction of the macropores volume as a consequence of the increase of the bentonite void ratio. The macrostructural void ratio linearly decreases with the logarithmic of suction from a maximum value of 0.28 at the as-compacted state to a minimum value 0.08 at full saturation. The bentonite pore volume tends to approach the total pore volume and the nanopores seem to be converted into micropores. A deeper discussion of these results is given in section 4.5.2.

The proposed criterion is applied for the data analysis of the pore structure evolution of the mixture tested under all the applied HCM loadings.
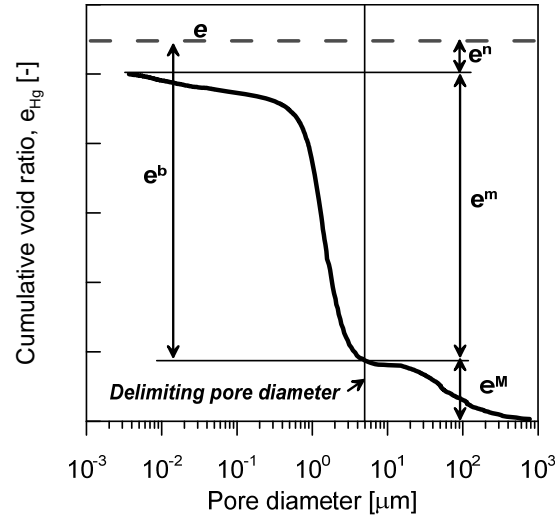
Figure 4.23: Criterion proposed by the author for the repartition of the void ratios.
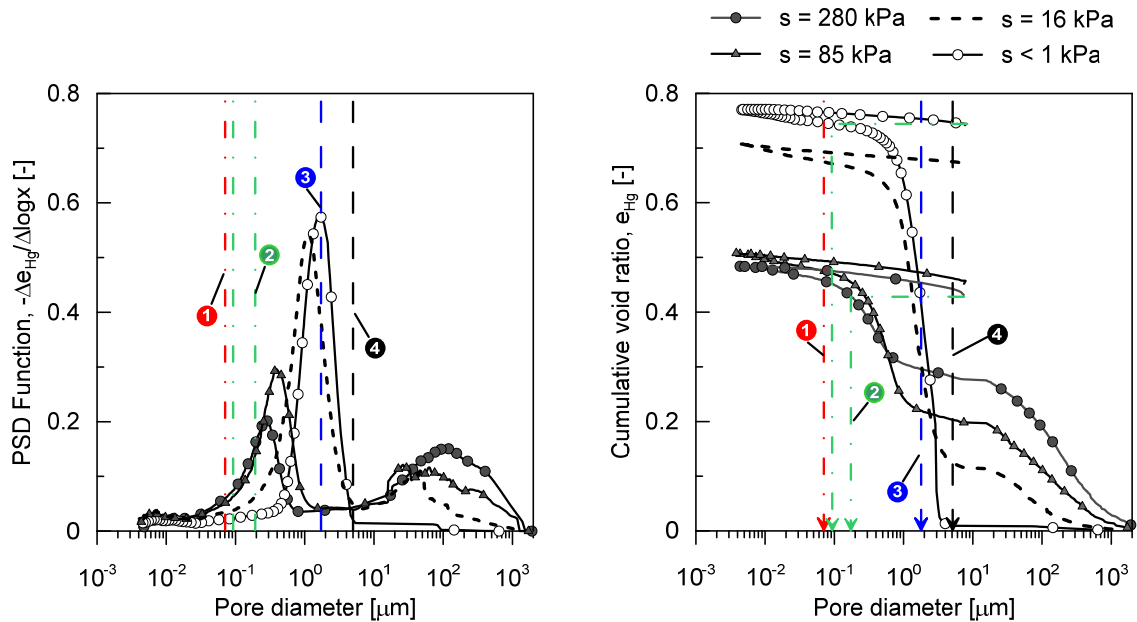
Figure 4.24: Positioning of the bentonite/macropores thresholds in agreement with four different criteria.

4.6.2 Phase relationship of generic sand/bentonite mixtures

When dealing with sand/bentonite mixtures, to allow the comparison with mixtures prepared at different densities or at different mixing ratios, it is convenient to refer to parameters that describe the hydro-mechanical state of the bentonite fraction within the mixture. With this regard, Komine and Ogata (1999) calculated the volumetric deformation of the montmorillonite minerals (ε_{sv}^*) as a function of the volumetric strain measured in free swelling tests. Komine (2004) used this parameters to compare the data on permeability of S/B mixtures prepared at different mixing ratios. Mollins et al. (1996) proposed to calculated the void ratio of the bentonite as the ratio of the water volume to its solid volume and used this parameter to compare the hydraulic conductivity of

mixtures prepared with different bentonite content. Dixon (2000), Agus and Schanz (2008a) and Karnland et al. (2008) use the bentonite dry density (also called effective clay dry density) to compare the swelling behaviour of various S/B mixtures.

In those studies, the calculations of the clay dry density, clay void ratio, and clay deformations were based on two main assumptions:

1) All the pores within the sand fraction are fully occluded by the swollen bentonite. The experimental results presented in section 4.5 shows that this assumption is applicable only when the S/B mixture is fully saturated with distilled water or with low charged aqueous solutions. Moreover, SEM observations proved that, in a mixture fully saturated with distilled water, the minum bentonite content to ensure that all the macropores are bentonite-sealed is 15 % in dry mass (Komine, 2004).

2) The volume of the voids of the bentonite is equal to the volume of the water stored in the mixture. This assumption, if applied for a mixture in unsaturated conditions, implies that the bentonite is always fully saturated during the hydration process. This hypothesis is proved to be wrong in section 4.6.4.

Based on equation (4.4), the bentonite void ratio (e^b), as well as the macrostructural void ratio, are referred to the total volume of solids (bentonite and sand). In this study, the relative bentonite void ratio is expressed as the ratio of the voids within the bentonite to the bentonite solid volume. In order to do so, a schematic representation of the phases composing a sand/bentonite mixture is presented in Figure 4.26. The solid phase is divided into the coarse solid phase (sand) and fine solid phase (bentonite).

The total volume of the voids in the mixture is written as the sum of the volume of the intra bentonite clusters pores (V_v^b) and the volume of the pores located between the clusters and the sand grains (V_v^M) as follows:

$$V_v = V_v^b + V_v^M \tag{4.12}$$

The combination of equation (4.12) and equation (4.4) yields to:

$$e = \underbrace{\frac{V_v^b}{V_s^{Mix}}}_{e^b} + \underbrace{\frac{V_v^M}{V_s^{Mix}}}_{e^M} \tag{4.13}$$

with $V_s^{Mix} = M_s^{Mix} / \rho_s^{Mix}$ being the volume of all the solid particles.
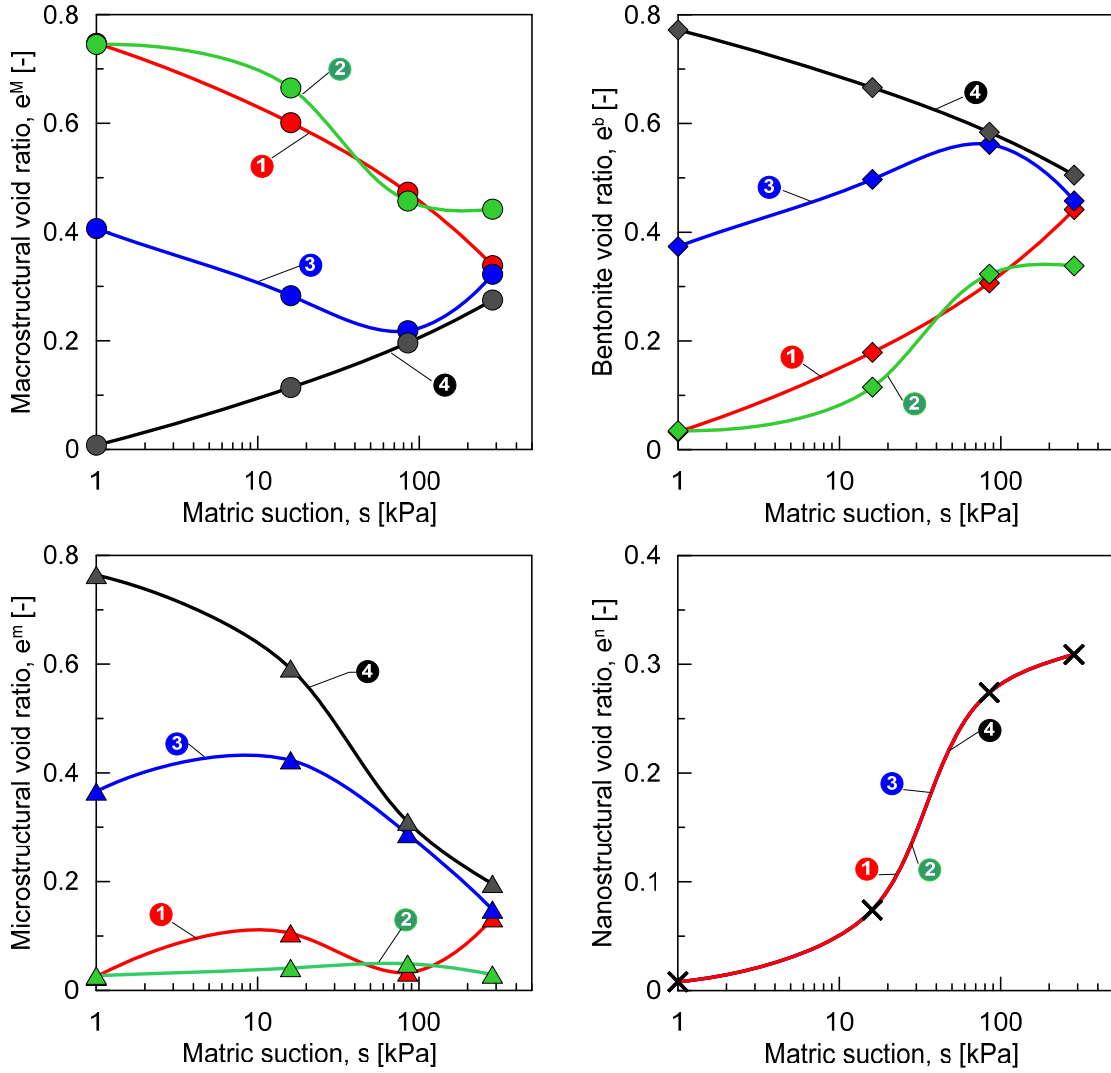
3) **Figure 4.25: Void ratios evolution based on the different tested partition criteria.**

The volume of void of the bentonite can be also written as:

$$V_v^b = e^{b,rel} \cdot V_s^b \tag{4.14}$$

where $e^{b,rel}$ is the bentonite void ratio referred to the volume of the solid of bentonite V_s^b.

The relative bentonite void ratio is obtained by combining equation (4.13) and equation (4.14), as follows:

$$e^b \cdot V_s^{Mix} = e^{b,rel} \cdot V_s^b \quad \rightarrow \quad e^{b,rel} = \frac{e^b \cdot V_s^{Mix}}{V_s^b} \tag{4.15}$$

Equation (4.15) can be further simplified by expressing the solid volume of the mixture and the solid volume of the bentonite as the ratio of the dry mass to its dry density, as follows:

153

$$V_s^{Mix} = \frac{M_s^{Mix}}{\rho_s^{Mix}}; \quad V_s^b = \frac{R^b M_s^{Mix}}{\rho_s^b} \tag{4.16}$$

Where R^b is the ratio of the bentonite in the mixture. With this final simplification the following expression of the relative bentonite void ratio is obtained:

$$e^{b,rel} = \frac{e^b \cdot \rho_s^b}{R^b \cdot \rho_s^{Mix}} \tag{4.17}$$

If similar developments are applied to the macrostructural void ratio, it is also possible to write the relative macrostructural void ratio as follows:

$$e^{M,rel} = \frac{e^M}{\left(1 - \frac{R^b \cdot \rho_s^{Mix}}{\rho_s^b}\right)} \tag{4.18}$$

Eq. (4.17) and eq. (4.18) allow rescaling the bentonite- and macro-void ratio obtained from the MIP measurements to account for the volume of the different solids and thus the direct comparison of the MIP measurement obtained at different compaction densities and mixing ratios.

The relative bentonite void ratio allowed the calculation of the relative bentonite dry density ($\rho_d^{b,rel}$) which is defined as the ratio of the dry mass of the bentonite to its total volume; i.e.:

$$\rho_d^{b,rel} = \frac{\rho_s^b}{1 + e^{b,rel}} \tag{4.19}$$

Equations (4.18) and (4.19) enable a direct comparison of the hydro-mechanical performances of sand/bentonite mixtures upon any HCM loading and prepared to any mixing ratio without making any of the restrictive assumptions discussed in the first part of this section.
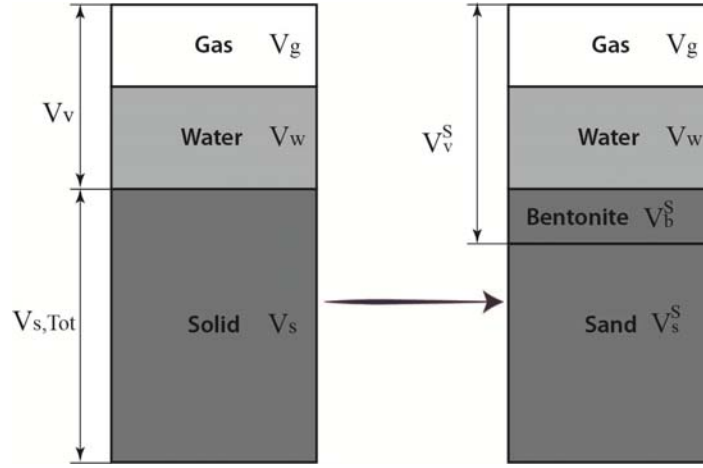
Figure 4.26: Phase diagram for sand/bentonite mixtures.

The dry density of the bentonite and the sand in the mixture are obtained as the ratio of the dry mass (of sand or bentonite) to the total volume as follows:

$$\rho_d^S = R^S \frac{\rho_s^{Mix}}{(1+e)} \tag{4.20}$$

$$\rho_d^b = R^b \frac{\rho_s^{Mix}}{(1+e)} \tag{4.21}$$

Knowing the relative void ratio of the bentonite, it is also possible to calculate its relative degree of saturation ($S_r^{b,rel}$) at any hydro-mechanical state as follows:

$$S_r^{b,rel} = \frac{w^b \rho_s^b}{e^{b,rel} \rho_w} \tag{4.22}$$

where w^b is the water content of the bentonite only. For this calculation it is assumed that the water is preferably stored within the bentonite pores rather than in the macropores. This assumption is justified when considering the higher retention capacity of the clayey fraction with respect to the sandy fraction and it is apply only when distilled water is used as pore fluid. Indeed, when the pore fluid contains dissolved salts the retention capacity of the bentonite is expected to decrease.

Water is stored in the macropores only when the pores of the bentonite are fully saturated ($S_r^{b,rel} = 1$). Based on this assumption the relative degree of saturation of the macropores ($S_r^{M,rel}$) is calculated as the ratio of the volume of water stored in the macropores (V_w^M) to the macropores volume (V_v^M):

$$S_r^{M,rel} = \frac{V_w^M}{V_v^M} \tag{4.23}$$

155

These volumes are calculated as follows:

$$V_w^M = V_w - V_w^b = \left(w - w^b R^b \right) \frac{M_s^{Mix}}{\rho_w},$$ (4.24)

$$V_v^M = e^M V_s^{Mix}$$ (4.25)

In eq. (4.24) the water content of the bentonite is calculated from eq. (4.22) considering $S_r^{b,L} = 1$.

The combination of eq. (4.23), (4.24) and (4.25) yields to:

$$S_r^{M,rel} = \frac{\left(w - w^b R^b \right)}{e^M} \frac{\rho_s^{Mix}}{\rho_w}$$ (4.26)

Similar to the total void ratio, the total degree of saturation is expressed as the sum of the degree of saturation of the bentonite (S_r^b) and the macropores (S_r^M) (Koliji, 2008, Della Vecchia et al., 2014):

$$S_r = S_r^b + S_r^M$$ (4.27)

In the equation above, the degrees of saturation of the bentonite and the one of the macropores are referred to the total volume of the voids. In order to link the relative degrees of saturation of bentonite and macropores in the equation, S_r^b and S_r^M need to be referred to total volume of the voids belonging to theirs own solid fractions, as follows:

$$S_r^b = S_r^{b,rel} \frac{e^b}{e}$$ (4.28)

$$S_r^M = S_r^{M,rel} \frac{e^M}{e}$$ (4.29)

The parameters $\dfrac{e^b}{e}$ and $\dfrac{e^M}{e}$ represent the volume fraction of pores belonging to the bentonite fraction and the macropores fractions, respectively. These will be referred in the next parts of the thesis as ϕ^b and ϕ^M. Finally, the combination of the equations (4.27), (4.28) and (4.29) yields:

$$S_r = \phi^b S_r^{b,rel} + \phi^M S_r^{M,rel}$$ (4.30)

4.6.3 Fabric evolution along hydro-chemo-mechanical loadings

4.6.3.1 The as-compacted state

The evolution of the void ratio of the different pore families defined in section 4.6.1 is illustrated in Figure 4.27. The values are also listed in Table 4.3.

The action of compaction causes the decrease of the relative macropore void ratio, which suggested the macropore closure, and simultaneous reduction of the relative bentonite void ratio (Figure 4.27, left). The reduction of the bentonite volume should be associated to the reduction of the volume of both the micro and nano pores. However, an increase of the micropores was observed suggesting the conversion of some macropores into micropores as a consequence of the fusing of the bentonite aggregates (Figure 4.27, right). At the as-compacted water content the bentonite water content (w^b =55% - calculated considering that all the water is stored in the bentonite) is close to its plastic limit. At this high water content, bentonite aggregates have a relatively low stiffness and are prone to compaction especially when subjected to the high applied vertical stress (σ_v up to 20 MPa) required to reach the higher mixture densities. This result is in contrast with the results obtained by other authors (e.g., Lloret and Villar, 2007, Cuisinier and Laloui, 2004, Romero et al., 2011) and proves that the volumetric deformations of the bentonite aggregates subjected to compaction under constant water content (and constant suction) are irreversible.

Figure 4.28 presents the evolution of the different pore families of specimens compacted to the same density and wetted with four different aqueous solutions to the 11% of water content. Data are here presented as a function of the total suction of the pore fluid. Numerical values of the different void ratios are reported in Table 4.4. A reduction of the bentonite volume, with the increase of the pore water salinity, is observed. The nano void ratio increases with the increase of the osmotic suction of the pore water, suggesting the partial inhibition of the mechanism of crystalline swelling, in agreement with the results of Suzuki et al. (2005). The macropore remains almost constant because the volume of the precipitate of the salts in the aqueous solution, that deposit on the grains surface (e.g., see Figure 4.13), compensates the increase of the macropore volume related to the shrinkage of the bentonite aggregates (Liu et al., 2014).

Table 4.3: Void ratios at the as compacted state for tree different compaction densities.

Specimen code	e^M [-]	e^b [-]	$e^{M,rel}$ [-]	$e^{b,rel}$ [-]	e^m [-]	e^n [-]
DW_01w	0.28	0.58	0.35	2.98	0.16	0.43
DW_02w	0.28	0.50	0.35	2.57	0.20	0.30
DW_03w	0.31	0.46	0.38	2.36	0.16	0.30
DW_10w	0.22	0.26	0.27	1.34	0.20	0.06
DW_11w	0.23	0.26	0.29	1.34	0.22	0.04
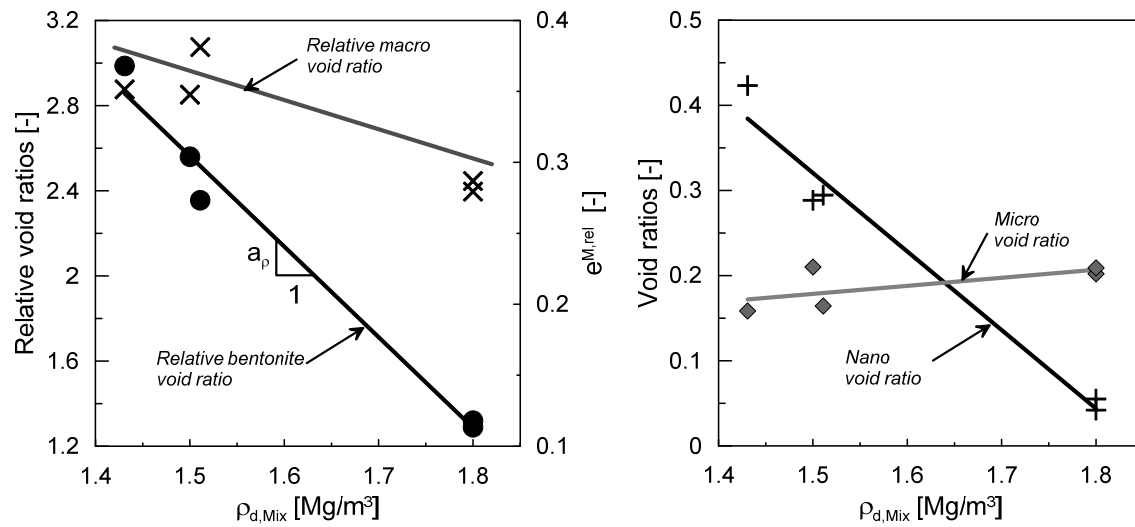
Figure 4.27: Microstructural evolution of the 80/20 S/B mixture at the as-compacted state.

Table 4.4: Void ratios at the as-compacted state for specimen prepared with different pore fluids.

Specimen code	e^M [-]	e^b [-]	$e^{M,rel}$ [-]	$e^{b,rel}$ [-]	e^m [-]	e^n [-]
DW_02w	0.28	0.50	0.35	2.57	0.20	0.30
DW_03w	0.31	0.46	0.38	2.36	0.16	0.30
SW_01w	0.25	0.53	0.31	2.72	0.15	0.38
1M NaCl_01	0.30	0.47	0.37	2.41	0.16	0.31
4M NaCl_01	0.31	0.47	0.38	2.41	0.12	0.36
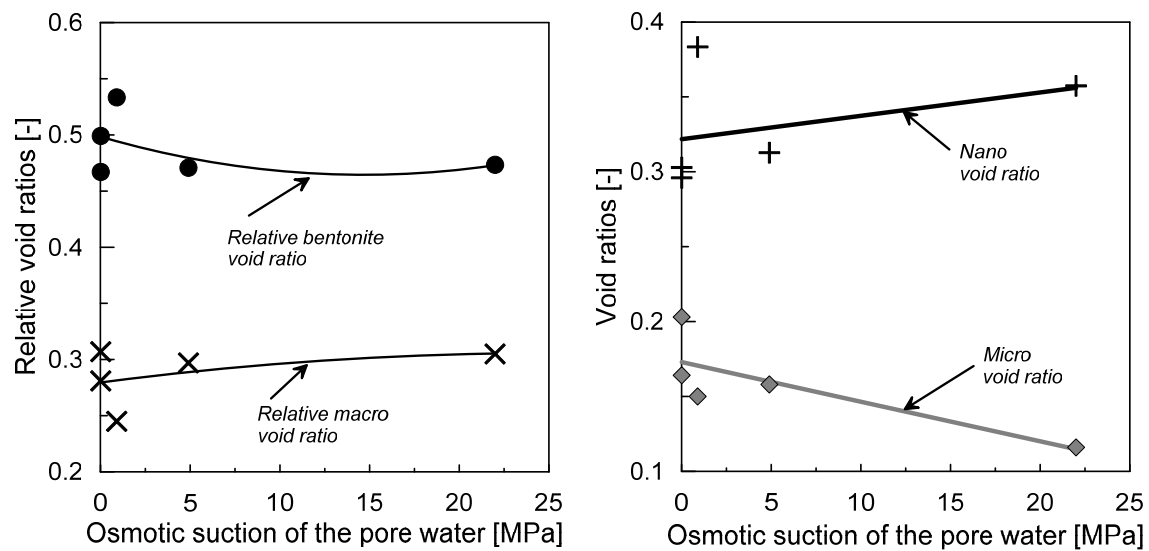
Figure 4.28: Microstructural evolution of the 80/20 S/B mixture at the as-compacted state prepared with different pore fluids.

4.6.3.2 *Fabric evolution along wetting and drying under constant volume conditions*

The evolutions of the defined structural void ratios during wetting with distilled water under isochoric conditions are derived from the data in Figure 4.17 and Figure 4.18 for specimens compacted to 1.5 and 1.8 Mg/m^3, respectively. The computed void ratios are listed in Table 4.5 and depicted in Figure 4.29 and 4.30 as a function of the matric suction.

Regardless of the tested density, the wetting process under isochoric conditions involves the expansion of the bentonite until the macropores are fully occluded (Figure 4.29.a and 30.a). In the S/B mixture under the as-compacted condition (w=11%), the majority of the smectite sheets already accommodate the maximum number of water molecules. In this configuration, a quasicrystal would consist of a stack of less than 10 smectite layers (Saiyouri et al., 1998, Bestel, 2014). Therefore, the swelling of bentonite aggregates can be attributed only to further splitting of the quasicrystals. At the lower density, the splitting phenomenon is clearly observable as a large reduction of the nanostructural void ratio. This reduction, along with the invasion of the macropores, causes the increase of the microstructural void ratio (Figure 4.29.b). In the saturated state, the micropore void ratio approaches the total void ratio. In this condition, the different pore families converge to the same pore size range and the distribution of the different pore families become uniform. At the higher density, the reduced space available for the bentonite expansion results in a partial splitting of the quasicrystals and in the compression of a fraction of the smaller intra-assemblage pores. This compression is observable in Figure 4.30.b as an increase of the nanostructural void ratio.

Table 4.5: Void ratios at along a drying and wetting cycle for specimen compacted to the target densities of 1.5 Mg/m^3 and 1.8 Mg/m^3.

Specimen code	e^M [-]	e^b [-]	$e^{M,rel}$ [-]	$e^{b,rel}$ [-]	e^m [-]	e^n [-]	s [kPa]
DW_02w	0.28	0.50	0.35	2.57	0.21	0.29	280
DW_03w	0.31	0.46	0.38	2.36	0.16	0.29	280
DW_04w	0.25	0.58	0.31	2.98	0.31	0.27	90
DW_05w	0.11	0.68	0.14	3.49	0.60	0.08	11
DW_06w	0.01	0.75	0.01	3.85	0.75	0.00	1
DW_01w2	0.20	0.58	0.25	2.98	0.33	0.25	60
DW_01d	0.19	0.55	0.24	2.82	0.36	0.19	500
DW_09w	0.22	0.25	0.27	1.28	0.20	0.05	280
DW_10w	0.25	0.23	0.31	1.18	0.15	0.08	280
DW_11w	0.23	0.26	0.29	1.34	0.21	0.05	280
DW_12w	0.20	0.29	0.25	1.49	0.23	0.05	60
DW_13w	0.16	0.33	0.20	1.69	0.24	0.10	11
DW_14w	0.01	0.47	0.01	2.41	0.27	0.20	1
DW_02d	0.02	0.46	0.02	2.36	0.26	0.20	500
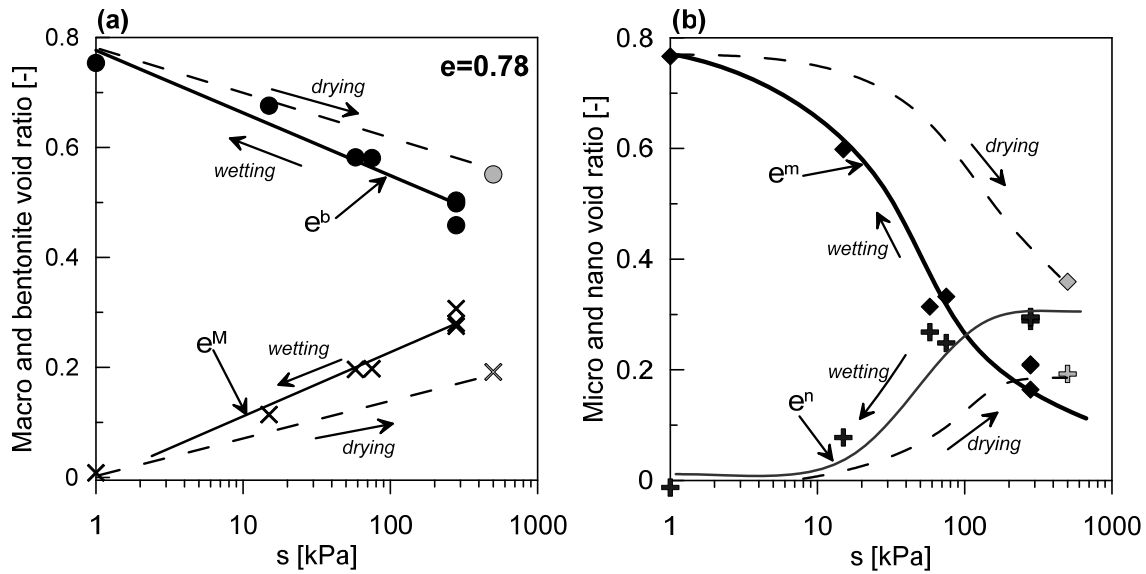
Figure 4.29: Evolution of the micro-, macro- and nano-structural void ratios versus suction for a specimen compacted to a dry density of 1.5 Mg/m³.
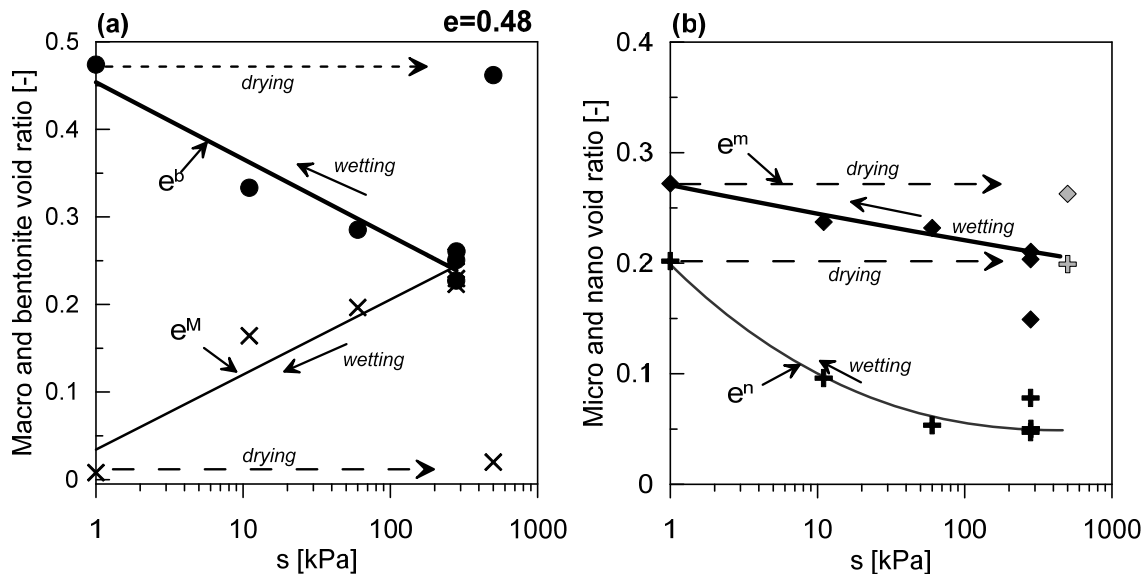
Figure 4.30: Evolution of the micro-, macro- and nano-structural void ratios versus suction for a specimen compacted to a dry density of 1.8 Mg/m³.

At the end of the drying path the two densities show an opposite behaviour. For the lower dry density, the partial reversibility of the internal volumetric deformation of the bentonite is observed because of the large reduction of the bentonite void ratio and the consequent creation of macropores. The bentonite shrinkage is believed to be due to the fusing of the smectite sheets to form some quasicrystals and is associated to the reversibility of the splitting phenomenon. For the mixture compacted to the higher density, it is observed that during the drying, the bentonite void ratio remains constant indicating that bentonite experienced irreversible volumetric deformations. This trend of the bentonite was already observed in an highly compacted MX-80 granular bentonite subjected to drying and wetting cycles by Seiphoori et al. (2014) and confirms that at high compaction density the mechanism of particle subdivision is irreversible. These last

160

observations, together with the observation of irreversible volumetric deformation under compaction at constant water content (section 4.6.3.1), proves that the assumption of the full reversible response of the microstructure in describing the behaviour of double structure clays (e.g., Gens and Alonso, 1992, Lloret et al., 2003, Airò Farulla et al., 2010b) is applicable only under certain conditions (e.g., low swelling clays).

The evolution of the relative void ratio of the bentonite and the macropore along wetting is depicted in Figure 4.31.a as a function of the matric suction. It is observed that the two curves for the two tested densities follow a parallel trend. The following expression is proposed to quantify the swelling of the bentonite:

$$e^{b,rel}\left(\rho,s\right) = e_0^{b,rel} - a_\rho \left[\rho_d - \rho_{d,0}\right] + a_s \, ln\left[\frac{s_0}{s+1}\right] \tag{4.31}$$

where $e^{b,rel}$ is the relative void ratio of the bentonite at the reference dry density $\rho_{d,0}$ and for the reference matric suction of s_0, and a_ρ and a_s are material parameters which are indicated in Figure 4.27 and Figure 4.31. The values of these parameters are listed in Table 4.6.

Table 4.6: Fitting parameters for the calculation of the relative bentonite void ratio.

$e_0^{b,rel}$	2.52	[-]
$\rho_{d,0}$	1.5	[Mg/m^3]
s_0	280	[kPa]
a_ρ	4.87	[m^3/Mg]
a_s	0.22	[-]
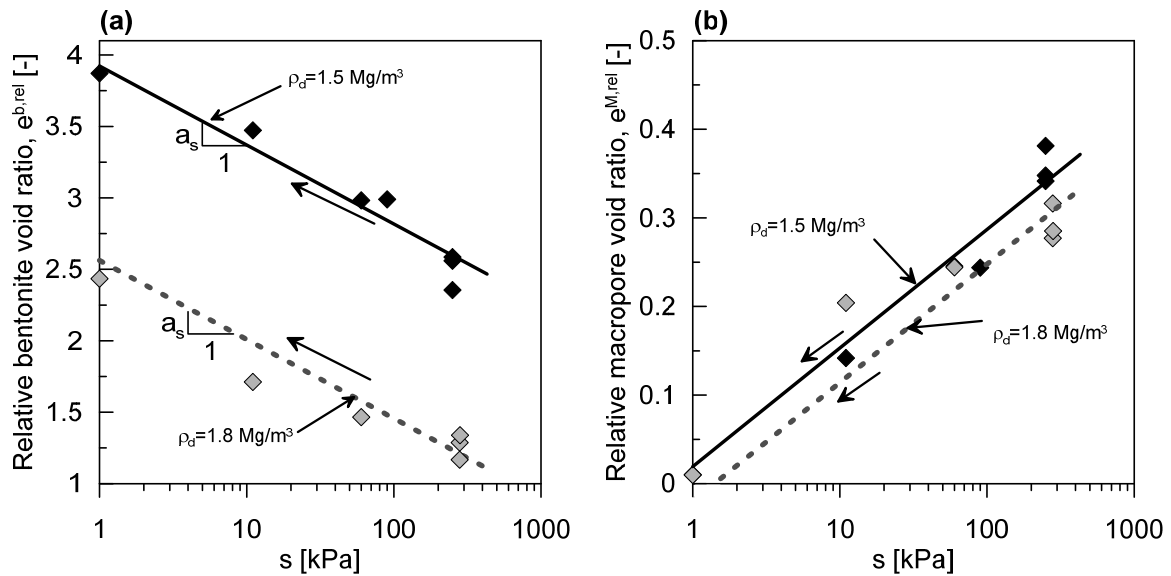
Figure 4.31: Evolution of the relative bentonite void ratio and relative macropore void ratio vs suction along monotonic wetting for two different dry densities.

Eq. (4.31) is a convenient method to compute the relative void ratio of the bentonite as a function of the initial dry density along a wetting path. Therefore, the bentonite and macro void ratios can be computed as follows:

$$\begin{cases} e^b(\rho,s)= e^{b,rel}\, \dfrac{R^b \rho_s}{\rho_s^b} \\ e^M(\rho,s)= e - e^b(\rho,s) \end{cases} \qquad (4.32)$$

4.6.3.3   *Fabric evolution under fully saturated conditions*

Influence of the relative bentonite dry density

Figure 4.32 reports the evolution of the relative bentonite void ratio, along with its two components (e^m and e^n) for specimens at full saturation and compacted to different dry densities. Results are presented as a function of the relative bentonite dry density (eq. (4.19)) and compared with the results obtained by Seiphoori et al. (2014) for a pure bentonite compacted to 1.8 Mg/m³ dry density. In the figure, e^m and e^n are normalised for the bentonite void ratio to show the relative importance of the different microscopic swelling mechanism for the different bentonite dry densities. Macrostructural void ratio is not reported because it approaches zero under full saturation. At full saturation and low mixture density, all the pores appear in the size of micropores and no nanopores are left as the splitting of the smectite quasicrystals fully took place. Under this conditions, voids among the coarse fraction are fully filled with a bentonite gel of very low density of 0.55 Mg/m³ organise in a honeycomb structure (Keller et al., 2014). For this low bentonite density, the swelling of the mixture involved the conversion of interlayer pores into micropores and the homogenisation of the pore structure.

The increase of bentonite dry density is reflected into an increase of the degree of confinement for the quasicrystals. In the case of denser mixture (ρ_d = 1.8 Mg/m³) the bentonite reaches a density of 0.79 Mg/m³. As the pores within the sand are smaller, and the free swelling of the bentonite is limited, the possibility of the quasicrystals to spit is partially impeded. This causes and increase of the swelling pressure of the mixture. Finally, the increasing in non-intruded pores reflects the compression of some micropores that became too small to be intruded by mercury.
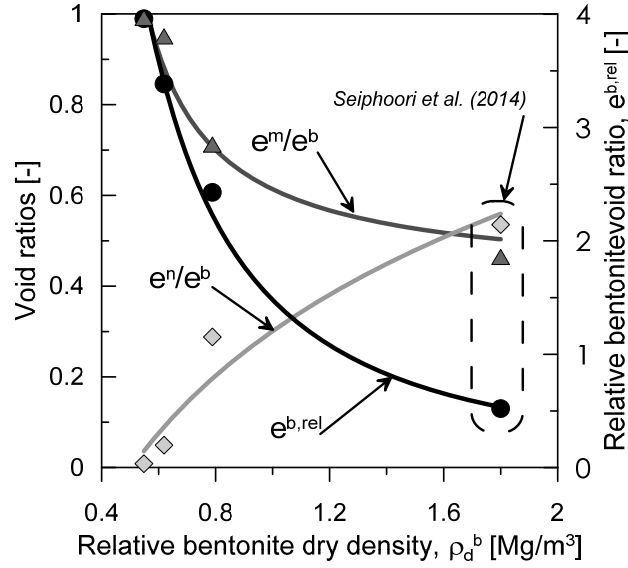
Figure 4.32: Evolution of the micro, macro and nano structural void ratios as a function of the bentonite dry density.

Because the pores within the sand are fully filled with expanded bentonite the relative bentonite dry density can be calculated also as the ratio of dry mass of the bentonite divided by the volume of the pores within the sand:

$$\rho_d^{b,rel} = \frac{R^b}{\left(\dfrac{1}{\rho_d^{mix}} - \dfrac{R^S}{\rho_s^S} \right)} \tag{4.33}$$

The ratio of micropores to the bentonite pores can be expressed as a function of the relative bentonite dry density as:

$$\frac{e^m}{e^b} = \frac{\rho_d^{b,rel}}{a + b\rho_d^{b,rel}} \tag{4.34}$$

where $a = -0.80\,[\text{Mg/m}^3]$ and $b = 2.43\,[-]$ are fitting parameters.

Influence of the pore water salinity

The void ratios of a mixture compacted to a dry density of 1.5 Mg/m^3 and fully saturated with different permeants were derived from Figure 4.20. The results are presented in Figure 4.33 as a function of the osmotic suction of the permeants. The reduction of the swelling of the bentonite aggregates and the consequent opening of the macropores with the increase of the osmotic suction is clearly observed. Shrinkage of the bentonite is attributed to the simultaneous reduction of the double layer swelling and the splitting of the quasicrystals. The reduction of the double layer swelling is observed as a reduction of the micropore volume and is attributed to the compression of the thickness of the electrostatic double layer, which varies from a maximum of 20 nm with distilled water to 3 Å when the concentration of salts in the free water exceeds 1 M (Tournassat and Appelo, 2011). The inhibition of the splitting process causes the augmentation of the

number of sheets per quasicrystal and is reflected in the increase of the nanostructural void ratio. The bentonite wetted with 1 M NaCl solution shows a slightly higher swelling capacity than the synthetic water. This result can be related to the presence of other divalent cations, in addition to Na, in the synthetic water. Divalent cations produce a larger compression of the EDL, whereas the Ca and Mg cations reduce crystalline swelling and inhibit the splitting of quasicrystals because of the cation demixing process.

The evolution of the bentonite void ratio with the osmotic suction of the pore water is described by the following equation:

$$e^b = -0.028 \, ln\left(\pi_w\right) + 0.655. \tag{4.35}$$

4.6.4 Insight into the hydro-chemo-mechanical behaviour of the 80/20 S/B mixture

4.6.4.1 Impact of fabric evolution on the swelling pressure development

Seiphoori et al. (2014) defines the swelling pressure as *"the attempt of the swelling material to expand and subdivide at the particle level to include more water molecules after reaching full saturation under constant volume conditions"*. Starting from this definition, the variations of the swelling pressure of the tested S/B mixture, and more in general on bentonite-based materials subjected to different hydro-chemo-mechanical loadings are discussed in the light of the important couplings happening at the various microstructural levels.
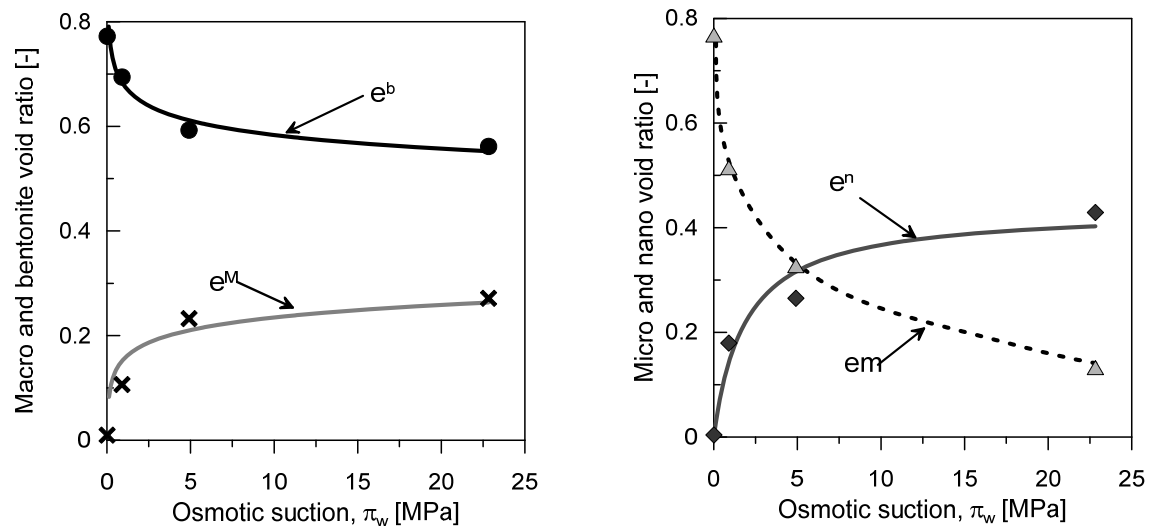
Figure 4.33: Evolution of the micro-, macro- and nano-structural void ratios as a function of the pore water osmotic suction for a specimen compacted to a dry density of 1.5 Mg/m³.

The generation of the swelling pressure is associated with the attempt - hindered by the sand grains - to develop the electrostatic diffuse double layer among the quasicrystals and the tendency of the particle to reorient while splitting. These mechanisms justify the generation of the swelling pressure before the material has reached the full saturation and the macropores are completely occluded by the expansion of the bentonite (Figure 2.17). As a consequence, the swelling pressure generation in unsaturated conditions is a partially-constrained intra-aggregated swelling process. However, the degree of constrain of the aggregates depends on the density of the solid skeleton constituted by the grains of sand.

Along the main drying, the deformations of the bentonite aggregates at the microstructural level are almost fully reversible, for a mixture compacted to 1.5 Mg/m³, and the related reduction of swelling pressure is observed. For a mixture compacted to the higher dry density, the deformations at the microstructural level are non-reversible and the related swelling pressure curve show a much larger hysteresis.

The use of the relative dry density of the bentonite is a powerful tool to compare data on the swelling of different bentonite-based materials prepared at different densities. Figure 4.34 reports the swelling pressure of the samples saturated with distilled water (Figure 2.15) as a function of the relative dry density of the bentonite attained at the end of the swelling process. The relative dry density is computed using equation (4.19), given the relative bentonite void ratio (Equation (4.17)). Data from other studies on pure MX-80 bentonite and mixtures containing MX-80 are also reported. A unique trend is observed for the final swelling pressure and is expressed as follows:

$$P_{sw}(kPa) = 7.58 \cdot exp\left(4.09 \cdot \rho_{d,b}^{rel}\right) \tag{4.36}$$

The possibility given by Equation (4.31) to compute the relative bentonite void ratio as a function of suction allowed the depiction in Figure 4.34 of the data obtained in the suction-controlled wetting tests (Figure 2.17). From the plot, it is possible to evaluate the generation of the swelling pressure with the decrease in suction associated with the reduction of the relative bentonite dry density. The final swelling pressures of the controlled-suction tests are in very good agreement with the trend of equation (4.36).
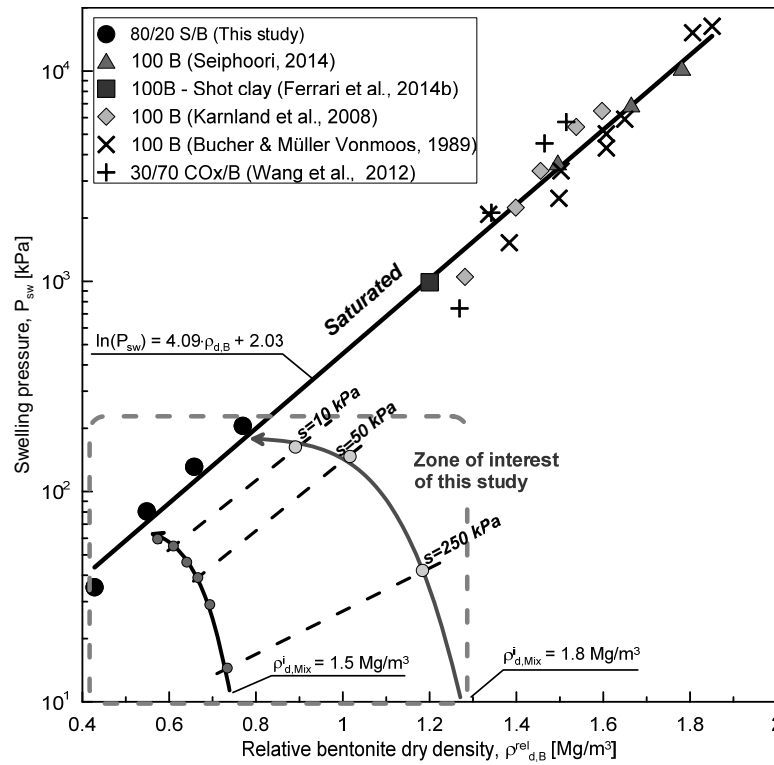
Figure 4.34: Swelling pressure versus bentonite dry density for different soil/bentonite mixtures.

Combing these last observations with the previous ones on the effect of dry density on the fabric of the saturated S/B mixture, some interpretations on the trend of the swelling reduction factor (Figure 2.13 and Figure 2.15) can be made. At the lower dry density, the bentonite wetted with distilled water consists of a gel of very low density arranged in a honeycomb-like structure (Keller et al., 2014). In this configuration, splitting of the quasicrystals is the dominant swelling mechanism, and the full development of the EDL is likely and necessary for the swelling pressure development. The increase in pore water salinity strongly reduces the development of the diffuse double layer and limits the splitting of the quasicrystals. Therefore, at low compaction densities, the macroscopic swelling pressure and strain generated by the material are strongly affected by the pore water salinity. At the higher mixture density, the compression of the macropores has the beneficial effect of reducing the available space for the development of the EDL. In this configuration, the material can generate swelling pressure through other swelling mechanisms, which are not the diffuse double layer swelling. Therefore, the material can preserve its swelling capacity in the presence of aqueous solutions.

4.6.4.2   Water retention behaviour

The results presented in section 2.4.3.2 allowed identifying two zones in the plane suction vs water content where the retention mechanisms are different. For suction higher than 3000 kPa the relationship suction versus water content is independent from the compaction density. For suction lower than 3000 kPa the water retention curves diverge for the two compaction densities.

To give an insight into the water retention behaviour of the tested S/B mixture, at lower suction, the relative degrees of saturation of the bentonite and the macropores are calculated based on the MIP data presented in Figure 4.29 and 4.30 on the evolution of the different void ratios upon wetting, and using equation (4.22) and (4.26). The obtained values are presented in Figure 4.35 and also listed in Table 4.7. Along with the water retention data at the microscopic level, Figure 4.35 also presents the data of the water retention behaviour at the macroscopic level obtained in section 2.4.3.2.

Due to the friable nature of the dry S/B mixture, it was not possible to obtain specimens suitable for the MIP analyses for matric suction higher than 280 kPa. As a consequence, the discussions on the water retention behaviour of the S/B mixture regard only the low suction region.

For the mixture compacted to the lower dry density, and for a suction that varies from 500 to 10 kPa, the local degree of saturation of the bentonite results lower than 1 ($S_r^{b,L} < 1$). The splitting and the reorientation of the smectite quasicrystals yield to the creation of large pores within the bentonite which host all the water. As a consequence, the local degree of saturation of the macropores is null until the mixture is approaching the full saturation and its matric suction is lower than 10 kPa. After this limit, a fast rise of the local degree of saturation of macropores is observed.

When the dry density of the mixture, at the as-compacted water content, is increased from 1.5 to 1.8 Mg/m³ the relative degree of saturation of bentonite aggregates increases from ~0.60 to nearly 1 because of the reduction of the bentonite void ratio (Figure 4.27). In this sense, the compaction process can be interpreted as the mechanical wetting of the bentonite aggregates (Tarantino, 2009). This result justifies the little decrease of matric suction observed when the mixture dry density was increased from 1.5 to 1.8 Mg/m³ (Figure 2.29). During hydration, the bentonite aggregates increase their volume while remaining always fully saturated. The local degree of saturation of the macropores is null at the as compacted state but increases with the increase of the soil water content.

The obtained results suggest that, at low dry density, the adsorptive mechanism of water retention is still active at low suction. Owing to the low degree of constrain imposed by the macropores, the bentonite is allowed to fully express its swelling potential through the splitting of the quasicrystals and the consequent increase of the external surface. As a consequence the transition between the adsorption and the capillary mechanism occurs at very low suctions. On the contrary, when the splitting of the quasicrystals is partially impeded by the reduced dimension of the macropores, the splitting of quasicrystals and the subsequent increase of the external surface of the quasicrystals reduces. Because of this, the water is filling the macropores and the mechanism of capillary retention contributes to the total retention capacity of the mixture.
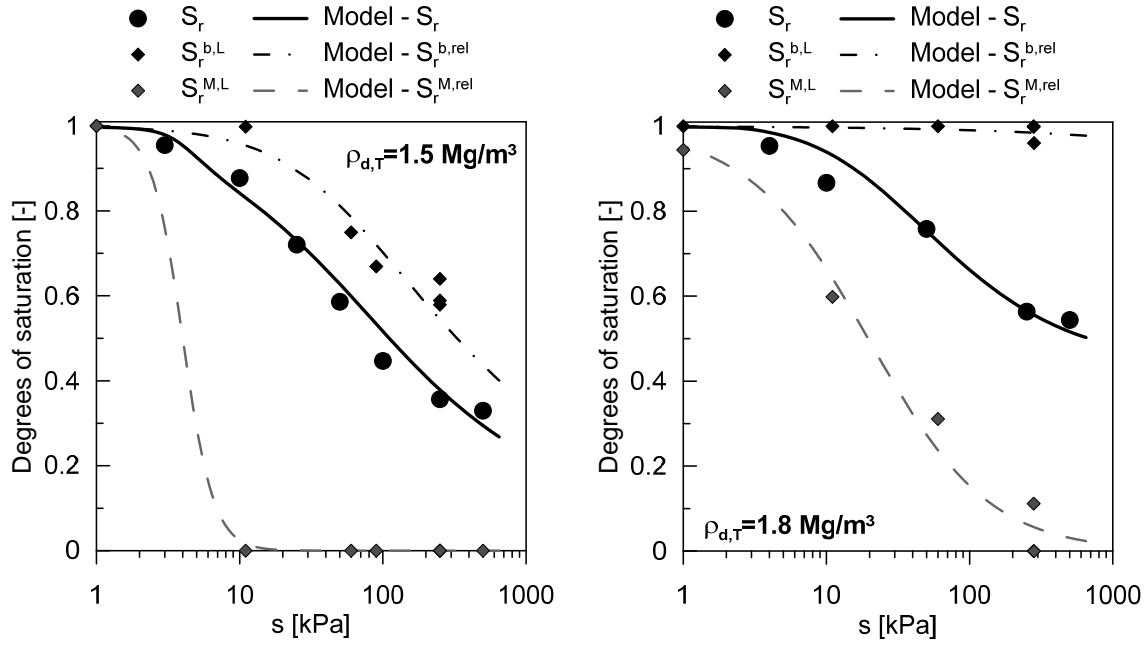
Figure 4.35: Main wetting path of the water retention curve at the microscopic and the macroscopic level for two different dry densities.

Table 4.7: Summary of relative degree of saturation of the bentonite- and the macro-pores.

Specimen code	e [-]	w [%]	S_r [-]	$S_r^{M,rel}$ [-]	$S_r^{b,rel}$ [-]	$\phi^M S_r^{M,rel}$ [-]	$\phi^b S_r^{b,rel}$ [-]	s [kPa]
DW_01w	0.78	0.11	0.38	0.00	0.59	0.00	0.38	280
DW_02w	0.77	0.11	0.38	0.00	0.64	0.00	0.38	280
DW_03w	0.78	0.15	0.50	0.00	0.67	0.00	0.50	90
DW_04w	0.79	0.25	0.85	0.00	1.00	0.00	0.85	11
DW_05w	0.76	0.29	1.03	1.00	0.99	0.01	0.99	1
DW_11w	0.78	0.16*	0.56	0.00	0.56	0.00	0.75	60
DW_01d	0.74	0.16**	0.56	0.00	0.56	0.00	0.76	500
DW_09w	0.47	0.09	0.53	0.00	1.00	0.00	0.53	280
DW_10w	0.48	0.10	0.47	0.11	1.00	0.06	0.47	280
DW_11w	0.49	0.09	0.51	0.00	0.96	0.00	0.51	280
DW_12w	0.48	0.13	0.72	0.31	1.00	0.13	0.59	60
DW_13w	0.50	0.16	0.87	0.60	1.00	0.20	0.67	11
DW_14w	0.48	0.18	1.00	0.94	1.00	0.02	0.98	1
DW_02d	0.50	0.14	0.73	0.00	0.75	0.00	0.72	500

The van Genuchten water retention model was applied to describe the relative water retention behaviour of the bentonite and the macropores for suctions lower than 500 kPa:

$$S_r^{M,rel} = \left[\frac{1}{1 + \left(\dfrac{s}{\alpha^M} \right)^{n^M}} \right]^{m^M} \tag{4.37}$$

$$S_r^{b,rel} = \left[\frac{1}{1 + \left(\dfrac{s}{\alpha^b} \right)^{n^b}} \right]^{m^b} \tag{4.38}$$

where α^M and α^b are associated to the local air entry values of the macropores and the bentonite pores, respectively; n^M, m^M are the fitting parameters for the macropores and n^b, m^b are the fitting parameters for the bentonite pores. The values of these parameters are listed in Table 4.8. The air entry values of the bentonite and the macropores are density dependent.

The relative retention curves of macropores and bentonite pores are well described by equations (4.37) and (4.38). The water retention behaviour at the macroscopic scale of the material is obtained combining equations (4.37) and (4.38) with equation (4.30). It is observed that with the proposed equations the experimental data at the macroscopic scale are very well reproduced.

The same procedure that was applied to obtain the water retention parameters along the main wetting is also used to obtain the main drying. This passage is possible only for the higher dry density because the wetting process produced the irreversible modification of the pore structure so that it was not needed any other MIP tests to capture the evolution of the pore structure along drying. Also, in this case the water retention behaviour of the mixture, along main drying, is well captured by the proposed equation. Because the macropores disappeared after the wetting, the water retention behaviour along drying is dominated only by the bentonite pores.

In the light of the present results, it is possible to state that the hysteretic nature of the water retention curve is also attributed to the hysteretic nature of the internal deformation of the bentonite aggregates and not only to the well-known pore constriction effect.

Table 4.8: Fitting parameters for the local water retention curves.

	$\rho_d = 1.5 \, Mg \, / \, m^3$	$\rho_d = 1.8 \, Mg \, / \, m^3$		
	Wetting	Wetting	Drying	
α^M	2.85	22.2	-	[kPa]
n^M	6.00	1.0	-	[-]
m^M	1.00	1.1	-	[-]
α^b	20	$1.0 \cdot 10^4$	$5.0 \cdot 10^4$	[kPa]
n^b	2.25	0.5	1.2	[-]
m^b	0.11	0.1	1.4	[-]
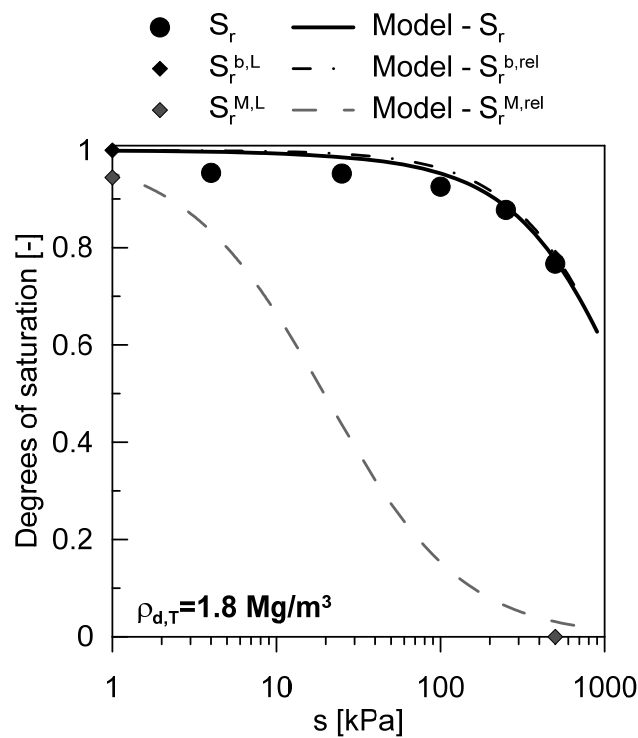
Figure 4.36: Main drying path of the water retention curve at the microscopic and the macroscopic level for the higher dry density.

4.6.4.3   Water and gas transport capacity

Soil fabric has a paramount importance on the permeability of soils. The factors that affect transport properties of soils are, among others, the geometry of the pore network, the properties of the permeating fluid, the presence of different fluids in the pores and the surface interaction between permeating fluid and the porous media, the contact area between aggregates (Manassero et al., 2005, Carminati et al., 2007, e.g., Berli et al., 2008, Romero, 2013). Microstructural investigation presented in the previous sections revealed that the microfabric of the tested S/B mixture evolves with the variation of the hydraulic, chemical and mechanical loading. Compaction at constant water content leads to the compression of the macropores and to the reduction of the volume of the bentonite

aggregates. Progressive saturation of the mixture causes the expansion of the bentonite as a consequence of the splitting of the quasicrystals (Figure 4.37). The geometrical configuration of the quasicrystals, at any suction, is influenced by the degree of confinement provided by the sand skeleton and by the salinity of the pore fluid (e.g., applied boundary conditions). Under full saturation with distilled water, at low dry density, the quasicrystals results very thin and organised in an edge to face arrangement (e.g., Figure 4.37.left). With the increase of the dry density, or the salinity of pore water, the nano void ratio increases suggesting that the thickness of the quasicrystals is increased, and the volume of the bentonite is reduced (Figure 4.37.right).

In this section the water and gas transport capacity of the S/B mixture is analysed. Based on the microstructural analyses, an attempt to quantify the contribution to transport of the different pore families is done using a simple hydraulic model to compute the geometrical permeabilities.

Influence of the bentonite dry density on the saturated water permeability

The goal of this section is to find a relationship between the saturated permeability of the tested S/B mixture and the saturated permeability of the bentonite-based materials, which solely depends on the dry density of the bentonite. For this purpose the domain Ω is considered (Figure 4.38).

By applying the principle of mass conservation, the macroscopic velocity v of the water (measured in the laboratory) is expressed as follow:

$$v \cdot \Omega = v_v^S \cdot \Omega_v^S \quad \rightarrow \quad v = v_v^S \cdot \frac{\Omega_v^S}{\Omega} \tag{4.39}$$

where Ω is the cross-sectional area of the considered domain, v_v^S is the velocity of the flow within the pores of the sand skeleton, Ω_v^S is the area of the voids within the sand and $\frac{\Omega_v^S}{\Omega}$ is equivalent to the relative porosity of the sand. This parameter is expressed as the ratio of the volume of voids within the sand only to the total (soil + voids) volume of the mixture:

$$\frac{\Omega_v^S}{\Omega} \cong n^{S,rel} = 1 - \frac{R^S}{1+e} \frac{\rho_s^{Mix}}{\rho_s^S} \tag{4.40}$$

For the specific case of the saturated S/B bentonite mixture, the grain of sand are considered as impervious obstacles for the water flow and the voids within the sand grains are considered fully filled by a gel of bentonite, at any mixture dry density higher than 1.5 Mg/m³. This last assumption is supported by the microstructural observations presented (e.g., Figure 4.19). The density of the bentonite gel can vary form 0.55 Mg/m³, for a mixture dry density of 1.5 Mg/m³, to 0.79 Mg/m³, for a mixture dry density of 1.8 Mg/m³. Higher dry density of the bentonite can be achieved both increasing the mixture

dry density, and maintaining the mixture dry density constant while increasing the bentonite percentage.

Because the grains of sand are considered as impervious, the water flow only occurs through the bentonite matrix and the velocity of the flow through the pores within the sand skeleton corresponds to the velocity of the flow through the bentonite matrix.

Considering a laminar flow within the mixture, the water macroscopic velocity is expressed with the Darcy's law as follows:

$$v = \frac{\gamma_w}{\mu} k_{sat}^{Mix} \nabla H \qquad (4.41)$$

where $\frac{\gamma_w}{\mu} k_{sat}^{Mix} = K_{sat}^{Mix}$ is the hydraulic conductivity of the S/B mixture measured in the laboratory (see chapter 2).

The velocity of the flow within the pores of the sandy skeleton is expressed as follows:

$$v_v^S = -\frac{\gamma_w}{\mu} k_{sat}^b \nabla H \qquad (4.42)$$

with k_{sat}^b being the saturated permeability of the bentonite.

Low dry density/low B content:
1) Thin quasicrystals;
2) Large micropores;
3) High ratio free water to total water;
4) Large wet surface;
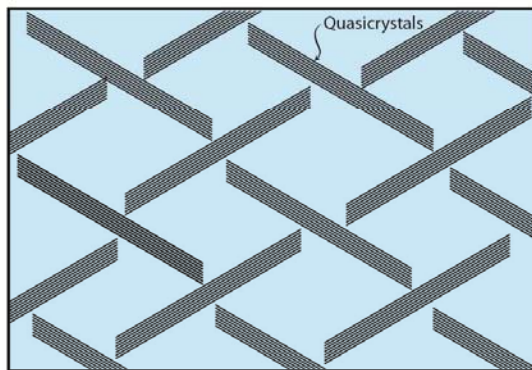
High dry density/High B content:
1) Thick quasicrystals;
2) Small micropores;
3) Low ratio free water to total water;
4) Small wet surface;

Quasicrystals
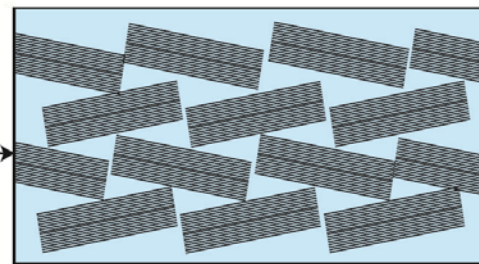
Compaction

Figure 4.37: Idealised arrangement of the smectite quasicrystals of a fully saturated bentonite at different compaction densities.
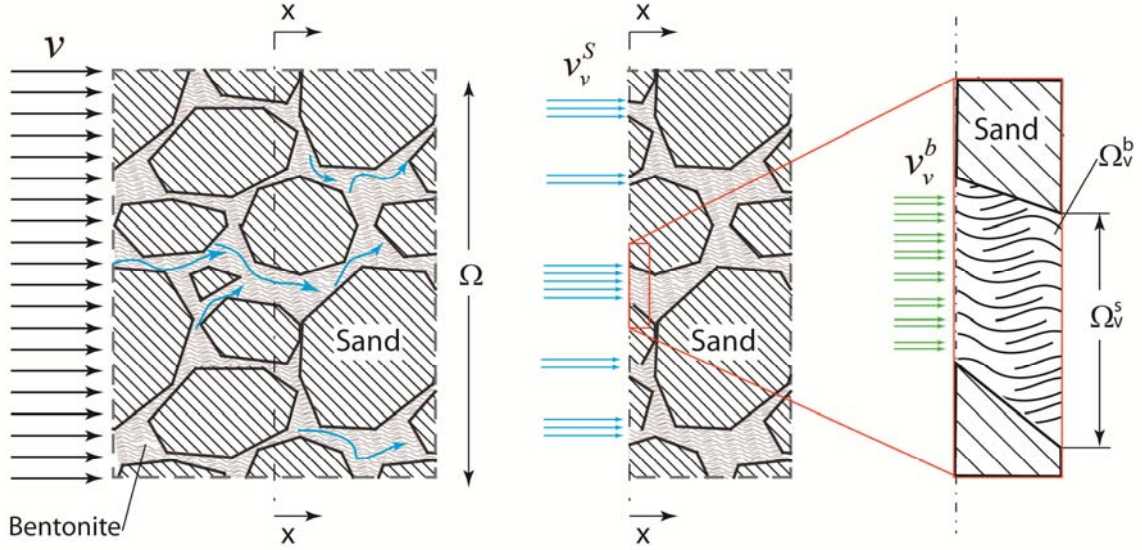
Figure 4.38: Schematic representation of the total space, pore space and flow velocity in a fully saturated S/B mixture.

The combination of eq. (4.39), eq. (4.41) and (4.42) allow to express the saturated permeability of the mixture as a function of the geometrical water permeability of the bentonite within the mixture:

$$k_{sat}^{Mix} = n^{s,rel} k_{sat}^{b} = \frac{R^S}{1+e} \frac{\rho_s^{Mix}}{\rho_s^S} k_{sat}^{b} \tag{4.43}$$

In order to compute the geometrical water permeability of the bentonite, the contribution to the flow of the micropores and the nanopores is considered separately:

$$k_{sat}^{b} = \frac{\Omega^m}{\Omega^b} k_{sat}^{m} + \frac{\Omega^n}{\Omega^b} k_{sat}^{n} \tag{4.44}$$

with Ω^m and Ω^n the area of the micropores and the nanopores, Ω^b the area of the bentonite within the sand, which is equal to the area of the voids within the sand skeleton only in some specific cases (macropores fully occluded). $\dfrac{\Omega^m}{\Omega^b}$ is equivalent to the relative porosity of the micropores and is expressed as the ratio of the micropore volume to the bentonite volume:

$$\frac{\Omega^m}{\Omega^b} = \frac{e^{m,rel}}{\left(1+e^{b,rel}\right)} \tag{4.45}$$

and $\dfrac{\Omega^n}{\Omega^b}$ is equivalent to the relative porosity of the nanopores and is expressed as the ratio of the nanopores volume to the bentonite volume:

$$\frac{\Omega^n}{\Omega^b} = \frac{e^{n,rel}}{\left(1+e^{b,rel}\right)} \tag{4.46}$$

Because the water in the interlayer is considered as immobile (Hueckel, 1992, Romero, 1999) the quasicrystals are considered as impervious structures and the contribution to the flow of the nanopores in equation (4.44) is neglected. As a consequence, the only active channels in the bentonite matrix are the micropores. As suggested by Romero (2013), the saturated permeability of the micropores can calculated with any function of the micro void ratio, e.g., a modified Kozeni-Carman equation:

$$k_{sat}^m = g(\,e^{b,rel}\,)\cdot\frac{\left(e^{m,rel}\right)^3}{\left(1+e^{m,rel}\right)} \tag{4.47}$$

with $e^{m,rel}$ the relative void ratio of the micropores and $g(\,e^{b,rel}\,)$ a function with depends on the relative bentonite void ratio. The relative micro void ratio, under condition of full saturation with distilled water, is obtained from eq. (4.34) as follows:

$$\frac{e^m}{e^b} = \frac{e^{m,rel}}{e^{b,rel}} \quad \rightarrow \quad e^{m,rel} = \frac{e^m}{e^b}e^{b,rel} \tag{4.48}$$

In order to derive the $g(\,e^{b,rel}\,)$ function some consideration are made. This function is inversely proportional to the external surface area of the quasicrystals. The splitting of the quasicrystals influences the ratio of immobile waters to the free water through the variation the external surface of the quasicrystals. Using equation (4.2) it would be possible to give and estimation of the external surface of smectite quasicrystals as a function of the number of smectite sheets (n_c). However, the number of smectite quasicrystals is not known at high bentonite water content because of the difficulties encountered in this type of measurements. Based on the microstructural analyses it is possible to state that under conditions of full saturation, n_c increases with the dry density and that the external specific surface of the quasicrystals decreases. The aim of the function $g(\,e^{b,rel}\,)$ is to account for this variation by expressing the external surface of the quasicrystals as a linear function of the relative bentonite void ratio as follows:

$$g(\,e^{b,rel}\,) = \frac{1}{C_{K-C}\cdot\left(S^m\cdot\rho_s^b 10^3\right)^2} \tag{4.49}$$
$$S^m(\,m^2\,/\,g\,) = b' - a'\left(e_0^{b,rel} - e^{b,rel}\right)$$

where $a' = 38\,\mathrm{m^2/g}$ and $b' = 150\,\mathrm{m^2/g}$ are the parameters adopted to fit the experimental data.

Finally, the combination of eq. (4.44) and eq. (4.47) yields to:

$$k_{sat}^{b} = g(\,e^{b,rel}\,)\frac{e^{m,rel}}{\left(1+e^{b,rel}\right)}\frac{\left(e^{m,rel}\right)^{3}}{\left(1+e^{m,rel}\right)} \qquad (4.50)$$

Figure 4.39 presents the permeability of the S/B mixture obtained in section 2.5.1.1 as a function of the relative bentonite void ratio. These results were rescaled based on eq. (4.43) and then compared with the results of a 100 B obtained by Seiphoori (2014). The results reveal that the permeability of a fully saturated S/B mixture is manly controlled by the hydro-mechanical state (relative dry density or void ratio) of the bentonite. The presence of the sand within the mixture only produced a slight reduction of its permeability with respect to the one of the bentonite.

Equation (4.43) enables to estimate the permeability of a mixture prepared at any S/B ratio once knowing the permeability of the bentonite matrix form eq. (4.47), under the assumption that all the pores within the sand are sealed with bentonite and the percolating fluid is distilled water. Figure 4.39 also reports the predicted hydraulic conductivity for a mixture prepared with 50% of bentonite in dry mass (grey dot-dashed line). This result reveals that the permeability of the 100B represents the upper boundary for the permeability of sand/bentonite mixtures prepared at any mixing ratio. Moreover, the influence of the sand on the reduction of the permeability of a generic S/B mixture is less and less important as the quantity of the bentonite increases.
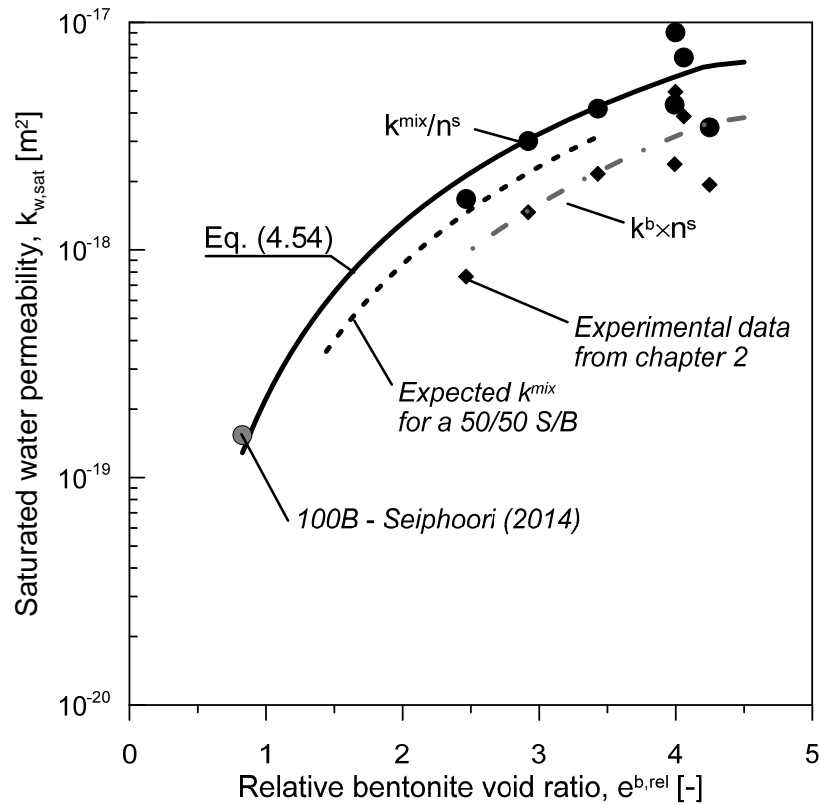
Figure 4.39: Saturated water permeability versus relative bentonite void ratio.

Influence of the pore water chemistry on the saturated water permeability

The saturated water permeability of the S/B mixture is fully governed by the void ratio of the bentonite when this is allowed to swell and seal the macropores. The increase of the pore water salinity leads to the reduction of the swelling capacity of bentonite, because of the dual reduction of the splitting phenomenon and the reduction of the diffuse double layer. As a consequence, macropores will represent preferential paths for the liquid flow. In order to capture this effect, the contribution of the macropores and bentonite pores to the flow is considered, for computing the geometrical permeability of the fully saturated mixture:

$$k_{sat}^{Mix} = \underbrace{\frac{\Omega^M}{\Omega_v^S} k_{sat}^M}_{Macropores} + \underbrace{\frac{\Omega^b}{\Omega_v^S} k_{sat}^b}_{Bentonite} \tag{4.51}$$

where k_{sat}^M is geometrical permeability of macropores and k_{sat}^b is the geometrical permeability of the bentonite (eq. (4.51)), calculated for a fully saturated mixture. The parameters $\frac{\Omega^M}{\Omega_v^S}$ and $\frac{\Omega^b}{\Omega_v^S}$ quantify the percentage of the area of the voids within the sands which is occupied by macropores and by the bentonite, respectively. These two parameters are expressed as follows:

$$\frac{\Omega^M}{\Omega_v^S} \cong \frac{e^M}{\rho_s^{Mix}} \left[\frac{1}{\frac{1}{\rho_d^{Mix}} - \frac{R^S}{\rho_s^S}} \right] \tag{4.52}$$

$$\frac{\Omega^b}{\Omega_v^S} \cong \frac{e^b}{\rho_s^{Mix}} \left[\frac{1}{\frac{1}{\rho_d^{Mix}} - \frac{R^S}{\rho_s^S}} \right] \tag{4.53}$$

The geometrical permeability of the macropores k_{sat}^M is calculated by applying a modified Kozeny-Carman model to the macropores system as:

$$k_{sat}^M = G \cdot \frac{\left(e^{M,rel} \right)^3}{\left(1 + e^{M,rel} \right)} \tag{4.54}$$

where G is a constant equal to $2.85 \cdot 10^{-12} \, \text{m}^2$.

The permeability of the bentonite fractions is calculated according to eq. (4.50).

Figure 4.40 presents the permeability data from chapter 2 (Figure 2.33) as a function of the relative macropore void ratio. In the figure, the values of water permeabilitie

obtained from eq. (4.51) are depicted, along with the relative water permeability of the macropores and the bentonite pores. Equation (4.51) is capable to reproduce the trend of the evolution of the mixture water permeability versus macropore void ratio within the range that was analysed. Thanks to the use of eq. (4.51) it is possible to identify two separate flow regions. When the macropore void ratio is lower than 0.07, the contribution of the flow through the bentonite is dominating the entire flow through the mixture. After this limit, the macropores become larger because of the reduced swelling of the bentonite aggregates. As a consequence, the permeability of the bentonite becomes negligible with respect to the permeability of the macropores. This result suggests that, because of the reduction of the splitting of the quasicrystals as a consequence of the increase of the pore water salinity, the bentonite aggregates tend to become as impervious structure. Under this condition, the macropores represent the preferential flow paths and that any change in this family of pores, e.g., compaction, would cause large variation of the saturated permeability of the mixture.
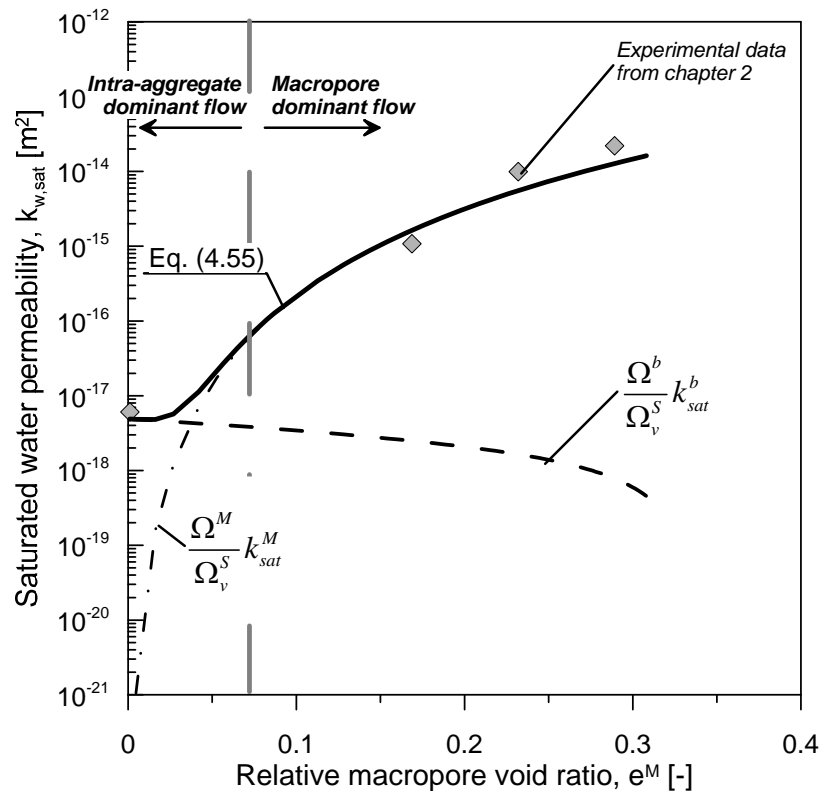
Figure 4.40: Hydraulic conductivity versus relative macro void ratio for a specimen compacted to 1.5 Mg/m³.

Unsaturated water and gas permeability

Equation (4.51) allows calculating the geometrical permeability of the mixture at any hydro-mechanical state based on the evolution of the different pore families upon different HCM loadings. The evolution of the geometrical permeability of the mixture along the main wetting, calculated for the two different target dry densities, is presented in Figure 4.41. In this figure, the geometrical permeabilities of the fully saturated bentonite and the macropores are also depicted to identify the contribution to the flow of the different pore families. The results revealed that the global geometrical permeability of the mixture is mainly controlled by the permeability of the macropores. Also, it is independent from the dry density because the evolution of the macro void ratio along wetting coincides for the range of densities tested in this thesis (Figure 4.31). The geometrical permeability of the bentonite fraction is clearly density dependent. These two observations are in agreement with the observed trend of the variation of the water and gas permeability. The gas permeability variation with suction that according to the results presented in chapter 3 is independent from the compaction density is related to the variation of the macropores, which indeed are preferably occupied by the gas phase. The water permeability variation with suction is density dependent. As a matter of fact, the water is mainly stored in the bentonite and the compaction of the mixture causes a reduction of the bentonite void ratio (Figure 4.31). The variation of about 4 orders of magnitude of the global geometrical permeability with reducing the matric suction also justifies the significant variation of the water and the gas saturated permeabilities.
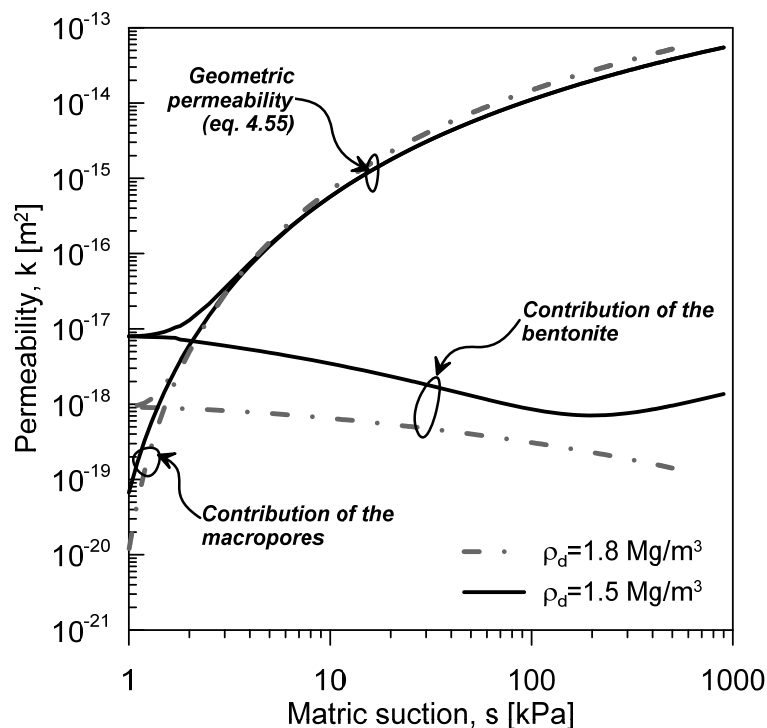
Figure 4.41: Evolution of the geometrical permeabilities with the matric suction.

4.7 SUMMARY AND CONCLUSIONS

This chapter presented the results of an investigation at the microscopic level on the effect of different hydro-chemo-mechanical loadings on the evolution of the fabric of the 80/20 S/B mixture.

The microstructural analyses revealed the evolution of the microstructure of the mixture upon different HCM loadings. This study substantially aided the interpretation of the behaviour of the S/B mixture at the laboratory scale, especially considering the different mechanisms that govern the swelling of smectite quasicrystals, such as crystalline, double layer swelling and splitting of the quasicrystals.

The analyses showed that the compaction of the mixture at the as-compacted state involved the closure of the macropores and the compression of the bentonite assemblages. The hydration of the mixture wetted with distilled water under constant volume conditions is characterised by the delamination of the quasicrystals that separate until the macropores are fully occluded. At the lower density, the process leads to a progressive decrease of the nanopores and to a uniform pore size distribution. Under these conditions, the development of the diffuse double layer and the splitting of the quasicrystals are the mechanisms responsible for the generation of macroscopic swelling pressure and strain. At the higher density, the splitting caused the compression of a certain fraction of micropores, which was reflected in the increase of non-intruded porosity.

An expression was derived to determine the relative bentonite dry density from the MIP data. Because of this expression, it was possible to compare the swelling pressure data obtained in this study with the data obtained for other bentonite-based materials. A unique relationship was found to satisfactorily fit all of the experimental data.

Analyses of the water retention behaviour of the mixture at the microscopic level revealed that, depending on the dry density and macroscopic water content the water can be store only in the bentonite fraction or also in the macropores. On one hand, when the mixture is compacted to the lower dry density, the water is stored in the bentonite pores because the quasicrystals have the possibility to fully split. On the other hand, at higher compaction the splitting of quasicrystals is impeded so that the water cannot completely infiltrate the quasicrystals and it remains in the macropores.

An expression to determine the geometrical permeability under different hydro-chemo-mechanical loadings was determined based on geometrical consideration at the pore scale and on the constitutive equations that describe the evolution of the mixture fabric. For this expression the contribution of the bentonite and the macropores to the flow is analysed separately. Thanks to this, it was possible to identify the conditions when the transport of water through the bentonite aggregates is dominant or when the transport of water through the macropores is dominant.

Regarding the effect of pore water chemistry on the macroscopic swelling and water permeability, it was found that the increase of the dry density causes the closure of the

macropores and thus the reduction of the available volume for the development of the electrostatic double layer. This yields to two main consequences; firstly, the capacity of the bentonite to sustain chemical loadings is improved, second, when the macropores are present in the mixture any factor that is influencing their size, such as the variation of the compaction density, the electrolyte concentration or degree of saturation, yields to large variation of the hydraulic conductivity.

5 Conclusions and perspectives

5.1 CONCLUSIONS

In the context of the disposal of L/ILW the investigation carried out in this thesis aimed at quantifying and understanding the impact of different hydro-chemo-mechanical loadings on the water and gas transport properties of the 80/20 Sand/Bentonite mixture used as backfilling material. With this purpose the material was characterised at both the macro and the micro scale.

The first step toward this goal required the development of a technique to obtain specimens characterised by the homogenous distribution of the moisture and dry density, the homogenous distribution of the two solid fractions (sand and bentonite grains), and that ensured the reproducibility of these characteristics. This allowed obtaining consistent results at the laboratory scale.

The grain size distribution, particle density, the Atterberg limits were determined. The dependency of the liquid limit on the chemistry of the pore water gave a first indication on the sensitivity of the mixture to the chemical loadings. The swelling capacity of the mixture was studied both in terms of swelling strain and swelling pressure and under a variety of applied hydro-chemical stress paths.

The water retention curve of the mixture was determined for two different compaction densities and under a wide range of suctions. This required the use of three different experimental techniques. Common features with the retention behaviour of double structure soils were found. During the determination of the water retention curve also the swelling pressure vs suction and the unsaturated hydraulic conductivity vs suction curve were determined. The swelling pressure vs suction, the water retention, and the hydraulic conductivity vs suction curves showed hysteresis along a wetting-drying cycle. This hysteresis of these curves was found density dependent.

After that, the mechanisms of gas transport, such as gas permeability and gas breakthrough pressure, were analysed using different experimental techniques. The gas permeability of the mixture, determined for specimens prepared to different water contents and accounting for the Klinkenberg effect, was found to be independent from the compaction density. The breakthrough pressure and the time for the breakthrough depended on the compaction density. The passage of gas occurred in the specimens without any appreciable change of their degrees of saturation. This suggested that the breakthrough occurred because of the creation of some preferential flow paths within the material. Perhaps, one of the most interesting results is that the gas passage through these preferential paths caused the displacement of a little amount of fine particles.

In order to aid the interpretation of the results obtained at the laboratory scale, a broad microstructural investigation was carried out. This study revealed the existence of different pore families that are continuously evolving upon the different hydro-chemo-mechanical paths. The swelling pressure generation upon wetting was associated to delamination and reorientation of the smectite particles that was impeded by the presence of the sand skeleton. The introduction of the parameter called relative bentonite dry density helped in comparing the swelling pressure data obtained in this study with the one of bentonite-based materials prepared at different mixing ratios. The hysteretic behaviour of the water retention, the swelling pressure vs suction and the unsaturated hydraulic conductivity vs suction curves was found to be dependent on the reversibility of the microstructural modification upon a drying-wetting cycle. The concept of geometrical permeability was introduced and an equation based on geometrical consideration at the pore scale was derived. For the development of this expression the contribution to the flow in the macropores and the bentonite pores was accounted separately.

5.2 PERSPECTIVES

The results show that the 80/20 S/B mixture is a complex material which required extreme careful during the preparation procedure and testing. During this work it was need to explore different experimental procedures to be able to cover a wide range of suctions and to find an appropriate method for injecting gas in the specimens. Moreover, the extremely low hydraulic conductivity under saturated and unsaturated conditions, associated with the low retention capacity, leads to very long time for the tests. This imposed some constrains in the number of test which were performed during the entire thesis. With this in mind, the following suggestions are given for the future work on the characterisation and modelling of transport properties of the mixture:

The water retention curve of the mixture was determined only for the mixture wetted with distilled water. This curve can be considered as reference condition because the bentonite experiences its maximum swelling capacity. However, in situ the mixture will be wetted with other types of water which will alter its retention capacity. In particular, one could expect a reduction of the retention capacity because of the increase of the salinity of the pore fluid.

The impact of the pore water chemistry on the hydro-mechanical behaviour of the mixture was addressed to account only for osmotic suction of the pore water. However, the pore water coming from the host rock can flow through some elements of the repository which are made of concrete. This type of water that is expected to have a very high pH can cause the partial or total loss of the swelling capacity due to the dissolution of the smectite minerals, changes in morphology, crystallinity, particle surface, interlayer charge and chemistry of the octahedral layers. As a consequence, the retention behaviour and the transport properties of the mixture will be altered.

The gas injection tests performed during this thesis were carried out at the laboratory scale on specimens which have maximum dimensions of 90×80 mm. The interpretation of these results was successfully made thanks to the microstructural analyses of the S/B mixture. However, due to the high non linearity of the gas transport problem, scale effects can be expected. This will require the development of a model for upscaling the transport parameters. In the future, the results obtained in the framework of this thesis at the laboratory scale, can be integrated with the results of real scale in situ experiments that are foreseen to be performed in Grimsel in the framework of the GAST project.

The results of the breakthrough test performed under triaxial conditions revealed that the mobilisation of some fine components in the mixture during the injection of highly pressurised gas is possible. To the author knowledge, the issue of fine transport as a consequence of the gas flow was never addressed. This phenomenon may cause in the long term a variation of the clay distribution within the S/B mixture altering its transport properties, swelling capacity and retention behaviour. As a consequence, this problem could be addressed in the context of nuclear wastes disposal.

The results of the water and gas permeability of the mixture were analysed in the light of the interaction happening between the different pore families. This allowed deriving an expression of the saturated geometrical permeability for different hydro-chemo-mechanical states. However, in order to derive a model for describing the water and gas transport through the mixture under unsaturated conditions the concept of relative permeability should be recalled. Models to derive the relative permeability functions are available for single structure soils and based on the global degree of saturation. However, it is believed that the development of models that accounts for the presence of a network of partially saturated bentonite and macropores that contribute differently to the water and gas transport is needed.

References

Abichou, T., Benson, C. H. & Edil, T. B. (2002) Micro-structure and hydraulic conductivity of simulated sand-bentonite mixtures. *Clays and Clay Minerals* **50(5)**:537-545.

Agus, S. S. & Schanz, T. (2005a) Comparison of four methods for measuring total suction. *Vadose Zone Journal* **4(4)**:1087-1095.

Agus, S. S. & Schanz, T. (2005b) Effect of shrinking and swelling on microstructures and fabric of a compacted bentonite-sand mixture In *Proceedings of International conference on problematic soils GEOPRPOB* (Bilsel, H., andNalbantoglu, Z. (eds)). Eastern Mediterranean University Press, Sakarya, Gazimağusa, Cyprus vol. 2, pp. 543-550.

Agus, S. S. & Schanz, T. (2008a) A method for predicting swelling pressure of compacted bentonites. *Acta Geotechnica* **3(2)**:125-137.

Agus, S. S. & Schanz, T. (2008b) Permeability of a heavily compacted bentonite-sand mixture as sealing and buffer element for nuclear waste repository In *Proceedings of Unsaturated Soils. Advances in Geo-Engineering. 1st European Conference, E-UNSAT* (Toll, D. G., Augarde, C. E., Gallipoli, D., andWheeler, S. J. (eds)). Taylor & Francis, pp. 305–331.

Ahmed, T. (2010) *Reservoir Engineering Handbook.* Fourth edn.

Airò Farulla, C., Battiato, A. & Ferrari, A. (2010a) The void ratio dependency of the retention behaviour for a compacted clay In *Proceedings of 5th International conference on unsaturated soils* (Alonso , E., andGens, A. (eds)). CRC press, Taylor and Francis Group., pp. 417-422.

Airò Farulla, C. & Ferrari, A. (2005) Controlled suction oedometric tests: Analysis of some experimental aspects. In *Proceedings of International Symposium on Advanced Experimental Unsaturated Soil Mechanics*. Taylor & Francis Group, London, pp. 43–48.

Airò Farulla, C., Ferrari, A. & Romero, E. (2010b) Volume change behaviour of a compacted scaly clay during cyclic suction changes. *Canadian Geotechnical Journal* **47(6)**:688-703.

Arifin, Y. F. (2008) Thermo-hydro-mechanical behaviour of compacted bentonite-sand mixtures: an experimental study. *PhD Thesis*. Bauhaus University, Weimar, Germany.

Arnedo, D., Alonso, E., Olivella, S. & Romero, E. (2008) Gas injection tests on sand/bentonite mixtures in the laboratory. Experimental results and numerical modelling. *Physics and Chemistry of the Earth, Parts A/B/C* **33**:S237-S247.

ASTM D5298-10 (2010a) Standard Test Method for Measurement of Soil Potential (Suction) Using Filter Paper.

ASTM D4318-10 (2010b) Standard Test Methods for Liquid Limit, Plastic Limit, and Plasticity Index of Soils.

Baille, W., Tripathy, S. & Schanz, T. (2010) Swelling pressures and one-dimensional compressibility behaviour of bentonite at large pressures. *Applied clay science* **48(3)**:324-333.

Bear, J. (1972) Dynamics of fluids in porous media. *Soil Science*.

References

Benamar, A., Ahfir, N.-D., Wang, H. & Alem, A. (2007) Particle transport in a saturated porous medium: Pore structure effects. *Comptes Rendus Geoscience* **339(10)**:674-681.

Berli, M., Carminati, A., Ghezzehei, T. & Or, D. (2008) Evolution of unsaturated hydraulic conductivity of aggregated soils due to compressive forces. *Water Resources Research* **44(5)**.

Bestel, M. (2014) Water–montmorillonite systems: Neutron scattering and tracer through diffusion studies. *PhD Thesis* Paul Scherrer Institute, Villigen, Switzerland.

Börgesson, L. & Sandén, T. (2006) *Piping and erosion in buffer and backfill materials. Current knowledge.*

Brace, W. F., Walsh, J. & Frangos, W. (1968) Permeability of granite under high pressure. *Journal of Geophysical research* **73(6)**:2225-2236.

BS 1377-2 (1990) Methods of test for soils for civil engineering purposes: Classification tests.

Bucher, F. & Müller-Vonmoos, M. (1989) Bentonite as a containment barrier for the disposal of highly radioactive wastes. *Applied clay science* **4(2)**:157-177.

Bulut, R., Lytton, R. L. & Wray, W. K. (2001) Soil suction measurements by filter paper In *Proceedings of Expansive clay soils and vegetative influence on shallow foundations*. ASCE, pp. 243-261.

Cardoso, R., Romero, E., Lima, A. & Ferrari, A. (2007) A comparative study of soil suction measurement using two different high-range psychrometers. In *Experimental Unsaturated Soil Mechanics*. Springer, pp. 79-93.

Carminati, A., Kaestner, A., Flühler, H., Lehmann, P., Or, D., Lehmann, E. & Stampanoni, M. (2007) Hydraulic contacts controlling water flow across porous grains. *Physical Review E* **76(2)**:026311.

Carminati, A., Kaestner, A., Lehmann, P. & Flühler, H. (2008) Unsaturated water flow across soil aggregate contacts. *Advances in water resources* **31(9)**:1221-1232.

Castellanos, E., Villar, M., Romero, E., Lloret, A. & Gens, A. (2008) Chemical impact on the hydro-mechanical behaviour of high-density FEBEX bentonite. *Physics and Chemistry of the Earth, Parts A/B/C* **33**:S516-S526.

Cerda, C. M. (1988) Mobilization of quartz fines in porous media. *Clays and Clay Minerals* **36(6)**:491-497.

Chau, J. F. & Or, D. (2006) Linking drainage front morphology with gaseous diffusion in unsaturated porous media: A lattice Boltzmann study. *PHYSICAL REVIEW-SERIES E-* **74(5)**:056304.

Cuisinier, O. & Laloui, L. (2004) Fabric evolution during hydromechanical loading of a compacted silt. *International journal for numerical and analytical methods in Geomechanics* **28(6)**:483-499.

Dana, E. & Skoczylas, F. (1999) Gas relative permeability and pore structure of sandstones. *International Journal of Rock Mechanics and Mining Sciences* **36(5)**:613-625.

Das, B. M. (2008) *Advanced soil mechanics.* Third edition edn., Taylor & Francis.

Delage, P., Audiguier, M., Cui, Y. & Howat, M. (1996) Microstructure of a compacted silt. *Canadian Geotechnical Journal* **33(1)**:150-158.

Delage, P. & Lefebvre, G. (1984) Study of the structure of a sensitive Champlain clay and of its evolution during consolidation. *Canadian Geotechnical Journal* **21(1)**:21-35.

Delage, P., Marcial, D., Cui, Y. & Ruiz, X. (2006) Ageing effects in a compacted bentonite: a microstructure approach. *Géotechnique* **56(5)**:291-304.

Delage, P. & Pellerin, F. (1984) Influence de la lyophilisation sur la structure d'une argile sensible du Québec. *Clay Minerals* **19(2)**:151-160.

Della Vecchia, G., Dieudonné, A. C., Jommi, C. & Charlier, R. (2014) Accounting for evolving pore size distribution in water retention models for compacted clays. *Int. J. Numer. Anal. Meth. Geomech.*

Derjaguin, B. & Churaev, N. M., V (1987) *Surface forces.* Consultants Bureau, New York.

Diamond, S. (1970) Pore size distributions in clays. *Clays and Clay Minerals* **18(1)**:7-23.

Dixon, D., Gray, M. & Thomas, A. (1985) A study of the compaction properties of potential clay—sand buffer mixtures for use in nuclear fuel waste disposal. *Engineering Geology* **21(3)**:247-255.

Dixon, D. A. (2000) *Porewater salinity and development of swelling pressure in bentonite-based buffer and backfill materials.* Helsinki, Finland Posiva Oy Report.

Dominijanni, A., Manassero, M. & Puma, S. (2013) Coupled chemical-hydraulic-mechanical behaviour of bentonites. *Géotechnique* **63(3)**:191-205.

Dunn, R. J. (1985) Laboratory measurement of fine-grained soil fluid conductivity. *Engineering Geology* **21(3)**:215-223.

Ferrari, A., Eichenberger, J., Fern, J. & Laloui, L. (2011) *Geomechanical analysis for the establishment of an early warning system in the llano grande mine (Costa Rica). Laboratory testing and numerical simulations.*Technical Note LMS/EPFL S6229.

Ferrari, A., Favero, V., Marschall, P. & Laloui, L. (2014a) Experimental analysis of the water retention behaviour of shales. *International Journal of Rock Mechanics and Mining Sciences* **72**:61-70.

Ferrari, A. & Laloui, L. (2013) Advances in the testing of the hydro-mechanical behaviour of shales. In *Multiphysical Testing of Soils and Shales.*   Springer, pp. 57-68.

Ferrari, A., Seiphoori, A., Rüedi, J. & Laloui, L. (2014b) Shot-clay MX-80 bentonite: An assessment of the hydro-mechanical behaviour. *Engineering Geology* **173**:10-18.

Fredlund, D. G. & Rahardjo, H. (1993) *Soil mechanics for unsaturated soils.* John Wiley & Sons.

Gallé, C. (2000) Gas breakthrough pressure in compacted Fo–Ca clay and interfacial gas overpressure in waste disposal context. *Applied clay science* **17(1)**:85-97.

Gallé, C. & Tanai, K. (1998) Evaluation of gas transport properties of backfill materials for waste disposal: H2 migration experiments in compacted Fo-Ca clay. *Clays and Clay Minerals* **46(5)**:498-508.

Geiser, F. (1999) Comportement mécanique d'un limon non saturé. Étude expérimentale et modélisation constitutive. *Thèse EPFL, n° 1942*. Ecole Polytechnique Fédérale de Lausanne.

Gens, A. & Alonso, E. (1992) A framework for the behaviour of unsaturated expansive clays. *Canadian Geotechnical Journal* **29(6)**:1013-1032.

Goldstein, J., Newbury, D., Joy, D., Lyman, C., Echlin, P., Lifshin, E., Sawyer, L. & Michael, J. (2007) *Scanning electron microscopy and X-ray microanalysis.* Third edn. New York, NY, USA, Springer.

Graham, J., Halayko, K. G., Hume, H., Kirkham, T., Gray, M. & Oscarson, D. (2002) A capillarity-advective model for gas break-through in clays. *Engineering Geology* **64(2)**:273-286.

Harrington, J. & Horseman, S. (2003) *Gas migration in KBS-3 buffer bentonite. Sensitivity of test parameters to experimental boundary conditions.*

References

Herbert, H.-J., Kasbohm, J., Moog, H. & Henning, K.-H. (2004) Long-term behaviour of the Wyoming bentonite MX-80 in high saline solutions. *Applied clay science* **26(1)**:275-291.

Herbert, H. J. & Kasbohm, J. (2009) Short and long term behavior of bentonite under the boundary conditions of a repository for high level radioactive waste In *Proceedings of WM2009 conference*.

Hoffmann, C., Alonso, E. & Romero, E. (2007) Hydro-mechanical behaviour of bentonite pellet mixtures. *Physics and Chemistry of the Earth, Parts A/B/C* **32(8)**:832-849.

Horseman, S., Harrington, J. & Sellin, P. (1996a) Gas migration in Mx80 buffer bentonite In *Proceedings of MRS Proceedings*. Cambridge Univ Press vol. 465, pp. 1003.

Horseman, S., Harrington, J. & Sellin, P. (1999) Gas migration in clay barriers. *Engineering Geology* **54(1)**:139-149.

Horseman, S., Higgo, J., Alexander, J. & Harrington, J. (1996b) Water, gas and solute movement through argillaceous media. *Nuclear Energy Agency Rep. CC-96/1. OECD, Paris.*

Horseman, S. T. & Harrington, J. F. (1997) *Study of gas migration in Mx80 buffer bentonite.*BGS internal report WE/97/7 to SKB.

Hueckel, T. A. (1992) Water-mineral interaction in hygromechanics of clays exposed to environmental loads: a mixture-theory approach. *Canadian Geotechnical Journal* **29(6)**:1071-1086.

Jacinto, A., Villar, M. & Ledesma, A. (2012) Influence of water density on the water-retention curve of expansive clays. *Géotechnique* **62(8)**:657-667.

Juang, C. & Holtz, R. (1986) A probabilistic permeability model and the pore size density function. *International journal for numerical and analytical methods in Geomechanics* **10(5)**:543-553.

Karnland, O., Nilsson, U., Weber, H. & Wersin, P. (2008) Sealing ability of Wyoming bentonite pellets foreseen as buffer material–laboratory results. *Physics and Chemistry of the Earth, Parts A/B/C* **33**:S472-S475.

Keller, L. M., Seiphoori, A., Gasser, P., Lucas, F., Holzer, L. & Ferrari, A. (2014) The pore structure of compacted and partly saturated MX-80 bentonite at different dry densities. *Clays and Clay Minerals* **62(3)**:174-187.

Kenney, T., Veen, W. V., Swallow, M. & Sungaila, M. (1992) Hydraulic conductivity of compacted bentonite-sand mixtures. *Canadian Geotechnical Journal* **29(3)**:364-374.

Kestin, J., Khalifa, H. E. & Correia, R. J. (1981) Tables of the dynamic and kinematic viscosity of aqueous NaCl solutions in the temperature range 20–150 C and the pressure range 0.1–35 MPa. *Journal of physical and chemical reference data* **10(1)**:71-88.

Klinkenberg, L. (1941) The permeability of porous media to liquids and gases In *Proceedings of Drilling and production practice*. American Petroleum Institute.

Koliji, A. (2008) Mechanical behaviour of unsaturated aggregated soils. *Thèse EPFL, n° 4011*. EPFL.

Koliji, A., Laloui, L. & Vulliet, L. (2010a) Constitutive modeling of unsaturated aggregated soils. *International journal for numerical and analytical methods in Geomechanics* **34(17)**:1846-1876.

Koliji, A., Vulliet, L. & Laloui, L. (2010b) Structural characterization of unsaturated aggregated soil. *Canadian Geotechnical Journal* **47(3)**:297-311.

Komine, H. (2004) Simplified evaluation on hydraulic conductivities of sand–bentonite mixture backfill. *Applied clay science* **26(1)**:13-19.

Komine, H. & Ogata, N. (1999) Experimental study on swelling characteristics of sand-bentonite mixture for nuclear waste disposal. *Soils and Foundations* **39(2)**:83-97.

Komine, H., Yasuhara, K. & Murakami, S. (2009) Swelling characteristics of bentonites in artificial seawater. *Canadian Geotechnical Journal* **46(2)**:177-189.

Kunze, R. J. & Kirkham, D. (1962) Simplified accounting for membrane impedance in capillary conductivity determinations. *Soil Science Society of America Journal* **26(5)**:421-426.

Laird, D. A. (2006) Influence of layer charge on swelling of smectites. *Applied clay science* **34(1)**:74-87.

Leong, E.-C., Tripathy, S. & Rahardjo, H. (2003) Total suction measurement of unsaturated soils with a device using the chilled-mirror dew-point technique. *Géotechnique* **53(2)**:173-182.

Liu, J.-F., Skoczylas, F. & Talandier, J. (2015) Gas permeability of a compacted bentonite–sand mixture: coupled effects of water content, dry density, and confining pressure. *Canadian Geotechnical Journal* **52(999)**:1-9.

Liu, J. F. (2013) Étanchéité de l'interface argilite-bentonite restaurée et soumise à une pression de gaz, dans le contexte du stockage profond de déchets radioactifs. *PhD Thesis*. École centrale de Lille.

Liu, X. F. D. C., R, Buzzi, O. P. & Fityus, S. G. (2014) Microstructural effects of environmental salinity on unbound granular road pavements In *Proceedings of 7th International Congress on Environmental Geotechnics : iceg2014* (Bouazza, A., Yuen, S. T. S., andBrown, B. E. (eds)).

Lloret, A. & Villar, M. (2007) Advances on the knowledge of the thermo-hydro-mechanical behaviour of heavily compacted "FEBEX" bentonite. *Physics and Chemistry of the Earth, Parts A/B/C* **32(8)**:701-715.

Lloret, A., Villar, M. V., Sanchez, M., Gens, A., Pintado, X. & Alonso, E. (2003) Mechanical behaviour of heavily compacted bentonite under high suction changes. *Géotechnique* **53(1)**:27-40.

Loosveldt, H., Lafhaj, Z. & Skoczylas, F. (2002) Experimental study of gas and liquid permeability of a mortar. *Cement and Concrete Research* **32(9)**:1357-1363.

Manassero, M., Rabozzi, C., Ribotta, L. & Musso, G. (2005) On the retention properties of a polluted sand-silt mixture In *Proceedings of Advanced Experimental Unsaturated Soil Mechanics: Proceedings of the International Symposium on Advanced Experimental Unsaturated Soil Mechanics, Trento, Italy, 27-29 June 2005*. CRC Press, pp. 459.

Manca, D., Ferrari, A. & Laloui, L. (2015) Fabric evolution and the related swelling behaviour of a sand/bentonite mixture upon hydro-chemo-mechanical loadings. *Accepted in Géotechnique*.

Marinho, F., Take, W. & Tarantino, A. (2008) Measurement of matric suction using tensiometric and axis translation techniques. *Geotechnical and Geological engineering* **26(6)**:615-631.

Mašín, D. (2013) Double structure hydromechanical coupling formalism and a model for unsaturated expansive clays. *Engineering Geology* **165**:73-88.

Méheust, Y., Løvoll, G., Måløy, K. J. & Schmittbuhl, J. (2002) Interface scaling in a two-dimensional porous medium under combined viscous, gravity, and capillary effects. *Physical Review E* **66(5)**:051603.

Minon, S., Salager, S. & Laloui, L. (2010) *Preliminary phase of the FORGE, Work Package 3.2.5. Sampling procedure for Sand/Bentonite MX80 mixture, modular columns setup.*, Lausanne.Technical Note TN 2010.

References

Mishra, A. K., Ohtsubo, M., Li, L. Y., Higashi, T. & Park, J. (2009) Effect of salt of various concentrations on liquid limit, and hydraulic conductivity of different soil-bentonite mixtures. *Environmental geology* **57(5)**:1145-1153.

Mitchell, J. K. & Soga, K. (2005) *Fundamentals of soil behavior.* Third edn., Wiley New York.

Mollins, L., Stewart, D. & Cousens, T. (1996) Predicting the properties of bentonite-sand mixtures. *Clay Minerals* **31(2)**:243-252.

Montanez, J. K. (2002) Suction and volume changes of compacted sand-bentonite mixtures. University of London (Imperial College of Science).

Muntohar, A. S. (2003) Swelling and compressibility characteristics of soil–bentonite mixtures. *Civil Engineering Dimension* **5(2)**:93-98.

Musso, G., Romero, E. & Della Vecchia, G. (2013) Double-structure effects on the chemo-hydro-mechanical behaviour of a compacted active clay. *Géotechnique* **63(3)**:206-220.

Nagra (2007) *ESDRED: Emplacement tests with granular bentonite MX-80. Laboratory results from ETH Zürich.* Nagra Tech. Rep. NTB 07-24.

Nagra (2008) *Effects of post-disposal gas generation in a repository for low- and intermediate-level waste sited in the Opalinus Clay of Northern Switzerland.*, Wettingen, Switzerland. Nagra Tech. Rep. NTB 08-07.

Nagra (2009) *The Nagra Research, Development and Demonstration (RD&D) Plan for the Disposal of Radioactive Waste in Switzerland.* Wettingen, Switzerland. Nagra Tech. Rep. NTB 09-06.

Nagra (2010) *Beurteilung der geologischen Unterlagen für die provisorischen Sicherheitsanalysen in SGT Etappe 2 - Klärung der Notwendigkeit ergänzender geologischer Untersuchungen.* Wettingen, Switzerland. Nagra Tech. Rep. NTB 10-01.

Nowamooz, H. & Masrouri, F. (2009) Density-dependent hydromechanical behaviour of a compacted expansive soil. *Engineering Geology* **106(3)**:105-115.

Nowamooz, H. & Masrouri, F. (2012) Soil fabric and soil water retention curve of a compacted silt-bentonites. *ASTM geotechnical testing journal* **35(1)**:18-30.

Penumadu, D. & Dean, J. (2000) Compressibility effect in evaluating the pore-size distribution of kaolin clay using mercury intrusion porosimetry. *Canadian Geotechnical Journal* **37(2)**:393-405.

Plötze, M. & Weber, H. P. (2007a) *ESDRED: Emplacement tests with granular bentonite MX-80. Laboratory results from ETH Zürich.* Nagra Tech. Rep. NTB 07-24.

Plötze, M. & Weber, H. P. (2007b) *ESDRED: Emplacement tests with granular bentonite MX-80. Laboratory results from ETH Zürich.* Wettingen. Nagra Working Report NAB 07-24.

Puma, S., Marchese, F., Dominijanni, A. & Manassero, M. (2013) Reuse of MSWI bottom ash mixed with natural sodium bentonite as landfill cover material. *Waste Management & Research* **31(6)**:577-584.

Pusch, R. (2001a) *Experimental study of the effect of high porewater salinity on the physical properties of a natural smectitic clay.* Stockholm, Sweden, Svensk Kärnbränslehantering AB/Swedish Nuclear Fuel and Waste Management Company.

Pusch, R. (2001b) *The microstructure of MX-80 clay with respect to its bulk physical properties under different environmental conditions.*

Pusch, R., Bluemling, P. & Johnson, L. (2003) Performance of strongly compressed MX-80 pellets under repository-like conditions. *Applied clay science* **23(1)**:239-244.

Pusch, R. & Carlsson, T. (1985) The physical state of pore water of Na smectite used as barrier component. *Engineering Geology* **21(3)**:257-265.

Pusch, R. & Hökmark, H. (1990) Basic model of water-and gas-flow through smectite clay buffers. *Engineering Geology* **28(3)**:379-389.

Pusch, R., Karlnland, O. & H, H. (1990) *GMM-a general microstructural model for qualitative and quantitative studies of smectite clays.*, Stockholm, Sweden, Report 90-43

Pusch, R., Ranhagen, L. & Nilsson, K. (1985) *Gas migration through MX-80 Bentonite. Final report.* Swedish Geological, Lund, Sweden.Technical report 85-39.

Pusch, R. & Yong, R. (2003) Water saturation and retention of hydrophilic clay buffer—microstructural aspects. *Applied clay science* **23(1)**:61-68.

Quirk, J., Pereira, C. & Tanton, T. (1986) Soil Permeability in Relation to Sodicity and Salinity [and Discussion]. *Philosophical Transactions of the Royal Society of London. Series A, Mathematical and Physical Sciences* **316(1537)**:297-317.

Rascol, E. (2009) Cyclic properties of sand: dynamic behaviour for seismic applications. *Thèse EPFL, n° 4546*. Ecole polytechnique fédérale de Lausanne.

Ritter, H. & Drake, L. (1945) Pressure porosimeter and determination of complete macropore-size distributions. Pressure porosimeter and determination of complete macropore-size distributions. *Industrial & Engineering Chemistry Analytical Edition* **17(12)**:782-786.

Romankiw, L. & Chou, I.-M. (1983) Densities of aqueous NaCl, LCl, MgCl2, and CaCl2 binary-solutions in the concentration range 0.5-6.1-m at 25 °C, 30 °C, 35 °C, 40 °C, and 45°C. *Journal of Chemical and Engineering Data* **28(3)**:300-305.

Romero, E. (1999) Characterisation and thermo-hydromechanical behaviour of unsaturated boom clay: an experimental study. Universite Polytechnique de Catalogne.

Romero, E. (2001) Controlled–suction techniques In *Proceedings of 4° Simpósio Brasileiro de Solos nâo Saturados* (Gehling, W. Y. Y., Schnaid, F., and(Abms), A. B. D. M. D. S. (eds)), pp. 535-542.

Romero, E. (2013) A microstructural insight into compacted clayey soils and their hydraulic properties. *Engineering Geology* **165**:3-19.

Romero, E., Alonso, E. E. & Knobelsdorf, J. (2002) *Laboratory tests on compacted sand-bentonite buffer material for the GMT emplacement project*. UPC, Barcellona

Romero, E., Della Vecchia, G. & Jommi, C. (2011) An insight into the water retention properties of compacted clayey soils. *Géotechnique* **61(4)**:313-328.

Romero, E. & Simms, P. H. (2008) Microstructure investigation in unsaturated soils: a review with special attention to contribution of mercury intrusion porosimetry and environmental scanning electron microscopy. *Geotechnical and Geological engineering* **26(6)**:705-727.

Romero, E. & Vaunat, J. (2000) Retention curves of deformable clays. *Experimental evidence and theoretical approaches in unsaturated soils*:91-106.

Rüedi, J., Marschall, P., Manca, D., Ferrari, A., Laloui, L., Kulenkampff, J., Gründig, M., Lippmann-Pipke, J. & Kontar, K. (2013) *FORGE (Fate of Repository Gases) Final Laboratory Report. Deliverables D03.34 and D3.36.*Arbeitsbericht NAB.

Saiyouri, N., Hicher, P. & Tessier, D. (1998) Microstructural analysis of highly compacted clay swelling In *Proceedings of 2nd International conference on unsaturated soils* (Publisher, I. A. (ed)). International academic publisher vol. 1, pp. 119 - 124.

Saiyouri, N., Tessier, D. & Hicher, P. (2004) Experimental study of swelling in unsaturated compacted clays. *Clay Minerals* **39(4)**:469-479.

References

Salager, S., Nuth, M., Ferrari, A. & Laloui, L. (2013) Investigation into water retention behaviour of deformable soils. *Canadian Geotechnical Journal* **50(2)**:200-208.

Scheidegger, A. E. (1958) The Physics of Flow Through Porous Media. *Soil Science* **86(6)**:355.

Seiphoori, A. (2014) Thermo-hydro-mechanical characterisation and modelling of MX-80 granular bentonite. *Thèse EPFL, n° 6159*. Ecole polytechnique fédérale de Lausanne.

Seiphoori, A., Ferrari, A. & Laloui, L. (2014) Water retention behaviour and microstructural evolution of MX-80 bentonite during wetting and drying cycles. *Géotechnique* **64(9)**:721-734.

Senger, R., Papafotiou, A. & Marschall, P. (2013) *Gas related property distributions in the proposed host rock formations of the candidate siting regions in Northern Switzerland and in the Helvetic Zone*. Wettingen. Switzerland.Arbeitsbericht NAB 13-83.

Shirazi, S., Wiwat, S., Kazama, H., Kuwano, J. & Shaaban, M. (2011) Salinity effect on swelling characteristics of compacted bentonite. *Environment Protection Engineering* **37(2)**:65-74.

SN 670 330 b (2005) Norme Enregistrée de l'Association Suisse de Normalisation sur les méthodes d'essai de détermination en laboratoire de la masse volumique de reference et de la teneur en eau – compactage proctor.

Studds, P., Stewart, D. & Cousens, T. (1998) The effects of salt solutions on the properties of bentonite-sand mixtures. *Clay Minerals* **33(4)**:651-660.

Suzuki, K., Asano, H., Yahagi, R., Kobayashi, I., Sellin, P., Svemar, C. & Holmqvist, M. (2013) Experimental investigations of piping phenomena in bentonite-based buffer materials for an HLW repository. *Clay Minerals* **48(2)**:363-382.

Suzuki, S., Prayongphan, S., Ichikawa, Y. & Chae, B.-G. (2005) In situ observations of the swelling of bentonite aggregates in NaCl solution. *Applied clay science* **29(2)**:89-98.

Tanai, K., Kanno, T. & Gallé, C. (1996) Experimental study of gas permeabilities and breakthrough pressures in clays In *Proceedings of MRS Proceedings*. Cambridge Univ Press vol. 465, pp. 995.

Tanikawa, W. & Shimamoto, T. (2006) Klinkenberg effect for gas permeability and its comparison to water permeability for porous sedimentary rocks. *Hydrology and Earth System Sciences Discussions* **3(4)**:1315-1338.

Tarantino, A. (2009) A water retention model for deformable soils. *Géotechnique* **59(9)**:751-762.

Tarantino, A. (2010) Basic concepts in the mechanics and hydraulics of unsaturated geomaterials. In *Mechanics of Unsaturated Geomaterials*. (Laloui, L. (ed) Wiley, pp. 1-28.

Teodori, S. P., Gaus, I., Köhler, S., Weber, H. P., Rösli, U., Steiner, P., Trick, T., Garcià Siñeriz, J. L., Nussbaum, C., Wieczorek, K., Schuster, K. & Mayor, J. C. (2011) *Long Term performance of Engineered Barrier Systems (PEBS), Mont Terri. HE-E Experiment: as-built report.*Arbeitsbericht Nagra Project. NAB 11-25.

Tessier, D., Lajudie, A. & Petit, J.-C. (1992) Relation between the macroscopic behavior of clays and their microstructural properties. *Applied geochemistry* **7**:151-161.

Thermo Electron (2006) Mercury intrusion porosimeter PASCAl 140 series. Intruction manual.

Thermo Scientific (2007) PASCAL software. For PASCAl 140-140-440 Series porosimeters. Operating Manual.

192

Tournassat, C. & Appelo, C. (2011) Modelling approaches for anion-exclusion in compacted Na-bentonite. *Geochimica et Cosmochimica Acta* **75(13)**:3698-3710.

Traber, D. (2011) *Recipe and preparation of a simplified artificial pore water for Opalinus Clay and Brown Dogger.*, Wettingen, Switzerland

Tuller, M. & Or, D. (2003) Hydraulic functions for swelling soils: pore scale considerations. *Journal of hydrology* **272(1)**:50-71.

Vanapalli, S. K., Nicotera, M. & Sharma, R. S. (2008) Axis translation and negative water column techniques for suction control. *Geotechnical and Geological engineering* **26(6)**:645-660.

Vaughn, P. (2006) Impact of Gas Generation on the Performance of the Waste Isolation Pilot Plant. In *Gas Transport in Porous Media.* Springer, pp. 385-406.

Villar, M. (2000) Thermo-hydro-mechanical characterisation of a bentonite from Cabo de Gata. Universidad Complutense de Madrid.

Villar, M. (2007) Water retention of two natural compacted bentonites. *Clays and Clay Minerals* **55(3)**:311-322.

Villar, M. & Lloret, A. (2001) *Variation of the intrinsic permeability of expansive clays upon saturation.* Balkema, Rotterdam.

Villar, M. & Lloret, A. (2004) Influence of temperature on the hydro-mechanical behaviour of a compacted bentonite. *Applied clay science* **26(1)**:337-350.

Villar, M. & Lloret, A. (2008) Influence of dry density and water content on the swelling of a compacted bentonite. *Applied clay science* **39(1)**:38-49.

Villar, M., Martín, P. L., Gutiérrez-Rodrigo, V., Romero, F. J. & Barcala, J. M. (2013) *Contribution of CIEMAT to WP3. FORGE final report*

Viola, R., Tuller, M., Or, D. & Drasdis, J. (2005) Microstructure of clay-sand mixture at different hydration states In *Proceedings of Advance experimental unsaturated soil mechanics* (Tarantino, A., Romero, E., andCui, Y. (eds)). Taylor & Francis Group vol. 1, pp. 437-442.

Wang, Q., Tang, A. M., Cui, Y.-J., Barnichon, J.-D. & Ye, W.-M. (2013) Investigation of the hydro-mechanical behaviour of compacted bentonite/sand mixture based on the BExM model. *Computers and Geotechnics* **54**:46-52.

Wang, Q., Tang, A. M., Cui, Y.-J., Delage, P. & Gatmiri, B. (2012) Experimental study on the swelling behaviour of bentonite/claystone mixture. *Engineering Geology* **124**:59-66.

Washburn, E. W. (1921) The dynamics of capillary flow. *Physical review* **17(3)**:273.

Webb, S. W. (2006) Two-phase gas transport. In *Gas Transport in Porous Media.* Springer, pp. 55-70.

Whitaker, S. (1986) Flow in porous media II: The governing equations for immiscible, two-phase flow. *Transport in porous media* **1(2)**:105-125.

Witteveen, P., Ferrari, A. & Laloui, L. (2013) An experimental and constitutive investigation on the chemo-mechanical behaviour of a clay. *Géotechnique* **63(3)**:244-255.

Wu, Y.-S., Pruess, K. & Persoff, P. (1998) Gas flow in porous media with Klinkenberg effects. *Transport in porous media* **32(1)**:117-137.

Zhang, H.-Y., Cui, S.-L., Zhang, M. & Jia, L.-Y. (2012) Swelling behaviors of GMZ bentonite–sand mixtures inundated in $NaCl–Na_2SO_4$ solutions. *Nuclear Engineering and Design* **242**:115-123.

References

Appendix A: The use of the fluid-fluid interface

INTRODUCTION

This report was compiled by Mr. Thomas Ardiet on May 2013 in the framework of his internship entitled:" Experimental determination of the water and gas permeability of a Sand/Bentonite mixture" carried out at the laboratory for Soil Mechanics under the supervision of Mrs. Donatella Manca, Dr. Alessio Ferrari and Prof. Lyesse Laloui.

In this report the use of the toxic interface is detailed and a calibration method is proposed.

This cell is composed of two chambers, separated by an impermeable membrane (Figure 1). The clean chamber (transparent) is filled with distilled water, and is connected to the PV controller. The dirty chamber is made of stainless steel to avoid any corrosion. This chamber is filled with highly corrosive water and is connected to the sample. Each chamber is equipped with a three-way valve.

The volume of the cell was determined both form geometrical measurements and by filling it with a PV controller:

- Geometrical measure: $V_c = \pi R^2 h = 190459$ mm^3;
- By filling the cell with a PV controller: $V_c = 191591$ mm^3.

Figure 1 - Interface cell.

FILLING PROCEDURE

The saline water that is injected in the dirty chamber is not previously de-aired. As a consequence, to proper convey the fluid pressure between the PV controller and the specimen, it was necessary to establish a standard procedure to minimise the amount of air stored in the dirty chamber. This procedure is proposed in the following:

- Connect the clean chamber to the vacuum system;
- Connect a tube to the dirty chamber that goes from the interface to the salty water reservoir;
- Apply the vacuum from the clean chamber to fill up approximately two thirds of the interface volume with salty water;
- Connect the clean chamber to the PV controller;
- Turn the interface upside down and fill the clean chamber with distilled de-aired water (the valve of the dirty chamber must be open to evacuate the air accumulated in it);
- Once the air in the dirty cell is close valve of the dirty chamber and turn the cell upside down again to place it in the standard position (clean chamber up);
- Fill the clean chamber with the PV controller. During this procedure air will accumulate in the clean chamber and the pressure in the entire interface will rise.
- When the pressure reach 50 kPa release the air accumulated in the clean chamber by opening the three valve of the clean chamber to the atmospheric pressure (the valve of the dirty chamber remains close).
- Repeat the point above as many times as it needs to evacuate the air in the clean chamber.
- Finally, turn again the cell upside down, pressurise the interface with the PV controller and release the pressure from the dirty chamber valve. In this manner the remaining air in it will be evaluated.

Flow calibration

To use the interface cell, the inlet flow in the clean chamber and the outlet flow from the toxic chamber have to be equal. To verify this assumption, the cell was filled as described previously with de-aired distilled water in both chambers, then given pressures was applied with the PV controller connected to the clean chamber (i.e.: 10 kPa, 20 kPa, 40 kPa). The outflow was measured with a precision balance by weighting the water coming out from the toxic chamber (Figure 2).

As water flowing out from the interface cell is in contact with the laboratory ambient (T = 21 °C; RH = 41 %), the measured outflow need to be corrected to take into account evaporation phenomena. To measure the rate of evaporation of the laboratory, distilled water was placed in a recipient open to ambient air and its weigh was recorded during six hours. A measured evaporated rate is $Q_{ev} = 1.04 \cdot 10^{-4}$ g/s.

Figure 2 - Flow calibration setup

Results of flow calibration are shown in Figure 3, were $\Delta V_{w,in}$ is the inlet volume of water in the cell, and $\Delta V_{w,out}$ is the volume of water flowing from the cell. The outlet volume takes into account the evaporated water by the follow expression:

$$\Delta V_{w,out} = -(M_w \rho_w + Q_{ev} t)$$

where M_w is the measured mass of water flowing out from the chamber, ρ_w is the density of water Q_{ev} is the rate of evaporation of the laboratory and t the time.

As shown in Figure 3, inflow and outflow are nearly equal for the three considered pressures proving that the membrane correctly conveys a given flow from clean water to toxic water.
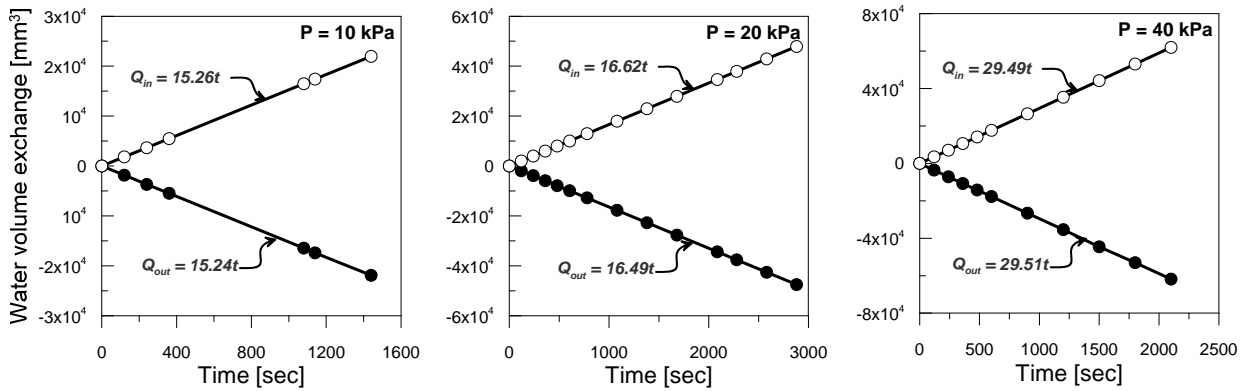
Figure 3: Flow calibration for different pressures: 10, 20 and 40 kPa

Pressure calibration

To verify if the membrane conveys well a given pressure, the setup showed Figure 4 in was used. Prior to the test the cell was filled as described previously with de-aired distilled water in both chambers. First a pressure sensor was connected directly to a PV controller and loading/unloading cycles were performed. Then the interface cell was placed between the pressure sensor and the PV controller (Figure 4). Pressure was imposed on one side by the controller, and measured on the other side by the sensor. Three pressure increase/decrease cycles in from 0 to 500 kPa were performed for each setup to measure hysteretic phenomena.

The Figure 5 below shows the response of the sensor to these cycles with, then with the interface cell. The figure shows that the presence of the interface do not causes any hysteresis.

Figure 4: Pressure calibration setup
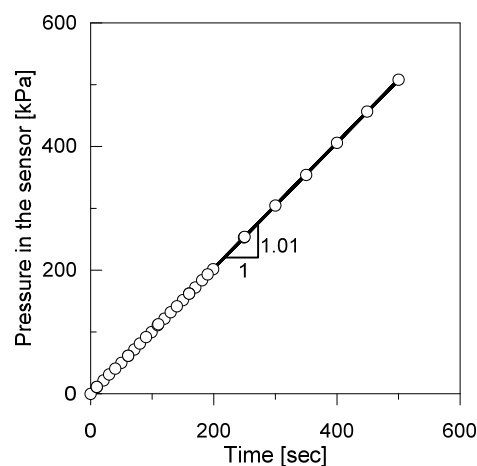
Figure 5: Loading/unloading cycles

The Figure 6 compares the results of the pressure increase-decrease cycles with and without the interface. The results show that the interface well conveys the imposed pressure. This simple calibration revealed that the relative error in the pressure produced when the interface is used is less than 1%.
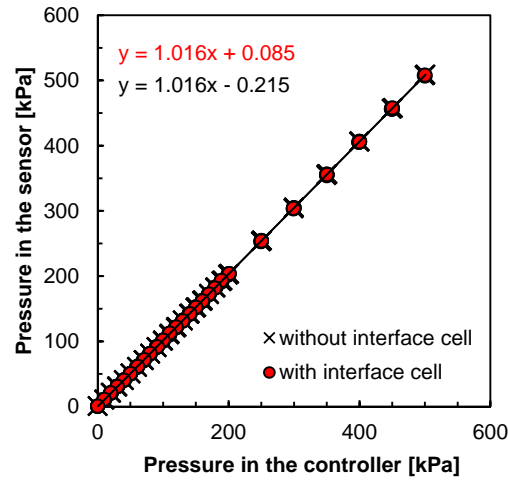
Figure 6 - Pressure calibration

Appendix B: Executive drawing of the gas injection system

Cross connection
SS-6M0-4

L connection
SS-6M0-2-4

Cylinder 1000 ccm
304L-HDF4-1000

Cylinder 75 ccm
304L-HDF4-75

Non rotating Stem Valve
SS-14DKS6MM

Adaptor for 1/4" NPT to 6 mm tube
SS-6-MTA-1-4

Ball valve
SS-42GS6MM

T connection
SS-6M0-3

200
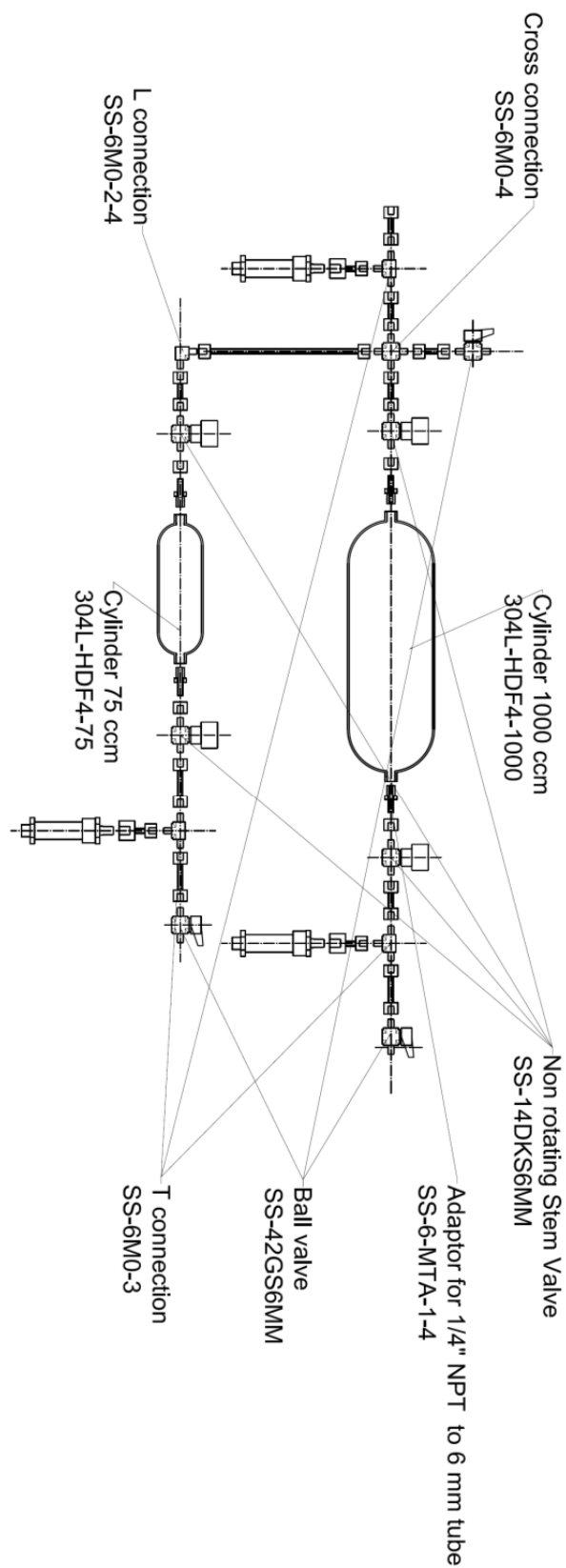
Appendix C: MATLAB code for solving the transient gas injection process

```matlab
clc;
clear all;
tic

%%%%%%%%%%%%%%%%%%%%%%%%%%%%%%%%%%%%%%%%%%%%%%%%%%%%%%%%%%%%%%%%%%%%%%%%%%%%%%%%
%%%%%%

%%%%%%%%%%%%%%%%%%%%%%%%%%%%%%%%%Input
Data%%%%%%%%%%%%%%%%%%%%%%%%%%%%%%%%%%%%%%%%%%%%%%
%%%%%%%%%%%%%%%%%%%%%%%%%%%%%%%%%%Gas
parameters%%%%%%%%%%%%%%%%%%%%%%%%%%%%%%%%%%%%%%%%%%%
kg=1.3e-12;%gaz permeability (kg/(phi*(1-Sr))
mug=17.6648e-6% dynamic viscosity of N2 (Pas)
mg=14.007*2*10^-3;%mass molar of N2 Kg/mol
R=8.3144621% gas constant J/(mol.K) = m3.Pa/(mol.K)
Temp=273.15+22; %temperature in Kelvin

%%%%%%%%%%%%%%%%Klinkenberg parameter from microstructure%%%%%%%%%%%%%%%%%%
suction=150;
%Imput suction [kPa]
rhod=1.5;
%Imput dry density [Mg/m3]
w=0.143;
%Imput water content [-]

B=0.15;
C=0.36;
%Parameter for Klinkenber calculation from Tanikawa 2006
CKC=5;
%Kozeni - Carman constant
RS=0.8;
%sand ratio in the mixture [-]
RB=1-RS;
%Bentonite ratio in the mixture [-]
rhosb=2.74;
%bentonite dry density [Mg/m3]
rhoss=2.65;
%Sand dry density [Mg/m3]
rhosmix=1./(RS/rhoss+RB/rhosb);
%Mixture dry density [Mg/m3]
voidratio=rhosmix/rhod-1;
SsM=0.15*1000000*2.65
%Macro specific surface
Ssn=580*1000000*2.84;

eb0rel=2.56;
%reference relative bentontie void ratio [-]
rhod0=1.5;
%reference mixture dry density [Mg/m3]
s0=280;
%reference suction [kPa]
```

Appendix C: MATLAB code for solving the gas injection process

```matlab
arho=5;
%material parameter [m3/Mg]
asuc=0.28;
%material parameter [-]
ebrel=eb0rel-arho*(rhod-rhod0)+asuc*log(s0/(suction+1));
%relative bentonite void ration
eb=ebrel*RB*rhosmix/rhosb;
%b3ntonite void ratio
eM=voidratio-eb;
%macropore void ratio
eMrel=eM/(1-(RB*rhosmix/rhosb));
%relative macropore void ratio
aStar=38;
%specific surface constant micro
bStar=150;
%specific surface constant 2 micro
Ssm=(aStar*(eb0rel-ebrel)+bStar)*1000*rhosb*1000;
%Secific surface micro

if rhod==1.5
%Nano pore void ratio
    en=0.0575*log(suction)-0.0214;
else if rhod==1.8
     en=-0.027*log(suction)+0.194;
    end
end

em=eb-en;
%micro void ratio
emrel=em/eb*ebrel;
%relative micro void ratio
Mratio=(eM/rhosmix)*(1/(1/rhod-RS/rhoss));
%Area macro divided total void radio
Bratio=(eb/rhosmix)*(1/(1/rhod-RS/rhoss))
%Area bentonite divided total void radio
kM=(1/(CKC*SsM^2))*((eMrel^3)/(1+eMrel));
%macropore permeability
kMM=kM*Mratio;
%real macropore permeability
km=(1/(CKC*Ssm^2))*((emrel^3)/(1+emrel));
nmrel=emrel/(1+ebrel);
kmm=nmrel*km*Bratio;

ki=kmm+kMM;
b = B*ki^(-C);

%%%%%%%%%%%%%%%%%%%%%%%%%%%%%%%Geometry%%%%%%%%%%%%%%%%%%%%%%%%%%%%%%%%%%%%
%%%%
H=0.0807;% the length of the sample m
Diam=0.080;%Cell diameter
As=pi*Diam^2/4;%sample area
Vr=1010e-6;%Volume of the reservoir (m3)

%%%%%%%%%%%%%%%%%%%%%%%%%%%%%%%%Sample
characteristics%%%%%%%%%%%%%%%%%%%%%%%%%%%%%%%%%%%%%%%%%%%
%The sample characterics are known know a priori thus the permeability
coefficent il calculated after mearuting the real water content.
phi=0.80/(1+.80);%sample porosity
Sr=w*rhosmix/0.80;%Sample degree of saturation
```

```matlab
%%%%%%%%%%%%%%%%%%%%%%%%%%%%%%%%%%%%%%%%%%%%%%%%%%%%%%%%%%%%%%%%%%%%%%%%%
%%%%%
%%%%%%%%%%%%%%%%%%%%%%%%%%%%%%Discretization%%%%%%%%%%%%%%%%%%%%%%%%%%%%%%
%%%%%%%%%
%%%%%%%Space discretization
dz=0.002
z=floor(H/dz)+1;% node number
 for j=1:z
     Z(j)=(z-j)*dz; % the height of each node
  end
%%%%%%%Time discretization
Ts = 6;        % Duration of simulation. Leave this as 1.0. Increase the
maxiter below to add more time
dt = 0.000001;          % Number of space steps
Nt = Ts/dt;      % Number of time steps


%%%%%%%%%%%%%%%%%%%%%%%%%%%%%%%%%%%%%%%%%%%%%%%%%%%%%%%%%%%%%%%%%%%%%%%%%%
%%%%%
p0=135.5e3;%initial gas pressure
pb=100.0e3;%gas pressure at the base
for i=1:1:z

    p(i)=p0;
    x(i)=p0;

end

p(1)=pb;
x(1)=pb;

for i=1:1:z
    rog(i)=mg*p(i)/(R*Temp);

end



S=kg/(2*mug*phi*(1-Sr)); % Constant in the mass balance equation
Sresv=Vr*mg/(R*Temp*As);
Sstar=kg*rog(z)*dt/(Sresv*mug*dz);
Sk=kg*b*As*dt/(Vr*dz);

for i=1:Nt

    %solving mass conservation equation
    for j=2:z-1 %p(1)is known at t=0 from the initial condition; j is the
time index



p(j)=p(j)+(S*dt*(p(j+1)^2-2*p(j)^2+x(j-1)^2)/ dz^2)+(2*b*S*dt*(p(j+1)-
2*p(j)+x(j-1))/ dz^2); %here the gas pressure is calculated in each node
along the specimen heigh

    end

      p(z)=(1/(1+Sstar+Sk))*p(z)+((Sstar+Sk)/(1+Sstar+Sk))*p(z-1);% Update
of the pressure at the upper boundary
```

```matlab
    for j=1:1:z
        x(j)=p(j);
    end

    rog(z)=mg*p(z)/(R*Temp);
    Sstar=kg*rog(z)*dt/(Sresv*mug*dz);


step=500;%time step at which the values will be saved
        if i==step*floor(i/step)
          time(floor(i/step))=i*dt;
          pR(floor(i/step))=p(z);
        end


end
time'
pRkpa= pR/1000;
pR'/1000
kg

Time2=time'
pRkpa2= pR'/1000;

%%%%%%%%%%%%%%IMPORTING EXPERIEMENTAL DATA%%%%%%%%%%%%%%%%%%%%%%%%%%%%%%%%
A=importdata('Data_071114_1.txt');
Extime=A(:,1);
ExP=A(:,2);


%%%%%%%%%%%%%%%%%%%%%%%%%%%%%%%PLOTTING GRAPHS FOR COMPARISION%%%%%%%%%%%%%%%%
figure(1);
hold on
plot(time,pRkpa,':k')
plot(Extime,ExP,'r-')
```

204

Appendix D: SEM images of the S/B mixture

DRY QUARTZ SAND
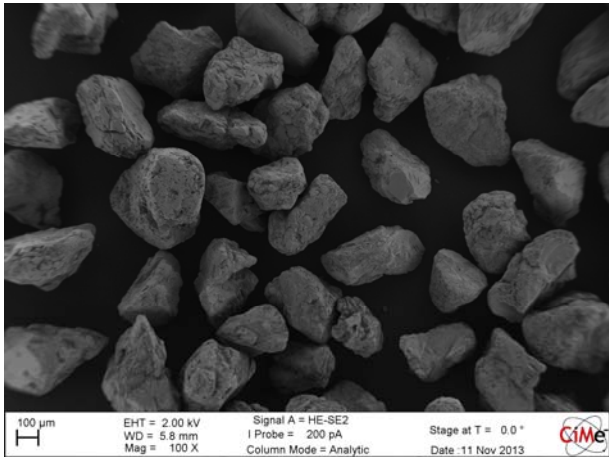
Figure 7: Sand grains
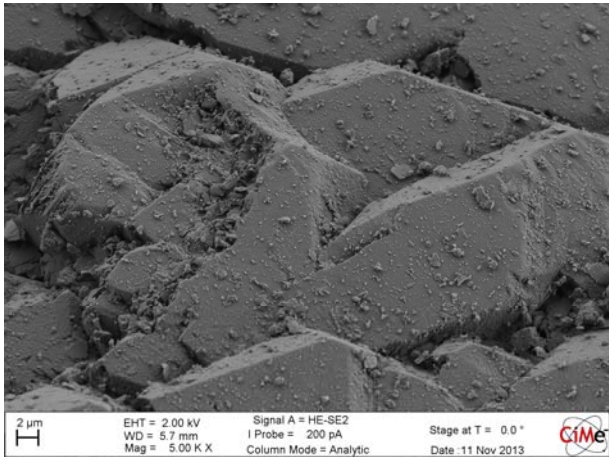
Figure 8: Surface of a sand's grain
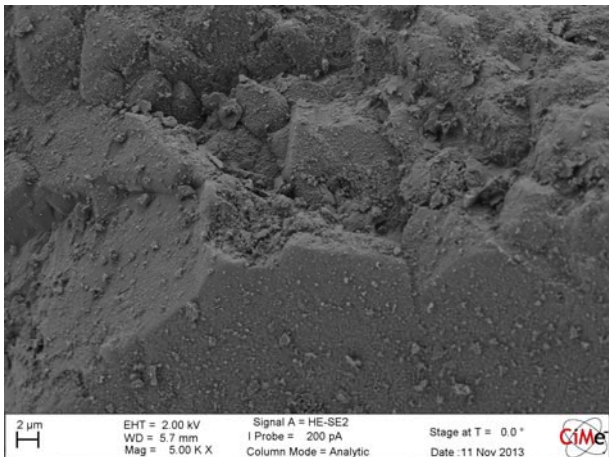
Figure 9: Surface of a sand's grain

DRY M8-80 BENTONITE
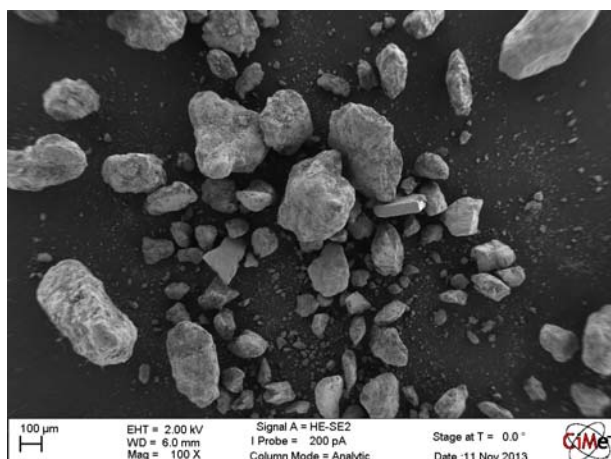
Figure 10: MX-80 Bentonite's grains
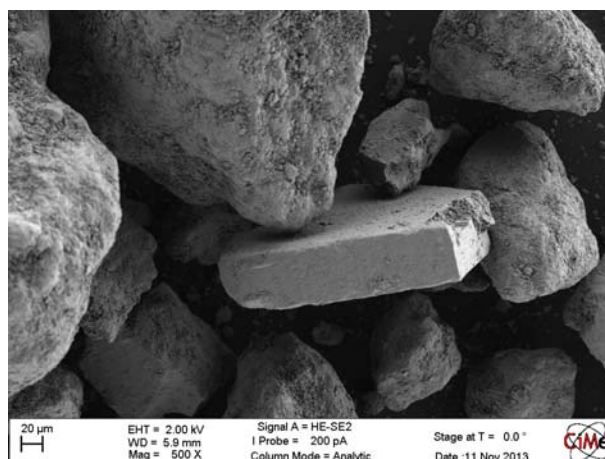
Figure 11: One impurity surrounded by bentonite's grains
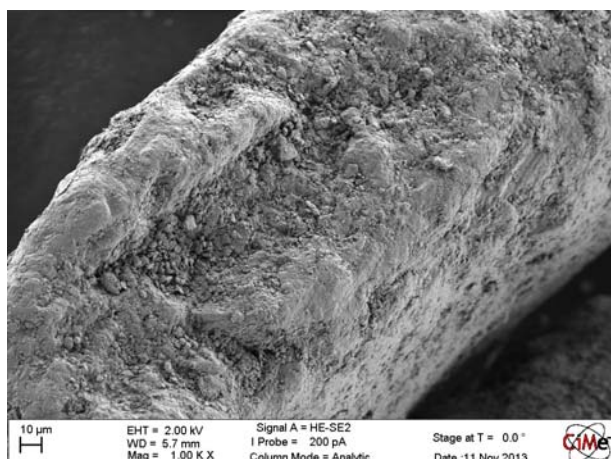
Figure 12: Closer observation of a bentonite's grain
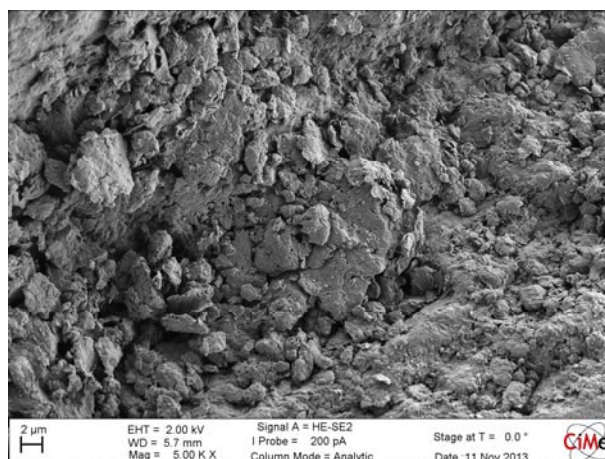
Figure 13: Bentonite finest particles covering a large grain
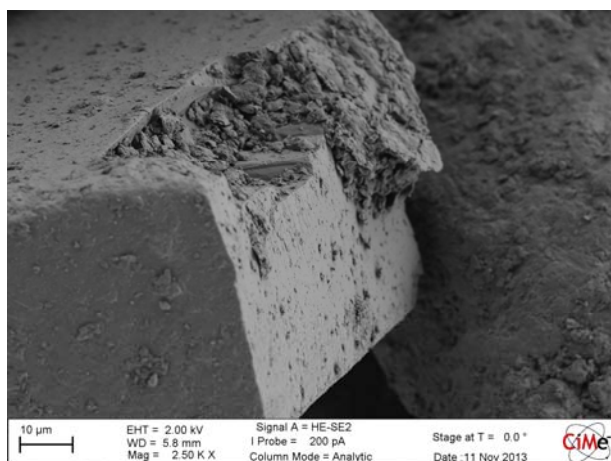
Figure 14: Closer observation of an impurity in the MX-80 granular bentonite
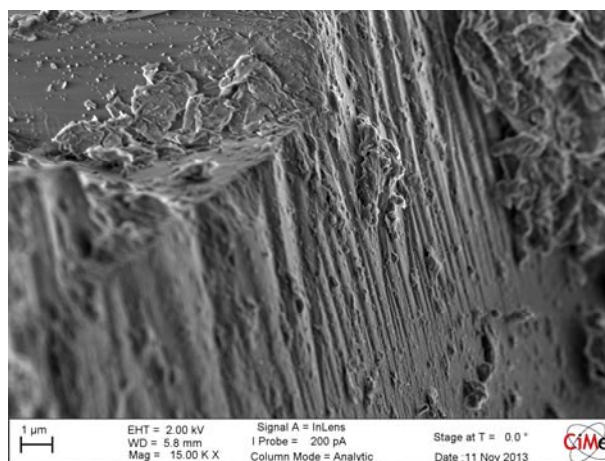
Figure 15: Closer observation of the surface of an impurity in the MX-80 granular bentonite

AS-COMPACTED 80/20 S/B - ρ_d= 1.5 Mg/m^3 - DISTILLED WATER
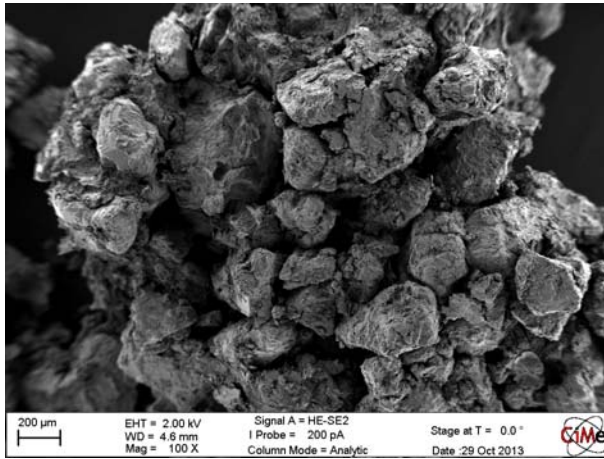
Figure 16: Aggregation of sand and bentonite
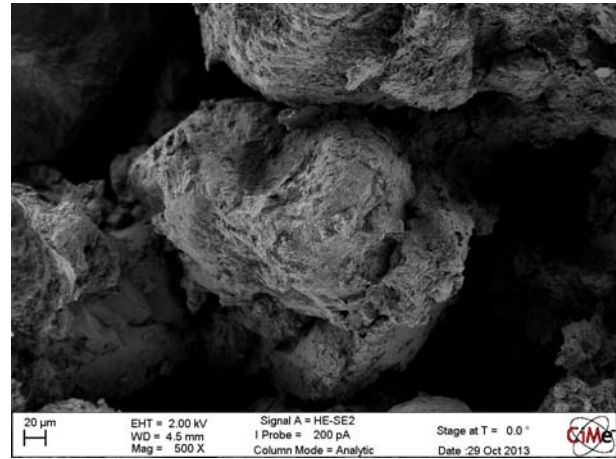
Figure 17: two grains of sand coated with bentonite large aggregates and fine bentonite particles
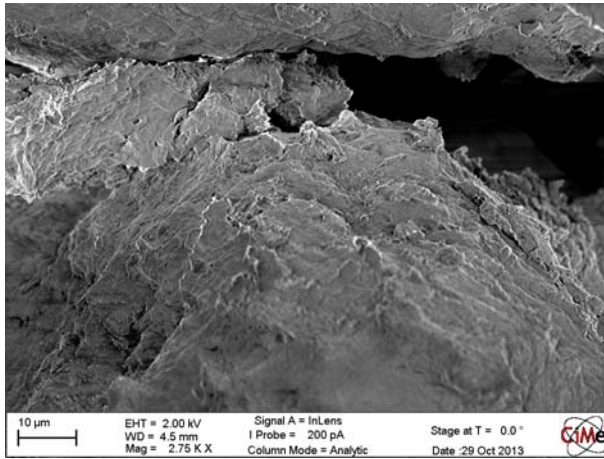
Figure 18: Aggregate of bentonite located between two grains of sand
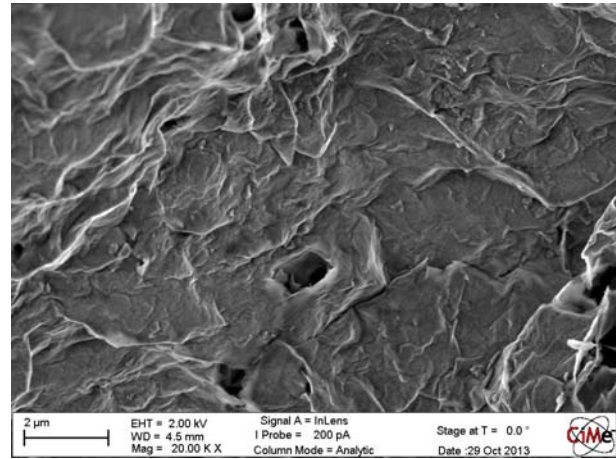
Figure 19: Micropore in the bentonite aggregate
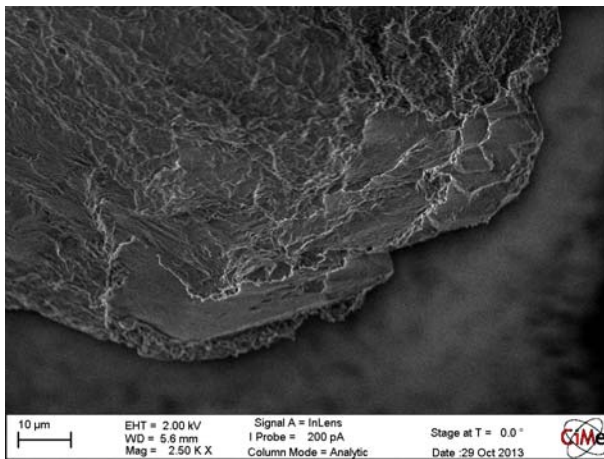
Figure 20: Surface of a sand's grain partially coated with bentonite
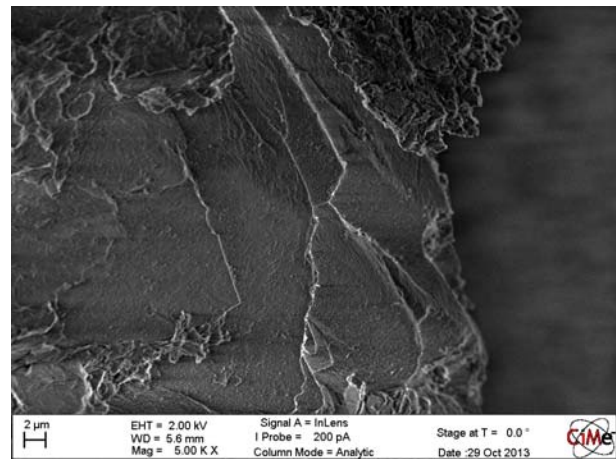
Figure 21: Surface of a sand's grain partially coated with bentonite

FULLY FATURATED 80/20 S/B - ρ_d= 1.5 Mg/m^3 - DISTILLED WATER
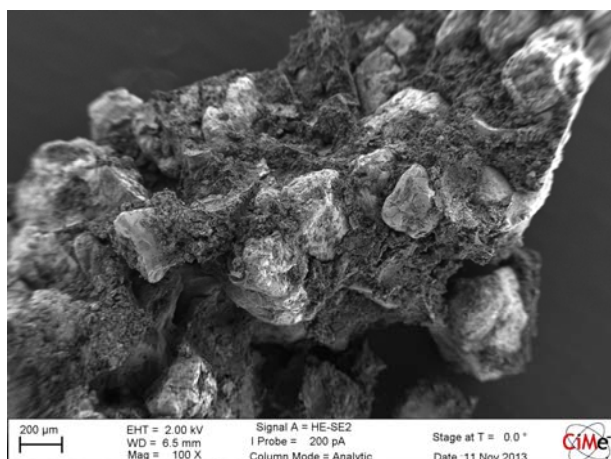
Figure 22: Aggregate of fully saturated 80/20 S/B bentonite
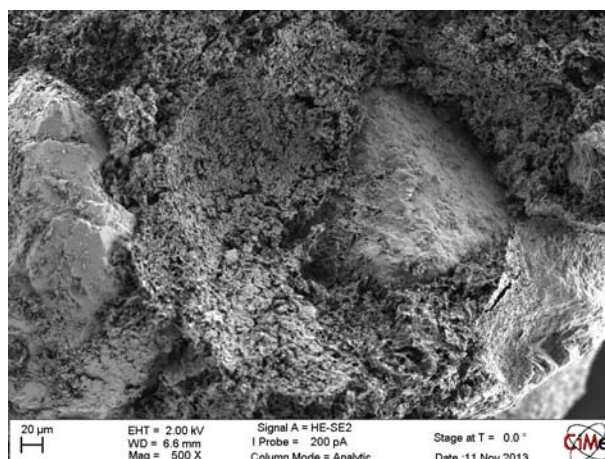
Figure 23: Fully expanded bentonite filling the space between two sand's grains
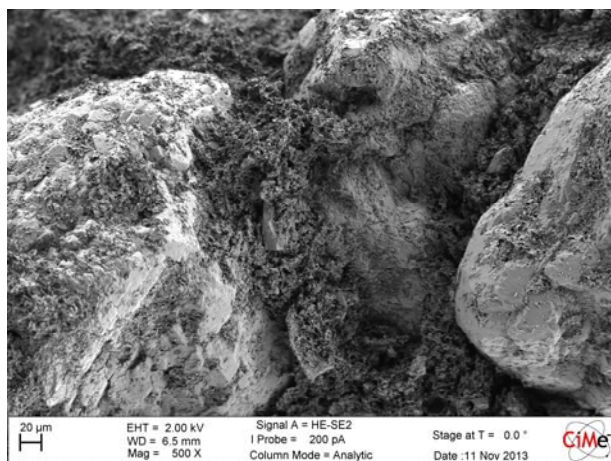
Figure 24: Expanded bentonite filling the space between sand's grains
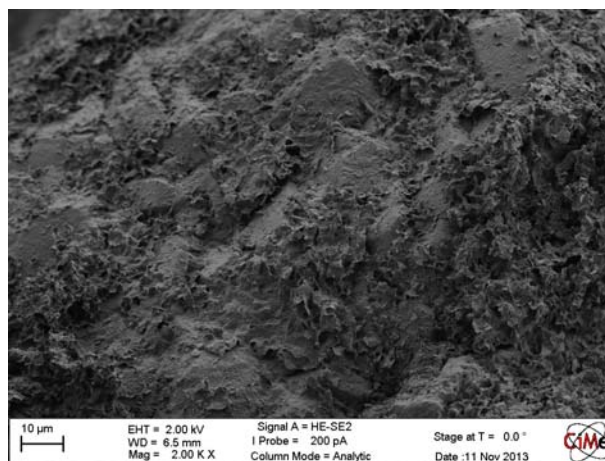
Figure 25: Fines bentonite particle occluding the crannies of the sand
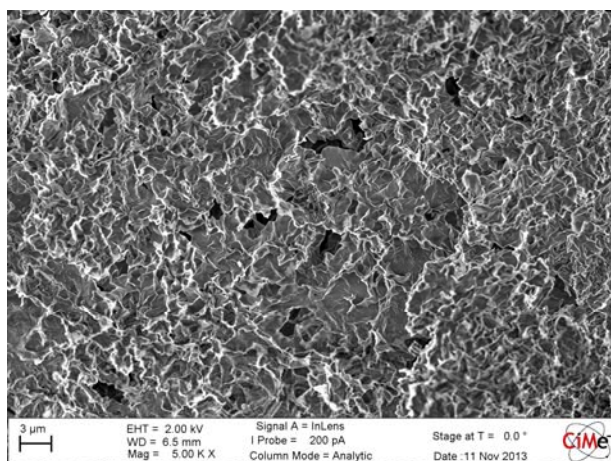
Figure 26: Fully expanded bentonite
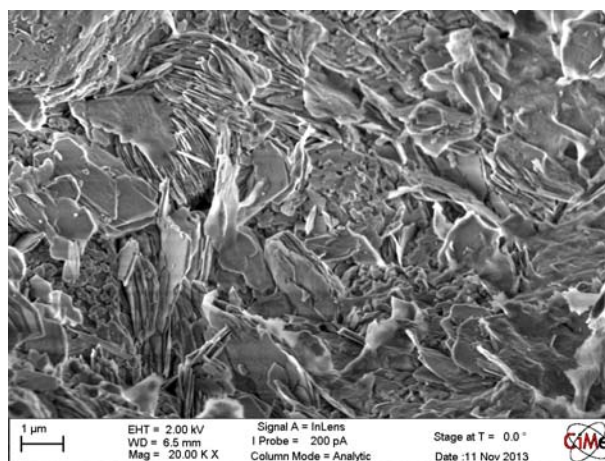
Figure 27: Observation of a colony of some unknown impurities in the 80/20 mixture

FULLY FATURATED 80/20 S/B - ρ_d= 1.8 Mg/m³ - DISTILLED WATER
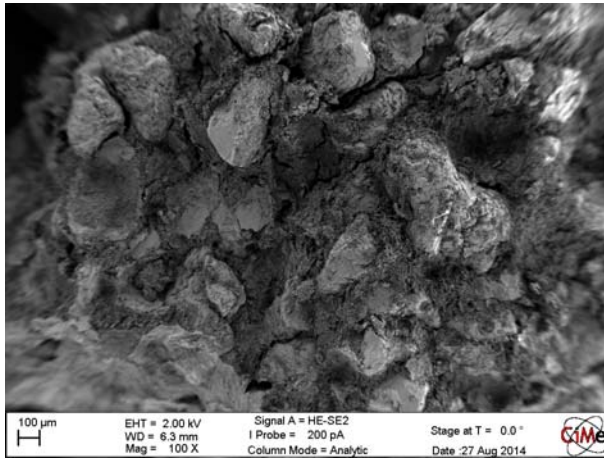
Figure 28: Aggregate of compacted - fully saturated S/B mixture
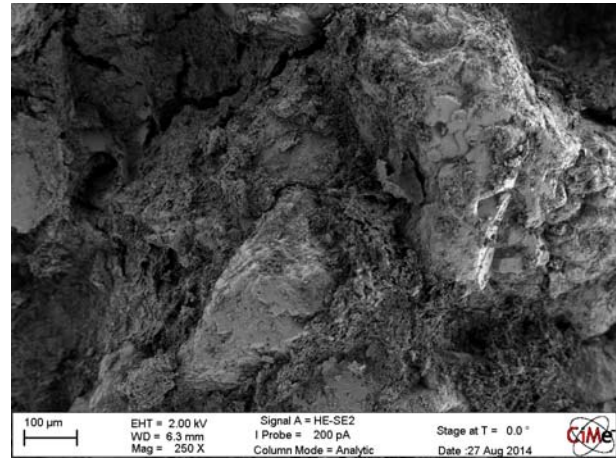
Figure 29: Closer observation of a sand to sand contact occluded with expanded bentonite
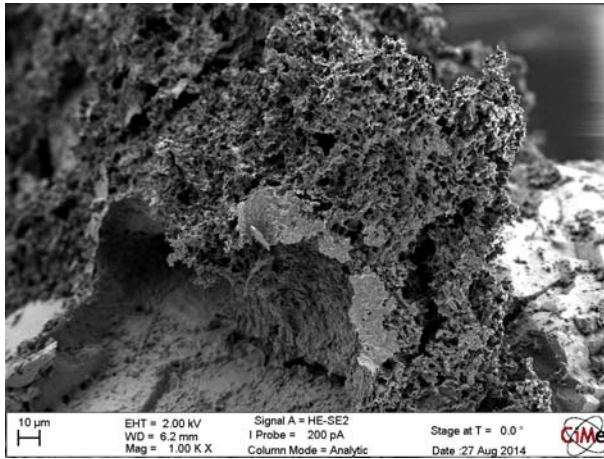
Figure 30: Aggregate of bentonite
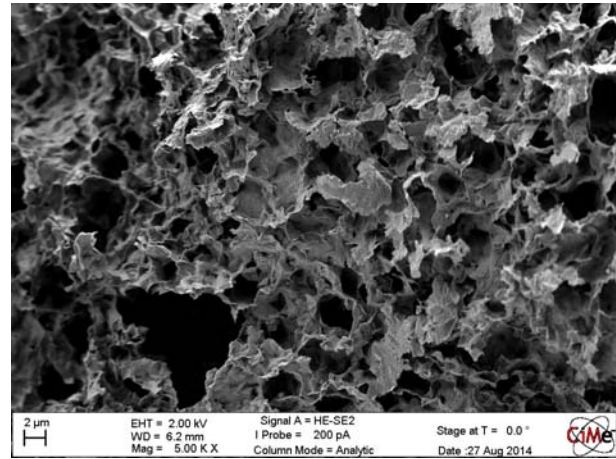
Figure 31: Aggregate of saturated bentonite. Close view of micropores
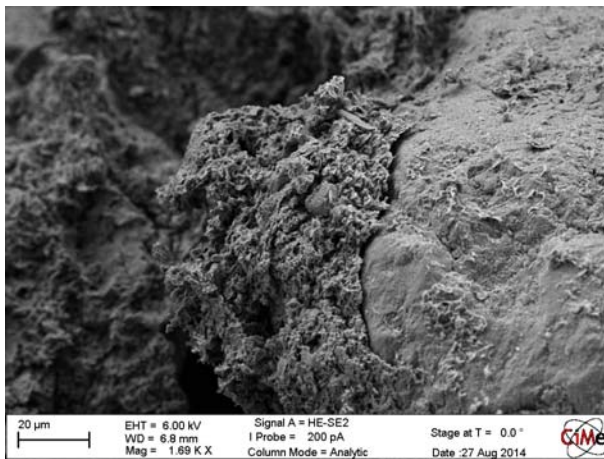
Figure 32: Aggregate of bentonite attached to a sand's grain
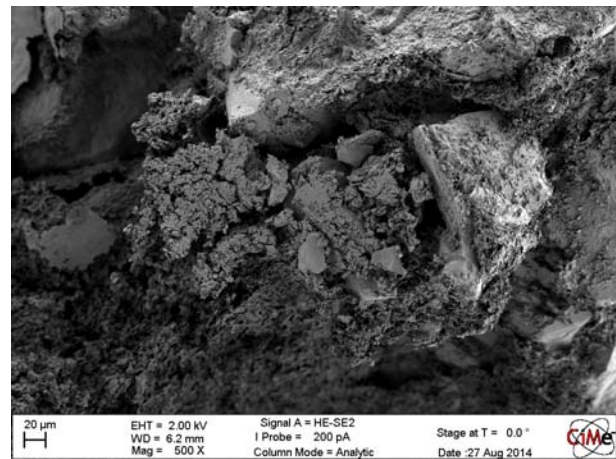
Figure 33: Aggregate of bentonite

209
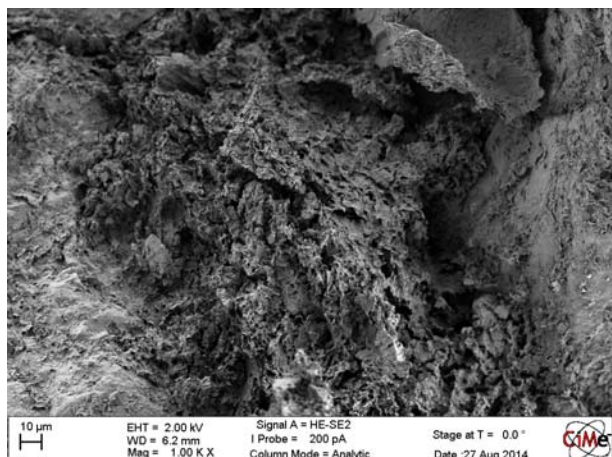
Figure 34: Aggregate of bentonite
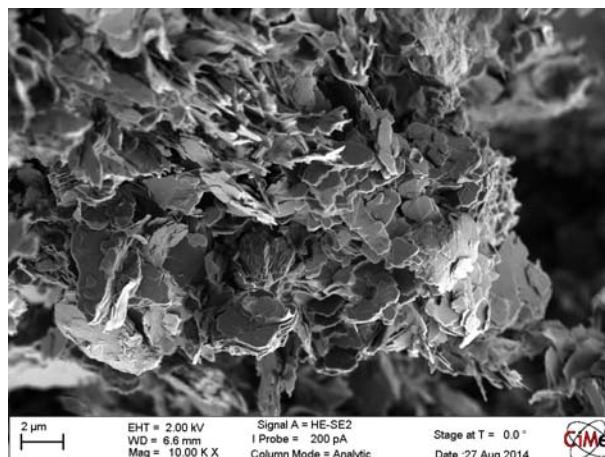
Figure 35: Aggregation of unknown impurities

MX-80 BENTONITE AT w=55% - DISTILLED WATER
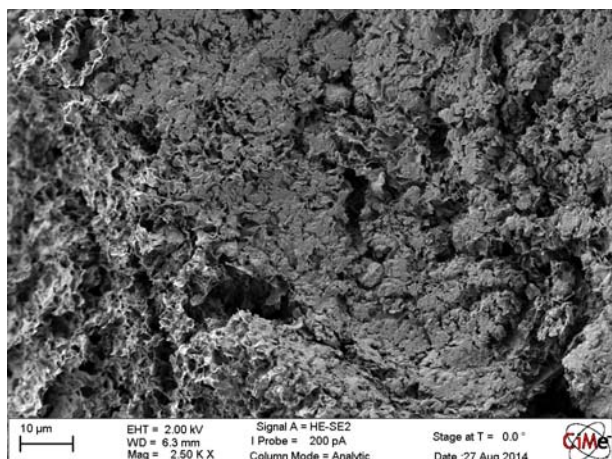
Figure 36: Aggregate of bentonite
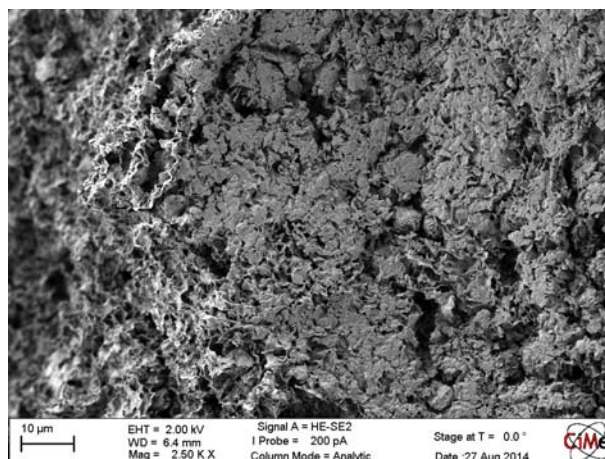
Figure 37: Aggregate of bentonite
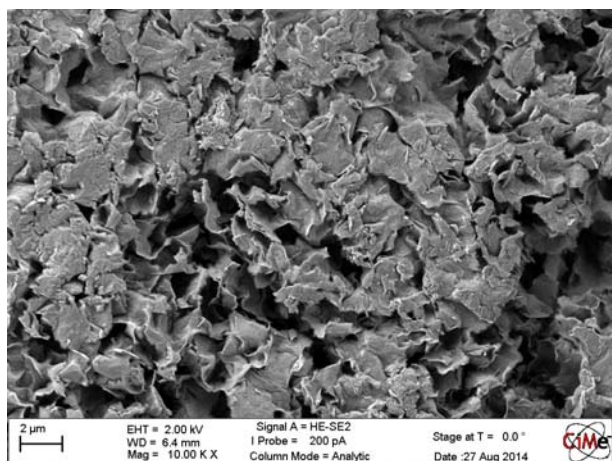
Figure 38: Closer observation of a bentonite aggregate
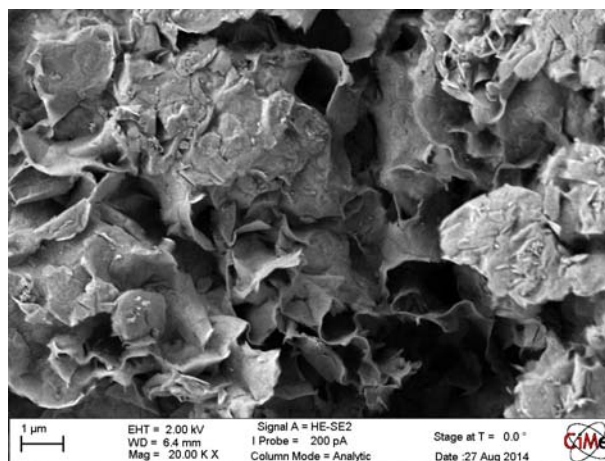
Figure 39: Flexible quasicrystals forming an hydrated bentonite aggregate

FULLY FATURATED 80/20 S/B - ρ_d= 1.5 Mg/m^3 - 1M NaCl
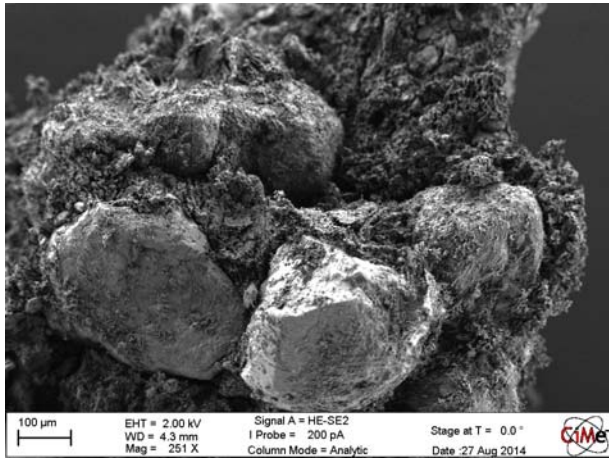
Figure 40: Aggregate of compacted S/B mixture
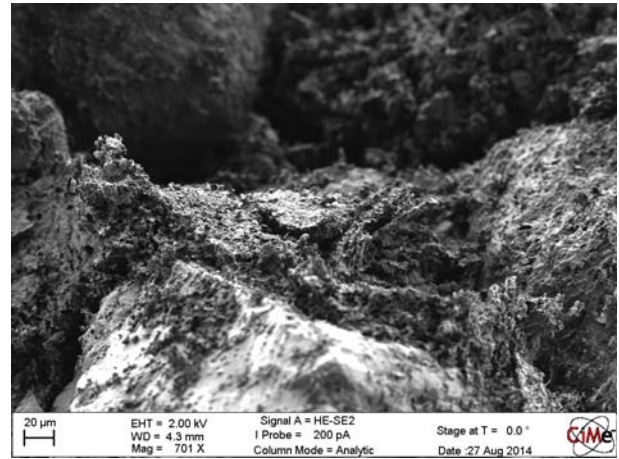
Figure 41: Aggregate of bentonite located between sand's grains
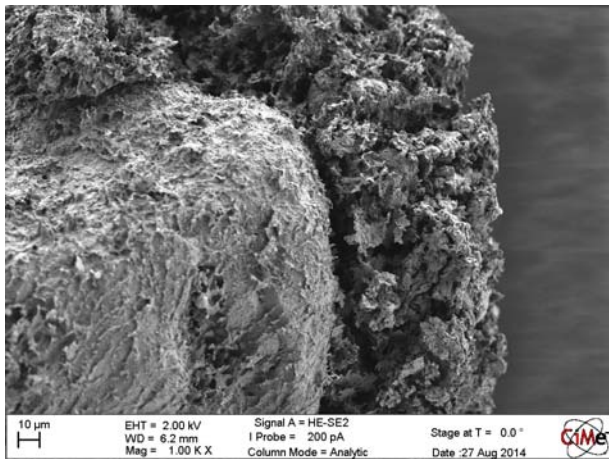
Figure 42: Aggregate of bentonite on a grain of sand
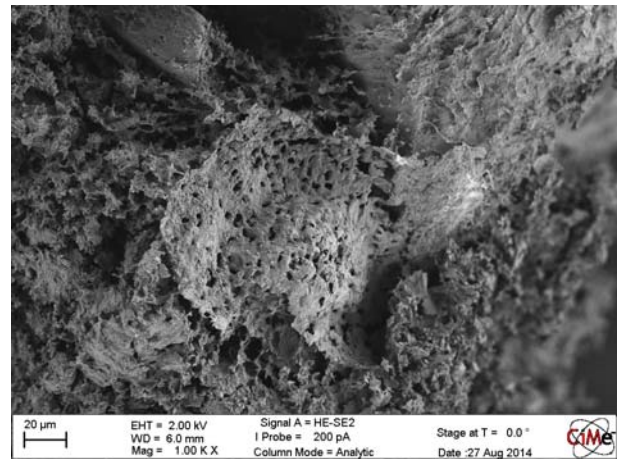
Figure 43: Aggregate of bentonite
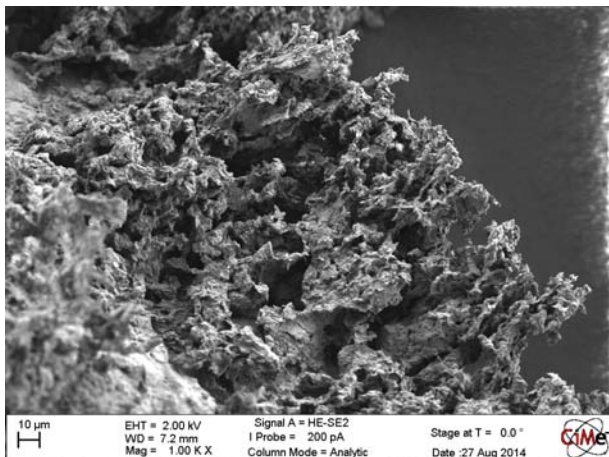
Figure 44: Aggregate of bentonite
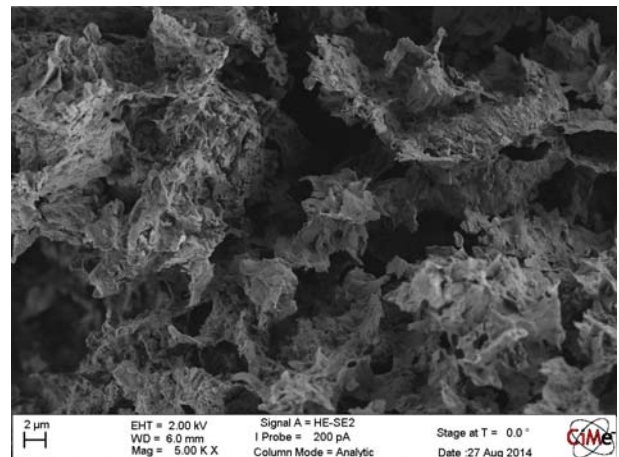
Figure 45: Tick quasicrystals of bentonite forming an aggregate

MX-80 BENTONITE AT w=52% - 4M NaCl
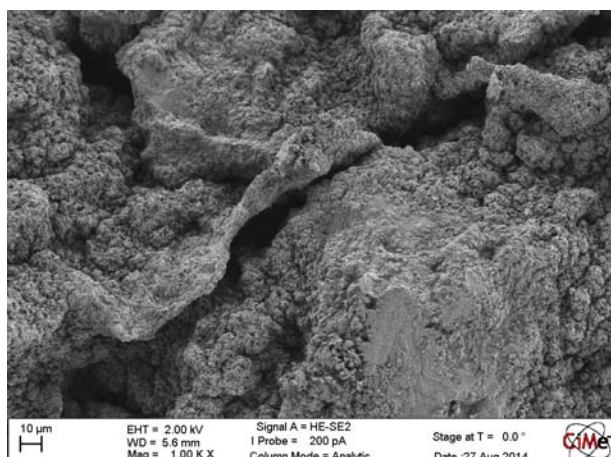
Figure 46: Aggregate of hydrated bentonite
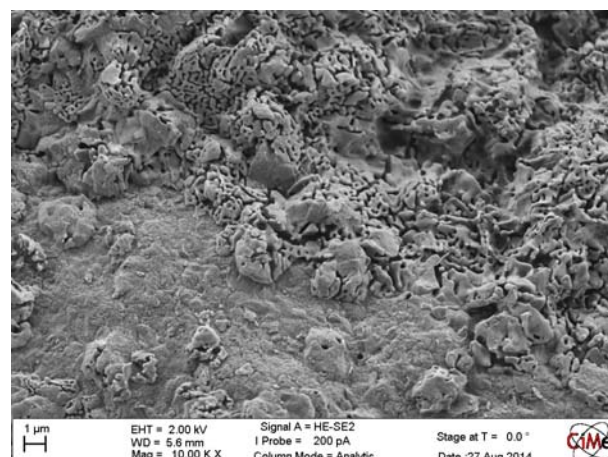
Figure 47: Surface of a sand's grain covered with fine bentontie mixed with precipitate NaCl
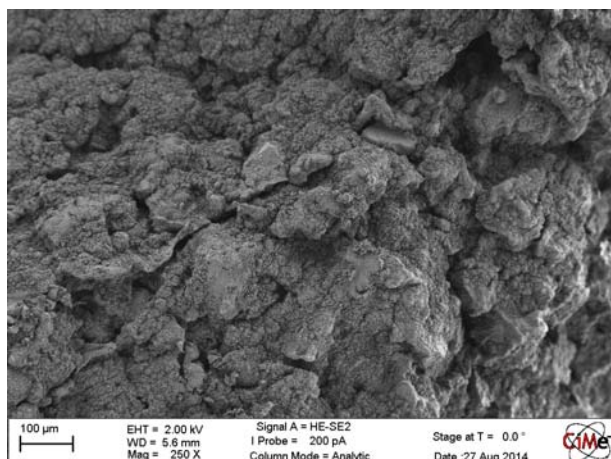
Figure 48: Closer observation of a bentonite aggregate hydrated with sodium chloride
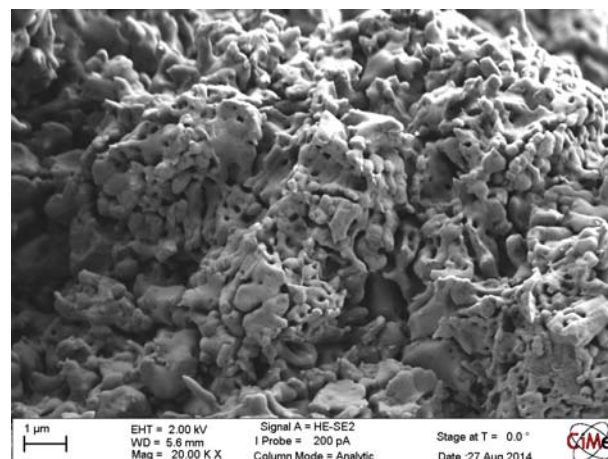
Figure 49: Aggregate of bentonite coated with NaCl
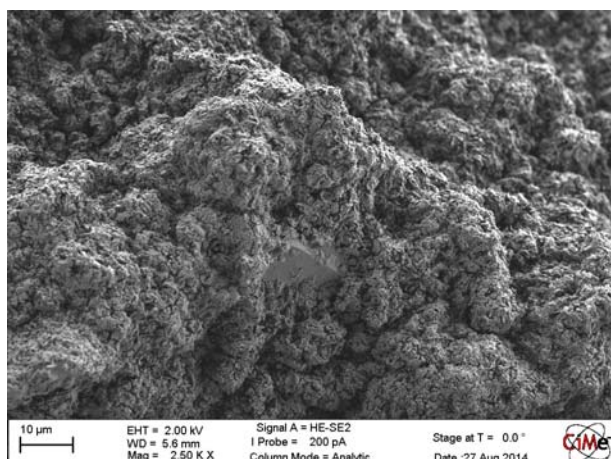
Figure 50: Unknown impurity surrounded by hydrated bentonite
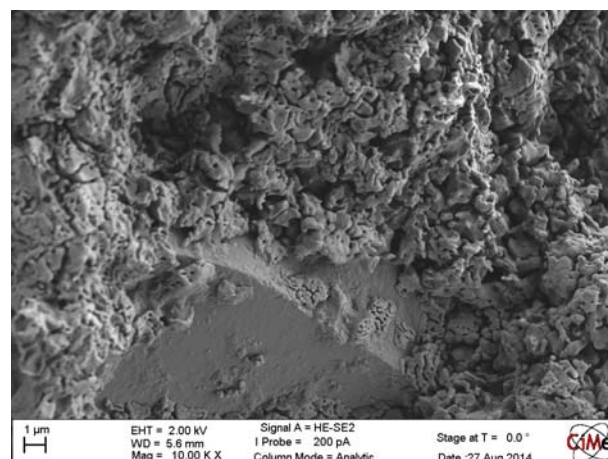
Figure 51: Close observation of the unknown impurity surrounded by hydrated bentonite

Appendix E : GAST Project: Laboratory pretesting of suction probes

Contents

List of figures

List of tables

1 Introduction

This report describes the activities performed at the Laboratory for Soil Mechanics (LMS) of the Swiss Federal Institute of Technology in Lausanne (EPFL) in the context of the GAST project for assessing sensors for suction monitoring.

The tested sensors are described in section 2. For each sensor, the principle of operation is detailed and the requirements in term of data acquisition system are specified. Finally, the calibration program is illustrated and the results are discussed. Final remarks and recommendations for the use and the installation of the sensors are presented in section 3.

2 Tested suction sensors

The selected sensors are:

- PST55 Psychrometer from Wescor (http://water.wescor.com).
- 229-WMP Heat dissipation matric water potential sensor from Campbell Scientific Inc., (http://www.campbellsci.co.uk).

The PST55 is a thermocouple psychrometer which is commonly used for in situ measurements of the soil total suction. The sensor has been tested in two different configurations (Figure 52). The first configuration is the one as-provided by the manufacturer and will be referred as PST55-Wescor. The sensor in the second configuration, provided by Aitemin (http://www.aitemin.es/), is enclosed in a stainless steel body which ensures its water tightness up to a pressure of 20 Bar; this configuration is referred as PST55-Aitemin.

The 229-WMP is a heat dissipation sensor used to measure the matric component of the soil suction and it is based on the relationship between the thermal conductivity and the matric suction of the sensor.

Table 1 summarizes the main characteristics of the tested sensors. In the following section the principle of measurement is detailed for the different types of sensors.

All tests were performed in a controlled temperature laboratory (T = 22±1°C).

Table 1 : Main characteristics of the tested sensors.

Sensor name	Sensor dimensions (cm)	Measured suction component	Output signal	Measurement range	Accuracy (as indicated by manufacturer)
PTS55-Elitech	0.5 x 1.0	Total	0-30 mV	To be determined in laboratory	-
PTS55-Aitemin	1 x 11	Total	0-30 mV	To be determined in laboratory	-
229-WMP	1 x 6	Matric	50±0.25 mA	10 – 2500 kPa	1 kPa for S>100 kPa

2.1 PTS55 PSYCHROMETERS

2.1.1 Sensor description and principle of operation

Psychrometers are commonly used for in situ measurements of the water potential. They give an indirect measurement of the total suction of a porous material using the psycrhometric law:

$$\psi = -\frac{RT\rho_w}{\omega_w}ln\left(RH\right) \tag{1}$$

where RH is the relative humidity in the pore air, R is the universal gas constant (8.31 J/mol K), T is the temperature of the material, ρ_w is the density of water (0.997 kg/m^3 at 25° C), ω_w is the molecular mass of the water vapour (18,016 kg/kmol).

The PTS55 consists of a tiny thermocouple, type T, which is enclosed in a stainless steel screen that allows the water vapour to enter in the sensor (Figure 53).

In order to describe the measurement process of the PTS55, Figure 54 illustrates the schematic diagram of the temperature evolution at the measuring junction. Once the probe is buried within the soil, the thermocouple is cooled by supplying a current of 8 mA (Wescor Inc., 2004). The current is maintained as long as the welded junction has reached a temperature below the dew point (T = T$_{WB}$). During the cooling period the relative humidity of the surrounding air increases and the water vapour condenses on the welded junction. Then, at $t = t_c$ the cooling current is terminated allowing the thermocouple to warm up toward the ambient temperature. During this time, the condensed water on the junction evaporates to the surrounding atmosphere. The evaporation of the water at the junction occurs while the temperature at the junction remains constant and equal to the wet bulb depression temperature ($T_J = T_{WB}$). During this time interval (t_m), the measurements are recorded by the data acquisition system. Several suction measurements can be taken and averaged in order to improve the accuracy of the measurement. The suction measurements must be taken after a certain delay time (t_c), when the temperature of the junction is equal to the wet bulb plateau. Measurements taken before the temperature of the junction reaches the wet bulb plateau can be affected by some errors.

The thermocouple requires being excited for a cooling period that varies from 5 to 60 seconds with a constant current of 8mA. The measurements time can vary from 5 to 250 seconds and during this time the thermocouple transmits an output that varies from 0 to 30mV depending on the measured suction.

The values of the cooling time, the delay time, the measurement time and the reading average used in this study for the calibration of the two psychrometers are listed in Table 2. These values were suggested by AITEMIN (Aitemin, 2014) and are the same values used for the sensors installed in the GAST experiment.
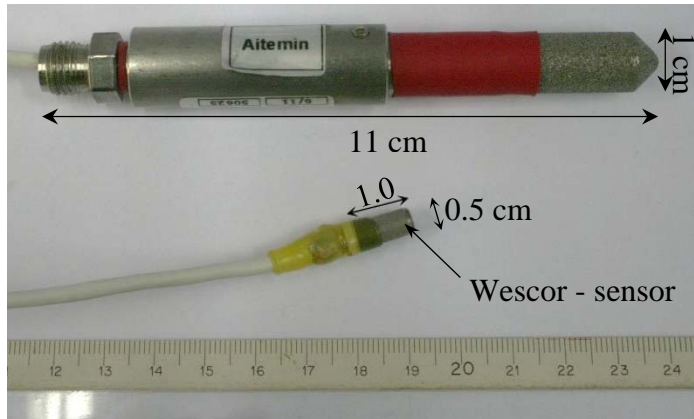
Figure 52: Psychrometers PTS55-Elitech (not water tight) and PTS55-Aitemin (water tight).
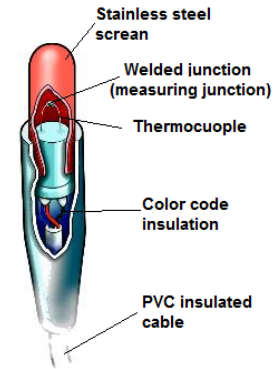

Figure 53 : Scheme of the Peltier thermocouple psychrometer (form http://water.wescor.com).

Table 2: Acquisition parameters set in the PSYPRO.

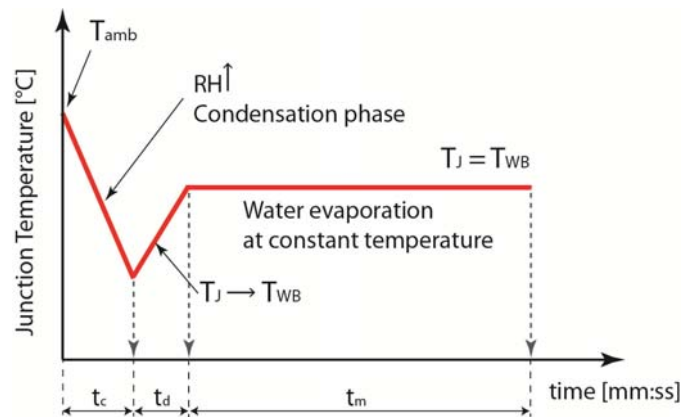| Parameter	Time (s)
Cooling time, t_c	50
Delay time, t_d	10
Measuring time, t_m	25
Reading average, t_r	5

Figure 54: Schematic diagram of the temperature evolution at the measuring junction during the measurement process.

2.1.2 Data acquisition system

The PTS55 is compatible with the data acquisition system (DAS) PSYPRO from Wescor (Wescor Inc., 2004). The PSYPRO console, together with the controlling software, was delivered at LMS/EPFL in November 2014. The PSYPRO is able to control the cooling and the measurement processes of the thermocouple and it allows the user to set the cooling time, the delay time, the measurement time and the reading time. The PRYPRO is equipped with eight channels for reading eight PTS55 sensors.

2.1.3 Calibration procedure

Psychrometers measure the relative humidity based on the temperature difference between the non-evaporating surface (dry bulb) and the evaporating surface (wet bulb) (Fredlund and Rahardjo, 1993). Standard calibration of psychrometer sensors consists in the determination of the relationship between the microvolt output of the sensor and the applied total suction values. However, for the specific case of the PTS55 this relationship is already programmed into the software of the PSYPRO so that the measured suction value can be immediately read. The reference conversion coefficient to relate the output voltage to the total suction is 4.7 µV/MPa. This number was programmed in the PSYPRO by the manufacturer.

Temperature variations may alter the measurement of the total suction. For this type of sensor, the values of total suction registered by the PSYPRO (ψ_r) are automatically corrected for the temperature variations as follows (Wescor Inc., 2004):

$$\psi_m = \frac{\psi_r}{\left(0.325 + 0.027T\right)} \tag{2}$$

where ψ_m is the corrected value of the measured total suction and T is the temperature in °C.

Due to the variability of the geometry of the junctions, and the nature of the elements surrounding the junction, the conversion factor (from microvolt to MPa) differs for each psychrometer. This implies that each psychrometer must be calibrated individually. Moreover, according to the manufacturer, the psychrometer gives measurements of the total suction from 0 MPa up to an upper limit (ψ_{up}) that depends on the cooling coefficient of the thermocouple (Π_v expressed in µV):

$$\psi_{up} = \frac{\Pi_v}{-4.7} \tag{3}$$

The cooling coefficient for Wescor thermocouples varies from 50 to 80 µV (Wescor Inc., 2004). As a consequence, assuming a conversion factor equal 4.7 as suggested by the manufacturer, the theoretical upper limit of the measurements ranges between 10.64 MPa and 17.02 MPa.

The thermocouple psychrometers calibration carried out at LMS/EPFL consisted in the determination of the relationship between the applied total suction and the total suction measured by the sensor and, the determination of the upper limit of the measurement range for each of the two tested PST55 sensors. Moreover, after the first calibration, the cable of the PST55-Wescor was cut, reconnected to a longer cable, and then the calibration was repeated. This operation was explicitly asked by Nagra to assess whether the cable cut would alter the output voltage at the plateau.

The total suction was imposed by means of salty solutions of known total suction values and using the sorption bench apparatus developed at the LMS/EPFL (Salager et al., 2011) (Figure 55). This device is equipped with 8 sealed desiccators which contain the selected salt solution. The desiccators are immersed in a thermo-regulated bath which allows maintaining a constant temperature during the measurements. For the calibration, the psychrometers were suspended above the salt solution inside the desiccators (Figure 56) and the total suction was read.

Pure water and five different saline solutions were used to apply the appropriate range of suction. These solutions are a saturated potassium sulphate (k_2SO_4) solution, and four partially saturated sodium chloride (NaCl) solutions. The relationship between the total suction (ψ in MPa) and sodium chloride concentration (expressed in M) at 20°C is given by the following expression (Witteveen et al., 2013):
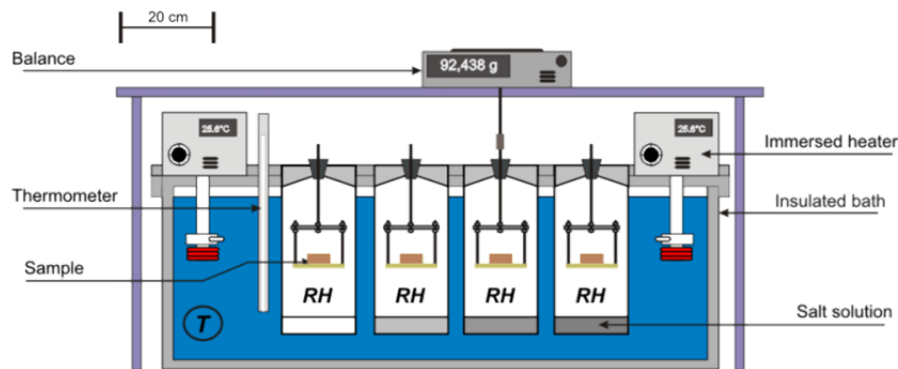
$$\psi = 0.407c^2 + 3.888c + 0.61 \tag{4}$$

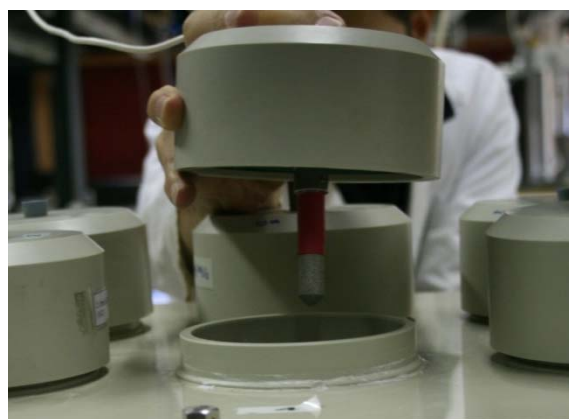**Figure 55: Layout of the sorption bench apparatus (Salager et al., 2011).**

Figure 56: Installation of the PTS55-Aitemin sensor in the sorption bench.

220

The values of the total suction applied for the calibration of the PTS55 are listed in Table 3. The suction was read every five minutes for several hours, until a stationary suction was measured. After the measurements, the sensors were extracted from the desiccators, dried with paper and then placed in the other desiccator. This procedure allows estimating the time for the response of the sensor when fast change of relative humidity occurs.

Table 3 : Values of the total suction applied for PTS55 calibration

Type of solution	Ionic concentration, c (M)	Applied total suction, Ψ (MPa)
Pure water	0.00	0.0
NaCl-1	0.35	2.0
K_2SO_4	-	4.0
NaCl-2	1.23	6.0
NaCl-3	1.55	7.6
NaCl-4	1.55	8.0

2.1.4 Results of the calibration

As a result of the calibration, a linear relationship between the applied total suction (ψ_a) and the total suction measured by the sensor (ψ_m) was obtained:

$$\psi_a = \alpha \psi_m \tag{5}$$

where α is the correction factor of the tested psychrometer. After the calibration, the correction factor obtained for each of the tested sensors needs to be inserted in the PSYPRO software, as shown in Figure 57.
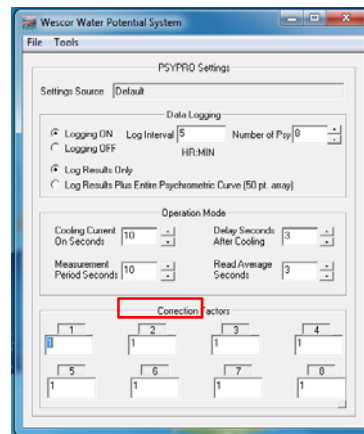

Figure 57: User interface of the PSYPRO software.

Figure 58 and Figure 59 show the total suction versus time curves measured by the two PTS55 psychrometers. It appears that the sensors take a certain time to equalize to the imposed suction. This time results equal to 300 minutes for the sensor PTS55-Wescor and about 400 minutes for the sensor PTS55-Aitemin. This result is attributed to the fact that the thermocouple is protected by a stainless steel screen (Wescor), or further encapsulated in a steel body (Aitemin), that retards the entering of the water vapour into the suction probe. When the measurements are taken using distilled water (0 MPa of applied matric suction) the suction versus time curve, registered with the PTS55-Wescor, appears very unstable and sensitive to small variation of temperature. A drop of temperature of 0.5 °C produces a suction reduction of -2 MPa (Figure 58). This result is related to the problem of condensation of water vapour on the sensor that is very likely at this high relative humidity. Condensation may lead to small variation of the relative humidity around the welded junction which causes a very large variation of the measured total suction because of the logarithmic nature of the Kelvin's law.

When a suction of 7.6 MPa is applied, the PTS55-Wescor returns a zero suction value at the beginning of the measurements and then a very unstable suction reading suggesting that this suction might be outside the measurement range. The PTS55-Aitemin showed realistic readings when a suction of 8 MPa was applied, suggesting a higher upper limit of the measuring range (ψ_{up}) with respect to the PTS55-Wescor.

The total suction versus time curves measured by the PTS55-Wescor, after the cutting/reconnection procedure, are depicted in Figure 60. The sensor after cut shows a similar behaviour than before the cut. Nevertheless, in this configuration the sensor returns a very unstable reading when a suction of 6 MPa is applied.

The measured suction versus applied suction relationship for the two tested psychrometers is depicted in Figure 61. As expected, the two sensors show different values for the correction factor.

In Figure 61.a the results of the sensor calibration performed after the cut/reconnection procedure are also reported. It was found that the measured suction values after the cut differed only slightly from the suction values measured after the cut.
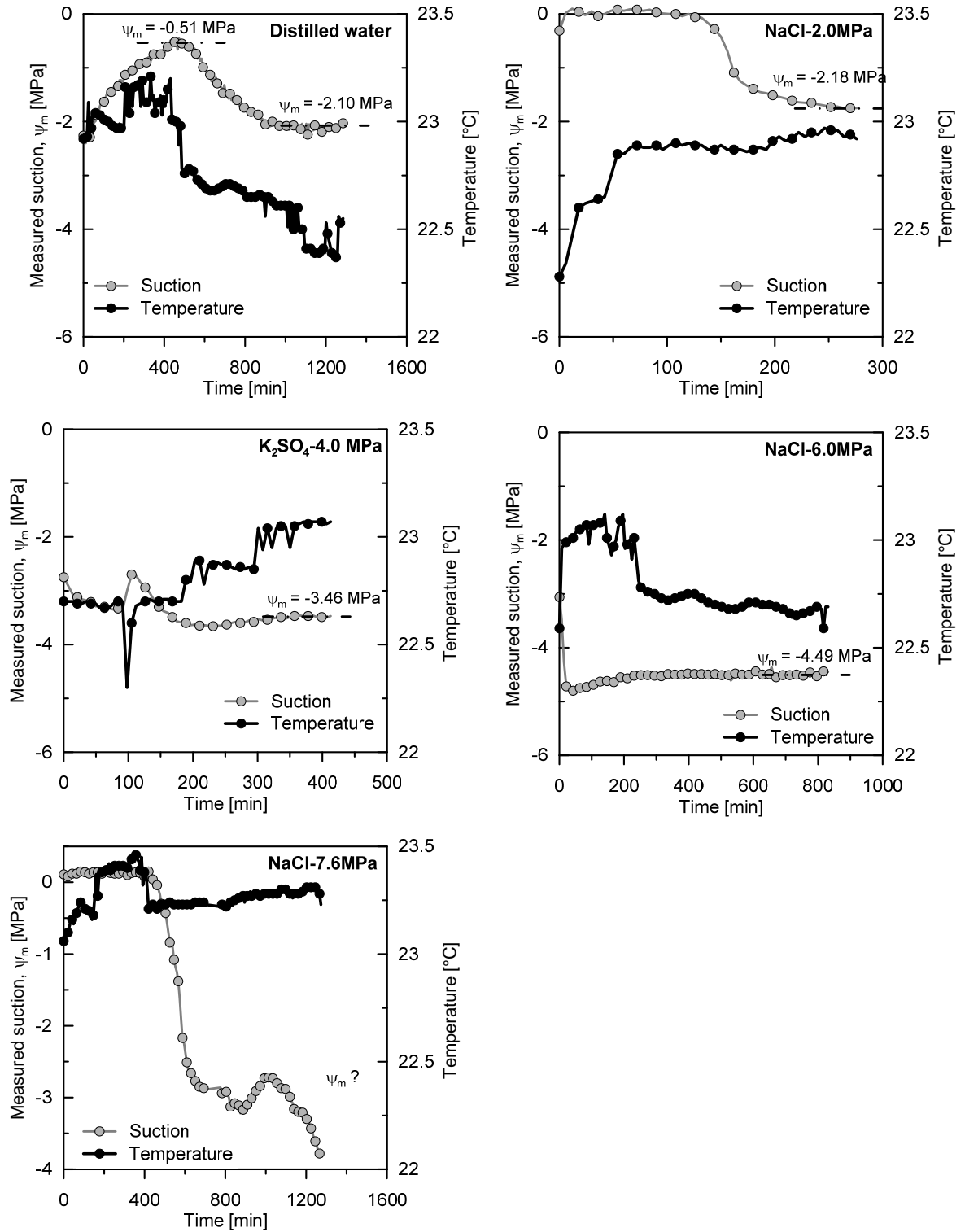
Figure 58: Time versus measured suction curves of the PTS55 from Elitech for the different salty solutions.
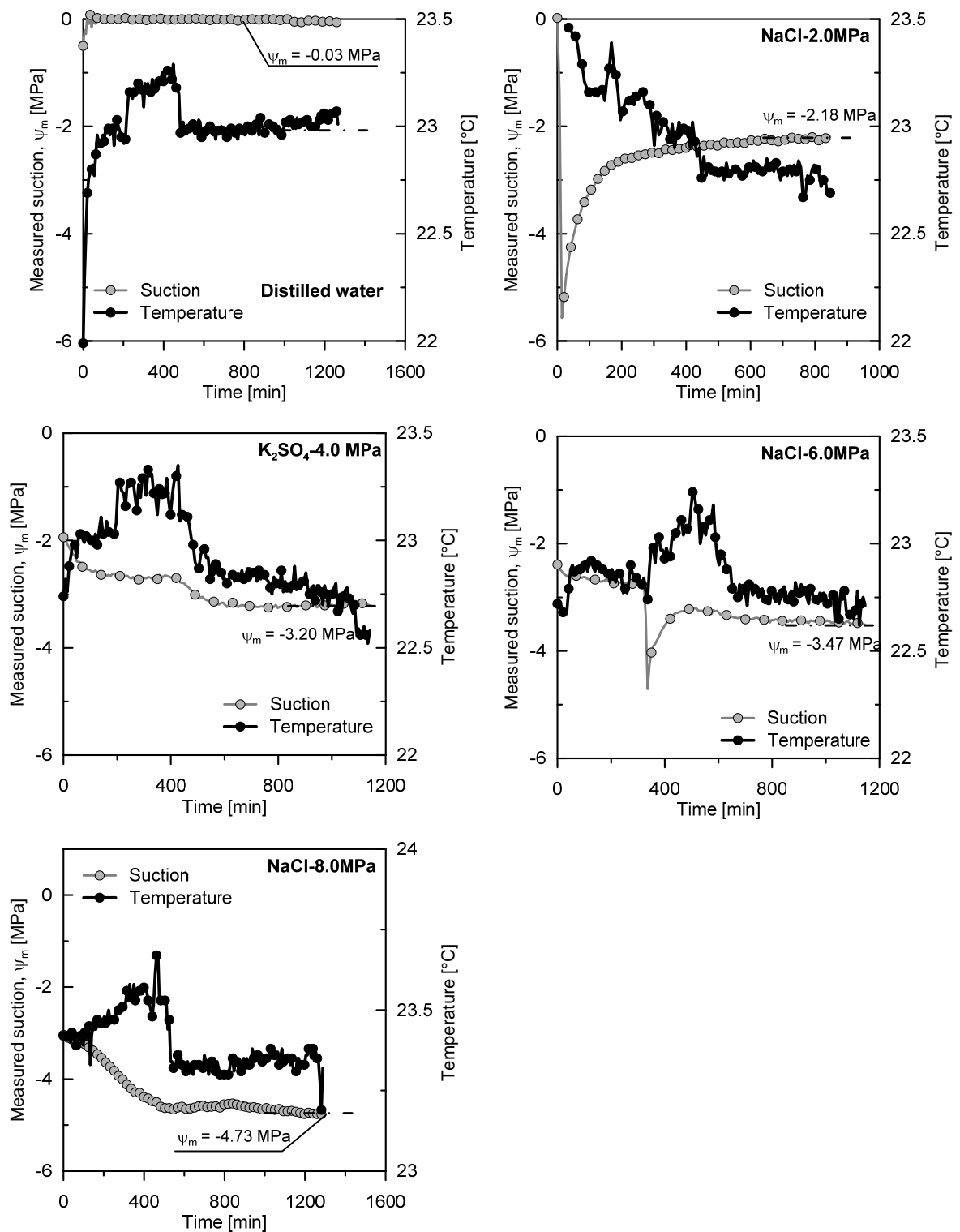
Figure 59: Time versus measured suction curves of the PTS55 from Aitemin for the different salty solutions.
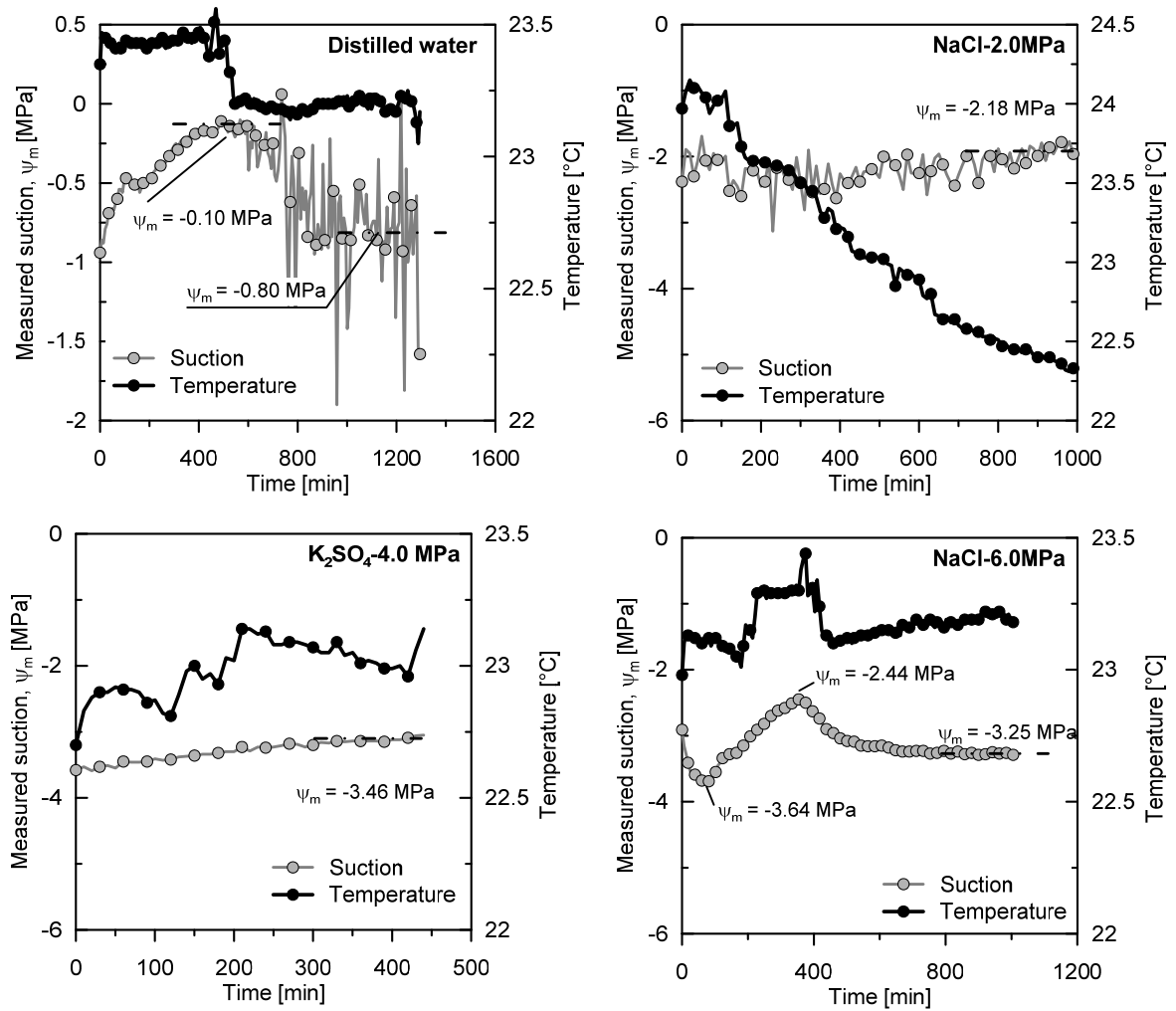
Figure 60: Time versus measured suction curves of the PTS55-Wescorfor the different salty solutions after cable cut.
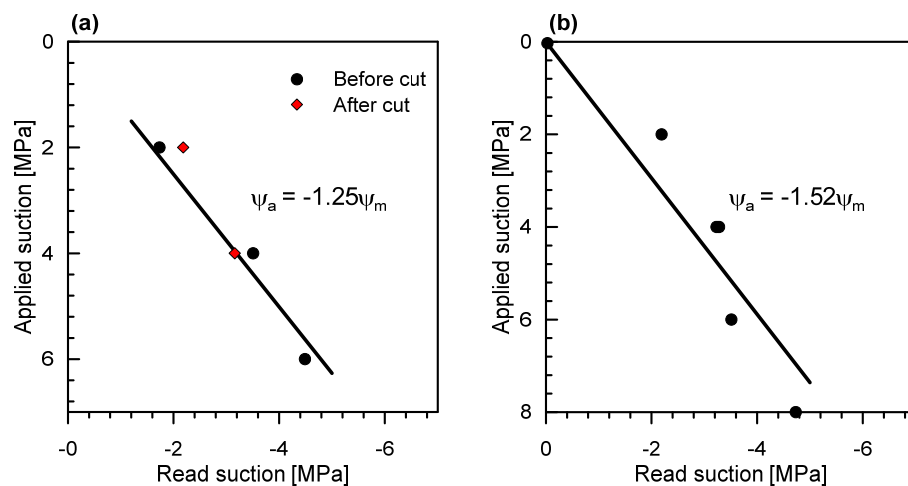

Figure 61: Calibration curve for the PTS55-Wescor before and after the cable cut (a). Calibration curve for the PTS55-Aitemin (b).

2.2 229-WMP THERMAL CONDUCTIVITY SENSOR

2.2.1 Sensor description and principle of operation

The 229-WMP is a cylindrically shaped element, of 60 mm in length and 15 mm in diameter (Figure 62). The cylinder consists of two parts, a ceramic element which is 36 mm in length and an epoxy element of 24 mm in length. A hypodermic needle is located in the centre of the ceramic element. A heating element (a small resistance) of the same length of the ceramic body and a thermocouple are placed inside the needle (Figure 63). The hypodermic needle has the double function of maintaining the thermocouple and the heating element in the right position and to protect the delicate wires. The volume inside the needle which is not occupied by the wirings is filled with epoxy.

The rate of heat conduction of the ceramic porous body depends on its water content. Thus, a change in water content in the ceramic element causes a chance in its thermal conductivity. The dry ceramic tip has a thermal conductivity of 0.35 W/mK thus negligible heat is dissipated by the air in the pores (Leong et al., 2012).

When the sensor is placed within the soil, water movement between the soil and the ceramic tip occurs due to gradient of water potential. At the equilibrium the matric suction of the soil surrounding the sensor and the ceramic element is the same. The time required for equilibrium depends on both the magnitude of the hydraulic gradient and the hydraulic conductivity of the soil. According to the manufacturer, this time can vary from minutes to tens of minutes and it can be reduced by filling the ceramic pores with water before the installation (Campbell Scientific Inc., 2009). On the contrary, according to Leong et al. (2012), the time required for the equalization can vary from hours to tens of hours and is strongly affected by the contact conditions between the soil and the porous body. At high suction values the tip is not fully saturated and its effective permeability reduces causing additional delay on the time required for the suction equalization.

Figure 62 : Thermal conductivity sensor 229-WMP (Campbell Scientific Inc.).
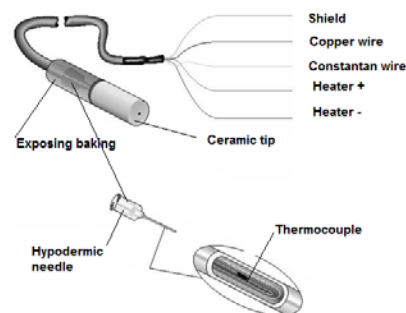

Figure 63 : Schematic representation of the 229-WMP (modified from 229-WMP user manual).

When the heater is turned on, heat is generated and the temperature increases near the heat source. The temperature increment is recorded by the temperature sensor (thermocouple). The magnitude of ΔT depends on the heat that is not dissipated so is a function of the thermal conductivity of the sensor. Considering that the thermal conductivity increases as the water content increases, and consequently more heat is dissipated, the augmentation of the water content causes a decrease of the registered ΔT.

2.2.2 Data acquisition system

Three copper wires, one constantan wire and the ground in burial-grade sheath provide a path for connecting the instrumentation to the excitation modulus and to the data acquisition system.

The 229-WMP requires being excited with a constant current source of 50 ±0.25 mA. The Campbell scientific allows to select between two excitation modules (CE4 and CE8) which can be used to excite up to 4 or up to 8 probes simultaneously by a voltage of 12 V.

In order to provide a constant current source, during the calibration the heater was connected to a power generator type Weir 4000 30V-1A from Telemeter Electron AB available at the LMS/EPFL. The temperature variations in time, with the applied current, were read with the thermocouple connected to a data acquisition system type 34970A (from Agilent) available at the LMS/EPFL.

2.2.3 Calibration procedure

According to the manufacturer, the sensor gives measurements of the matric suction in the range of 10 to 2500 kPa with an accuracy of 1 kPa for matric suctions higher than 100 kPa. The heat transfer property of the sensor depends on the thermal properties of the different materials composing the probe (e.g stainless steel needle, ceramic tip, resin etc.), on the interfaces between the different materials (the density of the point of contact between two materials) and on the arrangement of the wires within the probe. The uncontrollable variability in the heat transfer properties among the sensors requires that each sensor must be calibrated individually by the user (Campbell Scientific Inc., 2009).

The goal of the calibration is to determine a relationship between the matric suction and the temperature variation read by the thermocouple. This relationship is normally expressed by the following expression (Campbell Scientific Inc., 2009, Leong et al., 2012):

$$s = e^{\alpha\Delta T + \beta} \tag{6}$$

where s is the matric suction, ΔT is the temperature variation during the heating time, α and β are fitting parameters.

The calibration of the 229-WMP is performed by applying a range of matric suction on a soil in which the sensor is embedded and the corresponding values of ΔT are read.

For the calibration of the 229-WMP carried out at LMS/EPFL, cylindrical specimens (7 cm high and 8 cm in diameter) were created by compacting Sion silt at five different values of water content (4%, 8%, 12% 16%, 20%). The Sion silt has been selected because its hydraulic and retention properties have been extensively investigated (Geiser, 1999, Péron, 2007). The material has been classified according to the USCS method as CL (clayey silt with sand). The index properties of the Sion silt are reported in Table 4.

For the preparation of the specimens the dry silt was mixed with distilled water in order to achieve the target water content values. The wet silt was stored in a hermetic box for 2 days to allow the moisture equilibrium. Then the material was passed through a 4 mm sieve in order to limit the size of the aggregates. Finally, the specimens were prepared by static compaction in cylindrical moulds at the target dry density of 1.7 g/cm^3. After compaction the specimens were sealed in a hermetic container for minimum two days in order to let the matric suction to equalize within the whole specimen volume.

Two identical specimens were prepared for each of the target water content. The first one was used to determine the matric suction of the as-compacted material. The second one was used to perform the sensor reading. The matric suction was measured using the contact filter paper method (ASTM D5298-10). The method is used as an indirect means of measuring soil suctions in a wide range of suctions. It consists of placing a filter paper in contact with the specimen in order to reach suction equilibration between the specimen and the filter paper through the liquid phase (Figure 64). After two weeks, the filter paper is extracted from the specimens and its water content is measured. Matric suction is obtained through the use of the calibrated water retention curve of the paper (Figure 65). The need for precautions in the use of the filter paper method for suction measurements was pointed out (Leong et al., 2002). In particular the calibration curves reported in the literature are often different from those recommended in the ASTM D5298-10. Ad-hoc calibration curves were obtained in the laboratory before the measurements on the compacted specimens were performed. The calibration was performed on an oven-dried Schleicher and Schuell No. 589 filter paper. The oven-dried initial condition (two minutes at 105°C) ensures a transfer of water from the specimen to the paper during the measurement (Ferrari et al., 2011).

Table 4: Index properties of the Sion silt

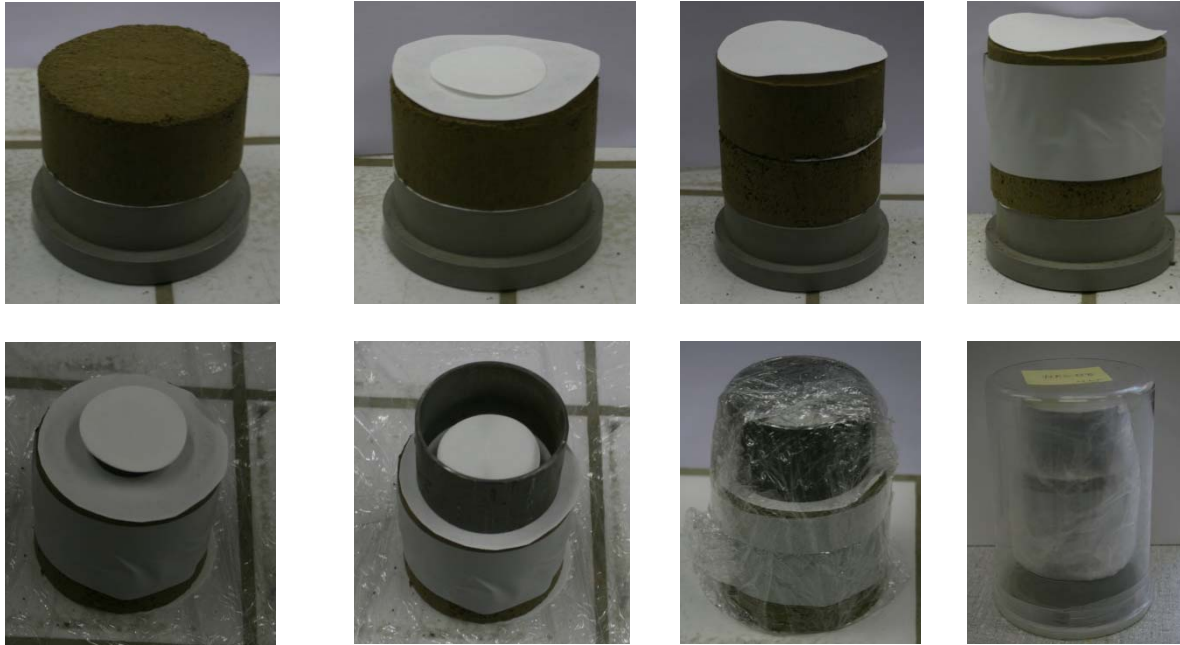| w_L (%)	w_P (%)	I_P	%<2μm	%<20 μm	%<60 μm	γ_s (kN/m^3)
25.4	16.7	8.7	8	41	84	27.41

Figure 64: Measurements of the matric and total suction of a Sion silt specimen using the filter paper method.

In order to insert the 229-WMP in the specimen, a hole of a diameter slightly smaller than the diameter of the sensor was drilled; then the sensor was pushed into the soil. This technique ensures a good contact between the soil and the porous body. The ΔT versus time curve was registered every hour until the matric suction equilibrium between the porous element of the sensor and the soil was achieved. In order to prevent water content loss and minimize the fluctuation of the temperature during the measurements, the specimen was sealed with paraffin tape and cover with insulating foam. The phases of the 229-WMP sensor installation are depicted in Figure 66.
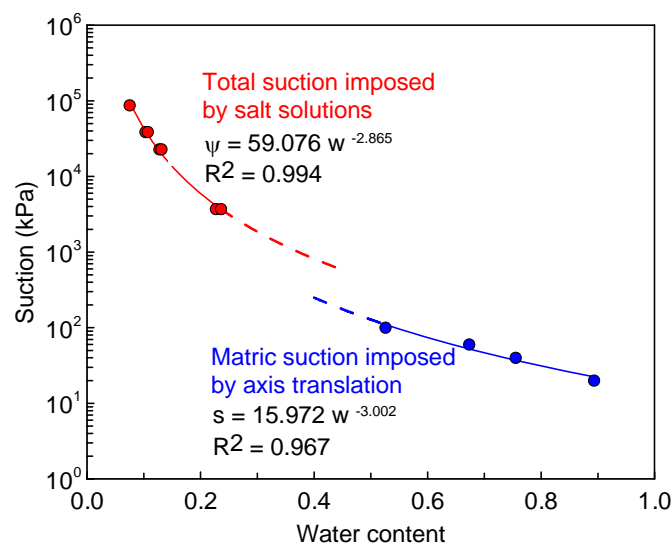

Figure 65: Calibration curves for total and matric suction obtained on Schleicher and Schuell No. 589 filter paper(Ferrari et al., 2011).

Figure 66: Phases of the insertion of the 229-WMP inside a compacted specimen of Sion silt

Before the installation of the sensor, the 229-WMP was submerged in distilled water for 24 hours in order to saturate the porous element. This procedure leads to an increasing of the hydraulic conductivity of the porous element and the equilibrium time is reduced.

Continuous measurement of ΔT during the equilibrium phase allows determining the sensor response time and the time required for suction equilibrium.

The measurements of ΔT were taken starting about 30 minutes after the sensor was inserted into the soil. Despite the manufacturer suggested that a heating period of 30 s was sufficient to reach the final ΔT, the measurements shows that the ΔT stabilization requires more time (section 2.2.4). For that reason, a heating time of 60 seconds was adopted for the calibration. As suggested by the manufacturer, the temperature rise during the test is calculated by subtracting the temperature at 1 second from the subsequent temperature measurements.

2.2.4 Results of the calibration

The water retention curve of the Sion silt obtained using the filter paper method is depicted in Figure 67. The experimental data obtained with the filter paper method were fitted with the equation proposed by Van Genuchten (1980):

$$S_r = \left(\frac{1}{1 + \left(\dfrac{s}{\alpha} \right)^n} \right)^m \tag{7}$$

where S_r is the degree of saturation, and α, n and m are material. The values of the obtained parameters are reported in Table 5.
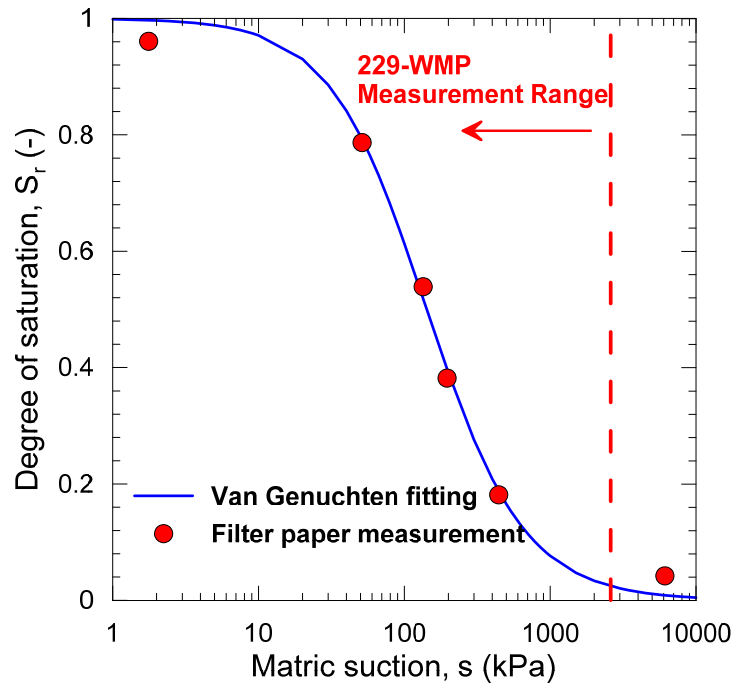
Figure 67: Water retention curve of the Sion silt.

Table 5: Van Genuchten parameter for the Sion silt.

Van Genuchten parameters	
α (kPa)	131.86
m	0.93
n	1.33

Figures 17 to 22 present the curves ΔT vs time obtained during the equalization phase of the 229-WMP, for each of the tested specimens. For each graph, the curves tend to become closer to each other during the equalization phase as the matric suction of the sensor equalizes with the one of the soil. The measurements are considered as concluded once a maximum different of 0.1°C (which corresponds to the accuracy of the available data acquisition system) between two subsequent measurements is reached. The measurements are taken on specimens prepared at the same water content, and same dry density, of the specimens used for the matric suction measurements with the filter paper technique. The characteristic of the twelve tested specimens are reported in Tables 6 to 17.

In Tables 6 to 17 the time necessary for equalization (t_{eq}) is also reported. As it is shown, there is not a clear dependency on the soil matric suction. This result can be justified considering that t_{eq} depends on the initial difference between the matric suction of the ceramic element and the one of the soil. This difference is not known *a priori* and for that reason the time necessary for equilibrium is not predictable. In the results of this study, a maximum t_{eq} of

about 5.5 hours was registered for the specimen prepared at 9% of water content. As rule of thumb, it is recommended to perform several subsequent measurements of the soil suction with a time interval of 1 hour until no significant difference is observed for two consecutive measurements.
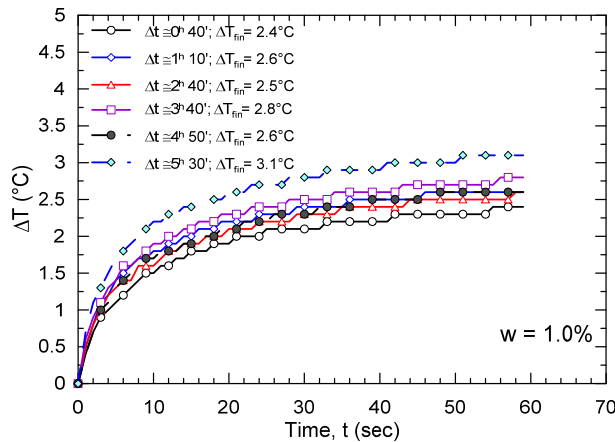

Figure 68 : ΔT – time curve obtained during the equilibrium phase of the 229-WMP calibration. (w = 1%).

Table 6: Characteristics of the specimen for the suction measurements at w = 1%.

Filter paper measurements	
ρ_d (g/cm^3)	1.68
e (-)	0.66
w (-)	0.01
S_r (-)	0.04
s (kPa)	6111
ψ (kPa)	67331

Table 7: Characteristics of the specimen for the ΔT measurements at w = 1%.

Sensor measurements	
ρ_d (g/cm^3)	1.73
e (-)	0.62
w (-)	0.01
S_r (-)	0.04
ΔT (°C)	3.1±0.1
t_{eq} (hours)	>5.5

Figure 69 : ΔT – time curve obtained during the equilibrium phase of the 229-WMP calibration. (w = 4.6%).

Table 8: Characteristics of the specimen for the suction measurements at w = 4.6%.

Filter paper measurements	
ρ_d (g/cm^3)	1.63
e (-)	0.72
w (-)	0.05
S_r (-)	0.18
s (kPa)	443
ψ (kPa)	2397

Table 9: Characteristics of the specimen for the ΔT measurements at w = 4.6%.

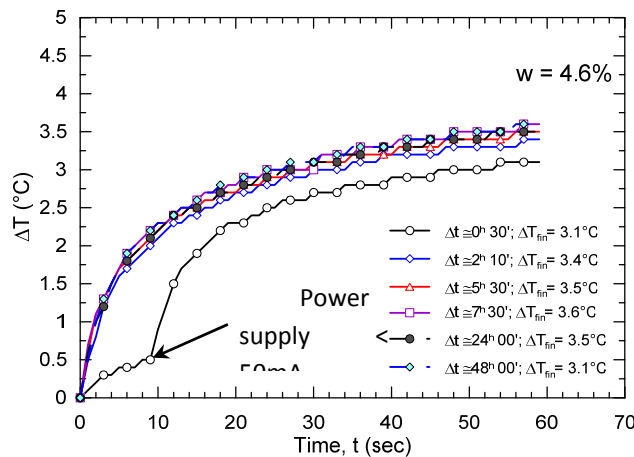| Sensor measurements	
ρ_d (g/cm^3)	1.67
e (-)	0.68
w (-)	0.05
S_r (-)	0.19
ΔT (°C)	3.4±0.1
t_{eq} (hours)	≈0.5

232

Figure 70 : ΔT – time curve obtained during the equilibrium phase of the 229-WMP calibration. (w = 9.0%).

Table 10: Characteristics of the specimen for the suction measurements at w = 9.0%.

Filter paper measurements	
ρ_d (g/cm^3)	1.69
e (-)	0.66
w (-)	0.08
S_r (-)	0.38
s (kPa)	196
ψ (kPa)	1145

Table 11: Characteristics of the specimen for the ΔT measurements at w = 9.0%.

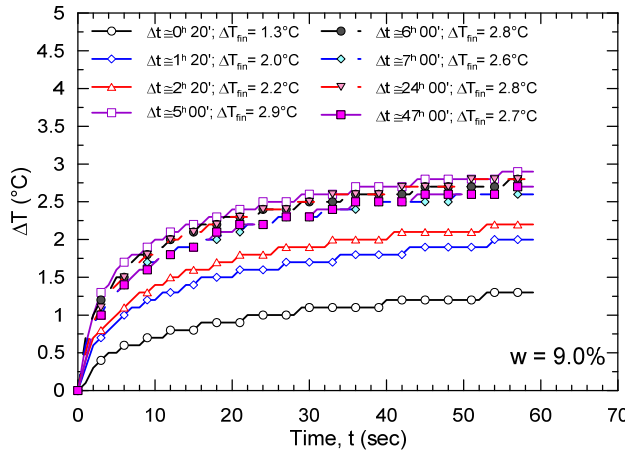| Sensor measurements	
ρ_d (g/cm^3)	1.69
e (-)	0.66
w (-)	0.08
S_r (-)	0.38
ΔT (°C)	2.8±0.1
t_{eq} (hours)	≈5.5

Figure 71 : ΔT – time curve obtained during the equilibrium phase of the 229-WMP calibration. (w = 12.5%).

Table 12: Characteristics of the specimen for the suction measurements at w = 12.5%.

Filter paper measurements	
ρ_d (g/cm^3)	1.69
e (-)	0.66
w (-)	0.13
S_r (-)	0.54
s (kPa)	134
ψ (kPa)	618

Table 13: Characteristics of the specimen for the ΔT measurements at w = 12.5%.

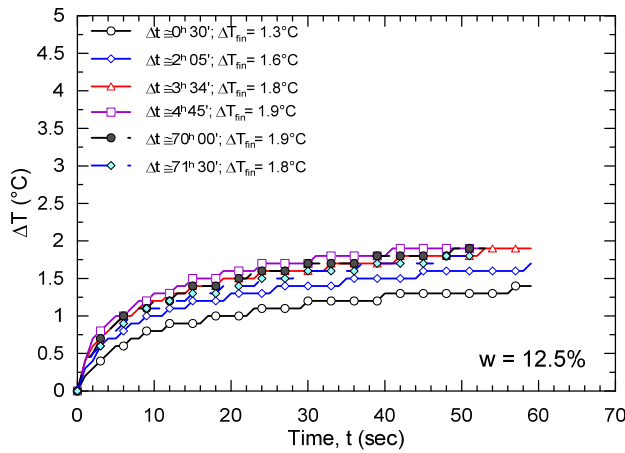| Sensor measurements	
ρ_d (g/cm^3)	1.63
e (-)	0.72
w (-)	0.13
S_r (-)	0.50
ΔT (°C)	1.9±0.1
t_{eq} (hours)	≈3.5

Figure 72: ΔT – time curve obtained during the equilibrium phase of the 229-WMP calibration. (w = 16.1%).

Table 14: Characteristics of the specimen for the suction measurements at w = 16.1%.

Filter paper measurements	
ρ_d (g/cm^3)	1.78
e (-)	0.57
w (-)	0.16
S_r (-)	0.79
s (kPa)	51
ψ (kPa)	620

Table 15: Characteristics of the specimen for the ΔT measurements at w = 16.1%.

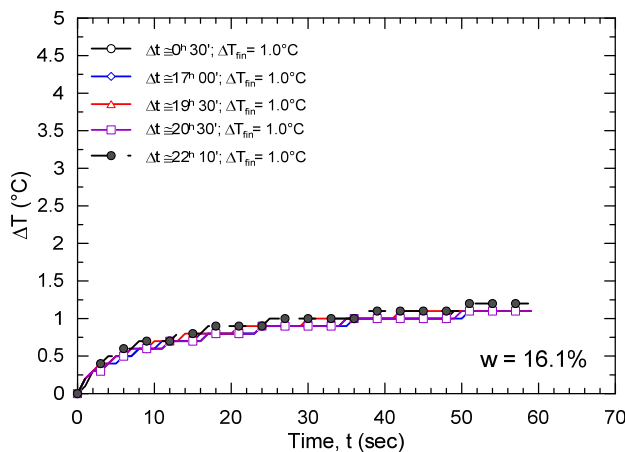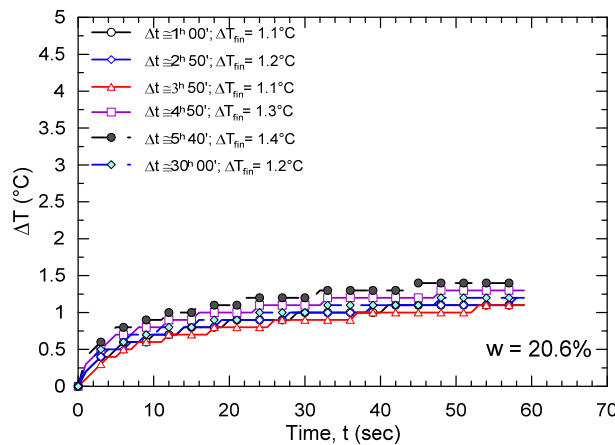| Sensor measurements	
ρ_d (g/cm^3)	1.79
e (-)	0.56
w (-)	0.16
S_r (-)	0.80
ΔT (°C)	1.0±0.1
t_{eq} (hours)	≈0.5

Figure 73: ΔT – time curve obtained during the equilibrium phase of the 229-WMP calibration. (w = 20.6%)

Table 16: Characteristics of the specimen for the suction measurements at w = 20.6%

Filter paper measurements	
ρ_d (g/cm^3)	1.75
e (-)	0.60
w (-)	0.21
S_r (-)	0.96
s (kPa)	2
ψ (kPa)	14

Table 17: Characteristics of the specimen for the ΔT measurements at w = 20.6%

Sensor measurements	
ρ_d (g/cm^3)	1.72
e (-)	0.63
w (-)	0.21
S_r (-)	0.92
ΔT (°C)	1.3±0.1
t_{eq} (hours)	≈1

The result of the calibration and the values of the two parameters α and β (defined in eq. (6)) are showed in Figure 74.

The specimen prepared at 1% of water content was not considered in the curve fitting due to the fact that its matric suction (6111 kPa) was much higher than the maximum suction measurable by the 229-WMP (2500 kPa, as reported by the manufacturer) (Figure 68). For the specimen prepared at 20.6% of water content, which corresponds to a suction of 2kPa, the measured ΔT was found to be higher than the ΔT measured for the specimen prepared at 16% of water content (s = 51 kPa). In this case, the result is related to the low accuracy of the probe when fully saturated conditions are approached.

The values of the parameters α and β obtained in this study are different from the values proposed by the manufactured (Campbell scientific, 2009) and the ones proposed by Leong et al. (2012). This difference is attributed to the different excitation module and data acquisition system used in the aforementioned study. The temperature rise readings result very sensitive to the excitation system. This observation is confirmed by Figure 69 in which the results of the specimen prepared at 4% of water content are depicted. During the first measurement a current lower that 50mA was supplied to the sensor for the first 10 seconds and lower values of ΔT were detected.
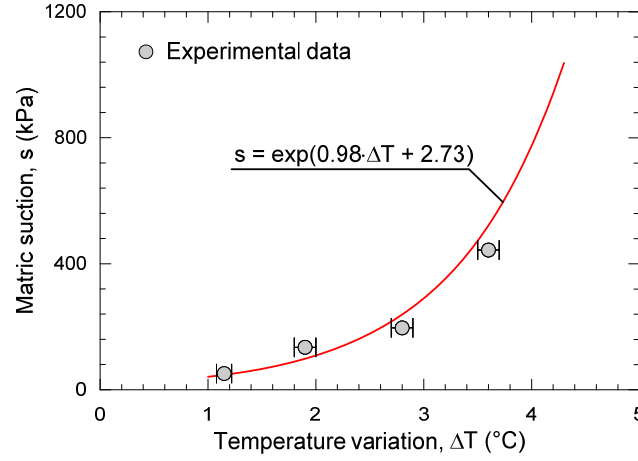
Figure 74: Calibration curve for the 229-WMP sensor

2.2.5 Error due to the DT accuracy

The 229-WMP measures the matric suction of the soil by means of the measurement of the temperature rise during the sensor heating. For this reason, the accurate measure of the ΔT is crucial for reaching a good accuracy in the determination of the soil matric suction.

The DAS available at LMS allows temperature measurements with an accuracy of $\varepsilon_T \pm$ 0.1°C.

The relationship between the error in the measured matric suction (*s*) and the temperature accuracy can be obtained considering the derivative of equation (6) with respect to temperature and normalizing the error with respect to the current matric suction:

$$\frac{\Delta s}{s} = \left(\frac{\partial s}{\partial T} \varepsilon_T \right) \frac{1}{s} = \alpha \left(e^{\alpha \Delta T + \beta} \right) \frac{\varepsilon_T}{s} \tag{8}$$

According to eq. (8), the error in percentage associated to the matric suction measurement results equal to 10% over the whole measurements range.

3 Final remarks

This section presents some recommendations for the use of the sensors, based on the experience gained during the testing activities.

Based on the calibration of the PTS55 psychrometer the following suggestions are given:

- Each PTS55 requires its own calibration in order to identify the conversion factor to obtain the actual suction from the measured suction and also to determine the upper limit of the measurement range.

- For the PTS55-Wescor, when 0 kPa total suction was applied to the sensor the measured suctions appeared very sensitive to temperature variations and the measurements were not realistic.
- The PTS55- Aitemin appeared less sensitive to temperature fluctuations.
- The suction equilibrium was achieved after about 300 to 400 minutes, depending on the configuration, showing that the sensor is not suitable for taking instantaneous suction measurement since it requires a certain time to give stable suction values.

Moreover, calibration must be repeated over time as the thermocouple into the psychrometers can deteriorate during the working life (Ridley and Wray, 1996).

Based on the calibration of the 229-WMP the following suggestions are given:

- Each 229-WMP must be calibrated individually.
- Despite the sensor results relatively easy to be handled and to be connected to the DAS available at the LMS, the ΔT measurements resulted very sensitive to the excitation and data acquisition system.
- The DAS available at LMS allows ΔT measurement reading with an accuracy of 0.1 °C which leads to an accuracy in the matric suction measurement of approx. 10%.

For this reason, before performing suction measurements, it is recommended to run the calibration with the DAS that will be used for performing laboratory or in-situ measurements.

4 References

Aitemin (2014). *GAST Project. A short guide for managing the PSYPRO loggers.*

ASTM D5298-10 (2010). Standard Test Method for Measurement of Soil Potential (Suction) Using Filter Paper.

Campbell Scientific (2009). 229 Heat dissipation matric water potential sensor. User manual.

Ferrari, A., Eichenberger, J., Fern, J. & Laloui, L. (2011). *Geomechanical analysis for the establishment of an early warning system in the llano grande mine (Costa Rica). Laboratory testing and numerical simulations.* Technical Note LMS/EPFL S6229.

Fredlund, D. G. & Rahardjo, H. (1993). *Soil mechanics for unsaturated soils.* John Wiley & Sons.

Geiser, F. (1999). *Comportement mécanique d'un limon non saturé. Étude expérimentale et modélisation constitutive.*

Leong, E. C., He, L. & Rahardjo, H. (2002). Factors affecting the filter paper method for total and matric suction measurements. *ASTM geotechnical testing journal* **25(3)**:322-333.

Leong, E. C., Zhang, X.-H. & Rahardjo, H. (2012). Calibration of a thermal conductivity sensor for field measurement of matric suction.

Péron, H. (2007). *Desiccation cracks in clayey soils.*

Ridley, A. & Wray, W. (1996). Suction measurement: a review of current theory and practices In *Proceedings of Proceedings of the first international conference on unsaturated soils/Unsat'95/Paris/France/6-8 September 1995. Volume 3.*

Salager, S., Rizzi, M. & Laloui, L. (2011). An innovative device for determining the soil water retention curve under high suction at different temperatures. *Acta Geotechnica* **6(3)**:135-142.

Van Genuchten, M. T. (1980). A closed-form equation for predicting the hydraulic conductivity of unsaturated soils. *Soil Science Society of America Journal* **44(5)**:892-898.

Wescor Inc. (2004). Water potential system. PSΨPRO. User manual.

Witteveen, P., Ferrari, A. & Laloui, L. (2013). An experimental and constitutive investigation on the chemo-mechanical behaviour of a clay. *Géotechnique* **63(3)**:244-255.

CONTACT DETAILS

Address	EPFL ENAC-IIC-LMS, GC D0 401, Station 18 CH 1015 Lausanne, Switzerland
Telephone	Fixed: [+41]21 693 2333 Mobile: [+41]76 275 6180
e-mail	Donatella.manca@epfl.ch

PERSONAL INFORMATIONS

Born on February 12th, 1985; Italian citizen; Single

Mother tongue:	Italian
Foreign languages	English, Spanish, French

WORK EXPERIENCE

From December 2011 to present	PhD assistant at the Laboratory for Soil Mechanics, EPFL, Lausanne Switzerland) on:
	o Hydro-chemo-mechanical characterisation of sand/bentonite mixtures, with a focus on the water and gas transport properties
From June to November, 2011	Research assistant at the Laboratory of soil mechanics, EPFL, Lausanne (Switzerland) on:
	o Experimental analysis on the hydro-mechanical behaviour of Shales
From June to October, 2010	Part-time collaboration at CESIT, Polytechnic of Turin, Torino (Italy)
	o Assistant for students in the computer laboratory of Polytechnic

TEACHING EXPERIENCE

2011 to present	Teaching assistant:
	o Soil mechanics. Bachelor level course at the Swiss federal institute of technology of Lausanne
	o Physics II. Bachelor level course at the Swiss Federal Institute of Technology of Lausanne
	o Geomechanics. Master level course at the Swiss federal institute of technology of Lausanne

EDUCATION

2011 - 2015	**Doctoral program in Mechanics** (EDME), Swiss Federal Institute of Technology of Lausanne, Lausanne (Switzerland). Supervisor: Prof. Lyesse Laloui; Dr. A. Ferrari
2008-2011	**Master degree in Civil Engineering**, Polytechnic of Turin, Torino (Italy) Dissertation: "Theoretical and experimental study on the state of strength and strain induced in the ground by the excavation of a slurry cut-off wall". Supervisor: Prof. V.N. Ghionna
Year 2009/2010	**Erasmus programme**, Universidad de Granada, Granada (Spain)
2005-2008	**Bachelor degree in Civil Engineering**, Polytechnic of Turin, Torino (Italy)

PUBBLICATIONS

J1   **Manca, D.,** Ferrari, A. & Laloui, L. (2015) Fabric evolution and the related swelling behaviour of a sand/bentonite mixture upon hydro-chemo-mechanical loadings. *Géotechnique.*

C1   **Manca, D.,** Ferrari, A. & Laloui, L. (2014) Gas injection and swelling tests on a sand bentonite mixture: investigation on the effects of pore water chemistry. International Conference on the Performance of Engineered Barriers, Hannover (Germany).

C2   A. Ferrari, V. Favero, **D. Manca** and L. Laloui (2013). Volumetric behavior and consolidation of shales at high confining stresses. 47th US Rock Mechanics/Geomechanics Symposium, San Francisco (USA).

C3   Todori, S.P., Rüedi, J., Reinhold, M., **Manca, D.** (2013) Design, testing and emplacement of sand-bentonite for the construction of a Gas-permeable Seal Test (GAST). 15th International Conference on Environmental Remediation and Radioactive Waste Management ICEM2013. Brussels, Belgium.

R1   Rüedi, J., Marchall, P., **Manca, D.**, Ferrari, A., Laloui, L., Kulenkampff, J., Gründig, M., Lippmann-Pipke, J. & Kontar, K. (2013) FORGE (Fate of Repository Gases) Final Laboratory Report. Deliverables D03.34 and D3.36.Arbeitsbericht NAB.

R2   Ferrari, A., Favero, V., **Manca, D.**, Laloui, L. Geotechnical characterization of core samples from the geothermal well Schlattingen SLA-1 by LMS/EPFL. Arbeitsbericht NAB 12-50